



Max-Planck-Institut für Polymerforschung  
Max Planck Institute for Polymer Research



# Ion Transport in Nanochannels Probed by *In Situ* Nanodielectric Spectroscopy

---

Dissertation zur Erlangung des Grades  
**‘Doktor der Naturwissenschaften (Dr. rer. nat)’**  
im Promotionsfach Physikalische Chemie

am Fachbereich Chemie, Pharmazie, und Geowissenschaften  
der Johannes Gutenberg-Universität, Mainz

Von  
**Yun Dong**

Mainz 2025



JOHANNES GUTENBERG  
UNIVERSITÄT MAINZ

DEPOSIT LICENSE:  
Attribution (CC-BY-4.0)

This thesis was carried out from September 2021 until August 2025 in the department of Prof. Dr. Hans-Jürgen Butt in the group of Prof. Dr. George Floudas at the Max Planck Institute for Polymer Research, Mainz.

Gutachter 1: Prof. Dr. Hans-Jürgen Butt

Gutachter 2: Prof. Dr. Holger Frey

Date of oral examination: 12.11.2025

I hereby declare that I wrote the dissertation submitted without any unauthorized external assistance and used only sources acknowledged in this work. All textual passages which are appropriate verbatim or paraphrases from published and unpublished text, as well as all information obtained from oral sources are duly indicated and listed in accordance with bibliographical rules. In carrying out this research, I complied with the rules of standard scientific practice as formulated in the statutes of Johannes Gutenberg University Mainz to ensure standard scientific practice.

Mainz, 08.08.2025

(Place, Date)



(Signature)

## Abstract

Understanding the way that ions penetrate in narrow pores is essential for the development of systems where precise control of transport properties is required (e.g. in high-performance materials used in energy storage, nanofluidics, and sensing technologies). This Thesis explores the ion transport behavior of ionic liquids (ILs), polymerized ionic liquids (PILs), and their mixtures (ILs/PILs) in nanopores, using *in situ* nanodielectric spectroscopy. The research addresses how the geometry of confinement, the molecular structure/design, and the interfacial interactions collectively govern ion transport, phase behavior, and polymer dynamics.

Confined ILs display different physical properties when compared to their bulk state. They include suppressed crystallization, shifted glass temperature, and reduced ionic conductivity. These changes can be largely attributed to interfacial interactions between the ions and the pore walls. Ion adsorption at the surface leads to a reduction in the number of mobile charge carriers, directly impacting ionic conductivity. Furthermore, spatial confinement affects nucleation, in some crystallizable ILs resulting in the suppression of crystallization in smaller pores. Notably, the geometry of confinement also plays a key role in determining ion dynamics. ILs within conically shaped nanopores, for example, exhibit higher ionic conductivity than within cylindrical ones. This enhancement is likely due to the uneven surface charge distribution in conically-shaped pores, which reduces the strength of Coulomb interactions in the vicinity of the narrower openings.

In PILs, the size and structure of the tethered cation significantly influence both imbibition dynamics and ionic conductivity. Cations whose charged imidazolium rings are located close to the polymer backbone restrict chain mobility and lead to a higher viscosity. In contrast, cations having additional phenyl spacers between the backbone and the imidazolium ring promote greater chain flexibility and improved ionic mobility. A strong decoupling between segmental dynamics and ion transport is observed below the glass temperature under strong confinement. This phenomenon is consistent with the “shoving model”, according to which ion movement in confined environment is facilitated by the ability to deform the local matrix.

IL/PIL mixtures are *dynamically heterogeneous* in the bulk. Their infiltration into nanopores leads to enhanced local segregation and eventually to compositional demixing. During imbibition, ILs are preferentially drawn into the pores by capillary forces and dominate early transport, while a minority of PILs infiltrate more slowly and tend to adsorb onto the pore walls, leading to reduction on ionic conductivity. The results suggest the possibility to separate

a mixture of ionic compounds (IL and PIL in this case) by the difference in the imbibition kinetics of its constituent components in nanopores and in the absence of solvent.

These insights deepen our understanding of ion transport under confinement. In the long term they could offer some guiding principles for the rational design of next-generation electrolytes and nanostructured materials for energy storage.

## Zusammenfassung

Das Verständnis darüber, wie Ionen in enge Poren eindringen, ist entscheidend für die Entwicklung von Systemen, bei denen eine präzise Kontrolle der Transporteigenschaften erforderlich ist (z. B. in Hochleistungsmaterialien für Energiespeicherung, Nanofluidik und Sensortechnologien). Diese Arbeit untersucht das Verhalten des Ionentransports von ionischen Flüssigkeiten (ILs), polymerisierten ionischen Flüssigkeiten (PILs) sowie deren Mischungen (ILs/PILs) in Nanoporen mithilfe der in-situ-nanodielektrischen Spektroskopie. Die Frage ist, wie die enge räumliche Begrenzung, die molekulare Struktur und damit den Ionentransport, das Phasenverhalten und die Dynamik der Polymere bestimmen.

Nanoskalig räumlich eingeschränkte ILs weisen gegenüber ihrem Zustand im Volumen veränderte physikalische Eigenschaften auf. Dazu gehören unterdrückte Kristallisation, verschobene Glasübergangstemperatur sowie reduzierte ionische Leitfähigkeit. Diese Veränderungen lassen sich auf Grenzflächenwechselwirkungen zwischen den Ionen und den Porenwänden zurückführen. Die Adsorption von Ionen an der Oberfläche verringert die Anzahl mobiler Ladungsträger und reduziert die Leitfähigkeit. Darüber hinaus beeinflusst die räumliche Einschränkung die Keimbildung, was insbesondere in kleineren Poren zur Kristallisation unterdrückt.

Die Geometrie der Poren spielt dabei ebenfalls eine wichtige Rolle: ILs in konisch geformten Nanoporen weisen beispielsweise eine höhere ionische Leitfähigkeit auf als in zylindrischen. Dies ist vermutlich auf die ungleichmäßige Oberflächenladungsverteilung in konischen Poren zurückzuführen, die die Stärke der Coulomb-Wechselwirkungen an den engen Porenöffnungen verringert.

In PILs beeinflussen die Größe und Struktur des gebundenen Kations die Eindringdynamik und die Leitfähigkeit erheblich. Kationen, deren Imidazoliumringe nahe der Polymerhauptkette sitzen, schränken die Kettenbeweglichkeit ein und führen zu höherer Viskosität. Hingegen fördern Kationen mit zusätzlichen Phenylgruppen zwischen der Polymerhauptkette und dem Imidazoliumring eine größere Flexibilität der Kette und eine verbesserte ionische Beweglichkeit. Bei starker räumlicher Einschränkung entkoppeln segmentale Dynamik und Ionentransport unterhalb der Glasübergangstemperatur. Dieses Phänomen steht im Einklang mit dem „Shoving-Modell“, wonach die Ionenbewegung im begrenzten Raum durch die Fähigkeit zur lokalen Matrixverformung begünstigt wird.

IL/PIL-Mischungen sind heterogen. Ihr Eindringen in Nanoporen führt zu lokaler Segregation und letztlich zu einer lokalen Entmischung. Während des Eindringens werden die ILs bevorzugt durch Kapillarkräfte in die Poren gezogen und dominieren den anfänglichen Transport. PILs hingegen dringen langsamer ein und lagern sich bevorzugt an den Porenwänden an. Das führt zu einer weiteren Reduktion der Leitfähigkeit. Diese Ergebnisse deuten darauf hin, dass sich ionische Komponenten (wie ILs und PILs) aufgrund unterschiedlicher Kinetiken während des Eindringens in Nanoporen selektiv trennen lassen – auch ohne Lösungsmittel.

Diese Erkenntnisse erweitern unser Verständnis des Ionentransports unter nanoskaliger Einschränkung und könnten langfristig als Grundlage für die gezielte Entwicklung neuer Elektrolyte und nanostrukturierter Materialien für die Energiespeicherung dienen.

# Contents

<b>Abstract.....</b>	<b>I</b>
<b>Zusammenfassung.....</b>	<b>III</b>
<b>Chapter 1. Introduction.....</b>	<b>1</b>
1.1 Ionic Liquids .....	3
1.1.1 Physical properties of ILs .....	6
1.1.2 ILs under nanoscale confinement .....	9
1.1.3 Relevant length scales for ion transport at the nanoscale.....	14
1.2 Polymerized Ionic Liquids .....	20
1.2.1 Structure-Property relationships in PILs .....	20
1.2.2 Decoupling of ion transport from the segmental dynamics in PILs .....	26
1.2.3 Zwitterionic PILs .....	30
1.2.4 Effects of nanoconfinement on ion transport in PILs.....	32
1.3 Scope of the Thesis .....	35
1.3.1 What determines the conductivity of ILs in the bulk and during infiltration in nanopores?.....	36
1.3.2 How the Cation Size Affects the Imbibition of Polymerized Ionic Liquids and the Ionic Conductivity in Nanopores?.....	37
1.3.3 Are mixtures of ILs/PILs homogenous? How do they infiltrate nanopores? .....	39
1.3.4 How V-shaped confinement affects the self-assembly and ion dynamics of ionic liquids? .....	40
1.4 Outlook and Future Work .....	42
1.4.1 Degree of confinement: size effects .....	42
1.4.2 Pore geometry: conical vs. cylindrical confinement .....	43
1.5 References.....	46
<b>Chapter 2. Experimental Section.....</b>	<b>50</b>
2.1. Materials .....	50
2.2. Template characteristion.....	50
2.3. Instruments and Characterization .....	57
2.4. References.....	65
<b>Chapter 3. Conductivity of Ionic Liquids in the Bulk and During Infiltration in Nanopores.....</b>	<b>66</b>
Abstract.....	67
3.1 Introduction.....	68
3.2 Experimental .....	71
3.3 Results and discussion .....	76
3.4 Conclusion .....	88
3.5 References.....	89
3.6 Supporting information.....	92

<b>Chapter 4. Effects of V-shaped Confinement on the Phase State and Ion Dynamics of Ionic Liquids Containing the 1-Butyl-3-methylimidazolium Cation .....</b>	<b>104</b>
Abstract.....	105
4.1 Introduction.....	106
4.2 Experimental Section .....	107
4.3 Results and Discussion .....	111
4.4 Conclusion .....	124
4.5 Reference .....	125
4.6 Supporting information.....	127
<b>Chapter 5. Tethered Cation Size Affects the Imbibition of Polymerized Ionic Liquids and the Ionic Conductivity in Nanopores.....</b>	<b>130</b>
Abstract.....	131
5.1 Introduction.....	132
5.2 Experimental section.....	133
5.3 Results and discussion .....	138
5.4 Conclusion .....	148
5.5 References.....	150
5.6 Supporting information.....	153
<b>Chapter 6. Demixing of Polymerized Ionic Liquid/Ionic Liquid Mixtures by Infiltration in Nanopores.....</b>	<b>156</b>
Abstract.....	157
6.1. Introduction.....	158
6.2. Experimental .....	160
6.3. Results and discussion .....	166
6.4. Conclusion .....	180
6.5 References.....	181
6.6 Supporting information.....	184
<b>Chapter 7. Fiber Formation of Semi-crystalline Polymers within Nanopores: The Role of Chain Entanglement and Infiltration Depth .....</b>	<b>193</b>
7.1. Introduction.....	193
7.2. Experimental .....	193
7.3. Results and discussion .....	195
7.4. Conclusion .....	199
7.5 References.....	200
<b>Conclusion.....</b>	<b>201</b>
<b>Acknowledgements.....</b>	<b>203</b>

## Chapter 1. Introduction

Nature has long mastered nanoscale ion transport by combining geometric confinement with interfacial control to achieve precise and energy-efficient regulation in biological systems. For instance, nephrons and neurons regulate membrane potentials through ionic pumps, while skeletal muscle cells—structured as long cylindrical fibers—modulate contraction and relaxation via calcium ion ( $\text{Ca}^{2+}$ ) signaling pathways.<sup>1</sup> The latter involve motor proteins such as tropomyosin. Skeletal muscles, consisting of long cylindrical cells, exemplify how ion transport regulates dynamic physiological functions. Within the cells, muscle contraction is regulated by calcium. An action potential generated by a motor neuron propagates on the muscle cell surface, activates voltage-gated calcium channels and allows calcium flow into the muscle cell. This calcium activates another ion channel which releases even more calcium to the cytoplasm of the cell. Calcium diffusing in the cytoplasm between myosin and actin filaments of the muscle fibrils causes the filaments to slide into each other, triggering the contraction of the entire muscle fiber. Inspired by such biological architectures, researchers have sought to mimic these functions using engineered nanopore and nanochannel systems with tunable surface properties and geometries.<sup>2</sup> As illustrated in **Figure 1**, these artificial systems span a range of physical models, from three-dimensional porous matrices to zero-dimensional nanocages (**Figure 1a**).<sup>3-6</sup> They offer versatile platforms to study and manipulate transport processes by leveraging physical and chemical principles (**Figure 1b**). These include size and shape selectivity<sup>7,8</sup>, wettability<sup>9</sup>, interfacial charge effects (such as the Debye layer)<sup>10</sup>, specific molecular recognition, and various non-covalent interactions<sup>11</sup>. Such design principles enabled selective and efficient ion/molecular transport under confinement, leading to a wide range of practical applications (**Figure 1c**).

In energy conversion, nanochannels are used to harvest energy from salinity gradients—a process known as "**blue energy**".<sup>12</sup> When ionic solutions with differing salinities (e.g., seawater and freshwater) flow across a nanoporous membrane, the chemical potential difference drives selective ion transport. In channels narrower than the Debye length, surface charges create unipolar environments that enhance ionic selectivity and osmotic current generation. This unidirectional ion flow can be harnessed to produce electrical power, with performance critically dependent on pore geometry, surface charge density, and confinement length. Capacitor applications, particularly electrical double-layer capacitors (EDLCs), benefit from tuning pore sizes to match the ionic dimensions.<sup>13</sup> When the pore size of the electrode

material closely matches the effective size of the electrolyte ions, maximal capacitance can be achieved. As illustrated in **Figure 1c**, when the pore diameter is slightly larger than the ion size, ions can efficiently enter the pores, partially or fully shed their solvation shells, forming densely packed electrical double layers (EDLs). This close packing of counterions maximizes charge storage capabilities with importance in the design of supercapacitors. In contrast, if the pores are too narrow, steric hindrance and the disruption of local ionic coordination prevent effective ion entry, leading to a significant drop in capacitance. On the other hand, excessively large pores reduce the interfacial charge density, diluting the EDL and lowering energy storage capacity. Therefore, optimal supercapacitor performance is achieved by fine-tuning the pore size to balance ion accessibility with efficient interfacial packing.

In another area, nanoscale sensing via nanochannels enables real-time detection of single biomolecules by monitoring ionic current modulations during their translocation.<sup>14-16</sup> For example, in DNA translocation studies, applied electric fields drive single-stranded DNA through narrow pores, allowing precise control and detection at the single-molecule level.<sup>16</sup> The resulting ionic current blockades reflect molecular properties such as length, sequence, or secondary structure, providing high-resolution analytical readouts. These diverse applications underscore the potential of nanopore/channel systems, where nanoscale confinement, interfacial chemistry, and structural geometry work in concert to enable tailored control of ion and molecule transport across disciplines ranging from biomedicine to energy technologies.

Among the most representative and versatile platforms for studying ionic transport under confinement are ionic liquids (ILs) and their polymerized counterparts, polymerized ionic liquids (PILs). These materials consist entirely or predominantly of ionic species, and exhibit high thermal and electrochemical stability, negligible volatility, and wide chemical tunability. Ion transport in ILs is governed by the intrinsic characteristics of the constituent ions. In PILs, an additional feature is the coupling between ion motion to the polymer segmental dynamics. When confined to the nanoscale, however, the transport behavior of ILs and PILs becomes far more complex. The interplay between molecular structure and confinement can alter ion dynamics relative to bulk. Understanding the way that ILs and PILs behave under confinement is essential not only for probing fundamental questions about nanoscale ion transport, but also for the design of next-generation energy materials and electrochemical systems with selective ion control. The aim of this Thesis is to identify the principles underlying ion transport within nanochannels and to suggest new processes with efficient ion transport. If successful, this fundamental understanding will be transformative for the field, enabling similar

materials/processes to be used in future energy devices. For this purpose, we employ a series of ion-containing systems that include ILs, PILs, and investigate: (i) the kinetics of imbibition in narrow pores using the newly established method of *in situ* nano-dielectric spectroscopy, and (ii) the molecular and ion dynamics under confinement.

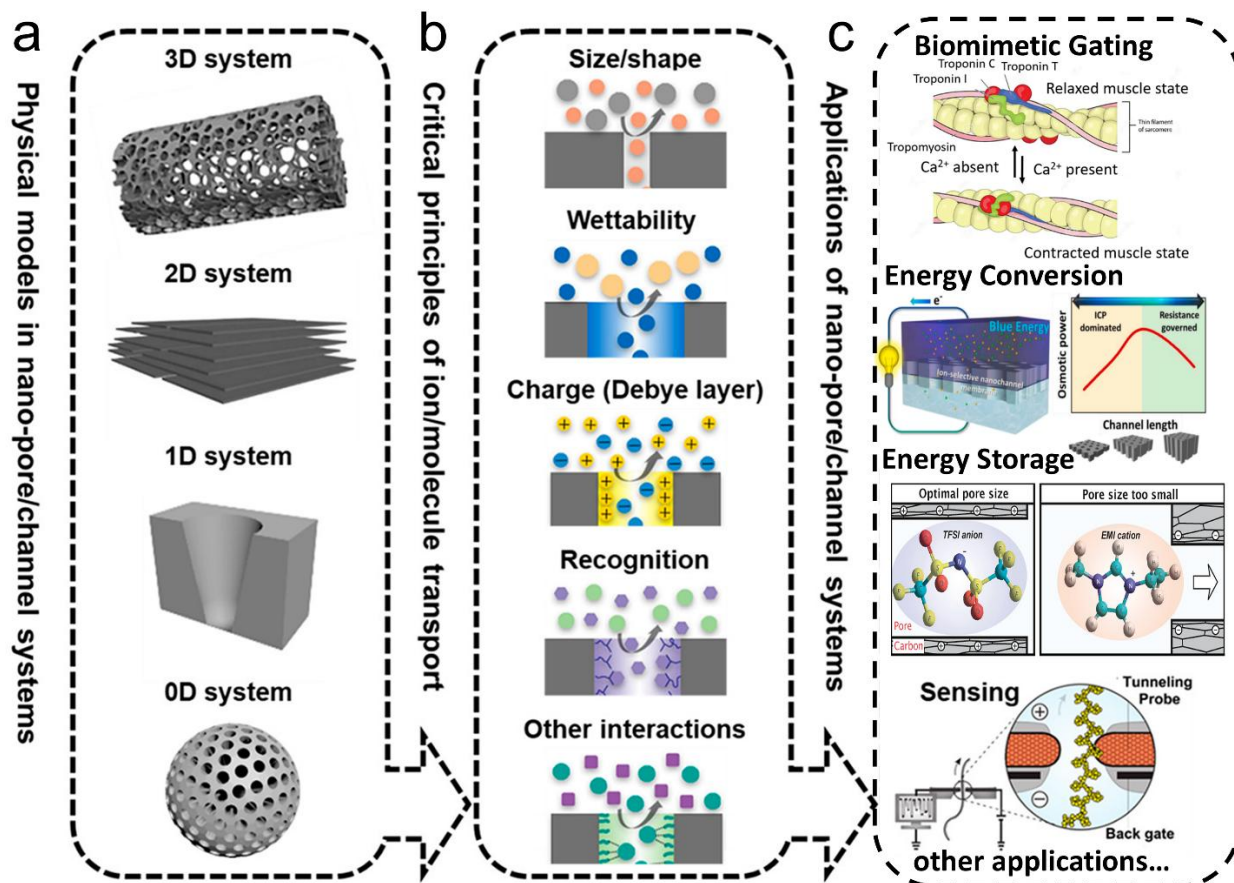


**Figure 1.** Schematic overview of nanopore/channel systems for confined ion transport and multifunctional applications. (a) Representative architectures of nanochannel systems across dimensional scales, ranging from porous networks (3D) to nanocages (0D).<sup>3-6</sup> (b) Key transport principles enabled by nanoscale confinement, including geometric selectivity, wettability, interfacial charge interactions (e.g., Debye layer), and specific molecular recognition, which collectively govern ion and molecular mobility. (c) Applications derived from these principles: such as biomimetic gating inspired by calcium-controlled muscle contraction<sup>1</sup>, salinity-gradient-driven energy conversion (“blue energy”)<sup>12</sup>, pore-size-optimized ion storage in supercapacitors<sup>13</sup>, and biological sensing<sup>16</sup>.

## 1.1 Ionic Liquids

Ionic liquids (ILs) are materials composed entirely of organic cations paired with either organic or inorganic anions, characterized by a melting point below 100 °C. Due to their irregular molecular structure, ILs exhibit a reduced tendency to crystallize. The first IL, ethylammonium nitrate ([TtNH<sub>3</sub>]<sup>+</sup>[NO<sub>3</sub>]<sup>-</sup>), was synthesized by Paul Walden in 1914.<sup>17</sup> For many decades, ILs were primarily regarded as solvents for catalysis and synthesis, owing to their high affinity for

a broad range of chemical compounds. In recent years, it has become evident that ILs possess far greater versatility beyond their role as solvents<sup>18</sup>. Their low vapor pressure, non-flammability, high chemical and thermal stability, high conductivity, recyclability, and tunable physicochemical properties make ILs promising candidates for various applications, in physical chemistry<sup>20</sup> including catalysis<sup>19</sup>, electrochemistry<sup>21, 22</sup> and biological systems<sup>23</sup> (**Figure 2**).

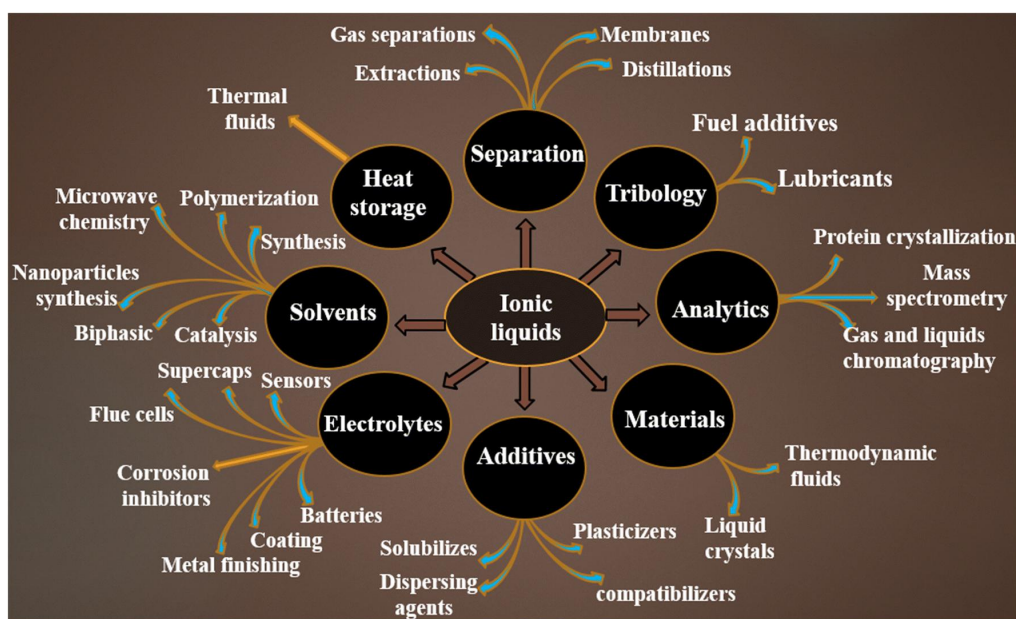


**Figure 2.** Applications of ionic liquids.<sup>24</sup> The broad application spectrum classifies ILs in six major categories: separation processes, heat storage, tribology, analytical applications, materials design, and functional additives. The versatility of ILs is further demonstrated by their use as solvents, electrolytes, and reaction media in fields such as catalysis, battery technology, gas separation, protein crystallization, and nanomaterial synthesis.

ILs can be broadly classified into three main categories: *protic*, *aprotic* and *zwitterionic* (**Figure 3**).<sup>25</sup> *Protic ILs* contain an active proton (*e.g.* ammonium or imidazolium with an N-H group). This active proton facilitates the formation of extensive hydrogen-bonding networks, which significantly influence both the structural organization and physicochemical properties of the IL. However, they result in a reduction of conductivity, as these intermolecular hydrogen bonds restrict the freedom of ionic movement. *Aprotic ILs*, in contrast, do not possess an active proton. They are typically composed of asymmetrically substituted organic cations (such as alkylated imidazolium, pyrrolidinium, or phosphonium) paired with weakly coordinating anions (*e.g.* bis(trifluoromethanesulfonyl)imide [TFSI]<sup>-</sup> or tetrafluoroborate [BF<sub>4</sub>]<sup>-</sup>). The absence of proton-donating groups reduces hydrogen bonding and promotes weaker ion-ion interactions, leading to higher conductivity and better electrochemical stability, making aprotic

ILs the most widely used class in energy storage and separation technologies. *Zwitterionic ILs* are unique in that they contain both positive and negative charges within the same molecular entity, often covalently tethered via a flexible linker. These intramolecular ionic pairs can form organized ion-rich domains while eliminating the need for separate anions or cations. Zwitterionic ILs typically exhibit low volatility, high thermal stability, and often lower fluidity, but they are of growing interest for applications in biomaterials, as lubricants, and as membranes due to their tunable polarity (e.g. high dielectric permittivity) and internal electrostatic ordering.

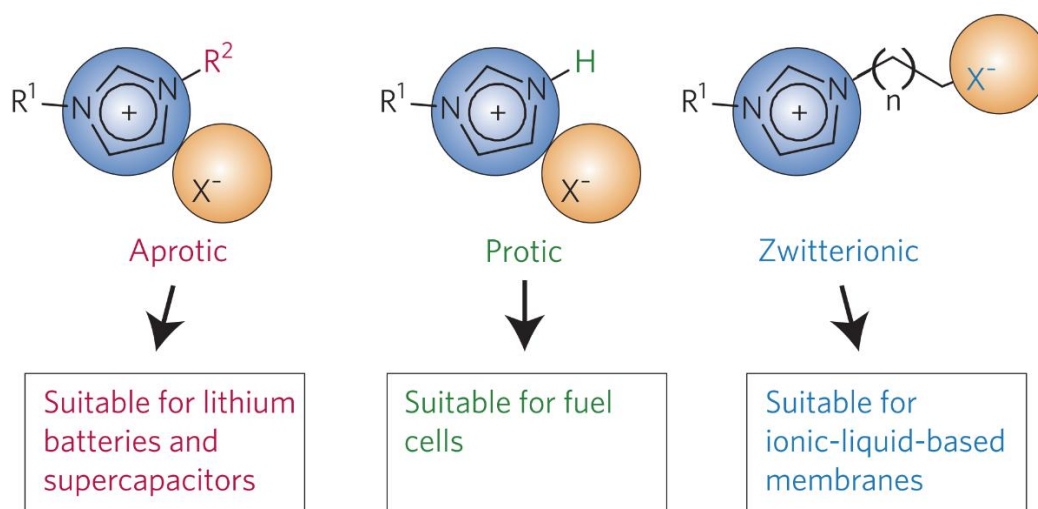


**Figure 3.** Different cation types most commonly used in ILs.<sup>25</sup>

The selection of cations and anions is crucial in determining the physical, chemical, and thermal properties of ILs. Among the wide variety of cations, imidazolium<sup>26-28</sup>, ammonium<sup>29</sup>, phosphonium<sup>30</sup> and pyridinium<sup>31</sup> are the most extensively studied. In addition, cations such as pyrrolidinium and piperidinium have gained increasing attention. While imidazolium, pyridinium, pyrrolidinium and piperidinium are ring-based structures, phosphonium and ammonium cations typically exhibit open-chain architectures – differences that significantly influence their physicochemical behavior and electrochemical performance. In terms of electrochemical stability, ILs with cyclic cationic structures have been identified as the more robust candidates. With respect to the anion composition, [TFSI]<sup>-</sup> stands out as the most commonly employed anion in ILs research. Its delocalized negative charge, the presence of multiple conformations with minimal energy differences and its asymmetric size contribute to its high ionic conductivity and thermal stability. The structure and physical properties of the main ILs are shown in **Table 1**.

### 1.1.1 Physical properties of ILs

**Viscosity.** The viscosity of ILs is a critical parameter that directly impacts their suitability for practical applications, e.g. in systems involving fluid transport, pressure-driven flow, and convective heat transfer rate.<sup>32-34</sup> Cation length and the size of the IL are the main factors influencing their viscosity. This results from ion-ion interactions that include electrostatic forces, van der Waals interactions, and hydrogen bonding. Okoturo *et al.*<sup>35</sup> reported that ILs containing small, symmetric cations with low molecular weight exhibit significantly lower viscosities, primarily attributed to reduced steric hindrance and weakened cation-anion interactions.<sup>24</sup> In contrast, ILs with long alkyl side chains or bulky substituents tend to form more structured ionic domains, that restrict molecular motion and increase viscosity. Tokuda *et al.*<sup>36</sup> investigated the influence of the anion type on the viscosity of ILs. As shown in **Figure 4**, anion type results in the following order for the viscosity:  $[\text{PF}_6]^- > [(\text{C}_2\text{F}_5\text{SO}_2)_2\text{N}]^- > [\text{BF}_4]^- > [\text{CF}_3\text{SO}_3]^- > [\text{CF}_3\text{CO}_2]^- > [\text{TFSI}]^-$ . The influence of the type of anion on the viscosity is primarily governed by its molecular symmetry, size and charge distribution. In general, larger, more delocalized anions (such as  $[\text{TFSI}]^-$ ) present lower viscosities.

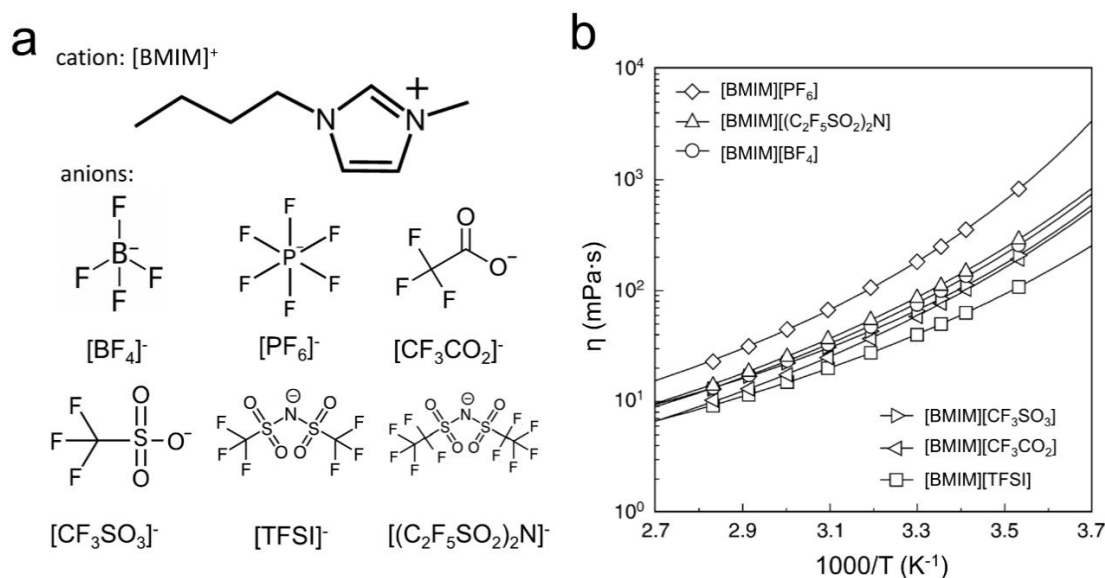


**Figure 4.** (a) Chemical structures of  $[\text{BMIM}]^+$  based ILs with different anions. (b) Viscosity of ILs as a function of inverse temperature.<sup>36</sup>

**Molecular packing - density.** Another important parameter for establishing the flow conditions of ILs is density and their packing in the solid state. Normally, phosphonium-based ILs have densities lower than water, while the ILs with cations of pyridinium, pyrrolidinium and sulfonium are denser (usually with densities higher than  $1.3 \text{ g/cm}^3$ ). In addition, density decreases with increasing length of alkyl substituents.<sup>37</sup> The structure (*i.e.* the packing) of ILs

refers to the spatial arrangement and local organization of cations and anions. The packing governs how efficiently ions interact and diffuse, thereby directly influencing key physicochemical properties such as density, viscosity, and conductivity. Tightly packed structures, often arising from small or symmetric ions, promote strong electrostatic interactions and can lead to locally ordered domains. However, such dense organization may also reduce ion mobility by promoting ion pairing and restricting the number of free charge carriers. Conversely, looser packing—typically associated with bulky side chains or large, charge-delocalized anions (*e.g.* [TFSI]<sup>−</sup> or dicyanamide [DCA]<sup>−</sup>), introduces greater free volume and weakens cation-anion interactions, resulting to higher ion mobility.

X-ray scattering experiments and computer simulations provided significant insight into the packing properties of ILs. ILs commonly have three peaks in X-ray diffraction (XRD). The origin and structure of these peaks were discussed by Margulis *et al.* (**Figure 5**)<sup>38</sup> At large distances (*i.e.*, low values of the modulus of the scattering vector,  $q = \frac{4\pi}{\lambda} \sin\left(\frac{2\theta}{2}\right)$ , where  $\lambda$  is the wavelength of X-rays,  $2\theta$  is the scattering angle), the pre-peak revealed nanophase separation between polar and apolar groups giving rise to a smectic-like layering. At intermediate distance, the second peak indicated the charge alternation distance. At shorter distances, the third peak was assigned to different correlations between adjacent atoms (**Figure 5a**). The latter can be both intermolecular and intramolecular. Comparing with ILs, conventional solvents have only one prominent peak at  $q$  values below  $2.5\text{\AA}^{-1}$ , known as the van der Waals peak.

It is by no means a general rule, but cations used in ILs are often more structurally rich and asymmetric and often the species possess distinct polar heads and apolar alkyl tails, giving rise to domains of polarity alternation. Despite this, anions contribute more strongly to X-ray scattering due to their higher electron density, making them dominant in shaping the scattering profile. An intriguing observation shown in **Figure 5b** was the anomalous increase in prepeak intensity with increasing temperature. The explanation lies in two competing effects, illustrated in the dashed box of **Figure 5b**: an enhancement in polar (cation-anion) interactions resulted in an intensity increase, while the apolar contribution to the structure factor,  $S(q)$ , diminishes with increasing temperature. These two opposite effects do not fully cancel; instead, the polar contribution dominates, driven largely by the strong scattering from the anions. This leads to a counterintuitive but experimentally consistent result: “if one seeks to understand the structural behavior of cations, it is often most effective to analyze the scattering behavior of the anions”.<sup>39</sup>

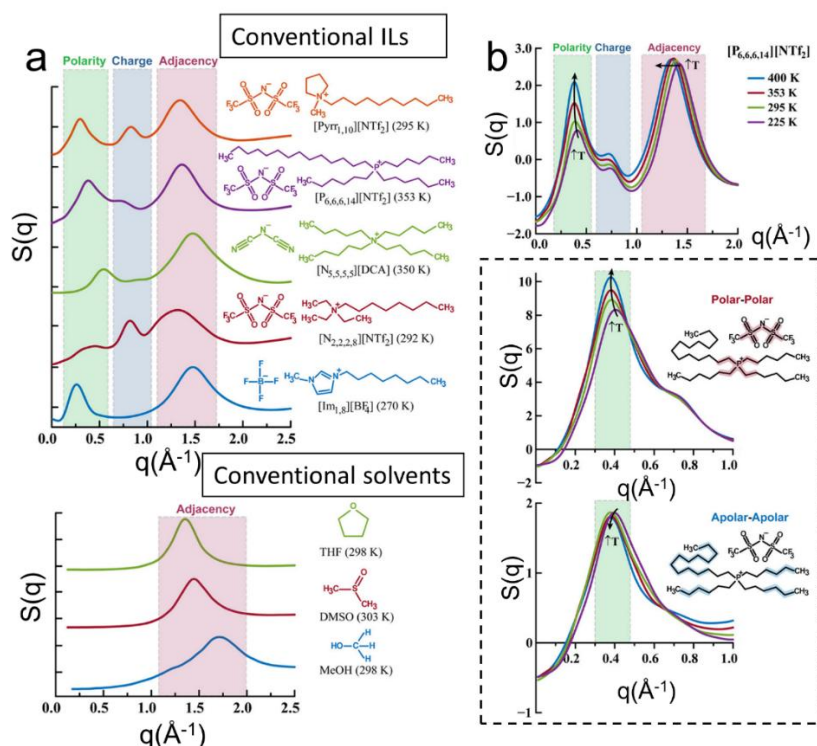


**Figure 5.** (a) Computationally derived structure factor,  $S(q)$ , for a diverse collection of ionic liquids and conventional solvents. (b) Total  $S(q)$ , polar–polar subcomponent of  $S(q)$ , and apolar–apolar subcomponent of  $S(q)$  for [P<sub>14,6,6,6</sub>][NTf<sub>2</sub>] at different temperatures.<sup>38</sup>

*Ion transport.* The electrical conductivity of ILs arises from the number of mobile charge carriers and their corresponding mobility (Drude model:  $\sigma = ne|\mu$ , where  $\sigma$  is the dc-conductivity,  $n$  is the number density of mobile ion,  $|e|$  is the electron charge, and  $\mu$  is the mobility of ions). Typically, conductivity is limited by reduced ion mobility, which is often caused by ion aggregation or strong Coulombic interactions. Leys *et al.*<sup>40</sup> systematically investigated the electrical conductivity of imidazolium-based ILs with varying chain length, [C<sub>*n*</sub>mim][BF<sub>4</sub>]. As illustrated in **Figure 6**, the conductivity decreased with increasing chain length. When the alkyl chain reached  $n = 10$ , the IL crystallized at lower temperatures, resulting in the loss of ionic conductivity. The reduced conductivity with longer alkyl chains was explained by two main factors: (i) increased van der Waals interactions due to extended alkyl chains promoting stronger interionic aggregation and increased viscosity, thereby hindering ion diffusion, and (ii) the larger molecular size of the cations introduced steric hindrance that further restricted ion mobility. In addition to cation structure, the choice of anion plays a significant role in determining the ionic conductivity. In general, anions influence both the degree of ion pairing and the fluidity of the system. Larger, weakly coordinating anions (such

as [TFSI]<sup>-</sup> or [BF<sub>4</sub>]<sup>-</sup>) promote ion dissociation and lower viscosity, resulting in enhanced conductivity. In contrast, smaller or more strongly coordinating anions (like [Cl]<sup>-</sup> or acetate) tend to form tight ion pairs or clusters with the cation, reducing the number of free ions and suppressing ion mobility.

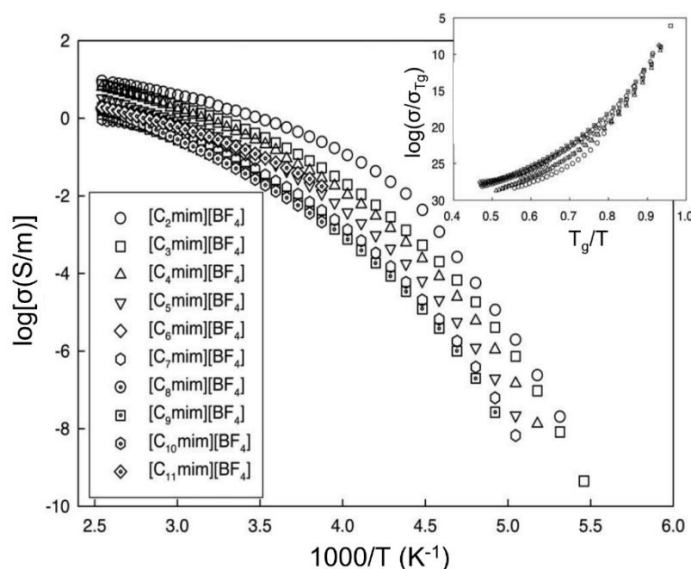


**Figure 6.** Conductivity values of [C<sub>n</sub>mim][BF<sub>4</sub>] as a function of inverse temperature. Inset: The same data rescaled as  $\ln(\sigma/\sigma_{T_g})$  vs  $T_g/T$ .<sup>40</sup>

### 1.1.2 ILs under nanoscale confinement

The ionic conductivity, viscosity, and structural properties of ILs in the bulk provide a strong foundation for their application in electrochemical systems. Compared to conventional organic and aqueous electrolytes, IL-based electrochemical energy storage (EES) devices operate reliably over a wide electrochemical potential window, in some cases extending up to 6 V, thereby significantly enhancing energy density. It is now increasingly recognized that these bulk properties can be markedly altered under confinement. In several cases, ILs are often used in environments such as porous electrodes, nanochannels, or solid interfaces, where spatial constraints, surface interactions, and structural frustration introduce new dynamics. Under such conditions, ion motion can decouple from the bulk relaxation process, ion pairing can be suppressed or enhanced, and new interfacial phases can emerge. These effects are not only size- and geometry-dependent but also highly sensitive to the chemical nature of the confined IL. Understanding confinement effects is therefore essential for bridging molecular design with device-level performance.

Nobori *et al.*<sup>41</sup> investigated the phase behavior of [C<sub>12</sub>mim]<sup>+</sup>[BF<sub>4</sub>]<sup>-</sup> in bulk and under confinement, revealing significant changes in dynamics due to spatial restrictions. The bulk IL

underwent an isotropic (I) to smectic (Sm) to metastable lamellar (LtSm) transition upon cooling, with a reverse sequence with intermediate crystalline phases (CrI, CrII) during heating (**Figure 7**). However, in confinement, particularly in pores with sizes below 40 nm, these transitions were broadened, shifted to lower temperatures, or completely suppressed. The I-Sm transition, evident in the bulk, become increasingly weakened with decreasing pore diameter (**Figure 7a**), while crystallization upon heating was largely inhibited in the smaller pores (**Figure 7b**). These effects were attributed to the interfacial interactions and restricted molecular mobility that hindered long-range ordering and stabilized disordered states.

The study also compared the glass temperatures ( $T_g$ ) of  $[C_{10}mim]^+[BF_4]^-$  and  $[C_{12}mim]^+[BF_4]^-$  across varying pore sizes. In both cases,  $T_g$  decreased with decreasing pore diameter, reflecting enhanced dynamics under confinement. Notably,  $[C_{10}mim]^+[BF_4]^-$  consistently showed a lower  $T_g$  than  $[C_{12}mim]^+[BF_4]^-$ , suggesting that shorter alkyl chains allow greater segmental flexibility and contribute more strongly to the  $\alpha$ -relaxation process.

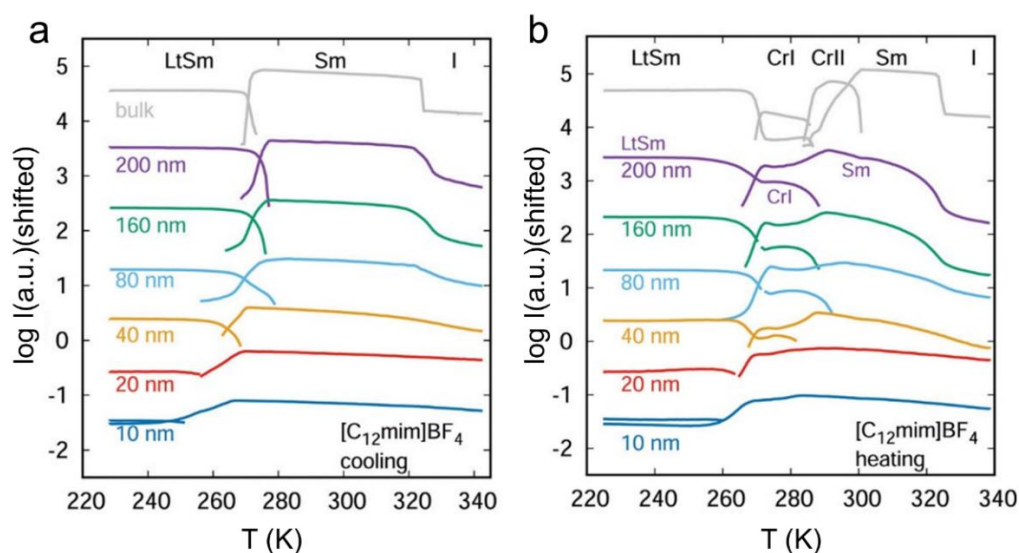


**Figure 7.** Temperature dependence of X-ray scattering intensity of the 001 reflections of various phases during (a) the cooling process and (b) the subsequent heating process at the rate of 10 K/min for  $[C_{12}mim]^+[BF_4]^-$  confined in nanopores with various pore diameters between 200 and 10 nm, in addition to the bulk. The data were shifted along the vertical axis.<sup>41</sup>

The influence of confinement on the phase transitions and the liquid-to-glass temperature (as demonstrated in  $[C_nmim]^+[BF_4]^-$ ) highlights the fact that nanoscale confinement can disrupt ionic self-assembly and phase stability. Suppressed crystallization, broadened transition regions, and altered  $T_g$ 's values, all point to a loss of long-range order and to restricted ion mobility. These confinement-induced structural and dynamic changes are expected to have direct consequences on the ion transport properties.

Iacob *et al.*<sup>42</sup> reported an enhancement of charge transport in 1-butyl-3-methylimidazolium tetrafluoroborate ([BMIM]<sup>+</sup>[BF<sub>4</sub>]<sup>-</sup>) confined within oxidized nanoporous silicon membranes with pore sizes ranging from 7.5 nm to 10.4 nm (**Figure 8**). They observed that at elevated temperatures, both the dc conductivity and the characteristic relaxation rate of charge transport within the nanopores closely matched the corresponding bulk values. However, at lower temperatures, these quantities increased with decreasing pore diameter, indicating enhanced ionic mobility under confinement. This behavior was attributed to changes in ion packing due to the reduction in IL density within the smaller pores.

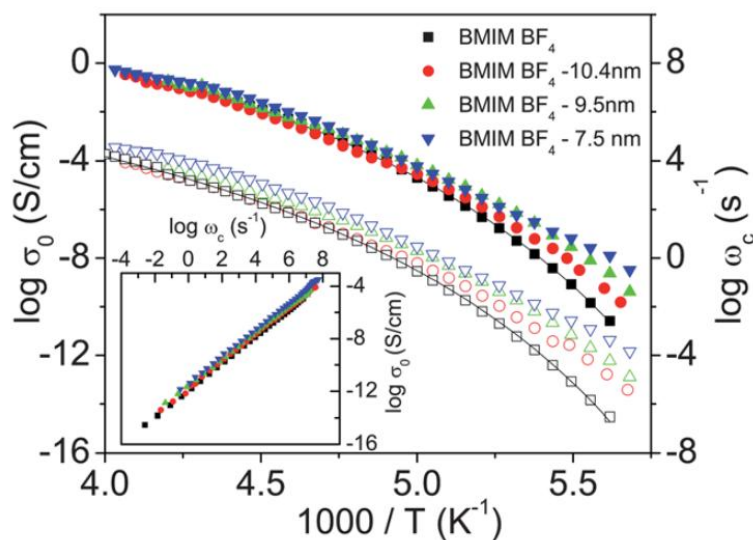


**Figure 8.** Temperature dependence of dc-conductivity  $\sigma_0(T)$  (open symbols) and characteristic rate of charge transport  $\omega_c$  ( $=2\pi f_c$ ) (filled symbols) for bulk and confined [BMIM]<sup>+</sup>[BF<sub>4</sub>]<sup>-</sup> in silica nanopores. Inset: dc-conductivity  $\sigma_0$  vs.  $\omega_c$  for bulk and confined [BMIM]<sup>+</sup>[BF<sub>4</sub>]<sup>-</sup>.<sup>42</sup>

Similarly, Tu *et al.*<sup>43</sup> observed enhanced ionic conductivity and faster diffusion rates at lower temperatures when [C<sub>6</sub>Pyrr]<sup>+</sup>[TFSI]<sup>-</sup> was confined within nanopores (**Figure 9**). As shown in **Figure 9b**, the temperature-dependent dc-conductivity increased markedly below a critical crossover temperature  $T_c$ , which marks the onset of deviation from bulk-like behavior. Correspondingly, the diffusion-related relaxation time (**Figure 9b, top**) displayed a similar crossover: above, both bulk and confined ILs have similar temperature dependences of  $\tau_\sigma$ , while below, the confined samples exhibit significantly faster relaxation. To probe the structural origins of this transition, they conducted temperature-modulated differential scanning calorimetry (TMDSC) to extract structural relaxation times and glass transition temperatures. As shown in **Figure 9b** (top), only a single  $T_g$  was observed in the bulk, whereas two distinct transitions appeared in the confined system: one associated with the interfacial region

( $T_{g\_interface}$ ) and the other with the core ( $T_{g\_core}$ ). Notably, the  $T_c$  obtained from dielectric measurements aligned well with  $T_{g\_interface}$ , suggesting that the changes in ion transport originate from the vitrification of the interfacial layer.

Additionally, their study addressed the role of surface interactions by comparing native and silanized nanopores (**Figure 9c**). While the core-related relaxation and  $T_{g\_core}$  remained nearly unchanged upon silanization, significant differences emerged in the interfacial dynamics. The silanized pores exhibited a higher  $T_{g\_interface}$ . They attributed this to the thicker interfacial layer for silanized nanopores as compared to the native ones. As a consequence, the denser packing of ions brought about higher  $T_{g\_interface}$  values.

A notable conflict emerges between the interpretation of Tu *et al.*<sup>43</sup> and Kardasis *et al.*<sup>44</sup> concerning the origin of dynamic alterations under confinement. Tu *et al.* attribute the observed changes in confined ion dynamics primarily to interfacial vitrification, as evidenced by the appearance of two distinct  $T_g$ s, which they interpret within the framework of a two-layer model comprising interfacial and core regions with different mobilities. In contrast, Kardasis *et al.* argued that the emergence of multiple  $T_g$ s is predominantly a manifestation of non-equilibrium phenomena, rather than solely interfacial effects. Their work identified a critical temperature ( $T_c$ ), below which non-equilibrium effects dominate, stemming from the sluggish dynamics of the adsorbed layer and slow equilibration processes. They further emphasized that the timescales required to reach equilibrium are highly sensitive to temperature, pore size, and functionality.

In addition, the absence of cooling scan data in Tu's study,<sup>43</sup> combined with their reliance on heating-only protocols, limits the robustness of assigning distinct  $T_g$ s solely to interfacial phenomena.

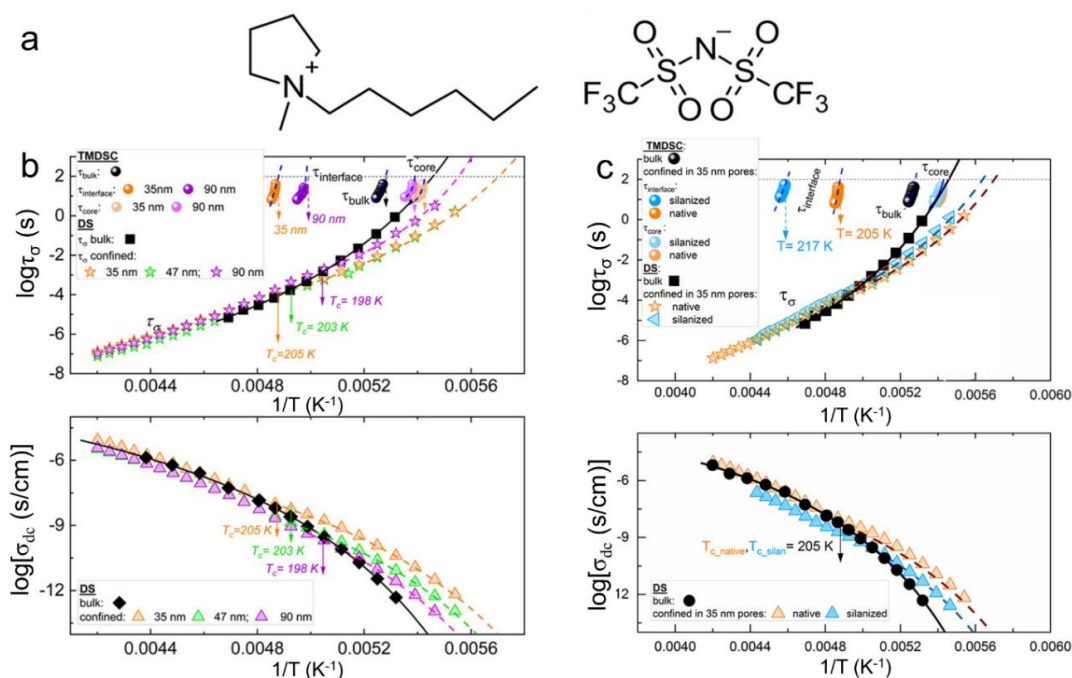


**Figure 9.** (a) Chemical structure of 1-Hexyl-1-methylpyrrolidinium cation ( $[C_6\text{Pyrr}]^+$ ), and of the counteranion,  $[\text{TFSI}]^-$ . (b) Temperature dependence of the characteristic relaxation time ( $\tau_\sigma$ ) and dc conductivity ( $\sigma$ ) for  $[C_6\text{Pyrr}]^+[\text{TFSI}]^-$  confined in AAO templates of various pore sizes (90, 47, and 35 nm). The inset indicates the calorimetric relaxation times determined using temperature-modulated differential scanning calorimetry (TMDSC). (c) Temperature dependence of the dielectric and calorimetric relaxation times for  $[C_6\text{Pyrr}]^+[\text{TFSI}]^-$  confined in native and silanized AAO membranes with an average pore size of 35 nm.<sup>43</sup>

In addition to experimental investigations, simulations were also employed in studying confined ILs. Molecular dynamics simulations of ILs based on 1-butyl-3-methylimidazolium  $[\text{BMIM}]^+$  with different anions at the quartz (001) surface revealed well-ordered ILs at the solid/liquid interfaces.<sup>45</sup> Interactions with the  $\text{Si}(\text{OH})_2$  surface were mainly determined by the H-bonding attractions of the anions with the silanol groups. Likewise, molecular dynamics simulations of the two IL/graphite interfaces ( $[\text{BMIM}]^+[\text{PF}_6]^-$  and  $[\text{OMIM}]^+[\text{PF}_6]^-$ ) revealed dense regions of ILs adsorbed at the interface with density variations extending to  $\sim 1.5$  nm away from the graphite surface.<sup>46</sup> There was a tendency for the polar groups to aggregate forming a polar network, while the nonpolar groups filled up the rest of the vacancy. Atomistic simulations were also employed to study the IL 1-n-hexyl-3-methylimidazolium bis(trifluoromethylsulfonyl)amide ( $[\text{HMIM}]^+[\text{Tf}_2\text{N}]^-$ ) confined into carbon nanotubes (CNTs).<sup>47</sup> It was shown that the distribution of anions and cations within the CNTs was heterogeneous with cations adsorbed preferentially close to the CNT wall, and the anions located at the tube center. Furthermore, IL molecules in the CNT exhibited self-diffusivity coefficients about 1-2 orders of magnitude longer than the corresponding bulk IL.

These conflicting reports on the effect of confinement of ILs dynamics, reflect the different ion-wall interactions and the concomitant effects of density modulation near the surface. To reconcile these contrasting findings, it is essential to consider the relevant characteristic length scales that govern confined IL behavior—namely, the size of the confining domain relative to molecular and interfacial correlation lengths.

### 1.1.3 Relevant length scales for ion transport at the nanoscale

In ionic systems, the origin of ionic conductivity is closely linked to momentum conservation principles.<sup>48</sup> Under an applied electric field, equal number of oppositely charged ions move in opposite directions, however, net charge transport can still occur, as long as the two species carry unequal momentum. When there is asymmetry in ion mass or size, the lighter/smaller ion typically acquires greater drift velocity and contributes more significantly to the system's net momentum flux. While bulk ionic conductivity is governed by collective ion dynamics and momentum transport, these mechanisms can be significantly altered under confinement. In porous environments, such as nanopores or thin films, interfacial effects become dominant, often leading to deviations from bulk behavior.<sup>49-52</sup> Charged surfaces can attract counterions and repel coions, creating immobilized interfacial layers that reduce the effective number of mobile carriers. This effect is illustrated in **Figure 10**, where positively (or negatively) charged surfaces preferentially attract anions (or cations), leading to immobilization at the interface and a reduction in the number of mobile ions. In contrast, neutral pore surfaces mitigate these interfacial interactions, thereby restoring ion mobility.

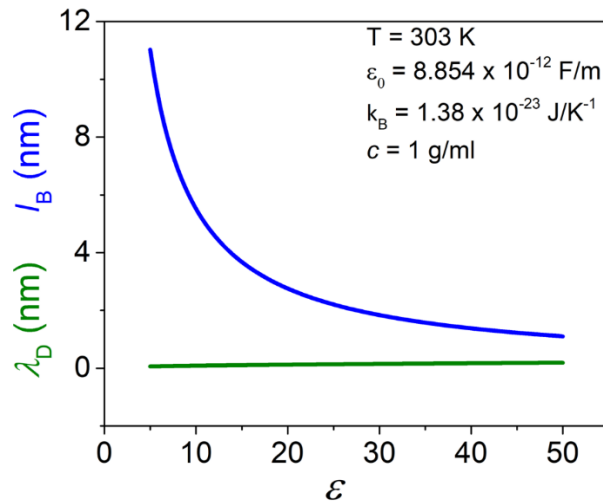


**Figure 10.** Schematic of the effect of the AAO surface charge on the dc-conductivity of ILs. (a,b) Charged surface: ions are immobilized at the pore surface. (c) Neutral surface: all ions are mobilized and contribute to the dc-conductivity. For simplicity, we show the same arrows for the cation and the anion. In reality, momentum conservation implies faster motion for the smaller ion, which effectively gives rise to a current.

To better understand how surface interactions influence ion transport in nanochannels, it is useful to consider different characteristic length scales that govern ion-ion correlations, interfacial screening, and cooperative dynamics. They refer to the: Bjerrum length, Debye length, Gouy-Chapman length, intrinsic length scales of self-assembly, length scale of density fluctuation near the pore walls, and the characteristic length association with the liquid-to-glass “transition”.

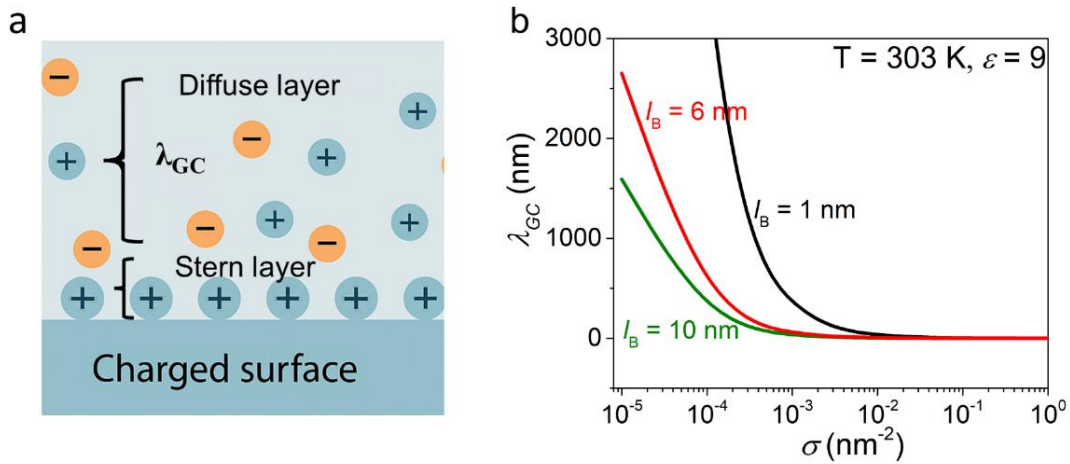
The *Bjerrum length* ( $l_B$ ) is a fundamental parameter in electrostatics. It refers to the distance at which the electrostatic interaction energy between two elementary charges in a dielectric medium is balanced by the thermal energy ( $k_B T$ ), where  $k_B$  is the Boltzmann constant and  $T$  is the temperature. It is given by  $l_B = e^2 / 4\pi\epsilon_0\epsilon k_B T$ , where  $e$  is the elementary charge,  $\epsilon_0$  the permittivity of free space and  $\epsilon$  is the dielectric permittivity of the medium. At distances below  $l_B$ , electrostatic interactions dominate, whereas at longer distances thermal fluctuations prevail and effectively replace discrete ion-ion Coulomb forces by a mean-field. In ILs, typically  $\epsilon \sim 13$ , and at a temperature of 218 K,  $l_B \sim 6$  nm. The *Bjerrum length* is inversely proportional to the dielectric permittivity of the medium (**Figure 11a**). When the dielectric permittivity of a medium is high, it reflects a strong ability to screen electric charges that reduce the strength of electrostatic interactions. As a result, the Bjerrum length decreases. Conversely, in materials with low-permittivity, the electric field induces less polarization, leading to weaker screening and thus to longer *Bjerrum lengths*.

The *Debye length* ( $\lambda_D$ ) is a parameter used to describe the screening length of an electric field in a plasma or electrolyte solution. It characterizes the distance over which the electrostatic potential is significantly reduced due to the presence of charged particles. The *Debye length* is given by  $\lambda_D = 1/\sqrt{(8\pi l_B c)}$ , where  $c$  is the solution concentration, and effectively gives the ion-ion interactions. Beyond  $\lambda_D$ , electrostatic fields are “screened” due to the polarization of charges. For bulk ILs with  $l_B \sim 6$  nm, the Debye length is only 0.08 nm. As shown in **Figure 11**,  $\lambda_D$  is positively correlated with  $\epsilon$ . A lower dielectric permittivity means that the medium is less polarizable and exhibits reduced ability to store electrical energy. In this case, the screening of electric charges is weaker, resulting in a shorter *Debye length*.



**Figure 11.** Dependence of different length scales ( $\lambda_D$ ,  $l_B$ ) on the dielectric permittivity of the medium.

The *Gouy-Chapman length* ( $\lambda_{CG}$ ) is a characteristic length scale that describes the thickness of the diffuse layer in the electrical double layer formed at the interface between a charged surface and an electrolyte solution. It is inversely proportional to the square root of the surface charge density ( $\sigma^*$ ) of a charged surface, defined as  $\lambda_{CG} = 1/2\pi l_B \sigma^*$ . Employing  $\sigma^* \sim 0.1 \text{ nm}^{-2}$  results to a  $\lambda_{CG} \sim 0.27 \text{ nm}$ . As illustrated in **Figure 12a**, the electrical double layer is composed of two regions: the Stern layer and the diffuse layer. The Stern layer lies closest to the charge surface, where counterions (here, positively charged) are tightly bound due to strong electrostatic attraction and hence relatively immobile. Beyond this region, within the diffuse layer, ions are more loosely distributed and gradually restore electroneutrality with increasing distance from the surface. When the surface charge density increases, the *Gouy-Chapman length* decreases (**Figure 12b**). This means that at higher surface charge densities, the electric potential decays more rapidly with distance from the surface, resulting in a thinner and denser electrical double layer.

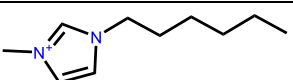
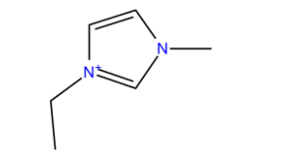
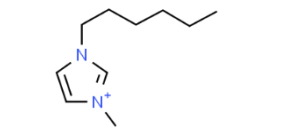
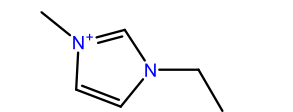
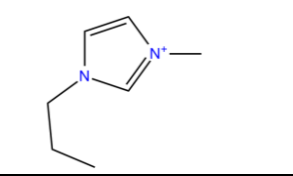
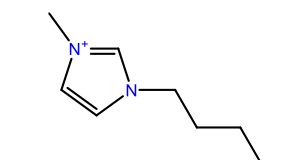


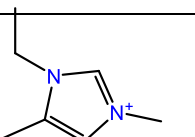
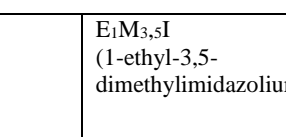
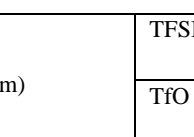
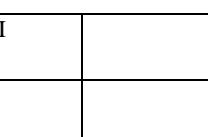
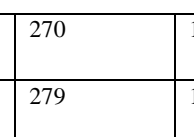
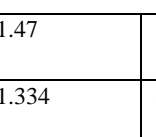
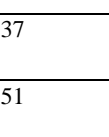
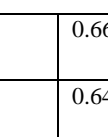
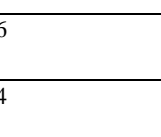
**Figure 12.** (a) Schematic of the electrical double layer. (b) Dependence of the Gouy-Chapman length on the surface charge density for different values of the Debye length.

The *density fluctuations* near the pore walls refers to the oscillatory variations in local ion concentration arising from spatial confinement and surface interactions. These fluctuations are especially pronounced when the pore size approaches the molecular dimensions, leading to a layered ion distribution perpendicular to the surface. They give rise to more/less dense ionic regions that affect ion transport.

The *characteristic liquid-to-glass length* ( $\zeta$ ) is the parameter used in the study of glass-forming systems. It associates with the freezing of dynamics at the liquid-to-glass temperature (typically is in the range of 1-2 nm). In polymers it associates with the freezing of the segmental motion at  $T_g$ .

**Table 1.** Physical properties of some known ILs.

Structure	Cation	Anion	$T_g$ (K)	$T_m$ (K)	Density ( $\rho$ , g/cm <sup>3</sup> )	Viscosity ( $\eta$ , mPa s)	Conductivity ( $\sigma_c$ , S/m)	Ref
	C <sub>1</sub> HI (1-methyl-3-hexylimidazolium)	TFSI		282		81		32
		PF <sub>6</sub>		389	1.0316			32
	C <sub>2</sub> HI (1-ethyl-3-hexylimidazolium)	BF <sub>4</sub>	186			41		32
		ClO <sub>4</sub>	192	294		112		32
		TFSI	184			54		32
		PF <sub>6</sub>	211			550		32
		TfO		281		58		32
	C <sub>1</sub> MI (1-methyl-3-methylimidazolium)	Cl		398	1.1399			42
		BF <sub>4</sub>		377		67		38
		TFSI		295	1.559	44	0.84 (20 °C)	54
	EMI (1-ethyl-3-methylimidazolium)	Cl		362	1.1362		0.343-3.709	55
		BF <sub>4</sub>	178	288	1.28	43	1.4	36
		TFSI	175	258	1.52	34	0.84	56
		PF <sub>6</sub>	193	332			0.52	56
	C <sub>3</sub> MI (1-propyl-3-methylimidazolium)	Cl		333	1.1014		0.332-4.969	34
		BF <sub>4</sub>	185	256	1.24	103	0.59	36
		TFSI	186		1.475		0.252	36
		PF <sub>6</sub>	199	313		312		37
	C <sub>4</sub> MI (1-butyl-3-methylimidazolium)	Cl	197	342	1.08			18
		BF <sub>4</sub>	202		1.12	219	0.35	36
		TFSI	169	269	1.429	52	0.39	32
		PF <sub>6</sub>	193	283	1.35	393	0.1	20
		TfO	191	289	1.29	90	0.37	42

	E1M3,5I (1-ethyl-3,5-dimethylimidazolium)	TFSI		270	1.47	37	0.66	25
		TfO		279	1.334	51	0.64	25
	DMPI (1,2-dimethyl-3-n-propylimidazolium)	TFSI	192	192		60	0.3	31
		PF <sub>6</sub>		351		34	0.05 (35 °C)	26, 31
		BF <sub>4</sub>					0.522	32
	P14 (n-methyl-N-butylpyrrolidinium)	TFSI	186	225	1.41	85	0.22	33
		MSI		215	1.28	1680	0.007	34
	C4-py (n-butylpyridinium)	BF <sub>4</sub>	206	288	1.224			36
		TFSI		299	1.453	9.9		37
	S111 (tri-methylsulfonium)	TFSI		318	1.58	44	0.82 (45 °C)	38
		BF <sub>4</sub>		490				
	S444 (tri-butylsulfonium)	TFSI		266	1.29	75	0.14	38
	N1114 (trimethyl-butylammonium)	TFSI	192	280	1.41	116	0.14	34
	N8111 (trimethyl-octylammonium)	TFSI	200	278	1.27	181	0.035	34
	TMPA (trimethylpropylammonium)	TFSI		290	1.44	72	0.33	39

All the data for viscosity, density and dc-conductivity refer to 25 °C unless otherwise noted.

## 1.2 Polymerized Ionic Liquids

Poly(ionic liquid)s (PILs), also called polymerized ionic liquids, refer to a subclass of polyelectrolytes that feature an ionic liquid species in each repeating unit, connected through a polymeric backbone to form a macromolecular architecture. Contrary to classic polyelectrolytes, which are water soluble and dissociate in aqueous solutions making the polymers charged (polysalts), most PILs are not soluble in water but in polar organic solvents. This is mainly due to the hydrophobic character of the counter-ion and the reduced Coulombic interactions. PILs can be classified as: polycations, bearing a cation in the backbone, polyanions bearing an anion, or polyzwitterions having both an anion and a cation (**Figure 13**).<sup>53</sup> Furthermore, different types of copolymers (random, alternating, block) and macromolecular architectures such as branched, dendritic or ramified structures are potentially possible. The different combinations among cations, anions and different polymer backbones and architectures make the number of PILs that can be synthesized very rich.

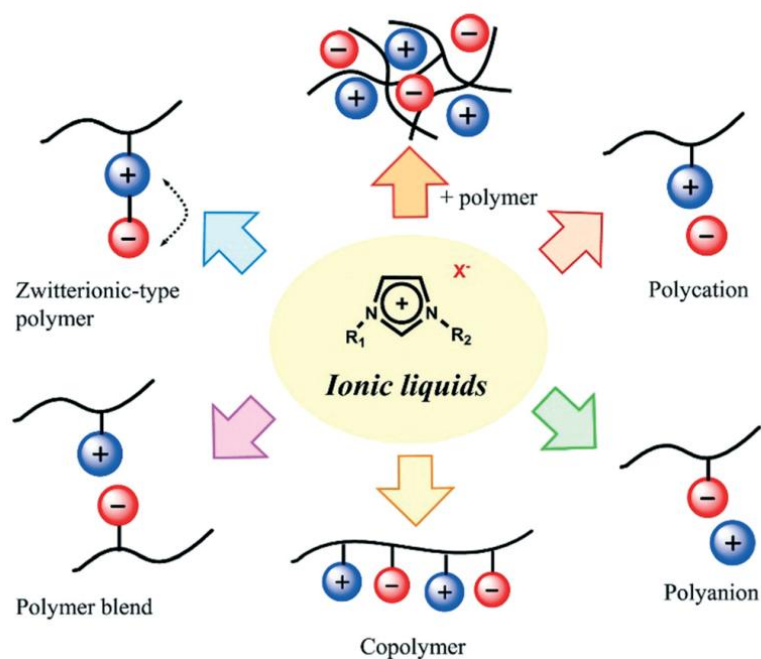


**Figure 13.** Possible chemical structures of polymerized ionic liquids.<sup>53</sup>

### 1.2.1 Structure-Property relationships in PILs

A common problem encountered with both liquid electrolytes and ion gels, is the propensity for electrolyte leakage. PILs enjoy many of the same favorable qualities with ILs, such as low flammability, chemical and thermal stability, and widely tunable physical properties, while

mitigating concerns related to electrolyte leakage by virtue of their polymeric structures. PIL “single-ion conductors” may thus serve as ideal polymer electrolytes for advanced electrical energy storage and conversion devices (e.g., fuel cells and batteries). Recent studies on the ionic conductivity of PILs, have demonstrated that materials with low glass temperatures ( $T_g$ ) are required, in order to obtain high levels of room temperature ionic conductivity. It is well documented in literature that ionic conductivity is largely controlled by the rate of polymer segmental mobility. Below we give a summary of the main contributions in ion transport in bulk PILs.

Colby *et al.*<sup>54</sup> investigated the relationship between  $T_g$  and repeating unit molecular volume,  $V_m$ , by examining PILs containing various chain length and anions (**Figure 14**). While the corresponding ILs generally showed lower  $T_g$  values with lower  $V_m$  – largely independent of anion type – the  $T_g$  values of PILs were significantly higher due to the decreased segmental motion inherent to the polymer backbone. Moreover, the type of anion played a critical role in modulating  $T_g$ . PILs with the smaller  $[\text{Br}^-]$  or  $[\text{BF}_4^-]$  counteranions exhibited higher  $T_g$ s than those with the larger  $[\text{TfO}^-]$ ,  $[\text{PF}_6^-]$ , or  $[\text{Tf}_2\text{N}^-]$  counterions. The smaller anions interacted more strongly with cations and the larger counterions acted as plasticizers. Side chain length was also found to affect  $T_g$ . Regardless of counterions,  $T_g$  was found to decrease with increasing,  $V_m$ , approaching a steady value in the high  $V_m$  limit.

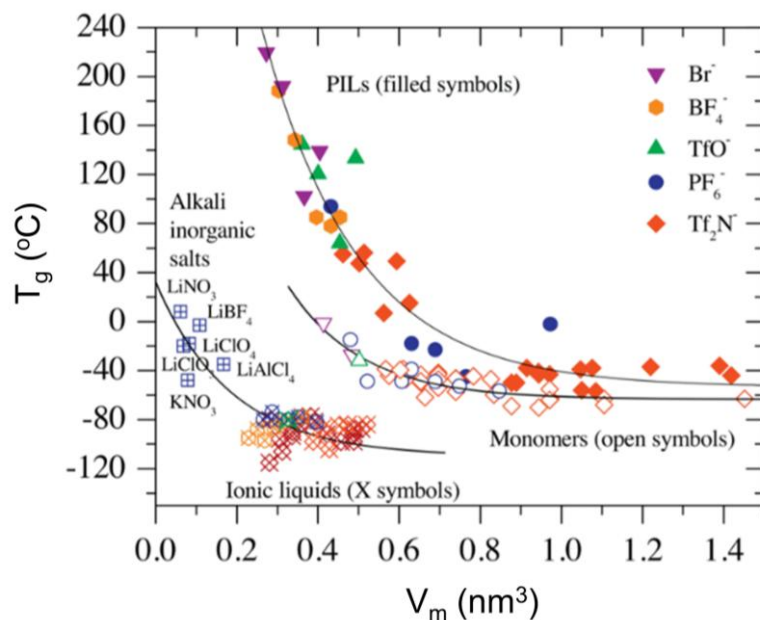


**Figure 14.** Correlation between glass temperature,  $T_g$ , and repeat unit molecular volume,  $V_m$ , (including the counterion) for imidazolium-based PILs with various side chains and counterions (filled symbols), monomers (open symbols), alkali inorganic salts (+ symbols), and ionic liquids (X symbols).<sup>54</sup>

Sokolov *et al.*<sup>55</sup> presented a comprehensive study on PILs with different chemical structures, counterion sizes, and chain rigidity, unveiling the importance of the molecular unit volume,  $V_m$ , dielectric constant,  $\epsilon$ , and chain rigidity in controlling the  $T_g$  of PILs. As illustrated in **Figure 15a**, the dependence of  $T_g$  on  $V_m$  followed a general behavior for PILs and their monomers. It decreased with increasing  $V_m$  and levels off at  $V_m \sim 0.8-1 \text{ nm}^3$ , which is consistent with Colby's earlier work. In the case of ILs,  $T_g$  goes through a minimum in the  $T_g(V_m)$  dependence. Importantly, their results revealed that chain rigidity exerts a strong influence on  $T_g$ . Flexible PILs exhibited  $T_g$  comparable to that of monomers, while rigid-chain PILs showed significantly higher  $T_g$  at the same  $V_m$ . Molecular dynamics simulations further confirmed these trends and demonstrated that an increase in the dielectric permittivity could markedly suppress  $T_g$  in both flexible and rigid systems (**Figure 15b**). The strong dependence of  $T_g$  on the dielectric permittivity emphasized the importance of electrostatic interactions in PILs. These insights culminated in a simplified empirical model capable of predicting  $T_g$  across structurally diverse systems. The study emphasized that tuning chain rigidity and enhancing dielectric permittivity are promising strategies for designing low- $T_g$  PILs with improved ionic conductivity at ambient conditions.

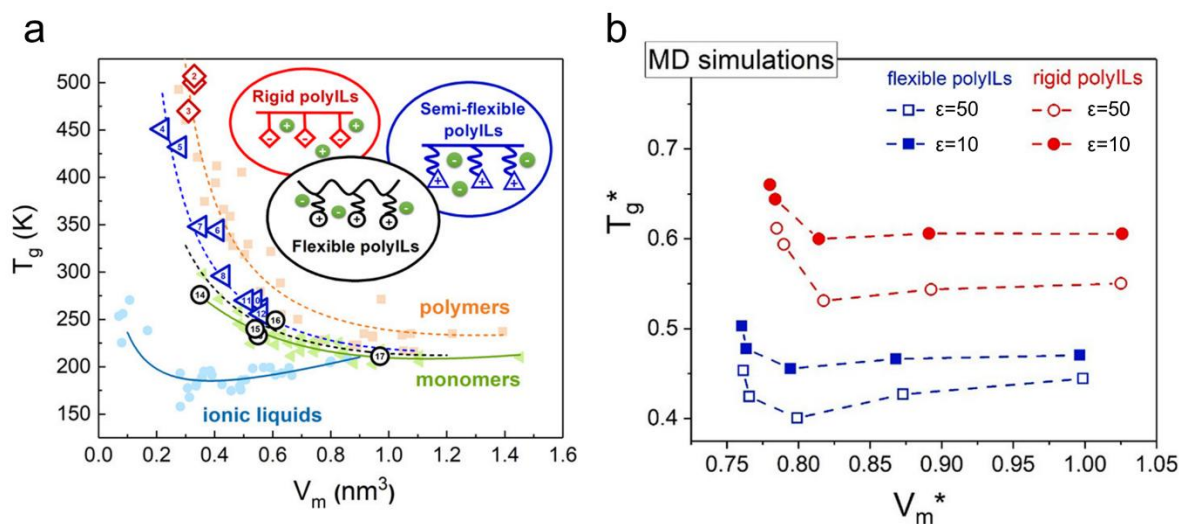


**Figure 15.** (a)  $T_g$  as a function of molecular unit volume for different PILs: open diamonds present rigid PILs, triangles refer to semiflexible, and circles to flexible PILs. (b) Results of MD simulations with two different values of the dielectric permittivity  $\epsilon$ . The asterisk on  $T_g$  and  $V_m$ , refer to quantities obtained from the MD simulations in reduced Lennard-Jones units.<sup>55</sup>

While glass temperature reflects the local segmental dynamics, the nanoscale ion packing structure provides critical insights into the organization of ionic domains and their impact on transport properties. The resulting morphological variations driven by ion packing

and modulated by anion type and chain length are closely linked to ionic conductivity, as they affect both the ion mobility and the continuity of conducting pathways. To this end, Colby *et al.*<sup>56</sup> explored the influence of anion and side chain length on the nanoscale morphology, ionic aggregation, and ion transport behavior of imidazolium-based PILs. As shown in **Figure 16a**, X-ray scattering revealed three structural features: the higher peak at  $q_I \approx 14 \text{ nm}^{-1}$  corresponds to the amorphous halo, the more subtle intermediate-angle peak at  $q_{II} \approx 8 \text{ nm}^{-1}$  was attributed to correlation between the anions, and the lower peak, at  $q_{III}$ , to the spacing between ion aggregates. The position of  $q_I$  and  $q_{II}$  shifted slightly to lower  $q$  with increasing anion size from  $[\text{BF}_4]^-$  to  $[\text{Tf}_2\text{N}]^-$ , indicating reduced local ordering. Notably,  $q_{III}$  became more intense and shifted to higher  $q$  in  $[\text{BF}_4]^-$ -based PIL, reflecting stronger ionic aggregation. This correlates with the suppressed ionic conductivity shown in **Figure 16b**, where  $[\text{Tf}_2\text{N}]^-$ -bearing PILs consistently show higher  $\sigma_{DC}$  due to weaker electrostatic interactions and enhanced ion mobility. Measurements of ion conductivity as a function of temperature (**Figure 16b**) revealed a characteristic “transition” from a Vogel–Fulcher–Tammann (VFT) behavior above  $T_g$  to an Arrhenius-type dependence below  $T_g$ , signifying a decoupling of ionic transport from the segmental motion. This behavior was systematically investigated in a series of PILs bearing identical anionic species ( $[\text{Tf}_2\text{N}]^-$ ) differing in side-group length. Notably, PILs with shorter alkyl side groups demonstrated sustained conductivity below  $T_g$ . It was attributed to the presence of continuous ion-rich domains that support conduction independent of segmental mobility.

To probe the microscopic origin of conduction, the authors quantified the concentration of simultaneously conducting ions ( $p$ , **Figure 16c**) and their mobility ( $\mu$ , **Figure 16d**). PILs containing  $[\text{Tf}_2\text{N}]^-$  exhibited higher  $p$  and  $\mu$ , consistent with greater ion dissociation and lower  $T_g$ . In systems with intermediate side group length,  $p$  decreased sharply near  $T_g$ , as compared to the long-length chains, indicating a change in the dominant charge transport mechanism. Above  $T_g$ , mobile anions were transiently coordinated by polymer segments and migrated in concert with segmental motion. Below  $T_g$ , segmental mobility was arrested, and only a small population of unbound free anions contributed to conduction. In addition, they investigated the role of imidazolium pendant structures, particularly tail type (N-*n*-butyl vs N-diethyleneoxy)<sup>51</sup> and length (N-*n*-butyl vs N-*n*-dodecyl)<sup>52</sup>. Substitution with a diethyleneoxy side chain (vs. *n*-butyl) reduced  $T_g$  and promoted ion dissociation. Conversely, long alkyl chains (e.g., *n*-dodecyl) promoted stronger ionic aggregation, reducing the dielectric permittivity and mobility, while short alkyl chains (e.g., *n*-butyl) led to weaker aggregation and increased dielectric permittivity.

Collectively, these results highlighted the interplay between ion morphology, aggregation, and decoupling behavior in determining the transport properties of PILs. They could suggest some rational design strategies through side-group and anion engineering to optimize conductivity.

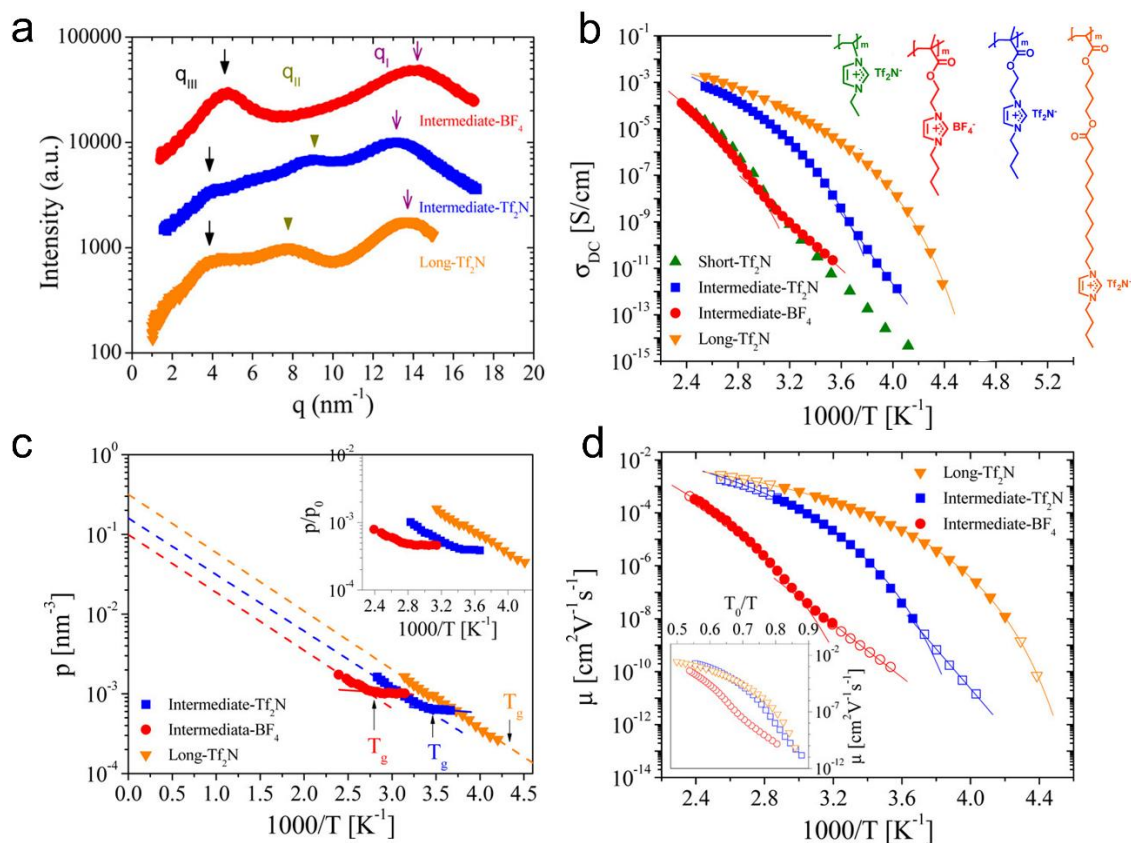


**Figure 16.** (a) X-ray scattering intensity as a function of the modulus of scattering wavevector  $q$  for the imidazolium-based PILs at room temperature. (b) Temperature dependence of ionic conductivity for PILs bearing different chain lengths and anion species ( $[\text{Tf}_2\text{N}]^-$  and  $[\text{BF}_4]^-$ ). (c) Temperature dependence of ion concentration  $p$ . The inset displays the fraction of anions participating in conduction. (d) Temperature dependence of the mobility of the conducting ions. The inset depicts the ionic mobilities with respect to inverse temperature normalized by  $T_0$ .<sup>56</sup>

To elucidate how molecular design influences  $T_g$ , ionic conductivity, and morphology in PILs, Pipertzis *et al.*<sup>57</sup> systematically investigated ion transport in imidazolium-based PILs by varying alkyl side-chain length and counteranion size (**Figure 17a**). Their study combined thermodynamic analysis and morphological characterization to reveal some clear structure–property relationships. As illustrated in the left pattern of **Figure 17 b**, for a fixed counteranion, increasing the alkyl side-chain length resulted in a decrease in  $T_g$ . This trend was attributed to internal plasticization, which enhances chain flexibility by reducing interchain interactions. Conversely, when the alkyl side-chain length was held constant, the nature of the counteranion significantly influenced  $T_g$ . Small, strongly coordinating anions (e.g.,  $[\text{Br}]^-$ ,  $[\text{BF}_4]^-$ ) increased

$T_g$  due to their strong electrostatic interactions with the imidazolium cation, thereby restricting polymer segmental mobility. In contrast, large, weakly coordinating anions (e.g., [TFSI]<sup>-</sup>, [BPh<sub>4</sub>]<sup>-</sup>) reduced  $T_g$ , a result of diminished Coulombic coupling and enhanced local chain flexibility. However, a further increase in anion size disrupted the ordered morphologies (**Figure 17c**). The transition from smectic or hexagonally close-packed (HPC) phases to disordered ionic domains coincided with an unexpected increase in  $T_g$ . In these disordered phases, bulky anions were less efficiently incorporated into ion-rich layers and hindered backbone reorientation by steric obstruction, thus raising  $T_g$ . This trend was clearly visible in **Figure 17b** (right), where the lower  $T_g$  values correlated with HPC or smectic morphologies. Their results suggested that anions are located away from the polymer backbone, possibly within ion-conducting "channels." To rationalize this behavior, Pipertzis *et al.* proposed a "stick-and-jump" model. In this framework, a charged layer ("channel") was located between the backbones and allows for local anion jumps. According to the model shown in **Figure 17d**, anions stick for certain time to the cation,  $\tau_b$ , whereas at later times, they dissociate and jump to another local site. The duration of this association was defined as  $\tau_b = \tau_\alpha \exp\left(\frac{E_{\text{complexation}}}{k_B T}\right)$ . Here,  $\tau_\alpha$  is the time for the cation to diffuse a distance  $d_{II}/2$  in the absence of any attractions between ions and  $E_{\text{complexation}}$  is the ion complexation energy. Smaller and more symmetrical anions (such as [Br]<sup>-</sup>) exhibited higher complexation energies and thus remained bound for longer times, restricting chain dynamics and increasing  $T_g$ . Despite their size enabling rapid diffusion, the long association time reduced the number of free charge carriers, leading to low ionic conductivity. Larger anions (such as [TFSI]<sup>-</sup> or [Picrate]<sup>-</sup>) had lower complexation energies due to charge delocalization and steric hindrance. They dissociated more readily, enabling greater segmental motion and thus lower  $T_g$ . While their larger size lead to slower diffusion rates, the higher concentration of mobile ions compensates, resulted in overall higher ionic conductivity. Additionally, by comparing relevant length scales, the authors showed that local jump distances for the anions range from  $R^+ + R^-$  (or  $d_{II}/2$ ) to  $R^-$ , depending on the morphology and local packing environment. Overall, ionic conductivity in polyelectrolytes is a balance between ion complexation and ion diffusion. The "stick and jump" model offered a guiding principle for selecting and designing PILs with tailored ion-polymer interactions. By choosing bulky, weakly coordinating anions and optimizing side-chain structure, one can reduce ion sticking and enhance mobility. This approach enables the development of high-conductivity PILs suitable for electrochemical applications.

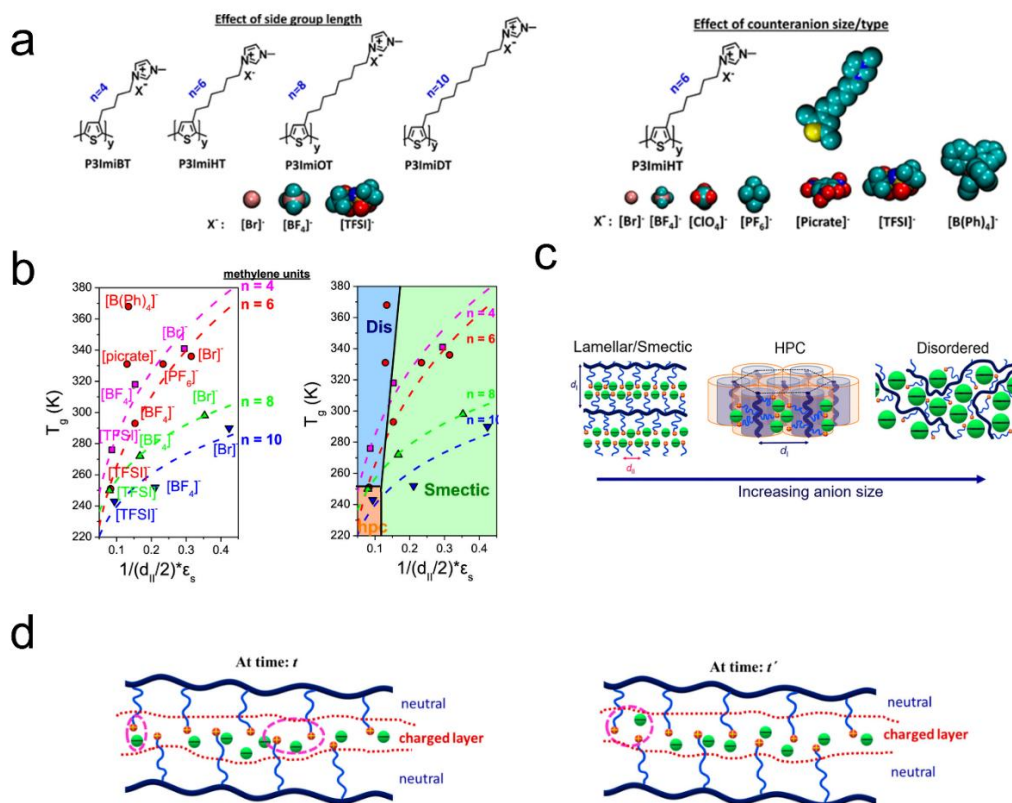


**Figure 17.** (a) Chemical structures of the studied polyelectrolytes. (b) (left) Glass temperature (from DSC) as a function of Coulombic interactions at the charge association length scale ( $d_{II}/2$ ) for the polyelectrolytes with different side group lengths and different counterions. (right) The different morphologies revealed from the WAXS (disordered, hpc, smectic). (c) Schematic representation of a lamellar (left), a cylindrical HCP morphology (center), and a disordered state (right). The domain spacing ( $d_I$ ) and charge alternation ( $d_{II}$ ) lengths are also indicated. (d) Highly schematic representation of the mechanism of ion transport.<sup>57</sup>

### 1.2.2 Decoupling of ion transport from the segmental dynamics in PILs

The ionic conductivity in polymer electrolytes can be described by the Nernst-Einstein relationship, in terms of the ion diffusion coefficient  $D$ :  $\sigma = \frac{Dk_B T}{ne^2}$ . At the microscopic scale,

ion motion can be modeled as a random walk with step length (hopping length)  $\langle r^2 \rangle^{1/2}$ , and step time (relaxation time)  $\tau_s$ , through the Einstein-Smoluchowski relation:  $D = \frac{\langle r^2 \rangle}{6\tau_s}$ .

Substituting into the Nernst-Einstein equation gives:  $\sigma = \frac{ne^2}{6k_B T} \frac{\langle r^2 \rangle}{\tau_s}$ . This relation has been validated in several flexible polymer systems. The underlying physical picture is that there is a *coupling* of ionic diffusion to the polymer segmental dynamics,  $\sigma\tau_s T = \text{constant}$ : Ion mobility is possible only when polymer segments undergo large amplitude rearrangement. Considering ions like spheres with radius  $r$ , their translational diffusion follows the Stokes-Einstein relation:

$D_{transl} = \frac{k_B T}{6\pi\eta r}$ ,  $\rightarrow \sigma = \frac{ne^2}{6\pi\eta r}$ . If ionic motion is fully coupled to the polymer matrix, then the ionic conductivity is inversely proportional to the viscosity  $\eta$ . Thus, as the temperature approaches  $T_g$ , and the segmental motion freezes, ionic conductivity drops sharply.

However, studies on rigid polymers have revealed a *decoupling* between ionic transport and segmental relaxation. Wang *et al.*<sup>58</sup> proposed an approach to illustrate this decoupling by plotting  $\sigma T\tau_s$  as a function of  $\tau_s$ , as shown in **Figure 18a, top**. For tightly coupled systems,  $\sigma T\tau_s$  should remain constant, producing a horizontal line. This behavior was indeed observed in PPEOMA and PPEOCL that have flexible backbones, while rigid polymers such as PPEOS-*b*-PSt, PNBCEM, and PPEOS*t* exhibited a change of nearly 4–6 orders of magnitude in  $\sigma T\tau_s$  as  $\tau_s$  varied from  $10^{-7}$  to  $10^2$  s, displaying significant decoupling. To further evaluate the validity of the Stokes–Einstein relationship, they plotted  $D\tau_s$  as a function of  $\tau_s$  (**Figure 18a, bottom**). Similar to the behavior of ionic conductivity for flexible polymers,  $D\tau_s$  remained roughly a constant, confirming the strong coupling between ion diffusion and segmental relaxation. However, for rigid polymers,  $D\tau_s$  increased markedly with  $\tau_s$  supporting the decoupling hypothesis. The decoupling behavior near  $T_g$  could be described by a power-law dependence:  $\sigma T\tau_s \sim \tau_s^{\varepsilon_1}$ ,  $D\tau_s \sim \tau_s^{\varepsilon_2}$ , here  $\varepsilon_2 = 0$  corresponds to the classical coupled case. The exponents  $\varepsilon_1$  and  $\varepsilon_2$  serve as quantitative measures of the decoupling strength. To further examine the correlation between the degree of decoupling and the properties of the polymer, they introduced the fragility index  $m$ <sup>59</sup>, defined as:  $m = \frac{d \log \tau_s}{d(T_g/T)} \Big|_{T = T_g}$ . It quantifies how sharply  $\tau_s$  changes near  $T_g$ , and reflects the degree of packing frustration in polymer matrix. In **Figure 18b**, the decoupling exponents ( $\varepsilon_1$  and  $\varepsilon_2$ ) for both  $\sigma T\tau_s$  and  $D\tau_s$  were compared with the fragility index  $m$  and  $T_g$  of the same polymer electrolytes studied in **Figure 18a**. The degree of decoupling showed a strong correlation with the fragility index  $m$ . In particular, PPEOS*t* and PPEOMA have similar  $T_g$  (265 K for PPEOS*t* and 240 K for PPEOMA) but show a large difference in decoupling (PPEOS*t*,  $\varepsilon_2 = 0.76$ ; PPEOMA,  $\varepsilon_2 = 0.05$ ). On the other hand, PPEOS*t* and PPEOS-*b*-PSt exhibited the same degree of decoupling ( $\varepsilon_2 = 0.76$ ), but their glass transition temperatures differed by 73 K. This result suggested that fragility, rather than the glass transition temperature, is the key factor that governs the decoupling between ionic transport and segmental relaxation in polymer electrolytes. This decoupling behavior is reminiscent to that observed in superionic glasses and crystals, where ionic conductivity remained high even as the structural matrix exhibited minimal mobility. In both cases, a high degree of packing

frustration leads to a loose, disordered local environment near  $T_g$ , which can preserve static free volume and facilitate ion transport independent of polymer chain dynamics (**Figure 18c**).

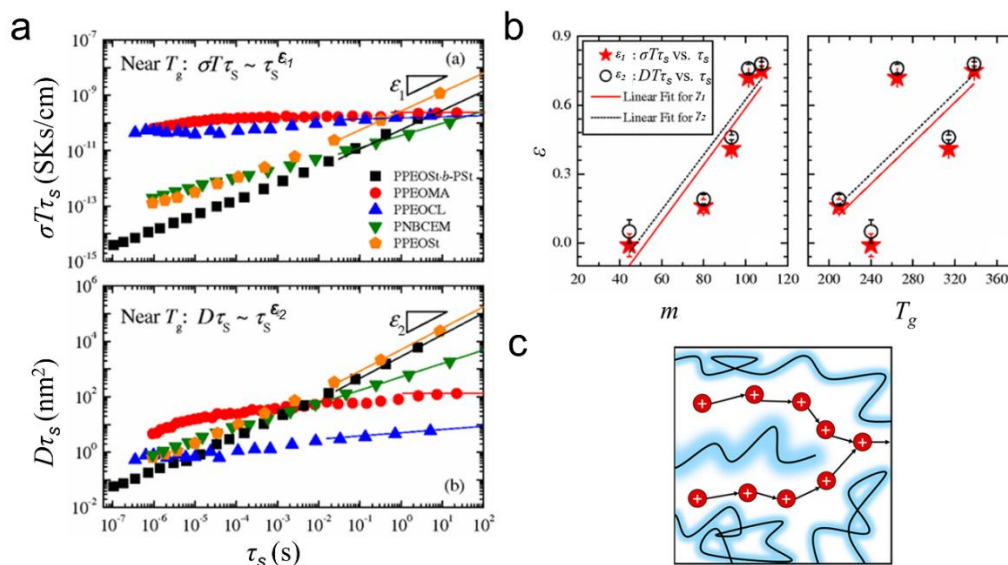


**Figure 18.** (a)  $\sigma T \tau_s$  and  $D \tau_s$  versus  $\tau_s$  for the polymer electrolytes. The dependence of  $\sigma T \tau_s$  and  $D \tau_s$  on near  $T_g$  can be fit by a power law (solid lines):  $\sigma T \tau_s \sim \tau_s$  and  $D \tau_s \sim \tau_s$ . (b) Correlation between the decoupling exponent ( $\epsilon$ ) and the fragility index ( $m$ ) and the glass temperature ( $T_g$ ).<sup>58</sup> (c) The channels of the electrolyte provide a network of vacancies through which ions can opportunistically hop.<sup>59</sup>

A criticism in their work is that their conclusion conflicts with earlier studies that emphasized  $T_g$  as the primary factor governing the coupling between ionic conductivity and polymer segmental dynamics. While Wang *et al.* proposed fragility as the key parameter, they did not thoroughly address why  $T_g$  fails to explain the observed behavior, nor do they reconcile their findings with existing models.

Beyond fragility-based interpretations, Stacy *et al.*<sup>60</sup> investigated the origin of decoupling from an energetic standpoint by analyzing the activation energy associated with ionic conductivity in the glassy state ( $T < T_g$ ). By fitting the temperature dependence of relaxation time  $\tau_\sigma(T)$  at  $T < T_g$  to an Arrhenius behavior, they extracted the activation energy  $E_\tau$ . When plotted as a function of the mobile ion radius,  $R$ , in **Figure 19**,  $E_\tau$  exhibited a nonmonotonic dependence, featuring a distinct minimum that reflected the balance between competing electrostatic and elastic contributions to ion transport. To rationalize these observations, they proposed a composite model that includes both electrostatic and elastic energy contributions. The electrostatic term represents the energy required to separate two oppositely charged species. It varies inversely with the ionic radius. The elastic contribution is modeled using the shoving model. The model assumes that the movement of an ion in a frozen polymer matrix is governed

by thermal fluctuations that locally increase volume. In this case,  $E_{\text{elastic}} = \alpha G_{\infty} V_{\text{ion}}$ , where  $G_{\infty}$  is the high-frequency shear modulus (characterizing the material's resistance to deformation at high frequencies),  $V_{\text{ion}}$  is the volume of the moving ion ( $\sim 4\pi R^3/3$ ), and  $\alpha$  is a constant for a given polymer ( $\alpha < 1$ ) representing how frustration in chain packing (free volume) locally softens the shear modulus. The total activation energy is then expressed as:

$$E_{\sigma}(T < T_g) = \frac{q^2}{4\pi\epsilon\epsilon_0 R} + \alpha G_{\infty} V_{\text{ion}}$$

Here  $q$  is the ion charge,  $\epsilon$  is the dielectric permittivity,  $\epsilon_0$  is the vacuum permittivity, and  $R$  is the distance between the ion and a counterion. The model captures the nonmonotonic size dependence by illustrating that, for small ions, electrostatic interactions dominate and decrease with increasing radius, while for larger ions, the elastic contribution becomes increasingly significant. Their findings emphasize that the elastic contribution governs  $E_{\tau}$  for most ions and is sensitive to polymer structure, particularly the degree of chain packing frustration and dielectric properties.

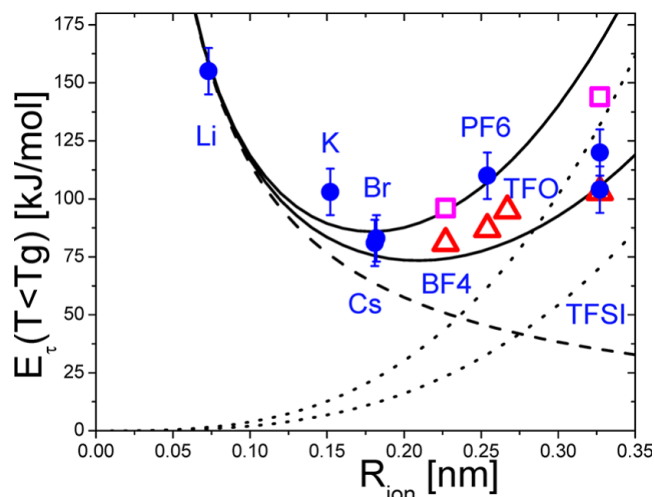


**Figure 19.** Activation energy for mobile ion diffusion (conductivity relaxation time) at  $T < T_g$  vs the ion radius (blue circles). Square and triangle symbols represent the data of different anions size from literature.<sup>56, 60, 61</sup> The dashed line gives the Coulomb contribution with  $\epsilon = 6$ , while the dotted lines present elastic contribution with  $\alpha=1$  and  $G_{\infty}=1.5$  GPa. The solid lines present the model predictions as a sum of the elastic and Coulomb contributions to the activation energy.<sup>60</sup>

Sangoro *et al.*<sup>62</sup> studied an IL and the corresponding PIL aiming to provide some experimental evidence for the origin of decoupling between ionic conductivity and structural relaxation in PILs (**Figure 20**). By comparing the temperature dependence of dc conductivity and zero-shear viscosity, they showed that while both properties exhibited similar VFT-type behavior in low-molecular-weight ILs, PILs displayed a pronounced divergence, particularly near  $T_g$ . Remarkably, when conductivity and viscosity were plotted against normalized

temperature ( $T_g/T$ ), PILs retained significantly higher conductivity at identical relative temperatures—by nearly four orders of magnitude at  $T_g$ . This suggested that ion transport in PILs was dominated by the motion of smaller, more mobile anions, while the polymeric cations, being part of the backbone, were dynamically frozen. Their analysis further revealed that the classical scaling relation  $\sigma\eta = \text{const}$ , valid in molecular ILs, breaks-down in PILs as  $T_g$  is approached, indicating a fundamental decoupling of ionic transport from the matrix relaxation. This decoupling was further attributed to the presence of local free volume and structural asymmetry between the ionic species, enabling anion mobility even in the absence of significant segmental motion.

A criticism in this work is that normally we do not compare at the same  $T_g/T$  but rather as a function of  $T$ . For the decoupling to be useful it has to take place at lower temperatures, where a particular application is needed.

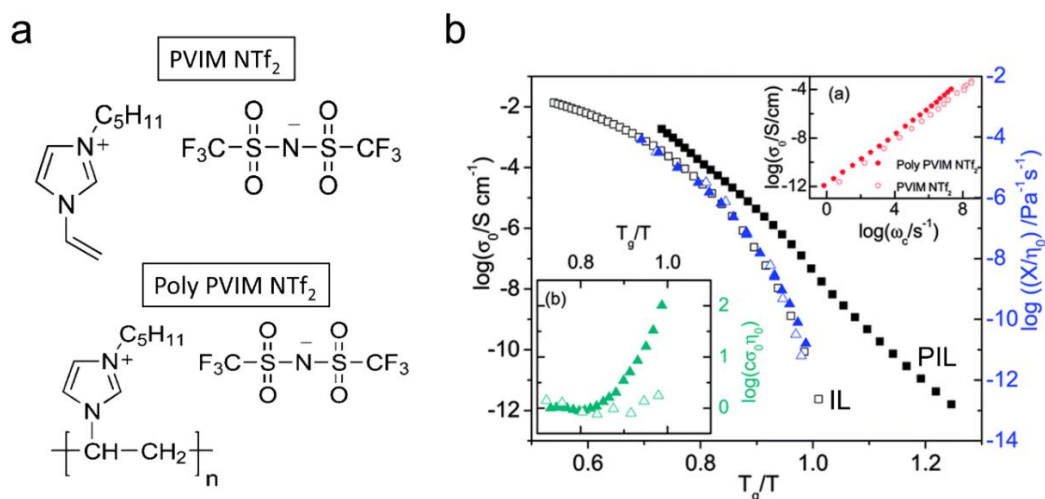


**Figure 20.** (a) Chemical structure of low molecular weight  $[\text{PVIM}]^+[\text{NTf}_2]^-$  and polymerized  $[\text{PVIM}]^+[\text{NTf}_2]^-$ . (b) The conductivity,  $\sigma_0$  (black symbols), as well as the inverse shear viscosity  $1/\eta_0$  (blue symbols) versus  $T_g/T$  for the PIL, Poly  $[\text{PVIM}]^+[\text{NTf}_2]^-$  (full symbols), and the IL,  $[\text{PVIM}]^+[\text{NTf}_2]^-$  (open symbols). Inset: (a) dc conductivity,  $\sigma_0$ , as a function of the characteristic frequency,  $\omega_c$ , and (b) product of the dc conductivity and the zero shear viscosity normalized with respect to the high temperature values for the systems investigated versus  $T_g/T$ .<sup>62</sup>

### 1.2.3 Zwitterionic PILs

As we discussed already, ion transport in conventional single-ion conductors is largely controlled by the segmental dynamics of the polymer matrix. Ion diffusion pathways, formed by interstitial and/or lattice site vacancies, can be designed to support ion hopping/migration. While these solid polymer electrolytes often exhibit a degree of decoupling between ionic

conduction and polymer motion, their overall conductivities remain low due to the inherent limitation of matrix-coupled transport.

To address this issue, Segalman *et al.*<sup>63</sup> developed a new class of semicrystalline zwitterionic PILs (PZILs) via a design strategy that introduced structural support and ion conduction pathways within the polymer matrix. These PZILs featured tethered zwitterionic moieties to the polymer backbone, where each repeat unit contained a covalently linked cation-anion pair (**Figure 21a**). This architecture offered intrinsic charge neutrality to the polymer while enabling the dissociation and transport of added lithium salts. As illustrated in **Figure 21b**, the PZILs self-assembled into nanostructures comprising both ordered and amorphous regions, supporting two distinct ion transport mechanisms: (i) “vehicular” transport, where lithium ions move through the amorphous matrix being carried with the aid of polymer segments, and (ii) fast, selective conduction through ordered ion-rich channels. This dual-mode transport was facilitated by the weak Coulombic interactions between bulky, pendant zwitterion groups and the asymmetry in mobile cation and the tethered anion sizes. Surprisingly, even at low salt doping levels (salt/monomer molar ratio  $r$ ,  $r = 0.1$ ), the PZILs exhibited conductivities several orders of magnitude higher than the undoped parent polymer, indicating that the ionic current is dominantly carried by the  $[\text{Li}]^+[\text{TFSI}]^-$  dopants. At high doping levels ( $r = 0.9$ ), the conductivity approached values observed in conventional high-conductivity systems such as PEO/LiTFS which normally dependence on fast segmental motion (**Figure 21c**). Furthermore, PZILs maintained substantial ionic mobility below  $T_g$ , highlighting their decoupled conduction mechanism. The spatial arrangement of the zwitterion (with the cation perpendicular to the backbone) was selected based on molecular calculations by Keith *et al.*<sup>64</sup> which suggested that this orientation results in greater selectivity for lithium motion. The large size of free anion, (e.g.,  $[\text{TFSI}]^-$ ) limits its ability to permeate ordered ion channels, thereby promoting selective  $\text{Li}^+$  hopping. This size-dependent ion selectivity behavior was evidenced by both the high lithium transfer number,  $t_+$  ( $t_+ \approx 0.7$ ) and limiting current fraction,  $\rho_+$  ( $\rho_+ \approx 0.6$ ) (when  $\rho_+$  approaches unity, nearly all ionic current is carried by cations) (**Figure 21d**). Interestingly, these values were achieved without sacrificing total ionic conductivity, unlike conventional polymer electrolytes. These results - provided that they prove to be correct/reproducible - may provide motivation for further studies of PZILs as tunable platforms for the selective transport of target ions.

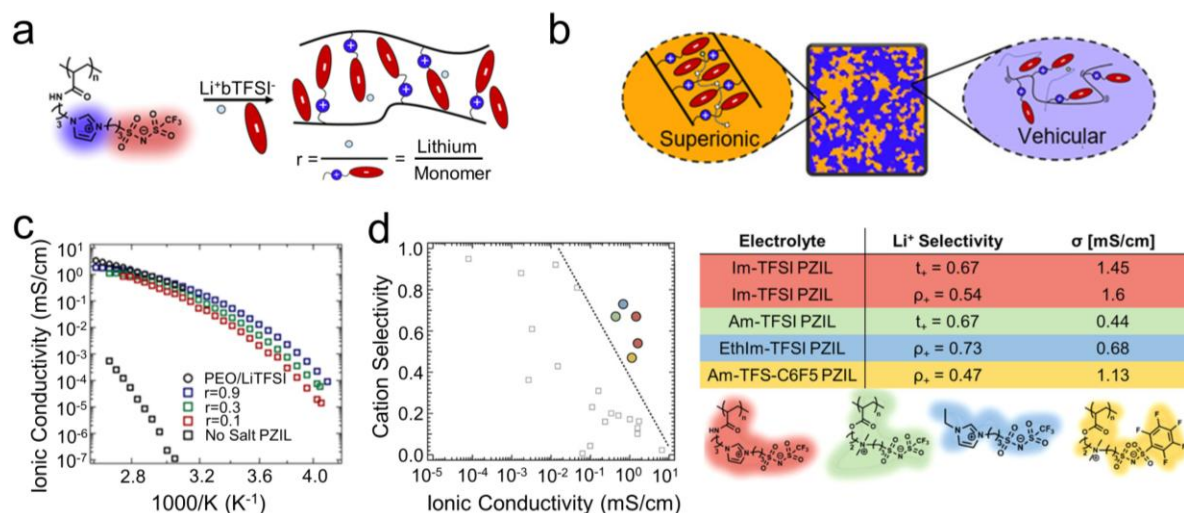


**Figure 21.** (a) The zwitterionic polymer comprises IL-inspired ions tethered to the backbone. Mobile ions were doped through the addition of a  $[\text{Li}]^+[\text{TFSI}]^-$  salt at select molar ratios. (b) Schematic representation of the conduction mechanism in the polymer. (c) Ionic conductivity of the salt-containing PZILs shown as a function of temperature is comparable to that of PEO.<sup>65</sup> (d) A plot of cation selectivity-ionic conductivity captures the traditional tradeoff between ionic selectivity versus conductivity. The table indicates the selectivity metrics and conductivities for PZIL electrolytes.<sup>63</sup>

### 1.2.4 Effects of nanoconfinement on ion transport in PILs

Confinement has emerged as a powerful strategy to tailor ion transport properties in PILs. Some earlier works have studied the effect of confinement in low molar mass or short-chain PILs. They revealed the importance of surface interactions and provided insight into PIL confinement. Evans *et al.*<sup>66</sup> systematically investigated the influence of nanoconfinement on ion transport by spin-coating PILs with varying ion pairs onto interdigitated electrodes. As shown in **Figure 22**, the ionic conductivity decreased notably when the PIL thickness was confined below 70 nm, with the strongest salt effect seen in the Poly[Am]<sup>+</sup>[BF<sub>4</sub>]<sup>-</sup> system. They attributed the effect to the charge–substrate interaction and to a possible  $T_g$  increase due to nanoconfinement which hinders ion transport. Under confinement, increasing the interface-to-bulk ratio leads to a greater significance of charge-surface interactions. To further interpret the interfacial effect, a two-layer conductivity model was employed as  $\frac{\sigma}{\sigma_{bulk}} = \frac{h-h_{int}}{h}$ , where  $h_{int}$  is the interfacial layer thickness. The intrinsic assumption was that each sample consisted of a low-conductivity interfacial layer adjacent to the substrate and a bulk-like inner layer. Fitting of the conductivity data (**Figure 22**) revealed a larger interfacial layer thickness in system with stronger electrostatic interactions. This suggested that ion-substrate interactions suppress mobility near the interface, contributing significantly to the overall conductivity loss.

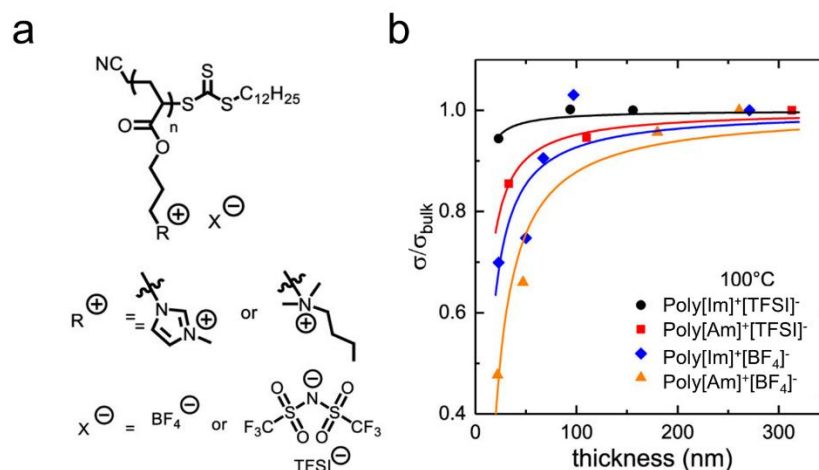


**Figure 22.** (a) Chemical structure of PILs with different alkyl lengths ([Am]<sup>+</sup>, [Im]<sup>+</sup>) and anion species ([BF<sub>4</sub>]<sup>-</sup>, [TFSI]<sup>-</sup>). (b) Ionic conductivity normalized to the thickest film of each PIL vs film thickness at 100 °C. Conductivity decreased as PIL film thickness approached 70 nm or below. The extent of decrease in conductivity or the thinnest film followed the trend Poly[Im]<sup>+</sup>[TFSI]<sup>-</sup> < Poly[Am]<sup>+</sup>[TFSI]<sup>-</sup> < Poly[Im]<sup>+</sup>[BF<sub>4</sub>]<sup>-</sup> < Poly[Am]<sup>+</sup>[BF<sub>4</sub>]<sup>-</sup>. The solid curves are fits based on the two-layer conductivity model.<sup>66</sup>

Sangoro *et al.*<sup>67</sup> reported the effect of confinement on the ionic conductivity of PILs located inside silica nanopores (~ 7.5 nm). Confined PIL exhibited up to a 3-order-of-magnitude increase in ionic conductivity compared to the bulk (**Figure 23**). This enhancement was attributed to the spatial heterogeneity in polymer dynamics reduced by confinement (*i.e.*, the conductivity relaxation was thought to be much faster at the center of the nanopores than in the bulk). Notably, as pore diameter decreased, conductivity increased, indicating a strong dependence on the confinement scale. The findings also showed that at low temperatures, confined PILs could achieve conductivities similar to or exceeding those of the corresponding ILs. They suggested that nanoconfinement not only alters polymer packing and ion coordination but also enables decoupling of ionic motion from polymer matrix dynamics.

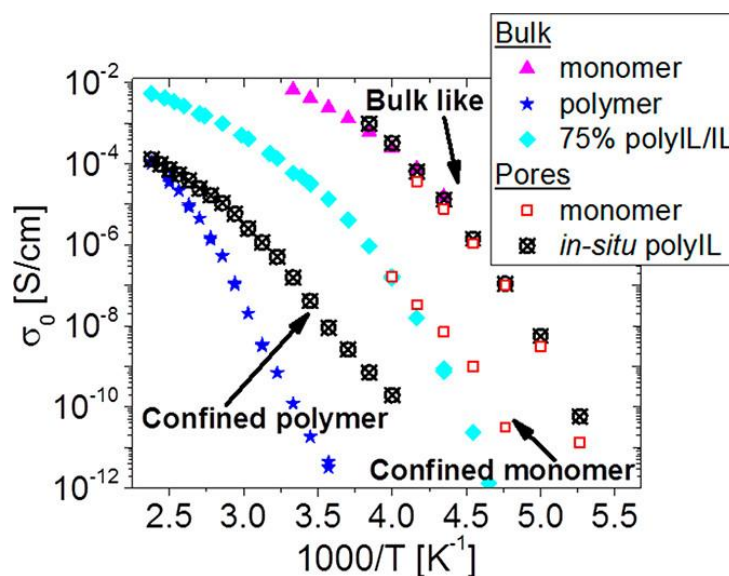


**Figure 23.** Dc conductivity ( $\sigma_0$ ) plotted against inverse temperature for all ILs and PILs.<sup>67</sup>

Experimental studies of confined ILs and PILs have led to conflicting results with respect to changes in the ionic conductivity. This reflects the different ion-wall interactions and the concomitant effects of density modulation near the surface. Addressing these issues requires different but complementary techniques (dielectric spectroscopy as a function of temperature and pressure as well as in situ measurements by nanodielectric spectroscopy nDS), differential scanning calorimetry (DSC), reflection optical microscopy, optofluidics, and several surface characterization techniques including SEM, contact angle, surface tension, and extensive structural characterization by X-rays. Significant progress in this field requires a combination of precise synthesis, modelling and simulation, and characterization of the physical properties with emphasis on ion transport.

### 1.3 Scope of the Thesis

In this Thesis, my aim is to identify the principles underlying ion transport within nanochannels and to possibly suggest new processes with efficient ion transport. In the long run, this fundamental understanding could be transformative for the field, enabling similar materials/processes to be used in future energy devices. Applications range from nanofluidic circuits, nanopore-based sensing devices, and bioinspired energy conversion systems. For each sub-area investigated different questions are addressed (**Table 2**).

**Table 2.** Areas of interest in confined ILs and PILs and their mixtures, scientific questions and means of verification.

Area of research	Scientific Questions	Systems to be investigated	Method
Ionic liquids (ILs)	• How ILs penetrate nanopores?		<i>In situ</i>
	• What is the effective viscosity and dc-conductivity?	[BMIM] <sup>+</sup> [BF <sub>4</sub> ] <sup>-</sup>	and <i>ex situ</i>
	• Can we decouple ion-conductivity from viscosity?	[BMIM] <sup>+</sup> [TFSI] <sup>-</sup>	nanodielectric spectroscopy
	• Can we enhance ion conduction by confinement?	[BMIM] <sup>+</sup> [PF <sub>6</sub> ] <sup>-</sup>	(nDS)
Polymerized ionic liquids (PILs)	• How PILs penetrate the same pores?		<i>In situ</i>
	• What is the effect of chain structure on ion transport in PILs?	poly[BMIM] <sup>+</sup> [TFSI] <sup>-</sup>	and <i>ex situ</i>
	• How polymer adsorption influences the conductivity?	poly[VBBI] <sup>+</sup> [TFSI] <sup>-</sup>	nDS
Imbibition of IL/PIL mixtures	• How PIL/IL mixtures penetrate nanopores?		<i>In situ</i>
	• Can we separate the constituent components by the difference in imbibition kinetics?	[BMIM] <sup>+</sup> [X] <sup>-</sup> / poly[BMIM] <sup>+</sup> [X] <sup>-</sup>	and <i>ex situ</i> nDS
Effect of confining geometry	• What is the effect of nanopore shape on the self-assembly and ion conductivity of ILs?	Cylindrically- vs. conically-shape nanopores	<i>Ex situ</i> nDS

### 1.3.1 What determines the conductivity of ILs in the bulk and during infiltration in nanopores?

In this area, a series of ILs bearing the same cation, 1-butyl-3-methylimidazolium ( $[\text{BMIM}]^+$ ), and six different anions ( $[\text{Cl}]^-$ ,  $[\text{Br}]^-$ ,  $[\text{I}]^-$ ,  $[\text{BF}_4]^-$ ,  $[\text{PF}_6]^-$  and  $[\text{TFSI}]^-$ ) with radii from 0.168 nm to 0.326 nm were investigated with respect to their self-assembly, the thermodynamics and the ionic conductivity in the bulk, during flow and under confinement in cylindrical nanopores with sizes in the range from 400 nm to 25 nm (**Figure 24a**). In the bulk, the  $[\text{BMIM}]^+[\text{X}]^-$  exhibited weak ordering as a result of cation-anion correlations (charge alteration peak), and nanophase separation of polar/apolar groups. Liquid-to-glass temperatures were found to differ by  $\sim 50$  K, their viscosities by a factor of  $\sim 270$ , and their conductivities by a factor of 24 (all at a temperature of 303 K). Electrostatic interactions were largely responsible for variations in the glass temperature, the viscosity and the conductivity.

Confined ILs behave differently from the bulk. The ILs penetrated the pores with an effective viscosity of the order of their bulk viscosity. However, within the pores the dc-conductivity was reduced relative to bulk, indicating the immobilization of ions at the pore walls. Hydrophobizing the internal AAO surface (silanization) – at least partially – recovered the bulk conductivity (**Figure 24b**). Changes in conductivity on cooling and heating were used as markers of crystallization/melting that allowed to construct the effective phase diagrams of the confined ILs. An interesting feature of the phase diagrams was the complete suppression of crystallization of  $[\text{BMIM}]^+[\text{TFSI}]^-$  and  $[\text{BMIM}]^+[\text{PF}_6]^-$  within pores with a diameter of 25 nm (**Figure 24c**). This is suggestive of the critical nucleus size needed for crystallization. Since both ILs have favorable ion conductivities and low glass temperatures, confinement proved to be an efficient method to suppress the undesired bulk crystallization during heating. Overall, confinement provided the means to increase conductivity by suppressing crystallization.

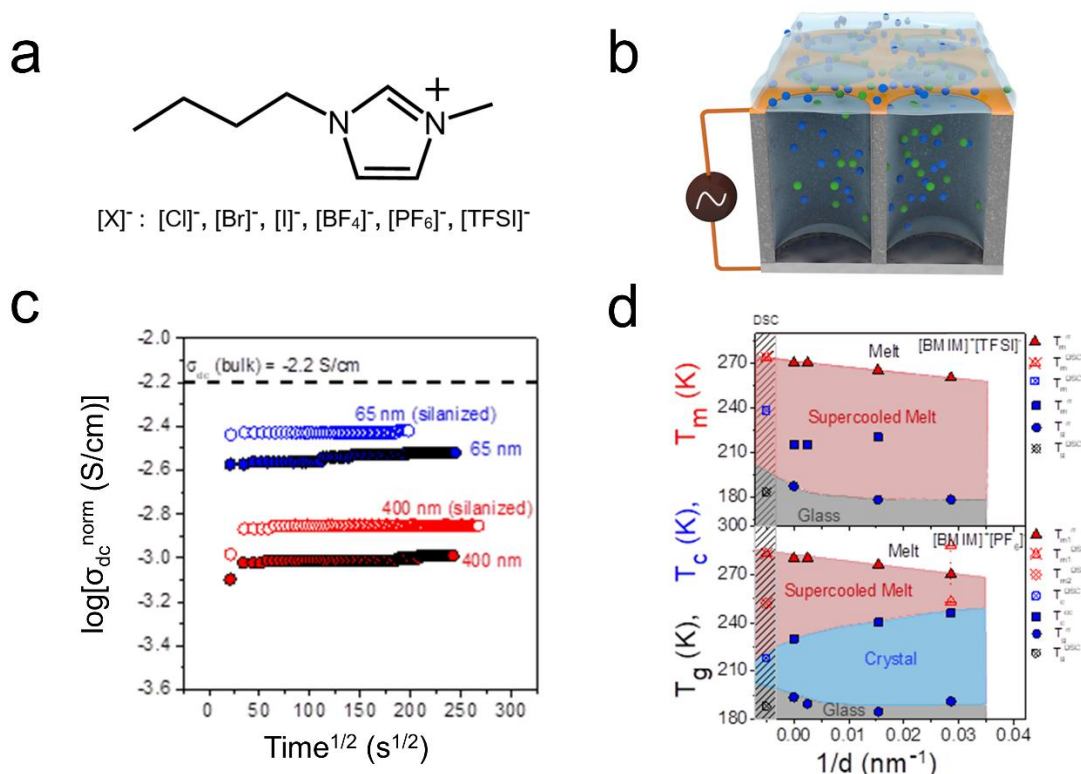


**Figure 24.** (a) Schematic of the chemical structure of the ILs bearing the 1-butyl-3-methylimidazolium cation and six different anions. (b) Schematic of the experimental setup of *in-situ* nDS. (c) Evolution of the normalized dc-conductivity for  $[BMIM]^+[BF_4]^-$  in native and silanized AAO pores at 303 K. The conductivity of the IL in the silanized AAO increases relative to native pores but remains lower than the bulk (dashed line). (d) Effective phase diagram of (top)  $[BMIM]^+[TFSI]^-$  and (bottom)  $[BMIM]^+[PF_6]^-$  as a function of inverse pore diameter.

### 1.3.2 How the Cation Size Affects the Imbibition of Polymerized Ionic Liquids and the Ionic Conductivity in Nanopores?

In this section we explored how the cation molecular structure and size in polymerized ionic liquids (PILs) influence ion transport both in the bulk and under nanoconfinement. For this purpose two PILs were synthesized: one with a compact imidazolium cation ( $[BVIM]^+$ ) (Synthesis by ...) and another with a bulky phenyl-substituted cation ( $[VBBI]^+$ ) (Synthesis by ...), both with the same anion ( $[TFSI]^-$ ) (Figure 25a). The  $[BVIM]^+$  cation, being closer to the polymer backbone, leads to stronger ion–polymer interactions, raising the glass temperature ( $T_g$ ) and reducing ionic mobility (Figure 25b).

In a second experiment we employed anodic aluminum oxide (AAO) nanopores, and investigated the imbibition kinetics and ionic conductivity under confinement via optical microscopy and nanodielectric spectroscopy. Results revealed that confinement reduces the

activation energy for ion transport and enhances ion–polymer decoupling, particularly at temperatures near  $T_g$  (**Figure 25c**). Notably, PILs exhibited higher effective viscosities in nanopores than in bulk, due to polymer–pore wall interactions. However, by cooling to lower temperatures a change in the temperature dependence of conductivity was found. Under these conditions, the temperature dependence of ion conductivity followed an Arrhenius temperature dependence with an activation energy that was reduced to  $\sim 108$  kJ/mol under confinement. It suggested that confinement provides the means of increasing conductivity at temperatures in the vicinity of  $T_g$  where, intrinsically, ion mobility is reduced.

The results offered some new insights into how molecular structure and confinement affect ion transport in PILs.

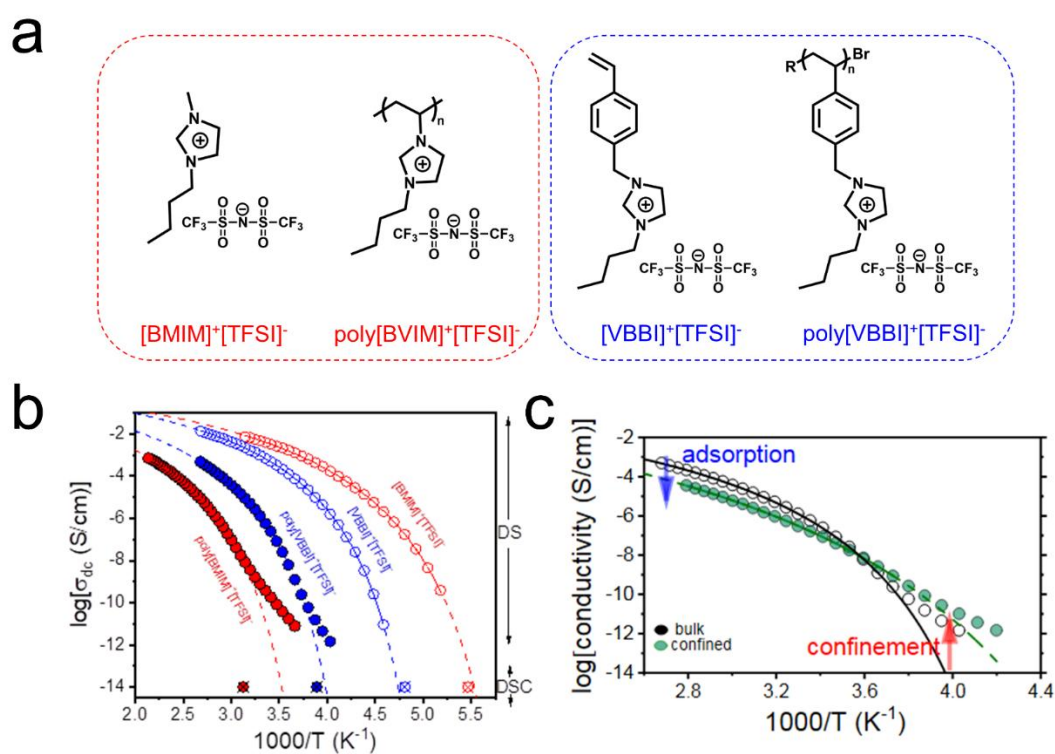


**Figure 25.** (a) Chemical structures of ILs, [BMIM]<sup>+</sup>[TFSI]<sup>-</sup>, [VBBI]<sup>+</sup>[TFSI]<sup>-</sup>, and of the corresponding PILs, poly[BVIM]<sup>+</sup>[TFSI]<sup>-</sup>, poly[VBBI]<sup>+</sup>[TFSI]<sup>-</sup>. (b) Temperature dependence of dc-conductivity for the ILs, shown with open circles, and corresponding PILs shown as spheres obtained on cooling; [BMIM]<sup>+</sup>[TFSI]<sup>-</sup> (open red circle), [VBBI]<sup>+</sup>[TFSI]<sup>-</sup> (open blue circle), poly[BVIM]<sup>+</sup>[TFSI]<sup>-</sup> (solid red circle), poly[VBBI]<sup>+</sup>[TFSI]<sup>-</sup> (solid blue circle). (c) Temperature-dependence of ionic conductivity of poly[BVIM]<sup>+</sup>[TFSI]<sup>-</sup> in bulk and under confinement. Below  $T_g$ , PIL shows strong decoupling between ion motion and segmental relaxation.

### 1.3.3 Are mixtures of ILs/PILs homogenous? How do they infiltrate nanopores?

Despite the common belief that mixtures of ILs with their corresponding PILs are homogeneous, here we show otherwise. We synthesized (Synthesis by ..) a series of PILs based on the 1-butyl-3-vinylimidazolium cation ( $[BVIM]^+$  with three different anions ( $[X]^-$ :  $[TFSI]^-$ ,  $[BF_4]^-$ ,  $[PF_6]^-$ ) (**Figure 26a**). In the bulk, thermal, viscosity, and conductivity measurements in symmetric PIL/IL mixtures revealed that they are locally heterogeneous. The viscosity in the PIL/IL mixtures had a VFT dependence that was biased towards the bulk PIL. In contrast, the dc-conductivity closely resembled that of pure IL (**Figure 26b**).

When the same symmetric mixtures were brought into contact with nanoporous membranes the capillary force enhanced the heterogeneity and triggered demixing in macroscopic length scales. *In situ* dc-conductivity measurements (**Figure 26c**) showed that the IL penetrates first the nanopores followed by a minority of the PIL. At later times, part of the minority PIL was adsorbed at the pore walls, producing a further reduction in dc-conductivity. By comparing the conductivities among pure IL, pure PIL, bulk PILs/ILs mixture and the mixture extracted from nanopores we further demonstrated the enrichment of pores by the IL (**Figure 26d**). The results demonstrated, for the first time, the separation of a mixture of ionic compounds composed from an IL and a PIL by the different imbibition speeds in nanopores. In addition, polymer adsorption and surface functionality played significant role in the ion dynamics. Overall, nanoporous templates can be viewed as model systems for the separation and adsorption of ionic systems in the absence of solvent.

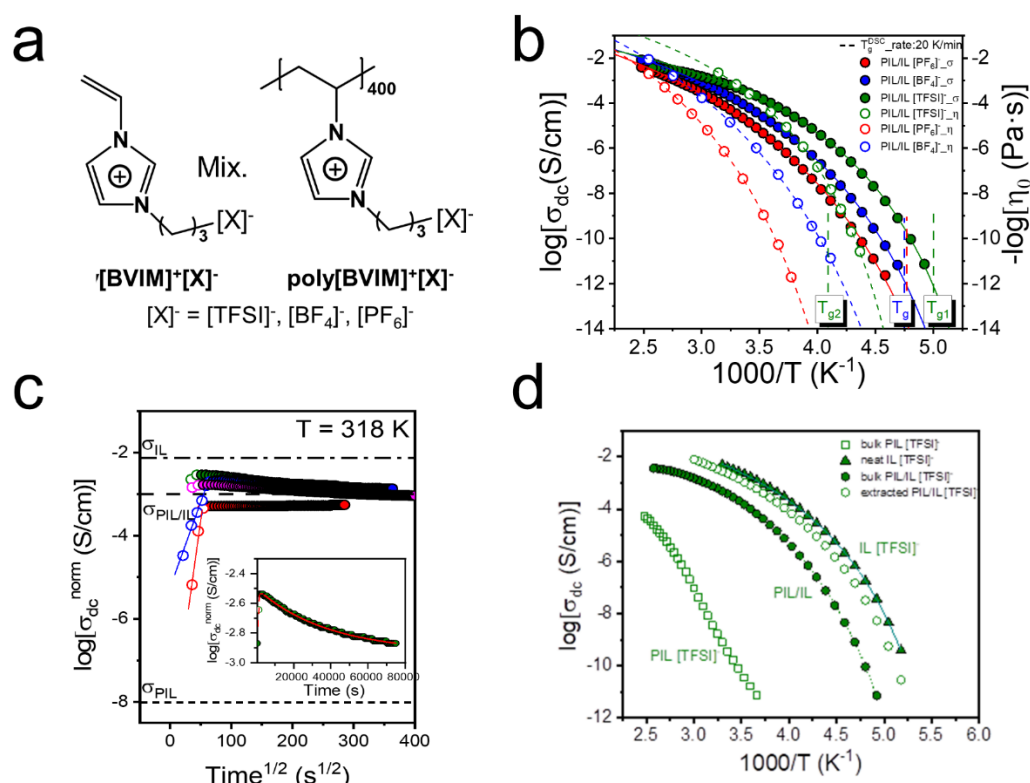


**Figure 26.** (a) Schematic of the chemical structure of PILs and ILs. (b) Temperature dependence of dc-conductivity (filled symbols) and zero-shear viscosity (open symbols) for PIL/IL mixtures bearing different anions, (red)  $[PF_6]^-$ , (blue)  $[BF_4]^-$ , (green)  $[TFSI]^-$ . The dashed lines are the results of Vogel-Fulcher-Tammann (VFT) fit. The vertical dashed lines represent the  $T_g$  obtained from DSC (rate of  $20 \text{ K}\cdot\text{min}^{-1}$ ). (c) Ionic conductivity from *in situ* nDS for the PIL/IL  $[TFSI]^-$  with a  $M_n$  of  $85 \text{ kg}\cdot\text{mol}^{-1}$  during and after flow in AAO nanopores with different pore sizes: 400 nm (red), 65 nm (blue), 35 nm (olive), 25 nm (magenta) plotted as a function of the square root of time at 318 K. (d) Ionic conductivity of the material extracted from AAO nanopores of 65 nm in diameter following the *in situ* nDS (open circles). The conductivity data are compared with the neat IL (filled triangles), the bulk PIL (open squares) and the bulk PIL/IL blend (spheres).

### 1.3.4 How V-shaped confinement affects the self-assembly and ion dynamics of ionic liquids?

This study examined how nanoscale confinement—specifically V-shaped *versus* cylindrical anodic aluminum oxide (AAO) nanopores—affects the ion mobility and the phase state of the confined ILs. The study focused on ILs containing the  $[BMIM]^+$  cation with three different anions:  $[BF_4]^-$ ,  $[TFSI]^-$ , and  $[PF_6]^-$  (**Figure 27a**). By employing dielectric spectroscopy and X-ray diffraction, we systematically investigated changes in glass temperature, conductivity, as well as thermal transitions under varying confinement conditions.

In the amorphous  $[BMIM]^+[BF_4]^-$ , cylindrical confinement increased  $T_g$  (by  $\sim 5\text{K}$ ) and the effect was stronger in the smaller nanopores (e.g. by reducing the pore surface and pore

volume). As a result, the dc-conductivity dropped by  $\sim 2$  orders of magnitude relative to bulk. V-shaped confinement had similar effects but the decrease in dc-conductivity (and the increase in  $T_g$ ) was much smaller when examined under the same pore surface and volume (**Figure 27b**). Lastly, silanization of the internal pore surface, in both templates, restored the bulk behavior providing further support to interfacial effects. The stronger effects within cylindrically shaped AAO can be explained by a uniform distribution of surface charge. Alternatively, an uneven charge distribution on the V-shaped pore surface can alleviate the Coulomb attractions enhancing the dc-conductivity back to the bulk values. The latter suggests electrostatic interactions extending much beyond a single IL layer.

ILs bearing the same cation but larger anions ( $[\text{BMIM}]^+[\text{TFSI}]^-$  and  $[\text{BMIM}]^+[\text{PF}_6]^-$ ) were structurally more complex. It was shown that V-shaped confinement produced the same structural changes as cylindrical confinement. Namely, changes from a larger to a smaller unit cell were shown in  $[\text{BMIM}]^+[\text{PF}_6]^-$  by increasing temperature. We have also employed the temperature dependence of dielectric permittivity as a fingerprint of the phase transitions in constructing the effective phase diagrams. Both V-shaped and cylindrical nanopores decreased the transition temperatures according to the Gibbs-Thomson equation. The result suggests a reduced solid-liquid interfacial energy independent of nanopore geometry. These effects need to be investigated in even smaller nanopores and for a series of ILs. Studies in this direction are planned in our lab.

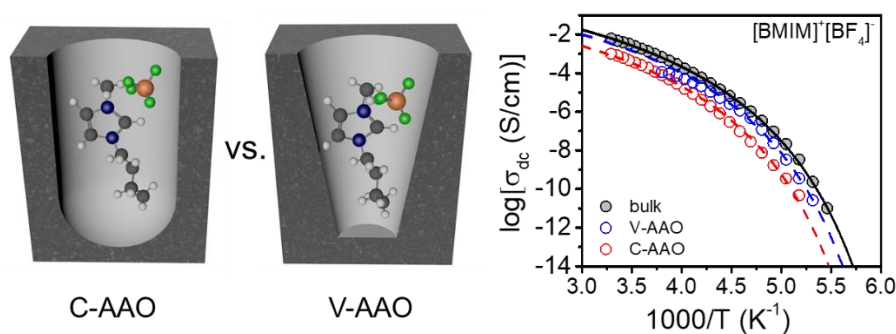


**Figure 27.** (left) Schematic of the chemical structure of the ILs in cylindrically (C)- and V-shaped AAOs. (right) Comparison of temperature dependence of dc-conductivity (normalized for the porosity) for bulk (gray) and confined  $[\text{BMIM}]^+[\text{BF}_4]^-$  in V-shaped (blue) and cylindrically shaped AAO (red) following full imbibition. The dashed lines represents VFT fits.

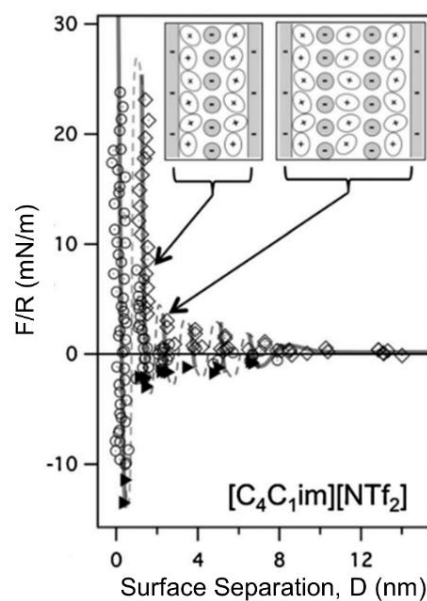
## 1.4 Outlook and Future Work

### 1.4.1 Degree of confinement: size effects

The degree of confinement plays an important role in the ion transport properties. It is defined as the ratio of the pore diameter to the size of the ions or, in the case of polymers, to the radius of gyration. As this ratio decreases, spatial restrictions imposed by the pore walls become increasingly important. It is usually the case than in weakly confined systems (e.g., pores larger than 50 nm), deviations from bulk dynamics are expected to be small. However, in moderately confined pores (10–50 nm), ion dynamics become sensitive to the size, shape, and flexibility of the constituent ions. Experimental studies have reported conflicting results, with both enhancement and reduction in ionic conductivity, depending on the interplay between ion–pore interactions and changes in local packing (density). Under strong confinement (<10 nm), the transport mechanism may change to a hopping-like behavior, often accompanied by interfacial layering or even the formation of glassy boundary regions.

A compelling example of size-dependent confinement effects was reported by Perkin *et al.*<sup>68</sup> who studied the structural organization of  $[\text{C}_4\text{C}_1\text{im}][\text{NTf}_2]$  confined between atomically flat mica surfaces. Using X-ray reflectivity and surface forces measurements, they observed well-defined oscillatory layering of ions, with a periodicity matching the ion-pair dimensions (**Figure 28**). As the confinement gap approached the scale of a few nanometers, the IL transitioned from a fluid-like to a solid-like layered state, effectively suppressing ion mobility. This study illustrated that extreme confinement can induce spatial ordering and reduce translational freedom.

**Figure 28.** Measured force,  $F_N$ , between two mica surfaces (normalized by the mica curvature,  $R$ ) versus film thickness,  $D$ , for  $[\text{C}_4\text{C}_1\text{im}][\text{NTf}_2]$  measured in mica membranes. Open diamonds indicate points measured on approaching the surfaces (decreasing  $D$ ) while open circles indicate data measured on retracting from the surfaces. Filled triangles indicate points measured from the jump-apart of the surfaces from an adhesive minimum. The cartoons in the inset show examples (for just two of the repulsive force ‘walls’) of the interpretation of the oscillatory forces: force walls—which correspond to energy minima—are due to stable films containing odd numbers of ion layers, alternating between cation and anion-rich layers with cations at each of the negatively charged surfaces.<sup>68</sup>



In this thesis, we primarily focused on understanding ion dynamics of ILs and PILs within weakly or moderately confining nanopores (pore sizes  $> 10$  nm). Several open questions can be addressed for ILs and PILs in strongly confining media (pore sizes  $< 10$  nm). For example: How does strong confinement affect the ion conductivity? Can ion mobility decouple from the hindered segmental motion within the polymer “dead layer”? Does ion transport change to a hopping mechanism, and if so, what governs the energetics and pathways of ion hopping in this limit? What is the role of interfacial layering? Addressing these questions is important for the molecular-design of ion-conducting materials tailored for extreme nanoscale confinement, e.g. in solid-state electrolytes, ion sieving membranes, and nanoporous sensors.

### 1.4.2 Pore geometry: conical vs. cylindrical confinement

Conical nanopores—also referred to as V-shaped or tapered pores—offer a unique confinement geometry characterized by a continuously decreasing diameter along the axial direction. The structural asymmetry introduces a spatial gradient in the degree of confinement, distinct from the uniform restriction imposed by cylindrical pores. As a result, conical pores represent a model system for studying geometry effects on ion dynamics, segmental relaxation, and structural organization in ionic systems.

However, the most striking features of conical pores is their capacity to introduce **ion selectivity**.<sup>69,70</sup> When the inner surface of a conical nanopore carries a negative net charge, the pore preferentially facilitates the transport of cations, while repelling anions (**Figure 29a**, left). Conversely, positively charged nanopores enhance anion-selective transport by excluding cations (**Figure 29a**, right). This selective ion migration arises from the interplay of electrostatic attraction/repulsion and geometric asymmetry, which together create direction-dependent ionic flux. Siwy et al. showed that modifying the pore surface with polyelectrolytes can switch the selectivity from cationic to anionic, offering tunable control over ion transport. When combined with PILs, the system offers additional length scales due to polymer segmental dynamics and ion–polymer interactions, which can either reinforce or counteract electrostatic selectivity.

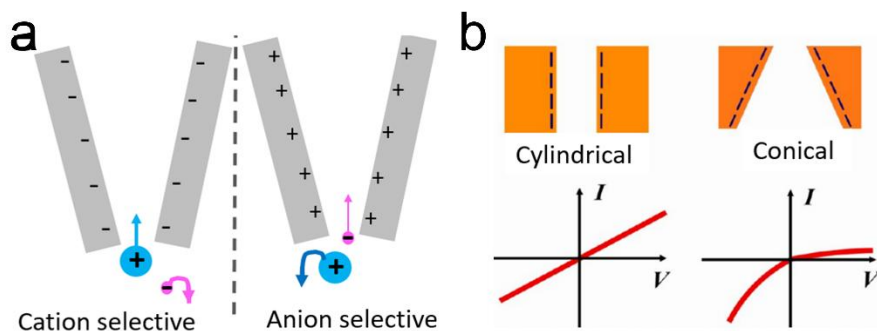


**Figure 29.** (a) Cation and anion-selective asymmetric nanopores. (b) Ionic current rectification in geometrically asymmetric nanopores. A linear  $I$ - $V$  behavior is found in cylindrical nanopores, but a *diode-like* behavior in charged conical nanopores.<sup>70</sup>

Building upon the ion-selective behavior observed in asymmetric nanopores, an especially intriguing manifestation of geometric and electrostatic asymmetry is the ability for **ionic current rectification** (ICR).<sup>69, 71-73</sup> Rectification refers to the nonlinear and direction-dependent current–voltage ( $I$ - $V$ ) response observed when an external potential is applied across a single conical pore. Unlike ion selectivity, which describes equilibrium partitioning of ions within confined regions, rectification reflects the dynamic asymmetry of ion transport, and serves as a hallmark of non-equilibrium ion flow in confined systems. Conical nanopores, by virtue of their spatially varying cross-section, naturally break the symmetry along the axial direction. When combined with surface charge, ion-specific interactions, or differences in ion mobility, this structural asymmetry results in a voltage-dependent imbalance in ion distribution and ionic flux. Under forward bias (e.g., ions entering from the wide base), ions encounter weaker confinement and reduced electrostatic crowding, enabling more facile transport. In reverse bias (e.g., entry from the narrow tip), ions experience stronger confinement, enhanced ion–wall interactions, and potential crowding effects, all of which can suppress ionic current. This asymmetry leads to a **diode-like behavior**, where the current at  $+V$  differs significantly from that at  $-V$ .<sup>70</sup> In contrast, cylindrical pores, due to their constant cross-section, generally lack rectification (**Figure 29b**).

The origin of rectification has been investigated extensively in both theoretical and experimental contexts. Siwy and co-workers pioneered the fabrication of single conical nanopores in polymer membranes and demonstrated strong ICR behavior under various electrolyte conditions. The degree of rectification could be tuned by modifying the pore surface charge, by adjusting the tip diameter, or by selectively functionalizing one end of the pore. Moreover, in ionic systems, coupling between ion mobility and confinement-induced

decoupling effects can amplify the differences in ionic response between forward and reverse biases. From an application standpoint, the ability to induce and control current rectification makes conical nanopores highly attractive for nanofluidic diodes, ionic logic elements, and asymmetric transport membranes. Their geometry provides a built-in mechanism for directional transport, without the need for external gating or complex fabrication steps.

Such investigations require much narrower V-shaped pores than the ones employed in this Thesis, followed by precise surface functionalization. Future efforts could address these issues by the use of *in-situ* nanodielectric spectroscopy, developed in our lab.

## 1.5 References

- (1) Berchtold, M.W.; Brinkmeier, H.; Müntemer, M. Calcium Ion in Skeletal Muscle: Its Crucial Role for Muscle Function, Plasticity, and Disease. *Physiological Reviews*. **2000**, *80*, 1215-1265.
- (2) Zhu, Z.; Wang, D.; Tian, Y.; Jiang, L. Ion/Molecule Transportation in Nanopores and Nanochannels: From Critical Principles to Diverse Functions. *J Am Chem Soc* **2019**, *141*, 8658-8669.
- (3) Song, Y. Y.; Li, X. L.; Fan, J. B.; Kang, H. J.; Zhang, X. F.; Chen, C.; Liang, X. M.; Wang, S. T. Interfacially Polymerized Particles with Heterostructured Nanopores for Glycopeptide Separation. *Adv. Mater.* **2018**, *30*, 1803299.
- (4) Fujibayashi, T.; Komatsu, Y.; Konishi, N.; Yamori, H.; Okubo, M. Effect of polymer polarity on the shape of "golf ball-like" particles prepared by seeded dispersion polymerization. *Ind. Eng. Chem. Res.* **2008**, *47*, 6445.
- (5) Liu, X. M.; Du, X.; He, J. H. Hierarchically structured porous films of silica hollow spheres via layer-by-layer assembly and their superhydrophilic and antifogging properties. *ChemPhysChem* **2008**, *9*, 305.
- (6) Jacobsen, C. J. H.; Madsen, C.; Houzvicka, J.; Schmidt, I.; Carlsson, A. Mesoporous zeolite single crystals. *J. Am. Chem. Soc.* **2000**, *122*, 7116.
- (7) Stock, N.; Biswas, S. Synthesis of Metal-Organic Frameworks (MOFs): Routes to Various MOF Topologies, Morphologies, and Composites. *Chem. Rev.* **2012**, *112*, 933.
- (8) Zhang, H. C.; Tian, Y.; Jiang, L. Fundamental studies and practical applications of bio-inspired smart solid-state nanopores and nanochannels. *Nano Today* **2016**, *11*, 61.
- (9) Lum, K.; Chandler, D.; Weeks, J. D. Hydrophobicity at small and large length scales. *J. Phys. Chem. B* **1999**, *103*, 4570.
- (10) Vlassioux, I.; Smirnov, S.; Siwy, Z. Ionic Selectivity of Single Nanochannels. *Nano Lett.* **2008**, *8*, 1978.
- (11) Powell, M. R.; Cleary, L.; Davenport, M.; Shea, K. J.; Siwy, Z. S. Electric-field-induced wetting and dewetting in single hydrophobic nanopores. *Nat. Nanotechnol.* **2011**, *6*, 798.
- (12) Su, Y.-S.; Hsu, S.-C.; Peng, P.-H.; Yang, J.-Y.; Gao, M.; Yeh, L.-H. Unraveling the Anomalous Channel-Length-Dependent Blue Energy Conversion Using Engineered Alumina Nanochannels. *Nano Energy* **2021**, *84*, 105930.
- (13) Simon, P.; Gogotsi, Y. Materials for Electrochemical Capacitors. *Nat. Mater.* **2008**, *7*, 845-854.
- (14) Blobel, G.; Dobberstein, B. Transfer of Proteins Across Membranes. I. Presence of Proteolytically Processed and Unprocessed Nascent Immunoglobulin Light Chains on Membrane-Bound Ribosomes of Murine Myeloma. *J Cell Biol.* **1975**, *67*, 835-851.
- (15) Movileanu, L.; Cheley, S.; Bayley, H. Partitioning of Individual Flexible Polymers into a Nanoscopic Protein Pore. *Biophysical Journal.* **2003**, *85*, 897-910.
- (16) Aksimentiev, A.; Heng, J. B.; Timp, G.; Schulten, K. Microscopic Kinetics of DNA Translocation through synthetic nanopores. *Biophys J* **2004**, *87*, 2086-2097.
- (17) Walden, P. Molecular Weights and Electrical Conductivity of Several Fused Salts. *Bull. Acad. Imper. Sci.* **1914**, *1800*, 405-422.
- (18) Rogers, R. D.; Seddon, K. R.; Volkov, S. editors. Green industrial applications of ionic liquids. NATO Science Series II. New York: Springer-Verlag, **2003**, 545.
- (19) Parvulescu, V. I.; Hardacre, C. Catalysis in Ionic Liquids. *Chem. Rev.* **2007**, *107*, 2615-2665.
- (20) Sun, P.; Armstrong, D. W. Ionic liquids in analytical chemistry. *Analytica Chimica Acta*, **2010**, *661*, 1-16.

- (21) Ohno, H. *Electrochemical aspects of ionic liquids*. New York: Wiley, **2005**.
- (22) Armand, M.; Endres, F.; MacFarlane, D. R.; Ohno, Hiroyuki; Scrosati, B. ionic-liquid materials for the electrochemical challenges of the future. *Nat Mater*, **2009**, *8*, 621-629.
- (23) Roosen, C.; Muller, P.; Greiner, L. Ionic liquids in biotechnology: applications and perspectives for biotransformations. *Appl Microbiol Biotechnol* **2008**, *81*, 607–614.
- (24) Verma, C.; Ebenso, E. E. Ionic liquid-mediated functionalization of graphene-based materials for versatile applications: a review. *Graphene Technology* **2018**, *4*, 1-15.
- (25) Fabre, E.; Murshed, S. M. A review of the thermophysical properties and potential of ionic liquids for thermal applications. *J. Matter. Chem. A*. **2021**, *9*, 15861-15879.
- (26) Krause, C.; Sangoro, J. R.; Iacob, C.; Kremer, F. Charge Transport and Dipolar Relaxations in Imidazolium-Based Ionic Liquids. *J. Phys. Chem. B* **2010**, *114*, 382-386.
- (27) Fujii, K.; Soejima, Y.; Kyoshoin, Y.; Fukuda, S.; Kanzaki, R.; Umebayashi, Y.; Yamaguchi, T.; Ishiguro, S.-i.; Takamuku, T. *J. Phys. Chem. B*. **2008**, *112*, 4329-4336.
- (28) Aparicio, S.; Atilhan, M.; Karadas, F. Thermophysical Properties of Pure Ionic Liquids: Review of Present Situation. *Ind. Eng. Chem. Res.* **2010**, *49*, 9580-9595.
- (29) Hajipour, A. R.; Rafiee, F. Basic Ionic Liquids. A Short Review. *J. Iran. Chem. Soc.* **2009**, *6*, 647-678.
- (30) Gordon, C. M.; Holbrey, J. D.; Kennedy, A. R.; Seddon, K. R. Ionic Liquid Crystals: Hexafluorophosphate Salts. *J. Mater. Chem.* **1998**, *8*, 2627-2636.
- (31) Tu, W.; Jurkiewicz, K.; Adrjanowicz, K. Confinement of Pyrrolidinium-Based Ionic Liquids [C<sub>n</sub>mpyrr]<sup>+</sup>[Tf<sub>2</sub>N]<sup>-</sup> with Long Cationic Alkyl Side Chains (n = 10 And 16) To Nanoscale Pores: Dielectric and Calorimetric Studies. *J. Mol. Liq.* **2021**, *324*, 115115.
- (32) Seddon, K. R.; Stark, A.; Torres, M-J. Viscosity and Density of 1-Alkyl-3-methylimidazolium Ionic Liquids. *ACS Symposiym Series*. **2002**, *819*, 34-39.
- (33) Padaszynski, K.; Domanska, U. Viscosity of ionic liquids: an extensive database and a new group contribution model based on a feed-forward artificial neural network. *J Chem Inf Model* **2014**, *54*, 1311-1324.
- (34) Yuan, W. L.; Yang, X.; He, L.; Xue, Y.; Qin, S.; Tao, G. H. Viscosity, Conductivity, and Electrochemical Property of Dicyanamide Ionic Liquids. *Front Chem* **2018**, *6*, 59.
- (35) Okoturo, O. O.; VanderNoot, T. J. Temperature dependence of viscosity for room temperature ionic liquids. *Electroanal. Chem.*, **2004**, *568*, 167–181.
- (36) Tokuda, H.; Hayamizu, K.; Ishii, K.; Susan, M. A. B. H.; Watanabe, M. Physicochemical Properties and Structures of Room Temperature Ionic Liquids. 1. Variation of Anionic Species. *J. Phys. Chem. B*, **2004**, *108*, 16593–16600.
- (37) Wang, X.; Salari, M.; Jiang, D.; Varela, J. C.; Anasori, B.; Wesolowski, D. J.; Dai, S.; Grinstaff, M. W.; Gogotsi, Y. Electrode material–ionic liquid coupling for electrochemical energy storage. *Nat RevMater*, **2020**, *5*, 787–808.
- (38) Araque, J. C.; Hettige, J. J.; Margulis, C. J. Modern Room Temperature Ionic Liquids, a Simple Guide to Understanding Their Structure and How It May Relate to Dynamics. *J Phys Chem B* **2015**, *119*, 12727-12740.
- (39) Kashyap, H. K.; Santos, C. S.; Annapureddy, H. V.; Murthy, N. S.; Margulis, C. J.; Castner, E. W., Jr. Temperature-dependent structure of ionic liquids: X-ray scattering and simulations. *Faraday Discuss* **2012**, *154*, 133-143.
- (40) Leys, J.; Wubbenhorst, M.; Preethy Menon, C.; Rajesh, R.; Thoen, J.; Glorieux, C.; Nockemann, P.; Thijs, B.; Binnemans, K.; Longuemart, S. Temperature dependence of the electrical conductivity of imidazolium ionic liquids. *J Chem Phys* **2008**, *128*, 064509.

- (41) Nobori, H.; Fujimoto, D.; Yoshioka, J.; Fukao, K.; Konishi, T.; Taguchi, K. Phase transitions and dynamics in ionic liquid crystals confined in nanopores. *J Chem Phys* **2024**, *160*, 044902.
- (42) Sangoro, J. R.; Serghei, A.; Naumov, S.; Galvosas, P.; Karger, J.; Wespe, C.; Bordusa, F.; Kremer, F. *Phys. Rev. E: Stat., Nonlinear, Soft Matter Phys.*, **2008**, *77*, 051202
- (43) Tu, W.; Chat, K.; Szklarz, G.; Laskowski, L.; Grzybowska, K.; Paluch, M.; Richert, R.; Adrjanowicz, K. Dynamics of Pyrrolidinium-Based Ionic Liquids under Confinement. II. The Effects of Pore Size, Inner Surface, and Cationic Alkyl Chain Length. *J. Phys. Chem. C* **2019**, *124*, 5395-5408.
- (44) Kardasis, P.; Sakellariou, G.; Steinhart, M.; Floudas, G. Non-equilibrium Effects of Polymer Dynamics under Nanometer Confinement: Effects of Architecture and Molar Mass. *J Phys Chem B* **2022**, *126*, 5570-5581.
- (45) Sieffert, N.; Wipff, G. Ordering of Imidazolium-Based Ionic Liquids at the  $\alpha$ -Quartz(001) Surface: A Molecular Dynamics Study. *J. Phys. Chem. C* **2008**, *112*, 19590-19603.
- (46) Wang, S.; Li, S.; Cao, Z.; Yan, T. Y. Molecular Dynamic Simulations of Ionic Liquids at Graphite Surface. *J. Phys. Chem. C* **2010**, *114*, 990-995.
- (47) Shi, W.; Sorescu, D. C. Molecular Simulations of CO<sub>2</sub> and H<sub>2</sub> Sorption into Ionic Liquid 1-n-Hexyl-3-methylimidazolium Bis(trifluoromethylsulfonyl)amide ([hmim][Tf2N]) Confined in Carbon Nanotubes. *J. Phys. Chem. B* **2010**, *114*, 15029-15041.
- (48) Kashyap, H. K.; Annapureddy, H. V.; Raineri, F. O.; Margulis, C. J. How is charge transport different in ionic liquids and electrolyte solutions? *J Phys Chem B* **2011**, *115*, 13212-13221.
- (49) Tagliazucchi, M.; Szleifer, I. Transport mechanisms in nanopores and nanochannels: can we mimic nature? *Materials Today* **2015**, *18*, 131-142.
- (50) Huber, P. Soft matter in hard confinement: phase transition thermodynamics, structure, texture, diffusion and flow in nanoporous media. *J Phys Condens Matter* **2015**, *27*, 103102.
- (51) Jiang, F.; Li, C.; Fu, H.; Wang, C.; Guo, X.; Jiang, Z.; Wu, G.; Chen, S. Temperature-Induced Molecular Rearrangement of an Ionic Liquid Confined in Nanospaces: An in Situ X-ray Absorption Fine Structure Study. *J. Phys. Chem. C* **2015**, *119*, 22724-22731.
- (52) Kolmangadi, M. A.; Zhuoqing, L.; Smales, G. J.; Pauw, B. R.; Huber, P.; Schönhals, A. Confinement-Suppressed Phase Transition and Dynamic Self-Assembly of Ionic Superdiscs in Ordered Nanochannels: Implications for Nanoscale Applications. *ACS Applied Nano Materials* **2023**, *6*, 15673-15684.
- (53) Ganesan, V. Ion transport in polymeric ionic liquids: recent developments and open questions. *Molecular Systems Design & Engineering* **2019**, *4*, 280-293.
- (54) Choi, U. H.; Mittal, A.; Runt, J.; Colby, R. H. Molecular Volume Effects on the Dynamics of Polymerized Ionic Liquids and their Monomers. *Electrochimica Acta* **2015**, *175*, 55-61.
- (55) Bocharova, V.; Wojnarowska, Z.; Cao, P. F.; Fu, Y.; Saito, T.; et al. Influence of Chain Rigidity and Dielectric Constant on the Glass Transition Temperature in Polymerized Ionic Liquids. *J Phys Chem B* **2017**, *121*, 11511-11519.
- (56) Choi, U. H.; Ye, Y.; Salas de la Cruz, D.; Liu, W.; Winey, K. I.; Elabd, Y. A.; Runt, J.; Colby, R. H. Dielectric and Viscoelastic Responses of Imidazolium-Based Ionomers with Different Counterions and Side Chain Lengths. *Macromolecules* **2014**, *47*, 777-790.

- (57) Pipertzis, A.; Papamokos, G.; Mühlinghaus, M.; Mezger, M.; Scherf, U.; Floudas, G. What Determines the Glass Temperature and dc-Conductivity in Imidazolium-Polymerized Ionic Liquids with a Polythiophene Backbone? *Macromolecules* **2020**, *53*, 3535-3550.
- (58) Wang, Y.; Agapov, A. L.; Fan, F.; Hong, K.; Yu, X.; Mays, J.; Sokolov, A. P. Decoupling of ionic transport from segmental relaxation in polymer electrolytes. *Phys Rev Lett* **2012**, *108*, 088303.
- (59) Jones, S. D.; Bamford, J.; Fredrickson, G. H.; Segalman, R. A. Decoupling Ion Transport and Matrix Dynamics to Make High Performance Solid Polymer Electrolytes. *ACS Polym Au* **2022**, *2*, 430-448.
- (60) Stacy, E. W.; Gainaru, C. P.; Gobet, M.; Wojnarowska, Z.; Bocharova, V.; Greenbaum, S. G.; Sokolov, A. P. Fundamental Limitations of Ionic Conductivity in Polymerized Ionic Liquids. *Macromolecules* **2018**, *51*, 8637-8645.
- (61) Nakamura, K.; Fukao, K.; Inoue, T. Dielectric Relaxation and Viscoelastic Behavior of Polymerized Ionic Liquids with Various Counteranions. *Macromolecules* **2012**, *45*, 3850-3858.
- (62) Sangoro, J. R.; Iacob, C.; Agapov, A. L.; Wang, Y.; Berdzinski, S.; Rexhausen, H.; Strehmel, V.; Friedrich, C.; Sokolov, A. P.; Kremer, F. Decoupling of ionic conductivity from structural dynamics in polymerized ionic liquids. *Soft Matter* **2014**, *10*, 3536-3540.
- (63) Jones, S. D.; Nguyen, H.; Richardson, P. M.; Chen, Y. Q.; Wyckoff, K. E.; Hawker, C. J.; Clement, R. J.; Fredrickson, G. H.; Segalman, R. A. Design of Polymeric Zwitterionic Solid Electrolytes with Superionic Lithium Transport. *ACS Cent Sci* **2022**, *8*, 169-175.
- (64) Keith, J. R.; Ganesan, V. Ion transport mechanisms in salt-doped polymerized zwitterionic electrolytes. *J. Polym. Sci.* **2020**, *58*, 578-588.
- (65) Galluzzo, M. D.; Maslyn, J. A.; Shah, D. B.; Balsara, N. P. Ohm's law for ion conduction in lithium and beyond-lithium battery electrolytes. *J. Chem. Phys.* **2019**, *151*, 020901.
- (66) Zhao, Q.; Bennington, P.; Nealey, P. F.; Patel, S. N.; Evans, C. M. Ion Specific, Thin Film Confinement Effects on Conductivity in Polymerized Ionic Liquids. *Macromolecules* **2021**, *54*, 10520-10528.
- (67) Kinsey, T.; Glynn, K.; Cosby, T.; Iacob, C.; Sangoro, J. Ion Dynamics of Monomeric Ionic Liquids Polymerized In Situ within Silica Nanopores. *ACS Appl Mater Interfaces* **2020**, *12*, 44325-44334.
- (68) Perkin, S.; Crowhurst, L.; Niedermeyer, H.; Welton, T.; Smith, A. M.; Gosvami, N. N. Self-assembly in the electrical double layer of ionic liquids. *Chem Commun (Camb)* **2011**, *47*, 6572-6574.
- (69) Siwy, Z. S. Ion-Current Rectification in Nanopores and Nanotubes with Broken Symmetry. *Advanced Functional Materials* **2006**, *16*, 735-746.
- (70) Guo, W.; Jiang, L. Asymmetric Ion Transport through Ion-Channel-Mimetic Solid-State Nanopores. *Acc. Chem. Res.* **2013**, *46*, 2834-2846.
- (71) Karnik, R.; Duan, C.; Castelino, K.; Daiguji, H.; Majumdar, A. Rectification of Ionic Current in a Nanofluidic Diode. *Nano Lett.* **2007**, *7*, 547-551.
- (72) Li, S.; Zhang, X.; Su, J. Ionic Current Rectification Induced by Charge Polarity in Janus Graphene Channels. *J. Phys. Chem. C.* **2023**, *127*, 12276-12286.
- (73) Yamamoto, T.; Doi, M. Electrochemical mechanism of ion current rectification of polyelectrolyte gel diodes. *Nat Commun* **2014**, *5*, 4162.

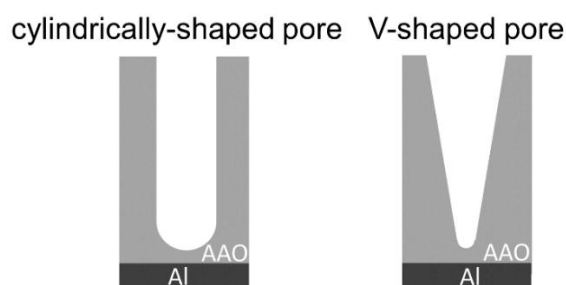
## Chapter 2. Experimental Section

### 2.1. Materials

1-Butyl-3-methylimidazolium bis(trifluoromethylsulfonyl)imide ([BMIM]<sup>+</sup>[TFSI]<sup>-</sup>, purity  $\geq$  98%), 1-Butyl-3-methylimidazolium bromide ([BMIM]<sup>+</sup>[Br]<sup>-</sup>, purity  $\geq$  98,5%), 1-Butyl-3-methylimidazolium chloride ([BMIM]<sup>+</sup>[Cl]<sup>-</sup>, purity  $\geq$  98%), 1-Butyl-3-methylimidazolium tetrafluoroborate ([BMIM]<sup>+</sup>[BF<sub>4</sub>]<sup>-</sup>, purity  $\geq$  98%), 1-Butyl-3-methylimidazolium hexafluorophosphate ([BMIM]<sup>+</sup>[PF<sub>6</sub>]<sup>-</sup>,  $\geq$  98%), 1-Butyl-3-methylimidazolium iodide ([BMIM]<sup>+</sup>[I]<sup>-</sup>, purity  $\geq$  99%), 1-butyl-3-vinylimidazolium hexafluorophosphate ([BVIM]<sup>+</sup>[PF<sub>6</sub>]<sup>-</sup>,  $\geq$  98%), 1-butyl-3-vinylimidazolium bromide ([BVIM]<sup>+</sup>[Br]<sup>-</sup>,  $\geq$  98%), Lithium bis(trifluoromethanesulfonyl)imide (LiTFSI,  $\geq$  98%), Sodim tetrafluoroborate (NaBF<sub>4</sub>  $\geq$  97%), Dichloromethane (DMF, extra dry  $\geq$  99.9%), Potassium hexafluorophosphate (KPF<sub>6</sub>, extra pure  $\geq$  99%), Silver nitrate solution (AgNO<sub>3</sub>), 2,2'-azobisisobutyronitrile (AIBN  $\geq$  98%), Ultra-15 Centrifugal Filter Unit (10 kDa MWCO), Tetrahydrofuran (THF  $\geq$  98%) and Ethanol were purchased from Merck and used without further purification. In addition, the water content of all ILs used for dielectric measurements was measured by a Karl-Fischer titration method (C20, Mettler Toledo). Following freeze-drying the water content was below 0.06 wt % for [BF<sub>4</sub>]<sup>-</sup>, and below 0.02 wt% for both [TFSI]<sup>-</sup> and [PF<sub>6</sub>]<sup>-</sup>.

### 2.2. Template characteristion

**AAO templates.** In this thesis, we utilized cylindrically shaped (C) and V-shaped (V) self-ordered nanoporous aluminium oxide (AAO) templates with only one open end as shown in **scheme 1**.



**Scheme 1.** Schematic of the nanopores in cylindrically (C)- and V-shaped AAOs.

Cylindrically shaped AAOs (pore diameters of 25, 35, 65, 400 nm; pore depth about 100  $\mu\text{m}$ , denoted as C-25, C-35, C-65, and C-400, respectively) were prepared according to previously reported procedures by Prof. Dr. Martin Steinhart.<sup>1-4</sup> V-shaped AAOs were purchased from Topmembranes Technology Co. Ltd. (Shenzhen, China) and featured different pore diameters and depths. One set of templates had a top pore diameter of 450 nm and a bottom pore diameter of 100 nm, with varying pore depths of 2.5  $\mu\text{m}$ , 1.5  $\mu\text{m}$ , 0.9  $\mu\text{m}$ , and 0.4  $\mu\text{m}$  (denoted, respectively, as V-450-100-2500, V-450-100-1500, V-450-100-900, and V-450-100-400). Another set had a top pore diameter of 125 nm, a bottom pore diameter of 40 nm, and a pore depth of 0.25  $\mu\text{m}$  (denoted as V-125-40-250). In both types of templates, the AAO layer was attached to a thick aluminium (Al) substrate that served as the bottom electrode in the dielectric measurements. Depending on the fabrication conditions, the backside of V-shaped templates often exhibited structural imperfections such as cracks, closed pores, and mechanical defects (“bad AAO layer”, **Figure 1b**), in contrast to the well-ordered porous layer observed on the top side (“good AAO layer”, **Figure 1a**). These defective layers, located on the Al substrate, can interfere with dielectric measurements and must therefore be removed prior to use. To selectively etch the undesired “bad AAO layer”, the templates were treated with 10 wt% aqueous NaOH solution. As illustrated in **Figure 1c**, the bottom surface of V-shaped template was immersed in NaOH solution, and after 40 – 60 minutes of exposure, the treated region exhibited a noticeable color change from matte grey to shiny white. This change indicates successful removal of the defective bottom AAO layer, as confirmed by SEM imaging, which revealed the complete disappearance of V-shaped nanopores in the etched area.

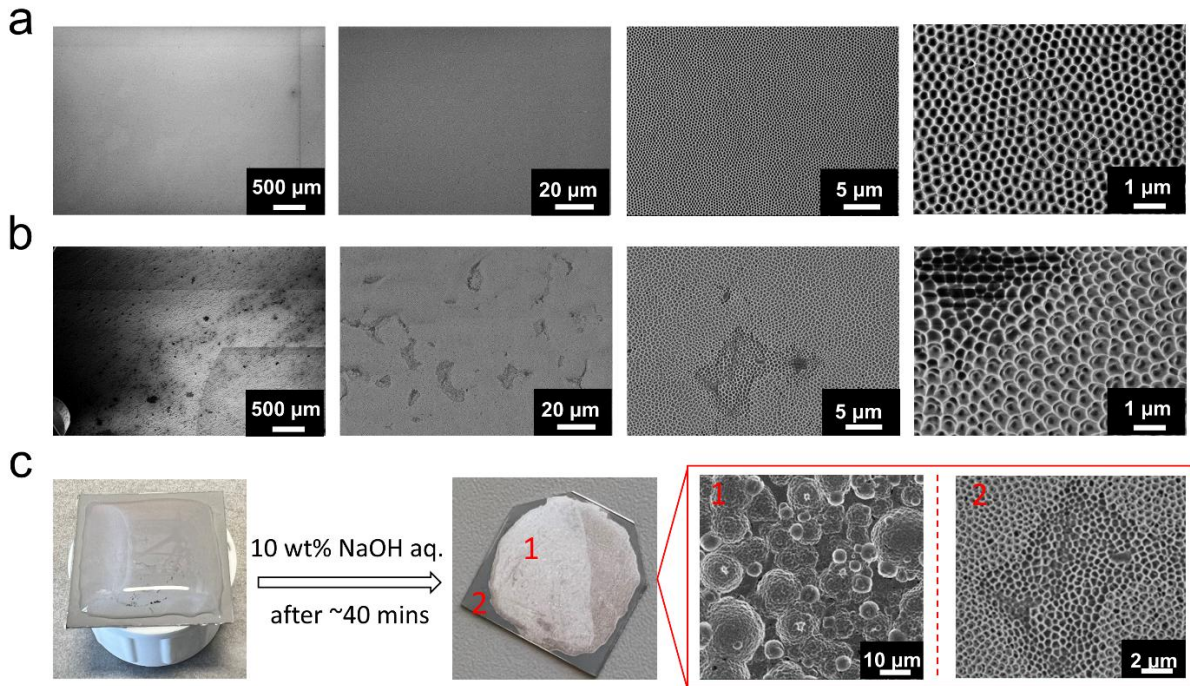


**Figure 1.** (a) The top side of V-450-100-900 template (good AAO layer) under SEM. (b) SEM images of the “bad AAO layer”, the bottom side of V-450-100-900 template. (c) Micrographs of V-450-100-900 template before and after removing the “bad AAO layer”.

The dielectric properties of both ILs and PILs are highly sensitive to the porosity of the confining template. Imperfections can always be introduced during template fabrication or subsequent processing steps (pore deformation, partial pore closure, or uneven surface coverage in both cylindrically and V-shaped templates **Figure 2**) can significantly reduce the effective porosity and hinder accurate interpretation of dielectric measurements. To ensure that all nanopores remain open and accessible, it is essential to thoroughly characterize the templates using scanning electron microscopy (SEM) before sputtering any electrode. This quality control step helps verify the structural integrity of the pores and ensures reproducibility and reliability of the *in situ* dielectric spectroscopy (DS) measurements.

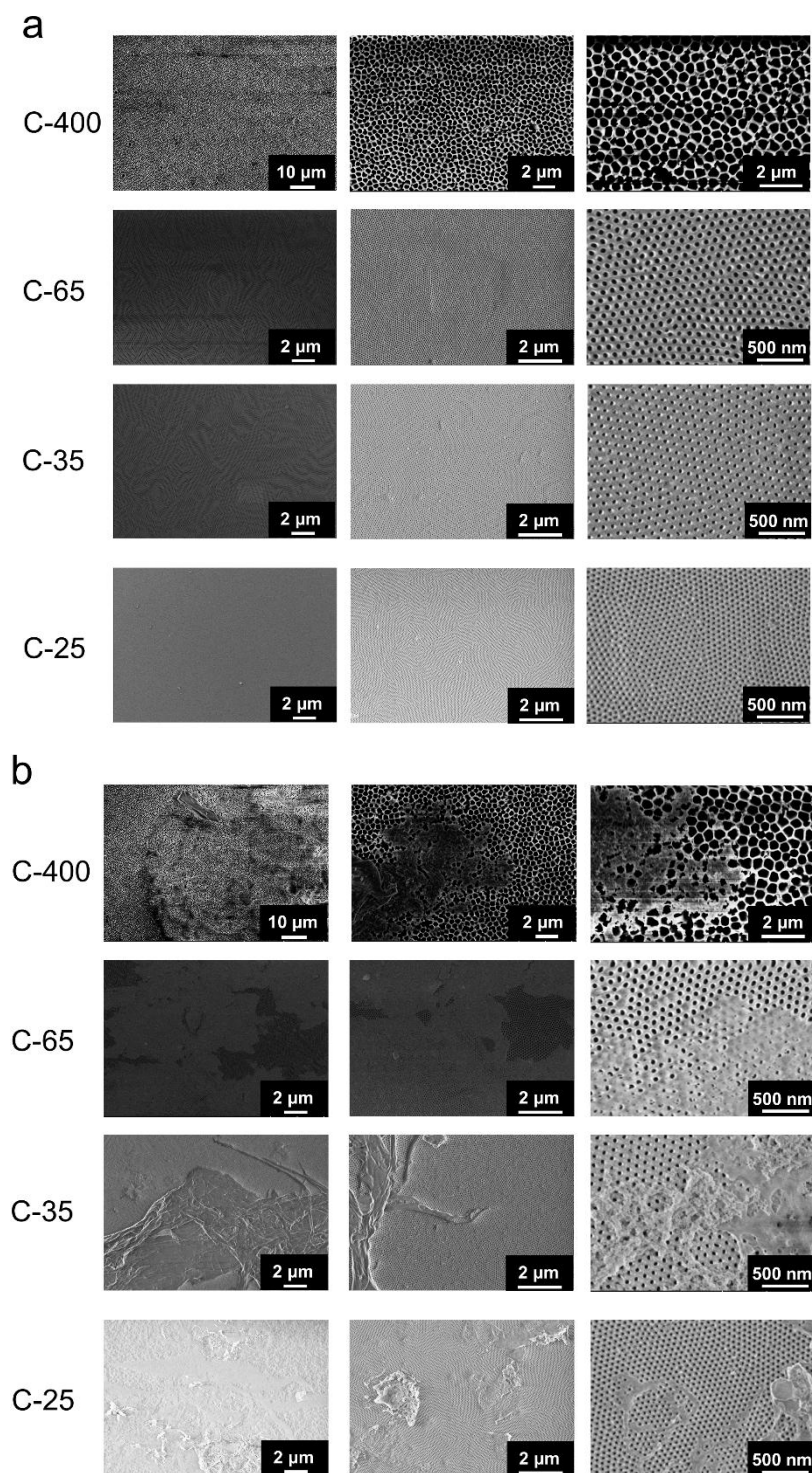


**Figure 2.** SEM images of C-AAO templates at different magnifications. (a) AAO template showing the “ideal” structure with uniform, well-ordered nanopores arranged in a hexagonal pattern. (b) AAO template with defective structure due to technical issues, where some pores are partially or completely closed. Such templates are unsuitable for use in DS experiments.

**Scanning Electron Microscopy (SEM).** High-resolution surface and cross-section images of AAOs were recorded using a Hitachi 8000 scanning electron microscope. To characterize the

pore depth, samples were cut, and the cross-sections were mounted vertically on aluminum SEM stubs using high-purity carbon tape (to characterize the top surface, the template was mounted horizontally on SEM stubs). Imaging was conducted at a working distance of 4 mm and a voltage of 3 kV. The pore depths of V-shaped AAOs, e.g., are shown in **Figure 3**.

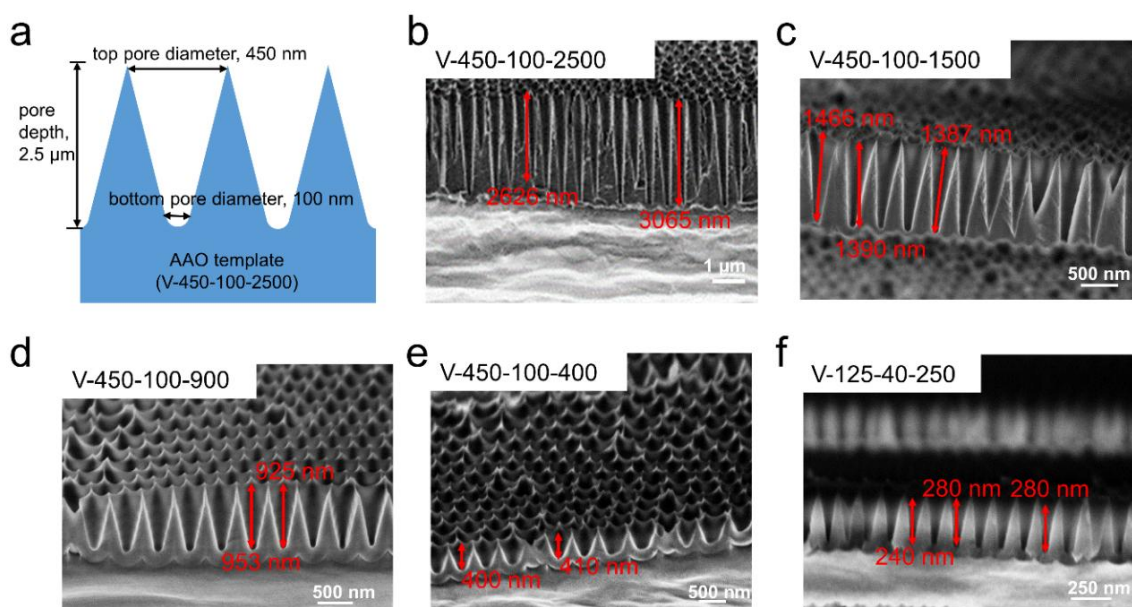


**Figure 3.** (a) Schematic of a V-shaped AAO template and its parameters. (b, c, d, e, f): Cross-sectional SEM micrographs of V-shaped membranes with different pore depths: 2.5  $\mu\text{m}$ , 1.5  $\mu\text{m}$ , 0.9  $\mu\text{m}$ , 0.4  $\mu\text{m}$ , and 0.25  $\mu\text{m}$ , respectively. The red arrows indicate the measured pore depths.

**Porosity Analysis of AAO templates.** The porosity of the AAO templates was determined from top-view scanning SEM images using the software ImageJ, shown in **Figure 4**. High-contrast SEM images were first converted to 8-bit grayscale and adjusted for brightness and contrast to optimize pore-wall distinction. The images were then thresholded to highlight pore regions (red). Following thresholding, binary conversion was applied such that the pores were represented as black areas and the alumina matrix as white. The total pore area was measured using the “Analyse > Measure” function after setting appropriate measurement parameters. As the pore depth remained constant, the porosity was calculated as the ratio of pore area to total image area, expressed as a percentage. We should comment here, that porosity determination from the smaller nanopores by SEM alone can have larger uncertainties (30 % or even higher).

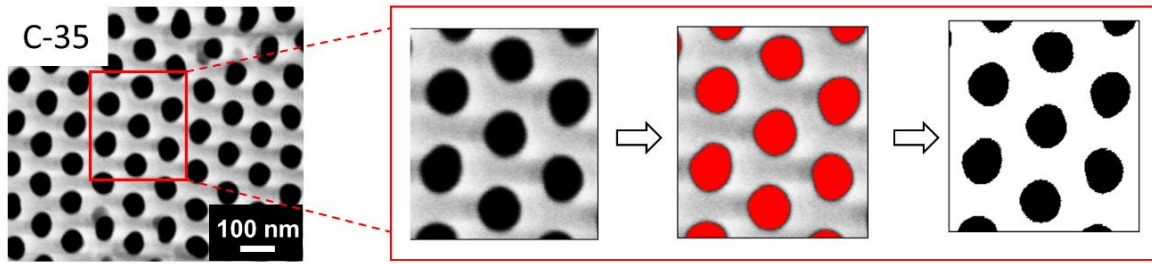


**Figure 4.** Porosity analysis of the indicated AAO template, C-35. Images were digitized with the software *ImageJ* and the porosity was calculated as  $\varphi = A_{\text{pore}}/A_{\text{total}}$ .

**Gold layer coating.** For the *in-situ* dielectric measurement, the top electrode was provided by a sputtered gold layer (thickness of 35 nm). The deposition of the gold layer was performed through a sputtering process under vacuum conditions (vacuum better than  $2 \times 10^{-5}$  Pa) using a Bal-tec MED 020 with a current density of 35 mA. The high vacuum environment is to ensure the uniformity of the sputtered Au layer. The current density was optimized to produce Au grains with appropriate size (too big will block the AAO pores; too small will hinder the current transport). Cooling water was used during sputtering. (Otherwise, the current density is unstable due to overheated temperature, resulting in non-uniform coating, as shown in **Figure 5**). Maintaining an adequate supply of gold target supply is another effective approach to prevent non-uniform coating. Normally, in a good sputtering process the spraying should be controlled at a rate of 0.1 nm/s. In addition to a uniform film deposited on top of AAO templates, some Au particles inevitably fall within the pores (depth of about 380 nm, **Figure 5d**).<sup>5</sup> However, given the high aspect ratio ( $> 10^3$ ) of nanopores, any inhomogeneities in the field lines can be neglected.

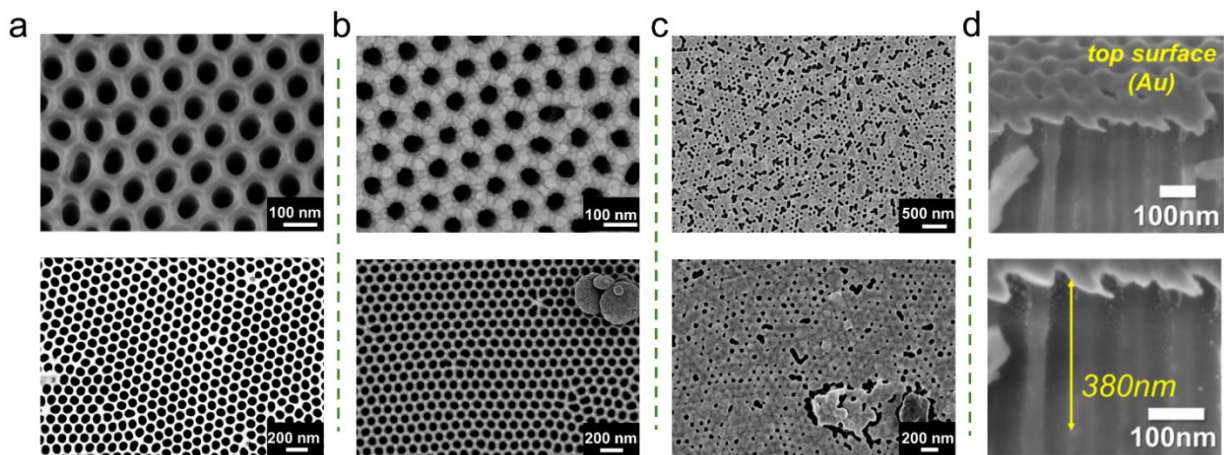


**Figure 5.** SEM images of AAO templates with diameter of 65 nm before and after gold sputtering. (a) Empty AAO template before sputtering, showing uniform and well-ordered open pores. (b) AAO template after sputtering with a uniform gold coating, where all pores remain open. (c) AAO template after non-uniform gold sputtering, resulting in partial or complete coverage of pores, making the template unsuitable for further use. (d) SEM images showing the top surface and cross section of AAO pores following Au sputtering.<sup>5</sup> The bottom figure is a zoom-in picture.

**Annealing.** Prior to infiltration, all AAO templates were annealed in a vacuum oven ( $\sim 2$  mbar) at 423 K for 10-12 h. This procedure not only removes some OH groups from the AAO surface. In addition, it removes traces of water from the templates, essential to the dielectric measurement (**Figure 6a**). After annealing, the dielectric permittivity of sputtered cylindrically shaped AAOs ranged from 5 to 10 depending on the pore size, as shown in **Figure 6b**. The comparison of dielectric permittivity measurements of V-shaped AAOs with different pore sizes is also shown in **Figure 6c**.

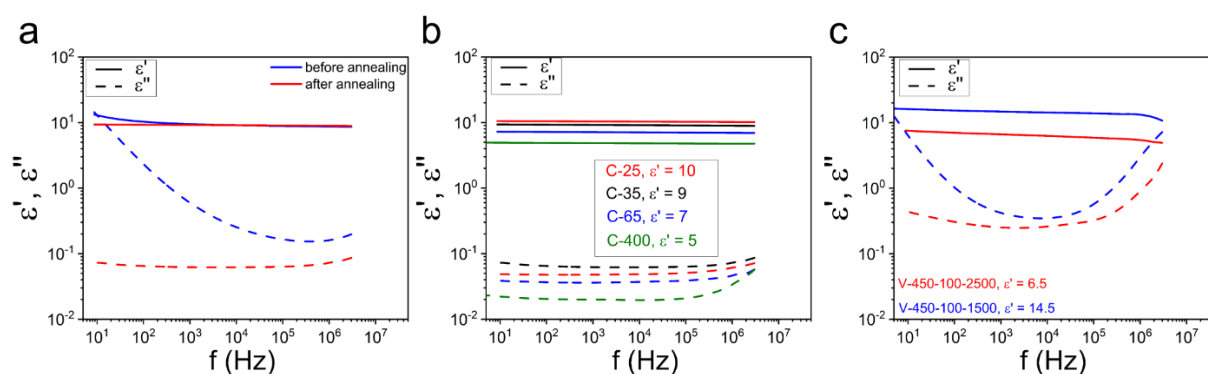


**Figure 6.** Dielectric permittivity as a function of frequency for AAO templates with different pore geometries. (a) Comparison of permittivity of cylindrically-shaped AAO templates with a diameter of 35 nm before and after annealing. (b) Cylindrically-shaped AAO templates with varying pore diameters: C-25 (red), C-35 (black), C-65 (blue), and C-400 (green), showing corresponding values of 10, 9, 7, and 5, respectively. (c) V-shaped AAO templates with different pore parameters: V-450-100-2500 (blue) and V-450-100-1500 (red), exhibiting values of 6.5 and 14.5, respectively.

**Inner pore silanization.** For the inner pore silanization, hexamethyldisilazane (HMDS) (purity  $\geq 99.0\%$ , purchased from Sigma-Aldrich) was injected into the chamber containing the AAOs at 350 K and the AAOs were completely submerged. After 30 minutes, the volatility of HMDS caused pressure to build-up in the chamber containing the AAOs, which was subsequently maintained at 350 K for 3 hours. By treating the original membranes (e.g. before annealing) with HMDS, -OH groups were replaced with trimethylsilyl groups turning the inner surface to hydrophobic. Notably, the inner surface silanization is incomplete due to the narrow space of nanopores (**Figure 7a**). To verify the successful hydrophobic modification of the AAO surface,

the contact angle of the IL on an electropolished Al disk which was modified in the same way to mimics the inner pore was measured (Figure 7b). Following silanization, the contact angle increased from  $50^\circ$  to  $70^\circ$ , confirming an enhancement in surface hydrophobicity.

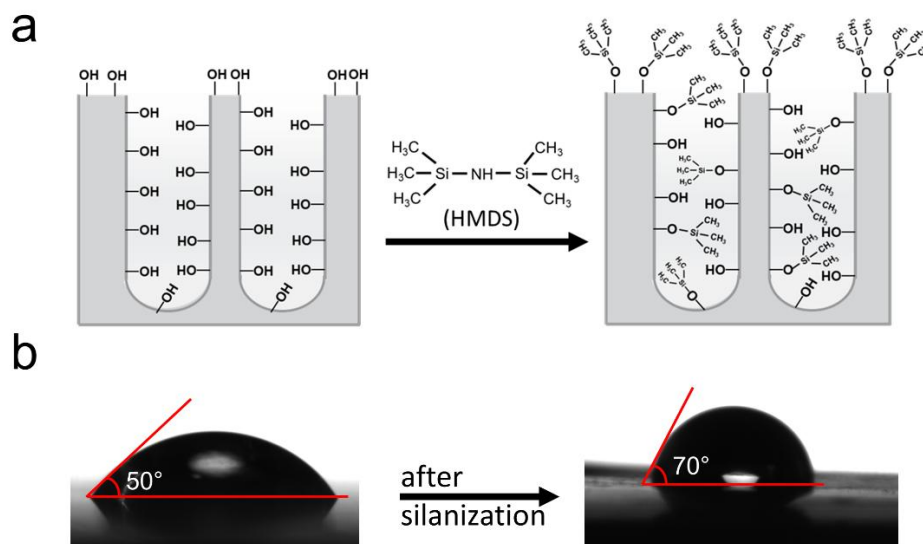


**Figure 7.** (a) Schematic illustration of the silanization process of AAO templates using HMDS. Due to spatial confinement within the nanopores, inner pore silanization is partial. (b) Contact angle measurements of the ionic liquid  $[\text{BMIM}]^+[\text{BF}_4]^-$  on the template surface before ( $50^\circ$ ) and after ( $70^\circ$ ) silanization, indicating an increase in surface hydrophobicity after the surface modification.

### 2.3. Instruments and Characterization

**Contact angle.** The contact angle was measured with a commercial goniometer (OCA35, DataPhysics) and evaluated with the software IDS uEye. For liquid sample, *e.g.* ionic liquid, a drop was placed on an electropolished Al disk coated by a thin native oxide layer. The latter comprises a flat model surface that mimics the inner AAO surface. With respect to polymer sample, *e.g.* the PIL, a nearly spherical polymer particles of  $\sim 1$  mm diameter was first prepared. To form spherical particle of the PIL, around 1 mg of sample was placed on a superamphiphobic surface.[] The sample was heated to a liquid state and kept for 24 h under vacuum to form a spherical shape caused by the surface tension of the polymer. Subsequently, the polymer sphere was slowly cooled and transferred onto the electropolished Al disk. The contact angle measurement at high temperature was conducted using a temperature-controlled stage. The temperature was gradually increased to the target temperature and maintained for at least 2 hours. The contact angle continuously decreased with increasing temperature. The

equilibrium contact angle at the target temperature was recorded once no further changes were observed (**Figure 8**).

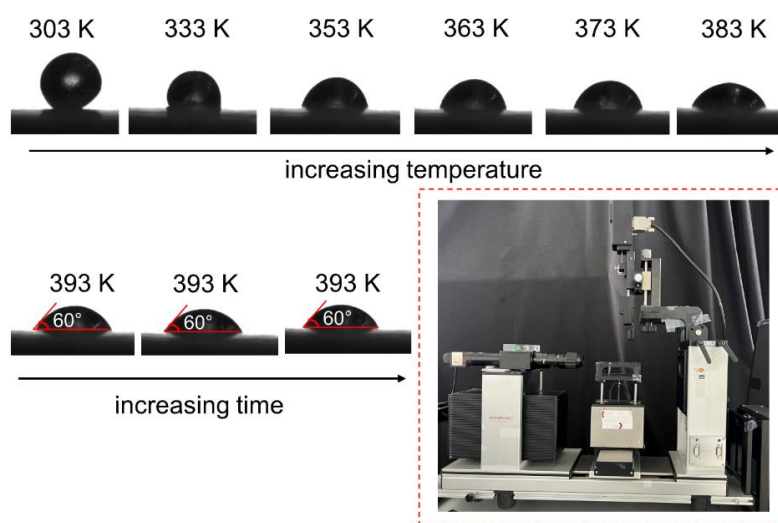


**Figure 8.** Contact angle images of poly[BVIM]<sup>+</sup>[PF<sub>6</sub>]<sup>-</sup> on the electroplated Al disk at different temperatures. At the target temperature (393 K), the contact angle was 60°. The image in the dashed box shows the experimental setup employed for the contact angle measurement.

**Surface tension.** The Wilhelmy plate method<sup>23</sup> was employed to measure the surface tension. A rod-like platinum-iridium plate with a diameter of 1.2 mm was vertically placed into the IL. The liquid had a contact angle of around 0° on the platinum-iridium rod surface. The surface tension exerted a downward force ( $F$ ), which was measured with a tension meter (DCAT 11BC, DataPhysics, **Figure 9**). The surface tension ( $\gamma$ ) was then calculated from  $F = l\gamma$ , where  $l$  is the circumference of the rod-like plate.

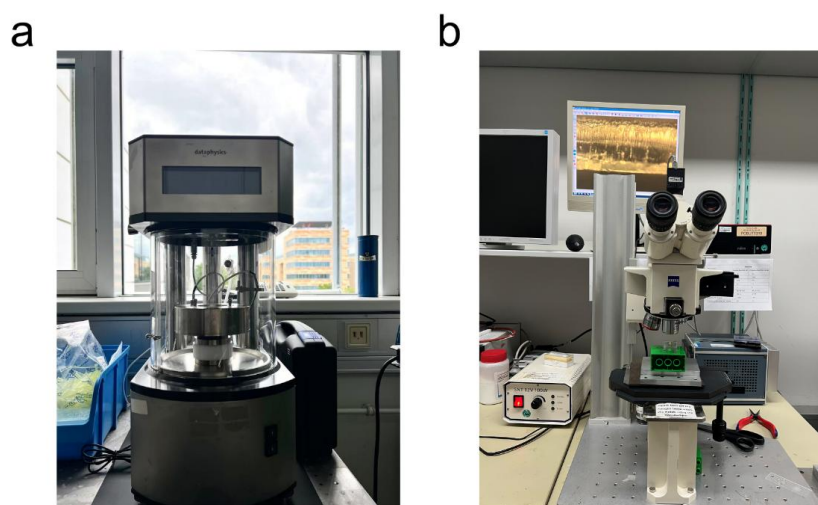


**Figure 9.** Images of the (a) surface tension measurement setup and (b) reflection optical microscopy setup.

**Reflection Optical Microscopy.** The top layer was removed, the AAO templates were cross sectioned and the imbibition length was determined from the cross sections by reflection optical microscopy (ROM) (Zeiss AxioTech vario). As ILs or PILs penetrate the pores they increase the refractive index as compared to the unfilled parts creating optical contrast that is detected from the changing reflectance.

**Rheology.** The zero shear viscosity and shift factors were investigated using a shear rheometer (ARES). Measurements were performed with an environmental test chamber as a function of temperature. Samples were prepared on the lower plate of the 25 mm diameter parallel plate geometry. The upper plate was brought into contact, and the sample thickness was adjusted. The storage ( $G'$ ) and loss ( $G''$ ) shear moduli were monitored as a function of frequency,  $\omega$ , for frequencies in the range  $10^{-1} < \omega < 10^2 \text{ rad}\cdot\text{s}^{-1}$ . All measurements refer to the linear viscoelastic range. Subsequently, the complex viscosity ( $\eta^*$ ) follows as  $\eta^* = G''/\omega - iG'/\omega$ . Master curves were made by use of the time–temperature superposition principle ( $tT_s$ ). The latter allows the frequency  $\omega$  dependence of the complex modulus  $G^*$  at any temperature  $T$  to be determined from a master curve at a reference temperature. At each temperature  $T$ , a single frequency-scale shift factor allows superposition of  $a_T$  allow superposition of all viscoelastic data at temperature  $T$  with the data at the reference temperature,  $T_{ref}$ , as  $G^*(\omega; T) = G^*(a_T\omega; T_{ref})$ .

**Dielectric spectroscopy (DS).** DS is a powerful experimental technique for probing the dielectric and electrical properties of materials over a wide range of frequencies, as shown in **Figure 10.**<sup>6</sup> The interaction of electromagnetic waves with matter in the frequency regime between  $10^{-6}$  and  $10^{12}$  Hz is the domain typically known as broadband dielectric spectroscopy (BDS). Within this extraordinarily broad dynamic range, molecular and collective dipolar fluctuations, charge transport, and polarization effects at inner and outer boundaries take place, and determine the dielectric properties of the material.

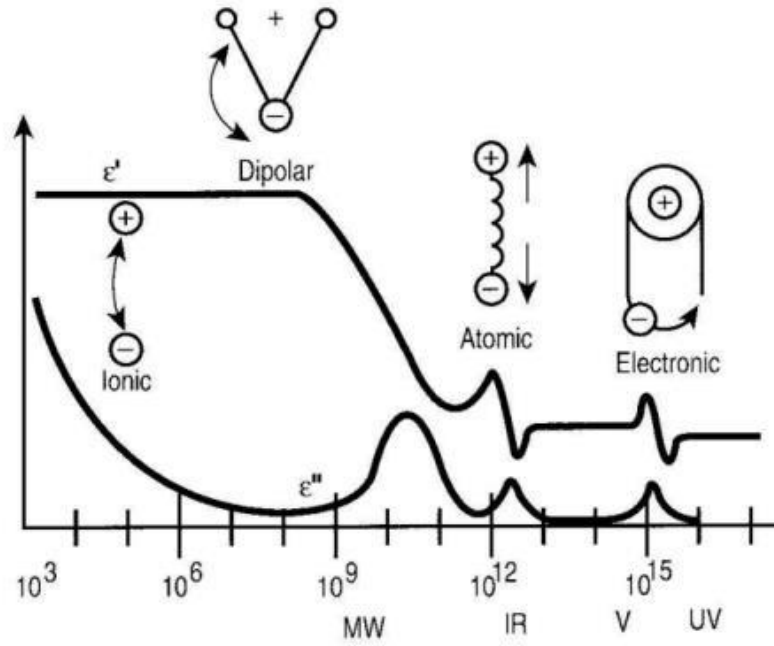


**Figure 10.** A schematic of the dielectric function  $\varepsilon^*$  ( $\varepsilon'$ , dielectric permittivity;  $\varepsilon''$ , dielectric loss) plotted over a broad of frequency range. The real,  $\varepsilon'$ , and imaginary,  $\varepsilon''$ , parts of the dielectric function are shown and various processes are depicted: ionic and dipolar relaxations at lower frequencies, followed by atomic and electronic resonances at higher frequencies.<sup>6</sup>

Its theoretical foundation is rooted to Maxwell's equations that describe the response of a material in electric and magnetic fields. In particular, the displacement current term in Maxwell-Ampère's law is central to understanding the dielectric response:

$$\nabla \times H = j + \frac{\partial D}{\partial t} \quad (1)$$

where  $j$  is the current density, and  $\frac{\partial D}{\partial t}$  is the displacement current. The electric displacement field  $D$  is related to the electric field  $E$  by:

$$D = \varepsilon_0 E + P = \varepsilon^* \varepsilon_0 E \quad (2)$$

where  $\varepsilon^*$  is the complex dielectric function,  $\varepsilon_0$  is the permittivity in vacuum ( $= 8.85 \times 10^{-12} \text{F/m}$ ), and  $P$  is the polarization of the material resulting from the response of the material to an external electric field.

Based on the Ohm's law, the current density is proportional to the electric field,

$$j = \sigma^* E \quad (3)$$

where  $\sigma^*$  is the complex dielectric conductivity,  $\sigma^* = \sigma'(\omega) + i\sigma''(\omega)$ . According to equation (1), the current density,  $j$ , and the time derivative of  $D$ , are equivalent quantities from (1), (2) and (3), it follows that

$$\sigma^* = i\omega\varepsilon_0\varepsilon^* \quad (4)$$

In a dielectric spectroscopy experiment, an alternating electric field is applied to the sample to probe its dielectric response (**Figure 11**). The interrelations among impedance, dielectric constant, conductivity, and capacitance are summarized in **Table 1**.

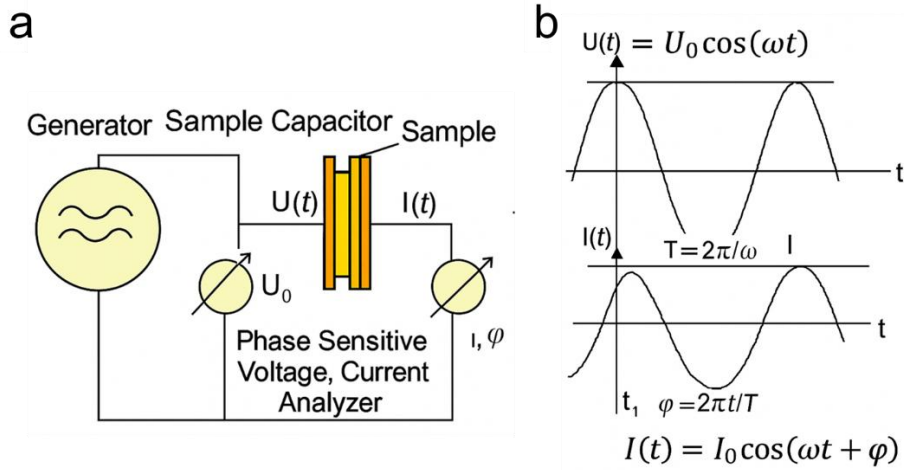


**Figure 11.** (a) Schematic diagram of the experimental setup used in dielectric spectroscopy. (b) Time-dependent plots of the applied voltage  $U(t) = U_0 \cos(\omega t)$  and the resulting current  $I(t) = I_0 \cos(\omega t + \varphi)$ .

**Table 1.** Summary of Key Parameters and Equations in Dielectric Spectroscopy.

Parameters	Equations
Impedance, $Z^*$	$Z^*(\omega) = Z' + iZ'' = \frac{U_0}{I^*(\omega)}$ (5)
Capatance, $C$	$C = \varepsilon^* \varepsilon_0 \left(\frac{A}{d}\right)$ (6)
Dielectric constant, $\varepsilon^*$	$\varepsilon^*(\omega) = \varepsilon' - i\varepsilon'' = \frac{1}{i\omega Z^*(\omega)C_0}$ (7)
Dielectric conductivity, $\sigma^*$	$\sigma^*(\omega) = \sigma' + i\sigma'' = \frac{1}{Z^*(\omega)} \frac{d}{A}$ (8)

In disordered or amorphous materials, ion transport deviates significantly from the long-range diffusion mechanisms observed in crystalline systems (vacancy mechanism: one ion jumps into the vacancy, then the next ion jumps into the new vacancy). Due to the lack of periodic lattice structure, ions in such systems experience a highly irregular potential energy landscape, characterized by spatially varying barrier heights and trapping sites (**Figure 12a**).<sup>7,8</sup> This complex environment hinders the formation of well-defined vacancy chains as in crystalline conductors, instead gives rise to a stochastic hopping mechanism. In this framework, ions thermally overcome local energy barriers and jump between metastable sites, leading to a net charge displacement over time.

At long timescales and low frequencies, ions explore the largest parts of space by overcoming highest energy barriers, these ions are contributed to the dc-conductivity. Mathematically, it appears as the plateau value in the real part of the complex conductivity. At shorter timescales, however, ions vibrate within the potential energy minimum. This frequency-dependent hopping conduction in a spatially disordered energy landscape can be modeled by a complex conductivity expression:

$$\sigma^*(\omega) = \sigma_{dc} \frac{i\omega\tau_e}{\ln(1+i\omega\tau_e)}, \quad (9)$$

Combined with equation (8), the real and imaginary components of the complex conductivity are given by:

$$\sigma'(\omega) = \frac{\sigma_{dc}\omega\tau_e \arctan(\omega\tau_e)}{\frac{1}{4}\ln^2(1+\omega^2\tau_e^2) + (\arctan\omega\tau_e)^2} \quad (10)$$

$$\sigma''(\omega) = \frac{\sigma_{dc}\omega\tau_e \ln^2(1+\omega^2\tau_e^2)}{\frac{1}{2}\ln^2(1+\omega^2\tau_e^2) + 2(\arctan\omega\tau_e)^2} \quad (11)$$

where  $\tau_e$  is an effective relaxation time associated with the distribution of energy barriers. The corresponding real and imaginary components that reflect the interplay between dynamic and static contributions to ion transport. At low frequency, additional deviations occur due to electrode polarization effects, where ions accumulate near blocking electrodes, forming space-charge regions that further distort the measured response (**Figure 12b**).

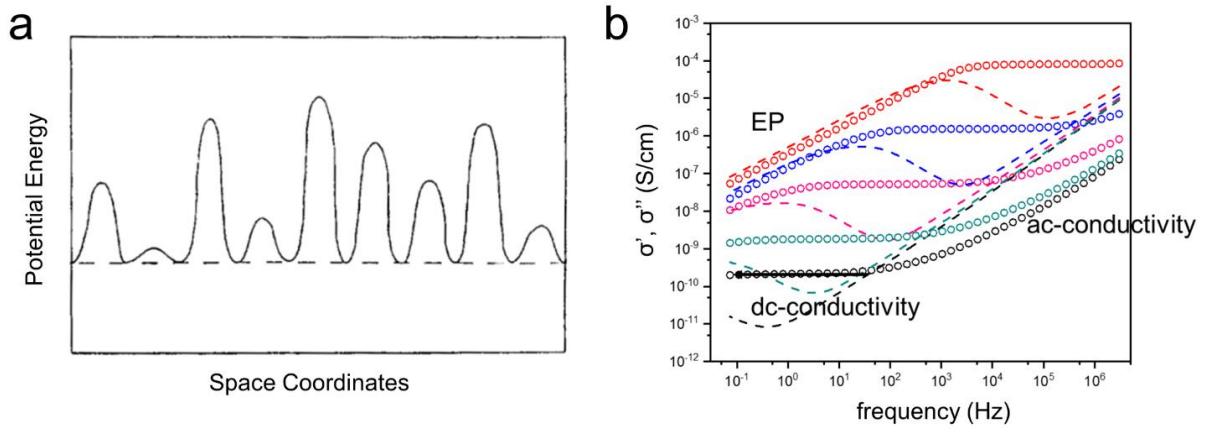


**Figure 12.** (a) Schematic figures illustrating hopping conduction in a spatially randomly varying energy barrier.<sup>7</sup> (b) Real (open circles) and imaginary (dashed lines) parts of the ionic conductivity of bulk  $[\text{BMIM}]^+[\text{BF}_4]^-$  shown for the indicated temperatures.

In this thesis, the dynamics of bulk and confined ILs and PILs was performed by DS. The instrument is equipped with a Novocontrol Alpha frequency analyzer composed of a broadband dielectric converter and an active sample head. For bulk samples, the IL/PIL were embedded between two stainless steel electrodes with a diameter of 20 mm accompanied with a Teflon

spacer of 250  $\mu\text{m}$  to maintain the thickness (**Figure 13a**). The sample preparation for *in situ* nanodielectric spectroscopy was more demanding. First, the AAO templates were sputtered with a gold layer with a thickness of 35 nm on the top side. Subsequently, a thin film or a drop of liquid was deposited on the top of the template. The frequency range also needed to be selected. A broad frequency ranges from  $10^{-2} - 10^7$  Hz was normally used in bulk DS measurements. Typically, the applied voltage was below 1 V. In contrast, a narrower frequency range, from  $10 - 10^6$  Hz, is applied to probe the faster imbibition kinetics since a shorter time is needed. The dielectric function depends on frequency, temperature and time. The complex conductivity function,  $\sigma^* = \sigma' + i\sigma''$ , where  $\sigma'$  and  $\sigma''$  are the real (*i.e.*, the dc-conductivity) and imaginary parts, respectively, was obtained from the impedance measurements. The plateau in the real part  $\sigma'$  was used to extract the dc-conductivity (**Figure 13b**).

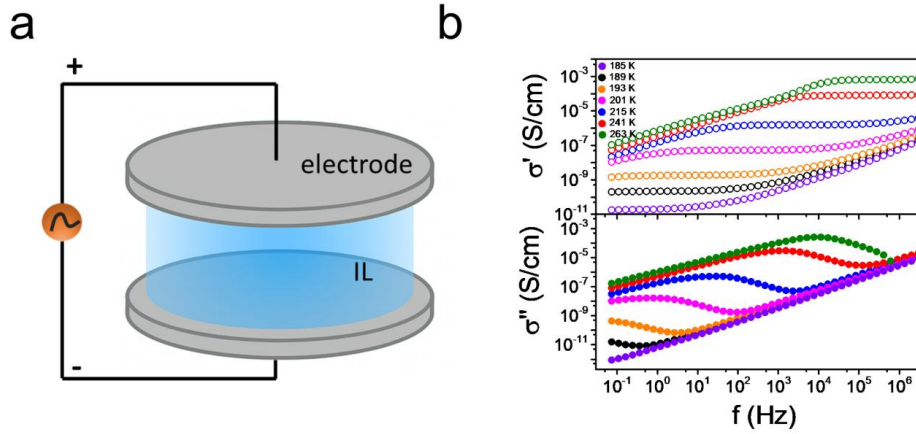


**Figure 13.** (a) Schematic illustration of the dielectric setup for bulk measurement. (b) Real (top) and imaginary (bottom) parts of the ionic conductivity of bulk  $[\text{BMIM}]^+[\text{BF}_4]^-$  shown for the indicated temperatures.

Briefly, we can assume a simple Debye model that includes the conductivity term to simulate the frequency dependence of complex conductivity as:

$$\varepsilon^* = \varepsilon_\infty + \frac{\Delta\varepsilon}{1 + i\omega\tau_D} + \frac{\sigma_{dc}}{i\omega\varepsilon_0} \quad (12)$$

with real ( $\varepsilon'$ ) and imaginary ( $\varepsilon''$ ) parts

$$\varepsilon' = \varepsilon_\infty + \frac{\Delta\varepsilon}{1 + (\omega\tau_D)^2} \quad (13)$$

$$\varepsilon'' = \Delta\varepsilon \frac{\omega\tau_D}{1 + (\omega\tau_D)^2} + \frac{\sigma_{dc}}{\omega\varepsilon_0} \quad (14)$$

because  $\sigma^*(\omega) = \sigma'(\omega) + i\sigma''(\omega) = i\omega\varepsilon_0\varepsilon^*(\omega)$ ,

$$\sigma'(\omega) = \omega \varepsilon_0 \varepsilon''(\omega) = \sigma_{dc} + \frac{\omega^2 \tau \varepsilon_0 \Delta \varepsilon}{1 + (\omega \tau_D)^2} \quad (15)$$

$$\sigma''(\omega) = \omega \varepsilon_0 \varepsilon'(\omega) = \omega \varepsilon_0 \left( \varepsilon_\infty + \frac{\Delta \varepsilon}{1 + (\omega \tau_D)^2} \right) \quad (16)$$

Here,  $\Delta \varepsilon$  is the dielectric strength,  $\varepsilon_\infty$  is the dielectric permittivity at very high frequencies,  $\tau_D$  is a characteristic relaxation time, and  $\sigma_{dc}$  is the ionic conductivity. To provide a comprehensive analysis for the imbibition of ionic materials within nanopores, the equivalent capacitance representation was employed (**Figure 14**).

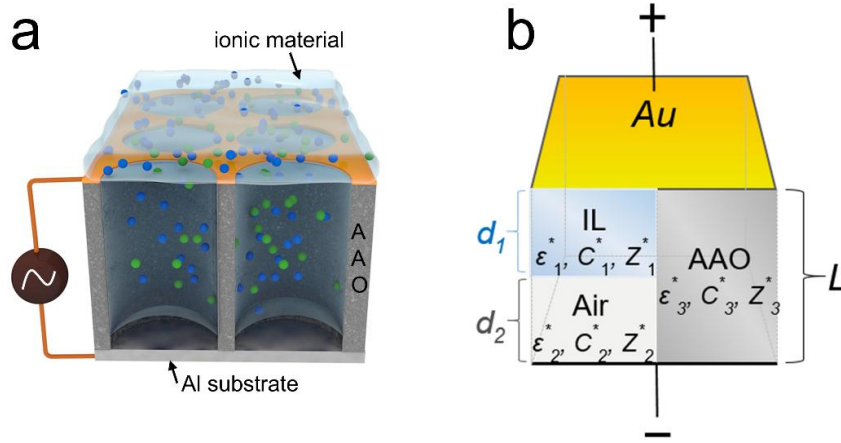


**Figure 14.** (a) Schematic of the experimental setup of *in-situ* nDS. (b) The equivalent capacitor circuit.

Here, the parallel model is considered, comprising the capacitance of the ionic material ( $C_1$ ) and air ( $C_2$ ) connected in series, whereas the combined ionic material/air capacitance ( $C_{12}$ ) connects in parallel with the AAO ( $C_3$ ). Therefore,

$$\frac{1}{C_{12}} = \frac{1}{C_1} + \frac{1}{C_2}, \text{ and } C_{123} = C_{12} + C_3 \quad (17)$$

By employing the above equations and the definition  $\sigma_{123}^* = i\omega \varepsilon_0 \varepsilon^*$ , results to:

$$\sigma_{123}^* = \sigma' + i\sigma'' = \left\{ \left[ \frac{L d_1 \sigma_1' (\omega \varepsilon_0)^2}{(d_2 \sigma_1')^2 + (d_1 \omega \varepsilon_0 + d_2 \sigma_1'')^2} \right] \varphi_{12} + \sigma_3' \varphi_3 \right\} + i \left\{ \left[ \frac{L [d_2 [(\sigma_1')^2 + (\sigma_1'')^2] \omega \varepsilon_0 + \sigma_1'' (\omega \varepsilon_0)^2 d_1]}{(d_2 \sigma_1')^2 + (d_1 \omega \varepsilon_0 + d_2 \sigma_1'')^2} \right] \varphi_{12} + \sigma_3'' \varphi_3 \right\} \quad (18)$$

In the above equation  $\varphi$  gives the porosity. We can employ typical values for the real and imaginary parts of the AAO complex conductivity (e.g.  $\sigma_3' = \sigma_{AAO}' = 10^{-10}$  S cm $^{-1}$  and  $\sigma_3'' = \sigma_{AAO}'' = 10^{-8}$  S cm $^{-1}$ ) and typical values for the bulk ionic materials to show that a conductivity plateau (dc-conductivity) only arises when the pores are fully infiltrated (**Figure 15**).

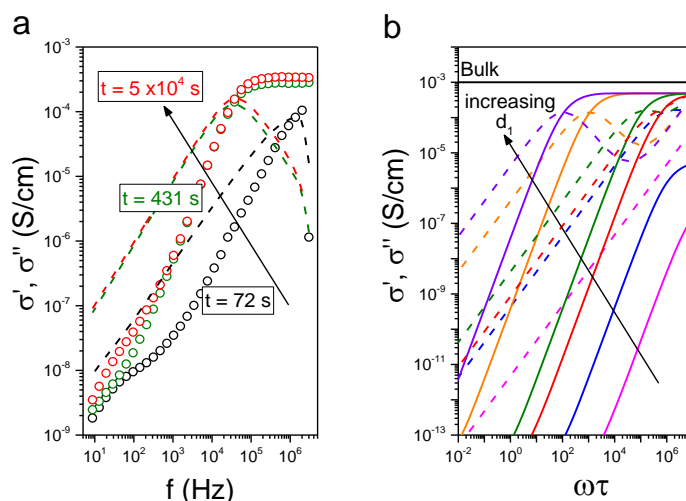


**Figure 15.** (a) Evolution of the real (symbol) and imaginary (dashed lines) parts of the complex conductivity for  $[\text{BMIM}]^+[\text{BF}_4]^-$  within AAO pores with a diameter of 400 nm at 303 K. (b) Simulation of the evolution of the real (solid lines) and imaginary parts (dashed lines) of the complex conductivity corresponding to the process in (a) for different imbibition lengths ( $d_1$ ) via the parallel model. Parameters are as follows:  $\Delta\varepsilon = 20$ ,  $\varepsilon_\infty = 10$ ,  $\sigma_{\text{dc}} = 10^{-3} \text{ S cm}^{-1}$ ,  $\tau = 1 \text{ s}$ ,  $\varphi_{12} (=1 - \varphi_3) = 0.484$ ,  $L = 100 \mu\text{m}$ ,  $\sigma'_3 = \sigma'_{\text{AAO}} = 10^{-10} \text{ S cm}^{-1}$ , and  $\sigma''_3 = \sigma''_{\text{AAO}} = 10^{-8} \text{ S cm}^{-1}$ . Different colors correspond to different imbibition lengths: (magenta)  $d_1 = 10 \mu\text{m}$ , (blue)  $d_1 = 99 \mu\text{m}$ , (red)  $d_1 = 99.5 \mu\text{m}$ , (olive)  $d_1 = 99.9 \mu\text{m}$ , (orange)  $d_1 = 99.999 \mu\text{m}$ , and (violet)  $d_1 = 99.9999 \mu\text{m}$ .

## 2.4. References

- (1) Masuda, H.; Fukuda, K. Ordered Metal Nanohole Arrays Made by a Two-Step Replication of Honeycomb Structures of Anodic Alumina. *Science* **1995**, *268*, 1466-1468.
- (2) Masuda, H.; Hasegawa, F.; Ono, S. Self-ordering of Cell Arrangement of Anodic Porous Alumina Formed in Sulfuric Acid Solution. *J. Electrochem. Soc.* **1997**, *144*, L127-L130.
- (3) Masuda, H.; Yada, K.; Osaka, A. Self-ordering of Cell Configuration of Anodic Porous Alumina with Large-Size Pores in Phosphoric Acid Solution. *Jpn. J. Appl. Phys.* **1998**, *37*, L1340- L1342.
- (4) Steinhart, M. Supramolecular Organization of Polymeric Materials in Nanoporous Hard Templates. *Adv. Polym. Sci.* **2008**, *220*, 123-187.
- (5) Tu, C.-H.; Zhou, J.; Butt, H.-J.; Floudas, G. Adsorption Kinetics of cis-1,4-Polyisoprene in Nanopores by In Situ Nanodielectric Spectroscopy. *Macromolecules* **2021**, *54*, 6267-6274.
- (6) Moeller, M.; Matyjaszewski, K. eds. *Polymer Science: A Comprehensive Reference*[M]. Amsterdam: Elsevier, **2012**.
- (7) Dyre, J. C.; Maass, P.; Roling, B.; Sidebottom, D. L. Fundamental questions relating to ion conduction in disordered solids. *Rep. Prog. Phys.* **2009**, *72*, 046501.
- (8) Dyre, J. C. The random free-energy barrier model for ac conduction in disordered solids. *J. Appl. Phys.* **1988**, *64*, 2456-2468.

## Chapter 3. Conductivity of Ionic Liquids in the Bulk and During Infiltration in Nanopores.

This chapter has been published as a research paper in *Journal of Physical Chemistry. B*.

*Yun Dong, Martin Steinhart, Hans-Jürgen Butt, and George Floudas*

J. Phys. Chem. B 2023, 127, 6958–6968

DOI: 10.1021/acs.jpcc.3c01216

### **Author contributions:**

**Yun Dong:** Dielectric spectroscopy, optical microscopy, surface tension measurements. AAO template modification. Data analysis and interpretation. Writing original draft of the manuscript.

**Martin Steinhart:** AAO template fabrication.

**George Floudas:** Design of the research topic. Discussion on results. Writing of the manuscript based on the original draft.

**Hans-Jürgen Butt:** Acquiring funding for the project. Discussion on the concept/research topic and results. Correction of the manuscript.

## Abstract

The conductivity of ionic liquids (ILs) in nanopores is essential for applications in energy materials. However, no consensus has been reached about the influence of confinement on the mobility of the ions. A series of ILs bearing the same cation, 1-butyl-3-methylimidazolium ([BMIM]<sup>+</sup>), and six different anions ([Cl]<sup>-</sup>, [Br]<sup>-</sup>, [I]<sup>-</sup>, [BF<sub>4</sub>]<sup>-</sup>, [PF<sub>6</sub>]<sup>-</sup> and [TFSI]<sup>-</sup>) with radii from 0.168 nm to 0.326 nm were investigated with respect to their self-assembly, the thermodynamics and the ionic conductivity in the bulk, during flow and under confinement in cylindrical nanopores with sizes in the range from 400 nm to 25 nm. In the bulk, the [BMIM]<sup>+</sup>[X]<sup>-</sup> exhibit weak ordering as a result of cation-anion correlations (charge alteration peak), and nanophase separation of polar/apolar groups. Liquid-to-glass temperatures were found to differ by ~ 50 K, their viscosities by a factor of ~ 270, and their conductivities by a factor of 24 (all at a temperature of 303 K). Electrostatic interactions were largely responsible for variations in the glass temperature, the viscosity and the conductivity. Confined ILs behave differently from the bulk. The majority of ILs in the bulk were prone to crystallization during heating but were unable to crystallize in the smaller pores. Changes in dc-conductivity were used as markers of the phase state. This allowed the construction of the effective phase diagrams under confinement. The ILs penetrate the pores with an effective viscosity of the order of their viscosity in their bulk state. However, within the pores the dc-conductivity was reduced relative to bulk, indicating the immobilization of ions at the pore walls. Hydrophobization of the pore walls by hexamethyldisilazane could partially restore the conductivity. ILs are model systems where the phase state and ion mobility can be controlled by confinement.

### 3.1 Introduction

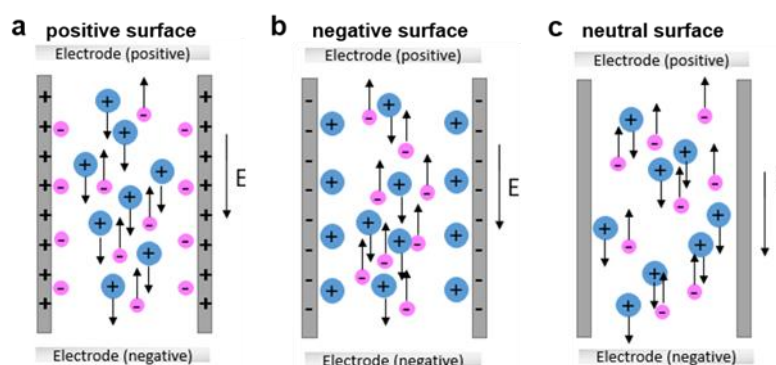
Ionic liquids (ILs) are molten salts at temperatures below 100 °C, formed by a large cation and a charge delocalized anion. This combination results to weak electrostatic interactions that give rise to some unique properties, such as nonvolatility, high thermal stability and relatively high ionic conductivity, making them attractive materials for energy storage and conversion.<sup>1-3</sup> Applications range from electrolyte materials for Li ion batteries, and nonhumidified fuel cells and as carbon precursors for electrode catalysts of fuel cells as well as electrode materials for batteries and supercapacitors.<sup>1,4,5</sup> In several of these applications ILs are confined in porous host matrices. Under these conditions, one needs to consider interactions within the formed interface. This has initiated an effort to explore the effect of confinement and of surfaces/interfaces on the structure and ionic conductivity of ILs.<sup>6-9</sup>

Experimental studies of confined ILs have led to conflicting results with respect to changes in the ionic conductivity. Ion transport in 1-butyl-3-methylimidazolium methylsulfate ([BMIM]<sup>+</sup>[CH<sub>3</sub>SO<sub>4</sub>]<sup>-</sup>) in a single conically shaped nanopore - prepared via track-etching of a polyethylene terephthalate film - was reduced relative to the bulk. This observation suggests the presence of electrostatic interactions beyond a single double-layer.<sup>6</sup> Moreover, modulation of the electric interactions with the pore walls resulted in an ionic diode of the confined IL.<sup>6</sup> The first study where inorganic (hard) confining media was employed refers to 1-hexyl-3-methylimidazolium hexafluorophosphate ([HMIM]<sup>+</sup>[PF<sub>6</sub>]<sup>-</sup>) in oxidized nanoporous silica membranes (pore size 7.5 nm).<sup>7</sup> A 10-fold decrease in conductivity and in the effective diffusion coefficient was found. The large changes in conductivity were attributed to hydrogen bonding of the silanol groups. This effect was partially removed by salinization of the membrane. In contrast, an enhancement of charge transport in 1-butyl-3-methylimidazolium tetrafluoroborate ([BMIM]<sup>+</sup>[BF<sub>4</sub>]<sup>-</sup>) inside the same oxidized nanoporous silicon membranes (pore sizes from 7.5 nm to 10.4 nm) was reported.<sup>8</sup> In this case, the inner surfaces of the nanoporous silica were modified by hexamethyldisilazane (HDMS), turning the surface to hydrophobic. Under confinement a change in the temperature dependence of conductivity from Vogel-Fulcher-Tammann to Arrhenius-like was found, resulting to an enhancement of diffusivities by more than two orders of magnitude.<sup>8</sup> Results were attributed to changes in ion packing (lower density). In a more recent investigation,<sup>9</sup> the charge transport of 1-hexyl-1-methylpyrrolidinium bis(trifluoromethanesulfonyl)imide ([C<sub>6</sub>MPyrr]<sup>+</sup>[Tf<sub>2</sub>N]<sup>-</sup>) infiltrated into nanoporous AAO membranes was studied as a function of pore size and surface functionality

for two cation alkyl chain lengths. Faster ion dynamics resulting to a higher ionic conductivity was found in the confined ILs relative to bulk.

Simulations were also employed to study confined ILs. Molecular dynamics simulations of ILs based on 1-butyl-3-methylimidazolium  $[\text{BMIM}]^+$  with different anions at the quartz(001) surface revealed well-ordered ILs at the solid/liquid interfaces.<sup>10</sup> Interactions with the  $\text{Si}(\text{OH})_2$  surface were mainly determined by the H-bonding attractions of the anions with the silanol groups. Likewise, molecular dynamics simulations of the two IL/graphite interfaces ( $[\text{BMIM}]^+[\text{PF}_6]^-$  and  $[\text{OMIM}]^+[\text{PF}_6]^-$ ) revealed dense regions of ILs adsorbed at the interface with density variations extending to  $\sim 1.5$  nm away from the graphite surface.<sup>11</sup> There was a tendency for the polar groups to aggregate forming a polar network, while the nonpolar groups filled up the rest of the vacancy. Atomistic simulations were also employed to study the IL 1-n-hexyl-3-methylimidazolium bis(trifluoromethylsulfonyl)amide ( $[\text{HMIM}]^+[\text{Tf}_2\text{N}]^-$ ) confined into carbon nanotubes (CNTs).<sup>12</sup> It was shown that the distribution of anions and cations within the CNTs was heterogeneous with cations adsorbed preferentially close to the CNT wall, and the anions located at the tube center. Furthermore, IL molecules in the CNT exhibited self-diffusivity coefficients about 1-2 orders of magnitude larger than the corresponding bulk IL.

These conflicting reports on the effect of confinement of ILs dynamics, reflect the different ion-wall interactions and the concomitant effects of density modulation near the surface. To exemplify this we plot in Scheme 1 three cases of surface-wall interactions in 2-D confinement (e.g. inside nanopores) that can lead to a reduction in the number of mobile ions. A positively (negatively) charged surface will attract anions (cations) thus reducing the number of mobile ions. On the other hand, a neutral pore surface will restore the ion mobility.



**Scheme 1.** Schematic of the effect of the AAO surface charge on the dc-conductivity of ILs. (a,b) Charged surface: ions are immobilized at the pore surface. (c) Neutral surface: all ions are mobilized and contribute to the dc-conductivity.

What are the relevant length scales affecting the transport of ions in nanochannels and in the presence of surfaces? First, the Bjerrum length between two point charges,  $l_B = e^2/4\pi\epsilon_0\epsilon k_B T$ , where  $e$  is the elementary charge,  $\epsilon_0$  the permittivity of free space and  $\epsilon$  the permittivity of the medium. It gives the characteristic separation between two ions at which Coulomb interactions are balanced by the thermal energy. For distances below  $l_B$ , electrostatic interactions dominate, whereas at longer distances thermal fluctuations prevail and effectively replace discrete ion-ion Coulomb forces with a mean-field. For ILs, typically  $\epsilon \sim 13$ , and at a temperature of 218 K,  $l_B \sim 6$  nm. Second, the Debye screening length, defined as  $\lambda_D = 1/\sqrt{(8\pi l_B C)}$  where  $C$  is the solution concentration, gives the ion-ion interactions. Beyond  $\lambda_D$ , electrostatic fields are “screened” due to the polarization of charges. For bulk ILs with  $l_B \sim 6$  nm, the Debye length is only 0.08 nm. Third, for charged surfaces the Gouy-Chapman length, defined as  $\lambda_{CG} = 1/2\pi l_B \sigma$ , where  $\sigma$  is the surface charge density. Employing  $\sigma \sim 0.1 \text{ nm}^{-2}$  results to a  $\lambda_{CG} \sim 0.27 \text{ nm}$ . The latter length scale dominates since it screens all other electrostatic interactions. Fourth, intrinsic length scales of self-assembly also related to stronger (Coulomb) and weaker (van der Waals) interactions typically in the range from 0.4 to 2 nm. Fifth, density fluctuations near the pore walls can influence ion-ion separation and dynamics. Lastly, all glass-forming systems have a length scale associated with their liquid-to-glass dynamics (typically in the range of 1-2 nm). All these length scales are smaller than the pore diameters usually explored in experiment but can affect charge transport (Scheme 1).

To address the effect of confinement on ion transport we employ nanodielectric spectroscopy (*nDS*).<sup>13-18</sup> The technique can provide simultaneous access to the kinetics of imbibition (*i.e.*, to penetration) and to the ion dynamics during and after flow. Nanopores here are provided by nanoporous alumina. Self-ordered nanoporous aluminum oxide (AAO) contains arrays of parallel cylindrical nanopores uniform in length and diameter that can easily be infiltrated.<sup>19,20</sup> An IL on the top surface of a template will penetrate the pores by capillary action. By recording the change in capacitance,  $C$ , we extract the complex dielectric permittivity ( $C \sim \epsilon^* = \epsilon' - i\epsilon''$ ), the complex conductivity ( $\sigma^* = \sigma' + i\sigma''$ ), and the complex electric modulus ( $M^* = \frac{1}{\epsilon^*} = i\omega\epsilon_0/\sigma^*$ ). These three parameter reflect the details of the ion dynamics *during* flow (e.g. *in situ*). In a recent investigation<sup>18</sup> we employed *nDS* to investigate the ion dynamics in the archetypal polymer electrolyte based on poly(ethylene oxide) (PEO) doped with lithium bis(trifluoromethane sulfone)imide (LiTFSI) during flow in nanopores. Overall, ion transport within AAO templates did not follow the bulk behavior as it was affected

by polymer adsorption. It was shown that ion motion was coupled to the polymer chains. The latter were transporting ions at the pore walls where there were immobilized thus reducing the ionic conductivity.

In this study we employ the same cation, 1-butyl-3-methylimidazolium ( $[\text{BMIM}]^+$ ), and six different anions ( $[\text{Cl}]^-$ ,  $[\text{Br}]^-$ ,  $[\text{I}]^-$ ,  $[\text{BF}_4]^-$ ,  $[\text{PF}_6]^-$  and  $[\text{TFSI}]^-$ ) with radii from 0.168 nm to 0.326 nm and investigate the structure, the thermodynamics and the ion dynamics in the bulk, during flow and under confinement in pores with sizes from 25 nm to 400 nm. Some ILs were prone to crystallization in the bulk during heating from lower temperatures. However, they were unable to crystallize in the smaller pores. This allowed us to construct the first effective phase diagrams of confined ILs. Measurements of the imbibition length revealed that the ILs penetrate the pores with an effective viscosity near their viscosity in the bulk state. Yet, the dc-conductivity was reduced revealing ion-wall interactions and the immobilization of ions at the pore surface. We explored the effect of surface treatment to show that conductivity can partially be restored by silinization. Overall, ILs are model systems where both the phase state and the ion mobility can be controlled by confinement.

### 3.2 Experimental

**Samples.** 1-Butyl-3-methylimidazolium bis(trifluoromethylsulfonyl)imide ( $[\text{BMIM}]^+[\text{TFSI}]^-$ ,  $\geq 98\%$ ), 1-Butyl-3-methylimidazolium bromide ( $[\text{BMIM}]^+[\text{Br}]^-$ , purity  $\geq 98,5\%$ ), 1-Butyl-3-methylimidazolium chloride ( $[\text{BMIM}]^+[\text{Cl}]^-$ , purity  $\geq 98\%$ ), 1-Butyl-3-methylimidazolium tetrafluoroborate ( $[\text{BMIM}]^+[\text{BF}_4]^-$ , purity  $\geq 98\%$ ), 1-Butyl-3-methylimidazolium hexafluorophosphate ( $[\text{BMIM}]^+[\text{PF}_6]^-$ ,  $\geq 98\%$ ), 1-Butyl-3-methylimidazolium iodide ( $[\text{BMIM}]^+[\text{I}]^-$ , purity  $\geq 99\%$ ) were purchased from Merck and used without further purification. The water content was extracted by  $^1\text{H-NMR}$  measurements in the non-dried and dried samples (Figures S1-S8, Supporting Information).

**Thermogravimetric analysis (TGA).** The thermal stability of the ILs was examined by TGA using a Mettler-Toledo TGA/SDTA851e. The temperature was increased from 303 to 873 K with a constant heating rate of  $10 \text{ K}\cdot\text{min}^{-1}$  under a nitrogen atmosphere. The TGA curves (**Figure S9**) show the loss of mass due to water evaporation especially in  $[\text{Cl}]^-$ ,  $[\text{Br}]^-$  and  $[\text{I}]^-$  ILs. Special care was taken when measuring the viscosity and ion conductivities for these particular samples (samples were stored under vacuum for 12 h at 373 K) and measurements were made in an inert atmosphere. Furthermore, the water content was measured by a Karl-Fischer titration method (C20, Mettler Toledo). The water content of the samples following

freeze-drying was below 0.06% (e.g. 0.06%, 0.02% and 0.02 % for  $[\text{BF}_4]^-$ ,  $[\text{PF}_6]^-$  and  $[\text{TFSI}]^-$ , respectively).

**AAO templates.** Self-ordered nanoporous aluminum oxide (AAO) templates (pore diameters of 25, 35, 65, 400nm; pore depth about 100  $\mu\text{m}$ ) with only one open end were prepared according to previously reported procedures.<sup>19-22</sup> The AAO layers were applied to 900  $\mu\text{m}$  thick aluminum substrates, which served as the bottom electrode. Prior to infiltration, all AAO templates were annealed in a vacuum oven at  $T = 423$  K for 10-12 h. This procedure removes the majority of OH groups from the AAO surface. AAO templates with both ends open were purchased from InRedox (Longmont). Pore diameters and the corresponding porosities were 100 nm ( $24 \pm 5\%$ ), 40 nm ( $12 \pm 4\%$ ), and 20 nm ( $11 \pm 5\%$ ), respectively, as determined by SEM measurements (**Figure S10**). These values are different from the ones provided by the manufacturer. The pore length was 100  $\mu\text{m}$  in agreement with the manufacturer value.

**Inner pore silanization.** For this modification, hexamethyldisilazane (HMDS) (purity  $\geq 99.0\%$ , purchased from Sigma-Aldrich) was injected into the chamber containing the AAOs at 350 K and the AAOs were completely submerged. After 30 min, due to the volatility of the HMDS, the chamber with AAOs was under pressure and kept it at 350 K for 3 h. By treating the membrane with HMDS, -OH groups were replaced with trimethylsilyl groups. Consequently, this made the inner surface hydrophobic.

**Differential Scanning Calorimetry (DSC).** A Mettler Toledo differential scanning calorimeter (DSC-822) was used for the thermal analysis. The glass temperatures of the ionic liquids were obtained from the second heating run at a rate of  $10 \text{ K}\cdot\text{min}^{-1}$ . DSC traces of bulk ILs were acquired using an empty pan as reference. Samples were weighed using a Mettler Toledo AX205 balance. 3–7 mg of sample was sealed in aluminum pans (100  $\mu\text{L}$ ). All samples were heated to 373 K under a nitrogen atmosphere to remove any thermal history. The same cycle was repeated twice. The melting, crystallization and the glass temperatures were determined from the second heating and cooling thermograms, respectively.

**Dielectric spectroscopy (DS).** Dielectric spectroscopy and in situ nanodielectric spectroscopy (nDS) were employed to follow the dynamics of bulk and confined ILs. In both cases, a Novocontrol Alpha frequency analyzer, consisting of a broadband dielectric converter and an active sample head was used. For bulk samples, the ILs were embedded between two stainless steel electrodes with a diameter of 20 mm accompanied by a 250  $\mu\text{m}$  Teflon spacer to maintain a constant thickness. For confined samples, a gold layer (diameter 8.4 mm; thickness 35 nm) was sputtered onto the AAO template, which served as the top electrode, while the aluminum

substrate of the AAO templates served as the bottom electrode. Sputtering was performed under vacuum (less than  $2 \times 10^{-5}$  Pa) using a Bal-tec MED 020 with a current density of 40 mA. IL was then deposited on the top of the AAO template (Figure 1). A broad frequency range from  $10^{-2}$  to  $10^7$  Hz was employed for the bulk DS measurements. From the measured impedance,  $Z^*(\omega)$ , the dielectric and conductivity functions are calculated, respectively, as  $\varepsilon^*(\omega)=1/(i\omega Z^*(\omega)C_0)$  and  $\sigma^*(\omega)=d/Z^*(\omega)A$ , where  $C_0$  is the vacuum capacitance, and  $d$ ,  $A$  the sample thickness and electrode area, respectively. For a typical capacitance of  $\sim 100$  pF, and within the frequency range 0.1 to  $10^6$  Hz, the absolute accuracy of the loss factor is  $\tan\delta \sim 3 \times 10^{-5}$ . In contrast, a narrower frequency range, from 10 to  $10^6$  Hz, was required to study the imbibition kinetics by nDS. The complex conductivity function,  $\sigma^* = \sigma' + i\sigma''$ , where  $\sigma'$  and  $\sigma''$  are the real (*i.e.*, the dc-conductivity) and imaginary parts, respectively, was obtained from the impedance measurements. The plateau in the real part  $\sigma'$  was used to extract the dc-conductivity. We have recently shown that nDS can be employed to follow the increase in the imbibition length<sup>13,18</sup> of a substance by monitoring the increase of conductivity during and after flow in AAO.<sup>13,18</sup> Briefly, we can assume a simple Debye model that includes the conductivity term to simulate the frequency dependence of complex conductivity as  $\sigma^*(\omega) = \sigma'(\omega) + i\sigma''(\omega) = i\omega\varepsilon_0\varepsilon^*(\omega)$ ,

$$\sigma'(\omega) = \omega\varepsilon_0\varepsilon''(\omega) = \sigma_{dc} + \frac{\omega^2\tau\varepsilon_0\Delta\varepsilon}{1 + (\omega\tau_D)^2} \quad (1)$$

$$\sigma''(\omega) = \omega\varepsilon_0\varepsilon'(\omega) = \omega\varepsilon_0\left(\varepsilon_\infty + \frac{\Delta\varepsilon}{1 + (\omega\tau_D)^2}\right) \quad (2)$$

Here,  $\Delta\varepsilon$  is the dielectric strength,  $\varepsilon_\infty$  is the dielectric permittivity in the limit of very high frequencies,  $\tau_D$  is the characteristic relaxation time, and  $\sigma_{dc}$  is the IL conductivity. A parallel model best describes the total equivalent capacitance (Figure 1), comprising the capacitance of the IL ( $C_1$ ) and air ( $C_2$ ) connected in series, whereas the combined IL/air capacitance ( $C_{12}$ ) connects in parallel with the AAO ( $C_3$ ). Therefore,

$$\frac{1}{C_{12}} = \frac{1}{C_1} + \frac{1}{C_2}, \text{ and } C_{123} = C_{12} + C_3 \quad (3)$$

By employing the above equations and the definition  $\sigma_{123}^* = i\omega\varepsilon_0\varepsilon^*$ , results to:

$$\sigma_{123}^* = \sigma' + i\sigma'' = \left\{ \left[ \frac{Ld_1\sigma_1'(\omega\varepsilon_0)^2}{(d_2\sigma_1')^2 + (d_1\omega\varepsilon_0 + d_2\sigma_1'')^2} \right] \varphi_{12} + \sigma_3' \varphi_3 \right\} + i \left\{ \left[ \frac{L[d_2[(\sigma_1')^2 + (\sigma_1'')^2]\omega\varepsilon_0 + \sigma_1''(\omega\varepsilon_0)^2 d_{11}}{(d_2\sigma_1')^2 + (d_1\omega\varepsilon_0 + d_2\sigma_1'')^2} \right] \varphi_{12} + \sigma_3'' \varphi_3 \right\} \quad (4)$$

In the above equation  $\varphi$  gives the porosity. We can employ typical values for the real and imaginary parts of the AAO complex conductivity (e.g.  $\sigma_3' = \sigma_{AAO}' = 10^{-10}$  S cm<sup>-1</sup> and  $\sigma_3'' = \sigma_{AAO}'' = 10^{-8}$  S cm<sup>-1</sup>) and typical values for the bulk IL to show that a conductivity plateau (dc-conductivity) only arises when the pores are fully infiltrated by the IL (**Figure S11**). The use of the Debye model above is the simplest one that, nonetheless, provides valuable information of the evolution of conductivity.

**X-ray diffraction.** The  $\Theta/2\Theta$  scans were taken with a Rigaku SmartLab X-ray diffractometer. The X-ray source was a rotating anode (Cu) operating at a voltage of 45 kV and a current of 200 mA. The incident optics employed a monochromator (Ge crystal for the 220 reflection) followed by a parallel slit (incident Soller slit 2.5<sup>0</sup>). A diffracted beam monochromator was inserted between the detector slit and the detector to suppress fluorescence radiation and the unwanted K <sub>$\beta$</sub>  radiation. The receiving optics had a parallel slit analyzer (PSA) followed by a receiving Soller slit. The wavelength was 0.154059 nm. A HyPix-3000 2D detector was used (pixel size 100  $\mu$ m  $\times$  100  $\mu$ m; active area 38.5 mm  $\times$  77.5 mm). Scans in the 2 $\Theta$ -range from 1 to 60<sup>0</sup> in steps of 0.01<sup>0</sup> were made at ambient temperature.

**Reflection Optical Microscopy.** The top layer was removed, the AAO templates were cross sectioned and the imbibition length was determined from the cross sections by reflection optical microscopy (ROM) (Zeiss AxioTech vario). As the ILs penetrate the pores they increase the refractive index as compared to the unfilled parts creating optical contrast that is detected from the changing reflectance.

**Surface Tension.** The Wilhelmy plate method<sup>23</sup> was employed to measure the surface tension of all ILs (**Figure S12**). A rod-like platinum-iridium plate with a diameter of 1.2 mm was vertically placed into the IL. The liquid had a contact angle of around 0<sup>0</sup> on the platinum-iridium rod surface. The surface tension exerted a downward force ( $F$ ), which was measured with a tension meter (DCAT 11BC, DataPhysics). The surface tension ( $\gamma$ ) was then calculated from  $F = l\gamma$ , where  $l$  is the circumference of the rod-like plate.

**Contact Angle.** The apparent contact angles<sup>24</sup> of the ILs were measured by placing a drop onto an electropolished Al disk coated by a thin native oxide layer (**Figure S13**). The latter

comprises a flat model surface that mimics the AAO surface. The contact angle was measured at 303 K with a commercial goniometer (OCA35, DataPhysics) and evaluated with the software IDS uEye.

**Rheology.** Prior to the viscosity measurements, all samples were stored under vacuum for 12 h at 373 K. Viscosities were measured using a Bohlin Instruments Gemini 200 rheometer (Malvern Panalytical Ltd., Malvern, UK). The instrument had a torque resolution of  $10^{-9}$  N·m and an angular resolution of  $5 \times 10^{-8}$  rad. It was calibrated with a Brookfield#1000 oil (Lot#062185) having a viscosity of 0.995 Pa·s at 298 K. Samples were prepared on the lower plate of the 25 mm diameter parallel plate geometry and the sample thickness was around 1 mm. Phosphorus pentoxide ( $P_2O_5$ , purchased from Merck) was used within a closed chamber near the sample in order to absorb water from the environment. The zero shear viscosities were measured at 303 K as a function of the shear rate in the range from  $10^{-3}$  to  $10^2$   $s^{-1}$ . Respective values for the  $[BMIM]^+[Cl]^-$ ,  $[BMIM]^+[Br]^-$ ,  $[BMIM]^+[I]^-$ ,  $[BMIM]^+[BF_4]^-$ ,  $[BMIM]^+[PF_6]^-$ , and  $[BMIM]^+[TFSI]^-$  were  $3.24 \pm 0.02$ ,  $1.84 \pm 0.02$ ,  $0.65 \pm 0.01$ ,  $0.066 \pm 0.002$ ,  $0.17 \pm 0.01$ , and  $0.040 \pm 0.002$  Pa·s, all measured at 303 K. The values reported here are the same (e.g.  $[BMIM]^+[TFSI]^-$ ) or somewhat lower than literature viscosity data.<sup>25-28</sup> In addition, for  $[BMIM]^+[BF_4]^-$ , the zero shear viscosity was measured as a function of temperature within the range 193-303 K. In this case, a Discovery HR-3 rheometer (TA Instruments) was used. The rheometer was equipped with a magnetic bearing that allowed for nano-torque control (torque resolution  $0.05 \times 10^{-9}$  N·m, displacement resolution  $2 \times 10^{-9}$  rad). The instrument was calibrated with two viscosity standards (Brookfield#1000 oil and a PDMS#17BWFA060-A with frequency and modulus data at the crossing of the real and imaginary parts, respectively, of  $5.964$  rad/s  $\pm 5\%$  and  $2.6109 \times 10^4$  Pa  $\pm 8\%$ ). Measurements were performed with an environmental test chamber (ETC). Temperature control was achieved through a nitrogen convection oven. The sample was prepared on the lower rheometer plate (8 mm) and the upper plate was adjusted to ensure a uniform gap thickness. Data of complex shear modulus as a function of frequency were obtained by frequency sweeps into the range of 0.1 – 100 rad·s<sup>-1</sup> for several temperatures.

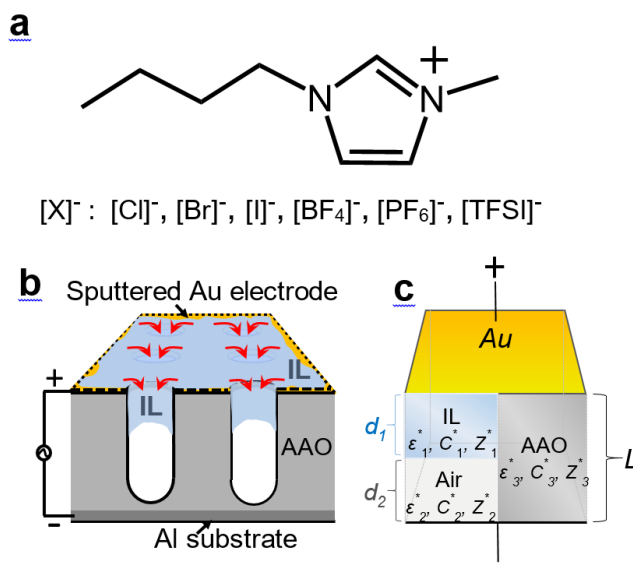


**Figure 1.** (a) Schematic of the chemical structure of the ILs bearing the 1-butyl-3-methylimidazolium cation and six different anions. (b) Experimental setup of in situ  $nDS$ . (c) The equivalent capacitor circuit.

### 3.3 Results and discussion

#### ILs in the bulk

The thermodynamic properties of the ILs are affected by the strength of electrostatic interactions and hence by the charge delocalization and the size and symmetry of anions. These characteristics are influencing the DSC traces (Figure 2). The cooling traces (with a rate of  $10 \text{ K}\cdot\text{min}^{-1}$ ) exhibit a liquid-to-glass temperature that is a function of anion size. Among the different anions,  $[Cl]^-$  with the smallest radius has the higher glass temperature,  $T_g$ , reflecting the proximity of ions and the stronger electrostatic interactions.  $[Br]^-$ , bearing the second smallest size has the second highest  $T_g$ . Based on the ionic radii alone one would expect that the largest anion ( $[TFSI]^-$ ) would have the lowest  $T_g$ . However, it is  $[BF_4]^-$  with an intermediate radius that has the lowest  $T_g$ . An additional feature can be seen in the cooling trace of  $[PF_6]^-$ . A weak exothermic peak ( $\Delta H=0.83 \text{ J}\cdot\text{g}^{-1}$ ) is evident at  $\sim 215 \text{ K}$ . This peak is present at the same temperature for different cooling rates (**Figure S14**). On heating, some ILs exhibit cold crystallization and melting peaks. The respective heats and actual temperatures are summarized in **Table 1**. Depending on the cooling/heating rates all ILs were prone to cold crystallization with the exception of  $[BMIM]^+[BF_4]^-$  that was completely amorphous. We discuss the phase behavior of  $[BMIM]^+[BF_4]^-$  separately.

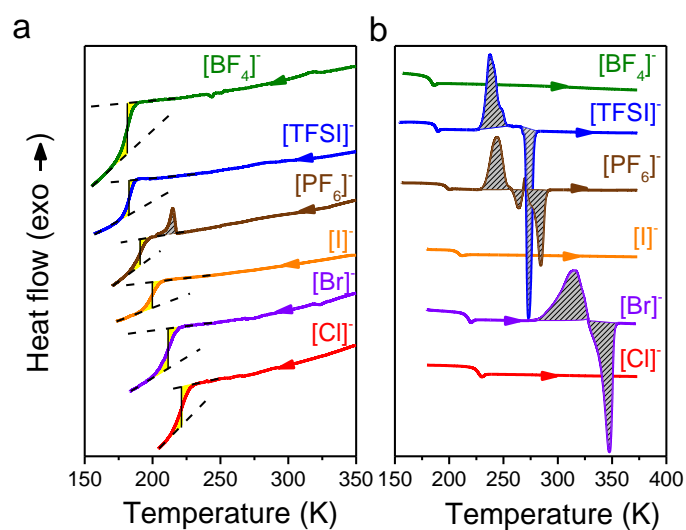


**Figure 2.** DSC traces of imidazolium-based ionic liquids with different anion species:  $[\text{BF}_4]^-$  (olive),  $[\text{TFSI}]^-$  (blue),  $[\text{PF}_6]^-$  (brown),  $[\text{I}]^-$  (orange),  $[\text{Br}]^-$  (purple),  $[\text{Cl}]^-$  (red). Traces are obtained from the cooling (a) and subsequent heating (b) run with a rate of  $10 \text{ K}\cdot\text{min}^{-1}$ .

**Table 1.** Ionic radii, glass temperatures, crystallization and melting temperatures and corresponding enthalpies obtained from DSC (rate  $10 \text{ K}\cdot\text{min}^{-1}$ ).

$[\text{X}]^-$	Radius (nm) <sup>29,30</sup>	$T_g^{\text{DSC}}$ (K)	$\Delta T_g^{\text{DSC}}$ (K)	$T_{\text{cc}}$ (K)	$\Delta H_{\text{cc}}$ ( $\text{J}\cdot\text{g}^{-1}$ )	$T_{\text{m1}}$ (K)	$\Delta H_{\text{m1}}$ ( $\text{J}\cdot\text{g}^{-1}$ )	$T_{\text{m2}}$ (K)	$\Delta H_{\text{m2}}$ ( $\text{J}\cdot\text{g}^{-1}$ )
$[\text{Cl}]^-$	0.168	222±2	21	--	--	--	--	--	--
$[\text{Br}]^-$	0.19	212±2	23	315	76.8	347	70.2	--	--
$[\text{BF}_4]^-$	0.205	181±2	22	--	--	--	--	--	--
$[\text{I}]^-$	0.211	200±2	16	--	--	--	--	--	--
$[\text{PF}_6]^-$	0.242	191±2	17	243	36.7	264	6.05	284	32
$[\text{TFSI}]^-$	0.326	183±2	13	238	46.7	274	56.6	--	--

The local structure of the  $[\text{BMIM}]^+[\text{X}]^-$  can be examined by X-ray diffraction. ILs are known to be structurally heterogeneous. Usually they exhibit three peaks.<sup>31-33</sup> At longer range

there exists nanophase separation between polar and apolar groups giving rise to a smectic-like layering. At intermediate distances, the scattering from the different form factors of the cation and the anions give rise to the charge alteration peak. At shorter distances, the nearest proximity of atoms gives rise to the van der Waals peak. The diffraction patterns from the present ILs are compared in Figure 3. Arrows 1, 2 and 3 indicate respectively, the smectic layering of polar-apolar groups, the charge alteration peak and the van der Waals peak of nearest neighbors. Figure 3b compares the characteristic spacings (obtained as  $d=2\pi/q$ ) corresponding to the period of smectic layering ( $d_1$ ), the charge alteration distances ( $d_2$ ) and the nearest approach of atoms ( $d_3$ ). The period of smectic layering ( $d_1$ ) corresponds roughly to the summation of radii of the cation and the anion. The charge alteration distance is given by the sum of radii of the imidazolium ring and the anion ( $0.41+R^-$ ). The van der Waals peak has a weaker dependence on the ionic radii. The local organization in the ILs is shown in a highly schematic representation in Figure 3c.

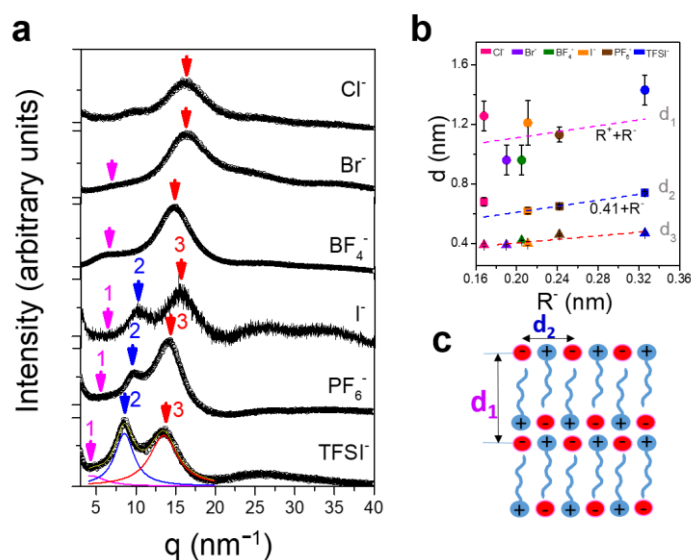


**Figure 3.** (a) XRD curves of the [BMIM]<sup>+</sup>[X]<sup>-</sup> with the different anions at ambient temperature. Arrows 1, 2 and 3 indicate respectively, the smectic layering of polar-apolar groups, the charge alteration peak and the van der Waals peak of nearest neighbors. Red, blue and magenta lines are the respective component contributions to the scattering curve for [TFSI]<sup>-</sup>. (b) Characteristic spacings (obtained as  $d=2\pi/q$ ) corresponding to the period of smectic layering ( $d_1$ ), the charge alteration distances ( $d_2$ ) and the nearest approach of atoms ( $d_3$ ). Magenta dashed line is not a fit but gives the sum of ionic radii; Blue dashed line is not a fit but a line calculated as  $0.41+R^-$  corresponding to the sum of radii of the imidazolium ring and the anion. The red dashed line is a linear fit to  $d_3$ . (c) Schematic representation of the correlation distances.

These structural features are expected to influence the dc-conductivity of the ILs. The dc-conductivity is extracted as shown in **Figure S15**. The Figure depicts the real and imaginary parts of the complex conductivity function,  $\sigma^*(\omega)$ , as a function of the frequency for a range of temperatures. At intermediate frequencies, the  $\sigma'(\omega)$  curves exhibit a plateau associated with the dc-conductivity that separates the high-frequency region associated with the ac-conductivity from the low-frequency dispersion associated with electrode polarization. The  $\sigma^*(\omega)$  curves are self-similar and obey scaling with the characteristic angular frequency  $\omega^*$  ( $=2\pi f^*$ ) associated with the onset of ac-conductivity. The dc-conductivity can be extracted either from the random barrier model (RBM)<sup>34,35</sup> or directly from the plateau.<sup>36,37</sup> The thus obtained dc-conductivity values for the different anions are plotted as a function of inverse temperature in Figure 4a on cooling and in Figure 4b on subsequent heating. For the [BMIM]<sup>+</sup>[BF<sub>4</sub>]<sup>-</sup> and [BMIM]<sup>+</sup>[TFSI]<sup>-</sup> ILs the agreement with literature conductivity data is good.<sup>8,38</sup> At a fixed temperature, conductivities can differ by several orders of magnitude. This reflects the distinctly different  $T_g$  of the ILs. With the exception of [PF<sub>6</sub>]<sup>-</sup> that crystallizes on cooling at  $\sim 243$  K, in all ILs the  $\sigma'_{dc}(T)$  dependencies obtained on cooling follow the Vogel-Fulcher-Tammann (VFT) equation written for the conductivity contribution as:

$$\sigma_{dc}(T) = \sigma_0^\# \exp\left(-\frac{B}{T-T_0}\right) \quad (5)$$

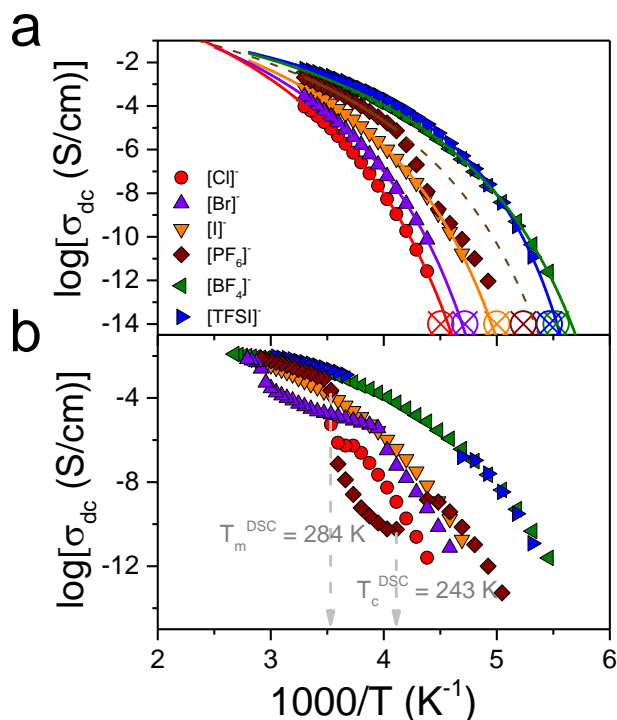
Here,  $\sigma_0^\#$  is the dc-conductivity in the limit of very high temperatures,  $B$  is the activation parameter and  $T_0$  is the “ideal” glass temperature (the parameters are summarized in **Table 2**, below). We note that the crystallization and cold-crystallization temperatures of [BMIM]<sup>+</sup>[PF<sub>6</sub>]<sup>-</sup> differ from the ones in DSC (in DSC [PF<sub>6</sub>]<sup>-</sup> undergoes cold crystallization at 230 K at 1 K/min) because of the different rates employed.

Figure 4 includes the estimated conductivity value at  $T_g$  as obtained from the Nernst-Einstein equation:

$$\sigma_{DC} = \frac{ne^2 \left(\frac{d_2}{2}\right)^2}{k_B T \cdot 6\tau} \quad (6)$$

Here,  $e$  is the elementary charge,  $n = \frac{\rho N_A}{M}$ , is the number density,  $\rho = 1.2 \text{ g}\cdot\text{cm}^{-3}$  is the mass density applicable to [BMIM]<sup>+</sup>[BF<sub>4</sub>]<sup>-</sup>,  $M = M_W^{cation} + M_W^{anion}$  is the molar mass (226.02 g·mol<sup>-1</sup> in the case of [BMIM]<sup>+</sup>[BF<sub>4</sub>]<sup>-</sup>),  $d_2/2$  is the distance between two adjacency ions of opposite charge extracted from Figure 3,  $\tau$  is the characteristic structural relaxation time at  $T_g$

and  $k_B$  is the Boltzmann constant. Using  $d_2/2 \sim 0.3$  nm and  $\tau = 10^2$  s in Eq. 6 results to  $\sigma_{dc} \sim 10^{-14}$  S·cm<sup>-1</sup>. On heating, a single VFT cannot describe the conductivity due to the discontinuous changes at the crystallization/melting. We will employ the corresponding temperatures later in constructing the effective phase diagrams.



**Figure 4.** Dc-conductivity of imidazolium-based ionic liquids with different counteranions upon the (a) first cooling, and (b) subsequent heating (b). (a) Crossed symbols are liquid-to-glass temperatures obtained from DSC and the use of Nernst-Einstein relation. Solid lines are fits to the VFT equation for the conductivity. [PF6]<sup>-</sup> undergoes weak crystallization on cooling at 243 K, hence the VFT was employed only at higher temperatures. (b) Discontinuities reflect cold crystallization and melting processes (more evident on heating [PF6]<sup>-</sup> and [TFSI]<sup>-</sup>). Arrows at temperatures 243 K and 284 K refer to the crystallization and melting of [PF6]<sup>-</sup>. Data obtained on heating are tabulated in Table S1.

**Table 2. Parameters of the VFT equation for the conductivity obtained on cooling.  $T_g$  as obtained from DSC is also shown for comparison.**

IL	$\sigma_0^\#/(S \cdot cm^{-1})$	$B$ (K)	$T_0$ (K)	$T_g^{DS}$ (K) (at $\sigma = 10^{-14}$ S/cm)	$T_g^{DSC}$ (K)
[BMIM] <sup>+</sup> [Cl] <sup>-</sup>	467.1	$2134 \pm 63$	$163 \pm 1$	$219 \pm 1$	$222 \pm 2$
[BMIM] <sup>+</sup> [Br] <sup>-</sup>	79.4	$1722 \pm 25$	$166 \pm 1$	$212 \pm 1$	$212 \pm 2$
[BMIM] <sup>+</sup> [I] <sup>-</sup>	28.2	$1536 \pm 23$	$159 \pm 1$	$202 \pm 1$	$200 \pm 2$

[BMIM] <sup>+</sup> [BF <sub>4</sub> ] <sup>-</sup>	6.9	1199 ± 23	142 ± 1	176 ± 1	181 ± 2
[BMIM] <sup>+</sup> [PF <sub>6</sub> ] <sup>-</sup>	14.1*	1328*	149 ± 1	186 ± 1	191 ± 2
[BMIM] <sup>+</sup> [TFSI] <sup>-</sup>	2.6	915 ± 18	153 ± 1	181 ±± 1	183 ± 2

\*Value held fixed

The dc-conductivity in the completely amorphous [BMIM]<sup>+</sup>[BF<sub>4</sub>]<sup>-</sup> requires some attention. A single VFT dependence on cooling or heating can only approximately describe the  $\sigma_{dc}(T)$  dependence (**Figure S16**). A first derivative analysis with respect to inverse temperature reveals deviations from a single VFT behavior at lower temperatures.<sup>39</sup> In this case, a second VFT can be used for temperatures below 200 K. Such deviations may arise from a liquid-to-liquid (LLT) transition. The existence of the LLT implies the coexistence of two competing liquid states in the IL. Recent efforts in some ILs revealed that the dynamic transition is accompanied by an enthalpic peak at the LLT temperature.<sup>40,41</sup> Since such a peak is absent in [BMIM]<sup>+</sup>[BF<sub>4</sub>]<sup>-</sup> (Figure 2a) we conclude that the liquid-to-liquid transition is very weak.

The degree of ion association, and in particular, ion pairing in ILs is a highly debated concept. Molecular dynamics (MD) simulations show that the lifetime of ion pairs in ILs and their jointly motions are too short to verify the existence of “neutral pairs”.<sup>42</sup> MD simulations further suggest cation-anion motional coupling (the cation-anion velocities are anti-correlated) as dictating the conductivity.<sup>43</sup> Nonetheless, one has to explain a 2-fold change in viscosity and conductivity and a 40 K change in  $T_g$  by anion size. This can be discussed with the help of Figure 5. Viscosity is largely controlled by  $T_g$  which in turn is influenced by the strength of electrostatic interactions. For example, [Cl]<sup>-</sup> with the smallest radius and the closest approach to the cation has the strongest electrostatic attraction. For monovalent charge carriers, the electrostatic energy is  $E_C = e^2/4\pi\epsilon_0\epsilon r_c$ , where  $r_c$  is the distance separating a point-like cation from a point-like anion. Because of this association the anion and the cation exhibit slower rotation and translation motions and thus freeze at a higher temperature. At the same time, the stronger ion-ion association reduces the dc-conductivity. Indeed, [Cl]<sup>-</sup> exhibits the lowest conductivity when examined at a fixed temperature. In line with this argument, [TFSI]<sup>-</sup> ions with the largest ionic radius and the weakest ion-ion interactions showed a high dc-conductivity can now move independently, freeze at a lower (glass) temperature and exhibit the highest conductivity. In addition, the product  $\sigma \times \eta$  follows an approximate  $R^{-1}$  dependence as  $\sigma = ne^2/6\pi\eta R$ . There is also some exception to these observations. [BF<sub>4</sub>]<sup>-</sup> with a radius comparable

to [I]<sup>-</sup> exhibits lower viscosity, lower  $T_g$  and a higher dc-conductivity, not in line with the rest of the ions, suggesting that other factors (anion shape and charge distribution) plays also a role.

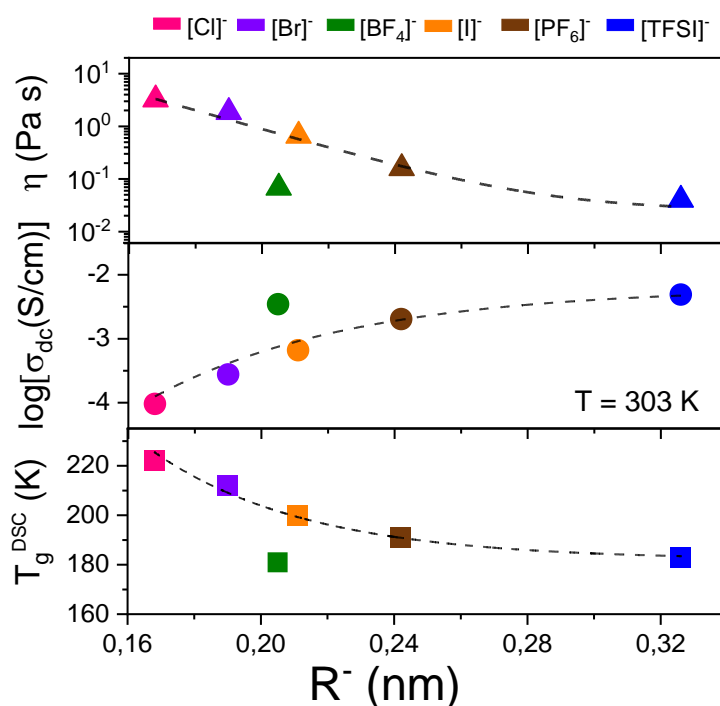


**Figure 5.** Measured viscosity (top), dc-conductivity (middle), both at 303 K, and glass temperature of the [BMIM]<sup>+</sup>[X]<sup>-</sup> as a function of anion radius. Dashed lines are to guide the eye.

## ILs in confinement

The imbibition of the ILs in AAO is fast due to their low viscosity. According to the Lucas-Washburn equation<sup>44,45</sup> the penetration length increase with time  $t$  as  $\propto t^{1/2}$  dependence as:  $L = \left(\frac{\gamma d \cos\theta}{4\eta}\right)^{1/2} \sqrt{t}$ , where  $\gamma$  is the surface tension,  $\theta$  is the contact angle,  $\eta$  is the viscosity and  $d$  the pore diameter. To test this we have employed [BMIM]<sup>+</sup>[Cl]<sup>-</sup> and measured the imbibition length within for AAO templates with pore sizes of 100 nm, 40 nm and 20 nm at ambient temperature by reflection optical microscopy. The results are shown in Figure 6. The imbibition lengths follow the  $t^{1/2}$  dependence; a typical dependence for a process that is fast at the beginning and slower at the end. For [BMIM]<sup>+</sup>[Cl]<sup>-</sup>, the extracted effective viscosity (using  $\cos\theta = 0.55$  and  $\gamma_L = 40$  mN/m applicable to 303 K) is somewhat lower than in bulk. Similar results were obtained for [BMIM]<sup>+</sup>[PF<sub>6</sub>]<sup>-</sup> within 20 nm pores (**Figure S17**). There, a viscosity of the liquid in the bulk adequately describes the penetration length. On the other hand, the imbibition of [BMIM]<sup>+</sup>[BF<sub>4</sub>]<sup>-</sup> was too fast to be well resolved due to its low viscosity.

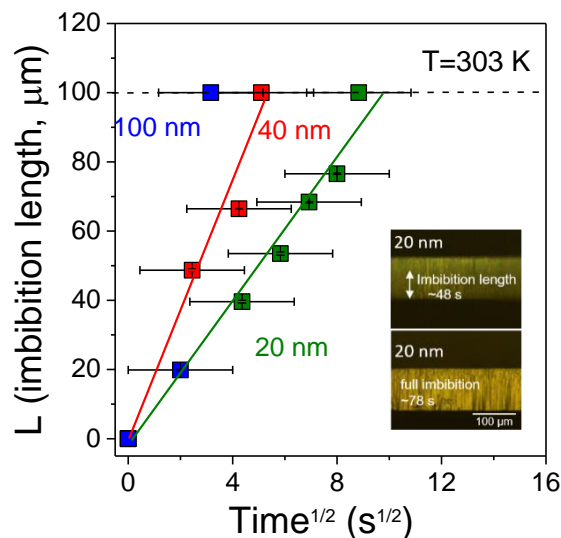


**Figure 6.** Imbibition lengths extracted via reflection optical reflection microscopy at selected times for  $[\text{BMIM}]^+[\text{Cl}]^-$  inside AAOs of different pore size at 303 K: (blue) 100 nm, (red) 40 nm, (green) 20 nm. Lines represent the result of a linear fit. The inset gives ROM images depicting cross-sections of AAO templates, 20 nm in diameter, at different infiltration times. The white arrow gives the imbibition length for the given time.

Subsequently, we followed the imbibition process *in situ* by *nDS* by recording the evolution of the ionic conductivity. Typically, at the beginning of the imbibition process there is no plateau in ionic conductivity (**Figure S11**). The plateau appears after the full imbibition by the IL (Figure 7). Following the full imbibition, the value of dc-conductivity remains constant for all pores investigated. However, the conductivity values are consistently lower than the bulk (indicated in the Figure with the dashed line).

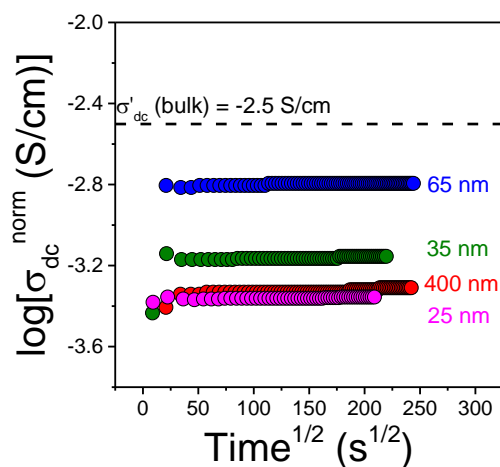


**Figure 7.** Evolution of dc-conductivity during imbibition of  $[\text{BMIM}]^+[\text{BF}_4]^-$  within AAO templates with different pore sizes at 303 K. The conductivity values were corrected for porosity. The dashed line indicates the dc-conductivity for the bulk IL at the same temperature.

To explore the origin of the conductivity reduction we performed cooling/heating scans after imbibition. The results for the dc-conductivity, as well as for the relaxation times, the latter extracted from the modulus representation (**Figure S15**), for the completely amorphous [BMIM]<sup>+</sup>[BF<sub>4</sub>]<sup>-</sup> are plotted in Figure 8. In all cases the  $\sigma_{dc}(T)$  dependence follows the VFT equation with parameters summarized in **Table 3**. The results reveal a lower dc-conductivity than the bulk for all pore diameters. At this point we should mention that the electrostatic properties of the native AAO pore walls are hardly accessible. First of all, the pore walls normal to the pore axes are not homogeneous, so that pore widening by isotropic etching changes the nature of the exposed pore walls. The AAO pore walls consist of an outer oxide containing layer, electrolyte anions etc. and a purer inner oxide (for templates prepared via phosphoric acid). Moreover, the history of the samples will play a role. In retrospect, the conductivity data may be used to characterize the AAO pore walls.

To further explore this possibility we have silanized the pores with HMDS and subsequently followed the imbibition process with *n*DS. The result of this procedure for the [BMIM]<sup>+</sup>[BF<sub>4</sub>]<sup>-</sup> is shown in Figure 9. The figure depicts an increased conductivity relative to the untreated pores. Yet, the bulk dc-conductivity is not fully recovered. This is attributed to the incomplete surface silanization. Another scenario, namely, that the pores are lubricated by the IL only at the walls and not at the pore center can be excluded on the basis of the simulation of dc-conductivity during imbibition (Fig. **S11**) revealing that the conductivity plateau requires the full imbibition of the IL.

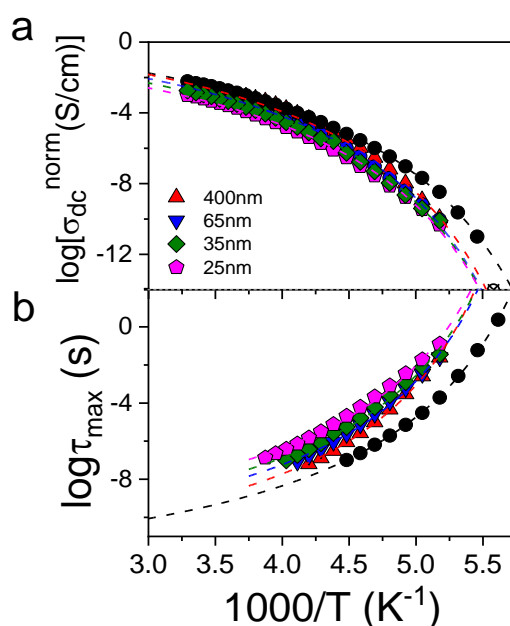


**Figure 8.** (a) Temperature dependence of the dc-conductivity for bulk and confined [BMIM]<sup>+</sup>[BF<sub>4</sub>]<sup>-</sup> following the imbibition experiments. The dashed line represent VFT fits. (b) Characteristic time of ion relaxation extracted from the maximum of the modulus representation as a function of the reciprocal of temperature.

**Table 3.** Parameters of the VFT equation for [BMIM]<sup>+</sup>[BF<sub>4</sub>]<sup>-</sup> pertinent to the temperature scan experiments following imbibition.

Pore diameter, $d$ (nm)	$-\log_{10}(\tau_0/s)$	$B^\tau$ (K)	$T_0^\tau$ (K)	$\log_{10}[\sigma/(\text{S}\cdot\text{cm}^{-1})]$	$B^\sigma$ (K)	$T_0^\sigma$ (K)
bulk	12.2	$919 \pm 10$	$147 \pm 1$	0.71	$1080 \pm 18$	$143 \pm 1$
25	10.5	$919^a$	$153 \pm 2$	0.05	$1080^a$	$149 \pm 1$
35	11	$919^a$	$153 \pm 1$	0.24	$1080^a$	$149 \pm 1$
65	11.3	$919^a$	$153 \pm 1$	0.49	$1080^a$	$150 \pm 1$
400	11.9	$919^a$	$155 \pm 1$	0.71	$1080^a$	$149 \pm 1$

<sup>a</sup>Value held fixed.

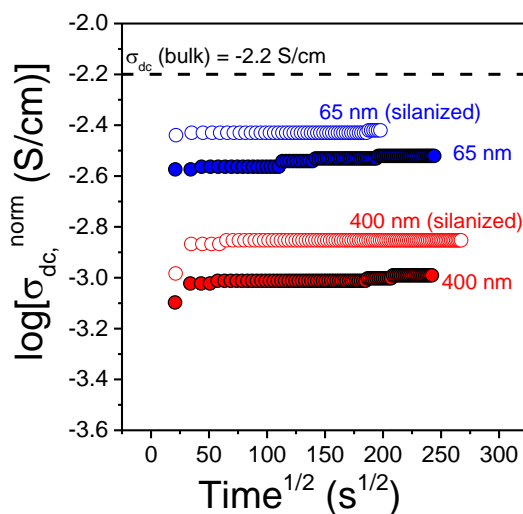


**Figure 9.** Evolution of the normalized dc-conductivity for [BMIM]<sup>+</sup>[BF<sub>4</sub>]<sup>-</sup> in native and silanized AAO pores at 303 K. The conductivity of the IL in the silanized AAO increases relative to native pores but remains lower than the bulk (dashed line).

The results of the imbibition process, and in particular of the temperature scans after imbibition, can be used to construct "effective" phase diagrams for the confined ILs. The [BMIM]<sup>+</sup>[BF<sub>4</sub>]<sup>-</sup> is amorphous in the bulk and under confinement. Corresponding "effective" phase diagrams for crystallizable ILs are shown in Figure 10 for [BMIM]<sup>+</sup>[TFSI]<sup>-</sup> and

[BMIM]<sup>+</sup>[PF<sub>6</sub>]<sup>-</sup>. In this case the dc-conductivity was considered together with DSC. Discontinuous decrease (increase) in dc-conductivity revealed crystallization (melting) processes. In 25 nm pores, crystallization was completely suppressed. For [BMIM]<sup>+</sup>[TFSI]<sup>-</sup> and [BMIM]<sup>+</sup>[PF<sub>6</sub>]<sup>-</sup> there was no hint for crystallization in the smaller pores during cooling/heating runs (**Figure S18** and **Figure S19**). This situation is very different from the bulk ILs. Effectively, suppression of crystallization leads to an increase in ionic conductivity by several orders of magnitude relative to bulk with promising applications. In addition, it suggests that the critical nucleus needed for the formation of the crystal phase is of the order of the smallest pore size. Similar effects have been reported earlier when liquid crystals<sup>46</sup> and semicrystalline polymers<sup>47,48</sup> were confined within the same AAO templates.

Another feature of the phase behavior is the dependence of the apparent melting temperature on inverse pore diameter. The melting temperature of the ILs decreases with confinement following the known Gibbs-Thomson equation as:<sup>49,50</sup>

$$T_m = T_m^{bulk} \left( 1 + \frac{2M}{\Delta_{fus}H \rho_s r} \sigma_{sl} \cos\theta \right) \quad (7)$$

Here,  $T_m^{bulk}$  is the melting temperature of bulk ILs,  $M$  is the molar mass,  $\Delta_{fus}H$ ,  $\rho_s$  is the molar enthalpy of fusion and the density, respectively,  $r$  is the radius of the crystal (in this case we assume that it is the radius of AAO pores,  $d/2$ ),  $\sigma_{sl}$  is the interfacial energy between the solid-liquid interface (*i.e.* between the IL crystal and the surrounding fluid), and  $\theta$  is the contact angle of the crystal and the contacting surface. Here, we make the usual assumption for the absence of wetting of the alumina surface by the crystals, *i.e.*  $\theta = 180^\circ$  for the contact angle at the solid-liquid interface. Based on this assumption the Gibbs-Thomson equation can be written as

$$T_m = T_m^{bulk} \left( 1 - \frac{4M}{\Delta_{fus}H \rho d} \sigma_{sl} \right) \quad (8)$$

For the [BMIM]<sup>+</sup>[TFSI]<sup>-</sup> the following linear dependence is extracted from Figure 10:  $T_m(1/d) = 271.1 \text{ K} - (394 \pm 30)/d$ ;  $d$  in nm. Using,  $M = 419.37 \text{ g} \cdot \text{mol}^{-1}$ ,  $\Delta_{fus}H = 56.6 \text{ J} \cdot \text{g}^{-1}$ , and  $\rho = 1.44 \text{ g} \cdot \text{cm}^{-3}$  gives a solid-liquid interfacial energy of  $\sigma_{sl} \sim 0.03 \text{ J} \cdot \text{m}^{-2}$ . For the [BMIM]<sup>+</sup>[PF<sub>6</sub>]<sup>-</sup> case,  $T_m(1/d) = 281.0 \text{ K} - (366 \pm 28)/d$ ;  $d$  in nm. Using,  $M = 284.18 \text{ g} \cdot \text{mol}^{-1}$ ,  $\Delta_{fus}H = 32.0 \text{ J} \cdot \text{g}^{-1}$ , and

$\rho=1.37 \text{ g}\cdot\text{cm}^{-3}$  gives a solid-liquid interfacial energy of  $0.014 \text{ J}\cdot\text{m}^{-2}$ . These are both reasonable estimates of crystal/liquid interfacial energies.<sup>51,52</sup>

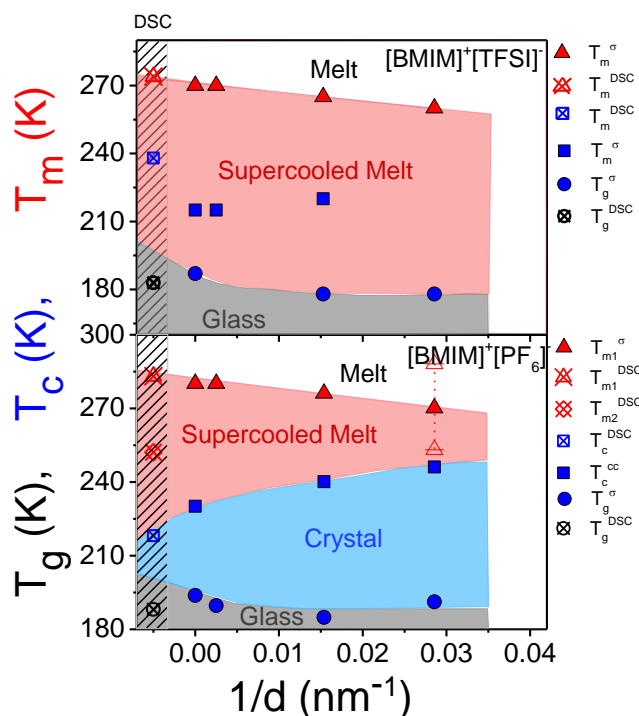


**Figure 10.** Effective phase diagram of (top) [BMIM]<sup>+</sup>[TFSI]<sup>-</sup> and (bottom) [BMIM]<sup>+</sup>[PF<sub>6</sub>]<sup>-</sup> as a function of inverse pore diameter. (Top) On cooling the [BMIM]<sup>+</sup>[TFSI]<sup>-</sup> remains in the supercooled amorphous state and has a liquid-to-glass temperature (filled spheres) that can be extracted from the  $\sigma_{dc}(T)$  dependence (by extrapolating the VFT dependence to a value of  $\sigma_{dc} \sim 10^{-14} \text{ S}\cdot\text{cm}^{-1}$ ). On heating, it remains in the amorphous state and undergoes some weak cold crystallization (filled squares) at the indicated temperatures. Finally, it melts at higher temperatures (red triangles) as seen from the discontinuous increase of conductivity. The red line is the result of a linear fit to the melting temperatures (Gibbs-Thomson equation). (bottom) [BMIM]<sup>+</sup>[PF<sub>6</sub>]<sup>-</sup> crystallizes on cooling (blue squares) as obtained from the changes in ionic conductivity and further the dynamics freeze at the glass temperature (filled spheres). On heating it eventually melts at higher temperatures (red triangles). Symbols in the shaded areas refer to the bulk samples as obtained from DSC at a rate of  $10 \text{ K}\cdot\text{min}^{-1}$ .

ILs of [BMIM]<sup>+</sup>[X]<sup>-</sup> confined in AAO templates suffer from loss of ion conductivity due to immobilization of ions at the pore walls. Nevertheless, confinement within smaller pores can be employed to suppress nucleation and growth, a procedure that can result to an increase of ionic conductivity by several orders of magnitude. On the other hand, confinement did not alter the self-organization (**Figure S20**). The same peaks reflecting correlation distances that correspond to smectic layering, charge alteration and van der Waals distances appeared under confinement.

### 3.4 Conclusion

The study of a series of ILs based on [BMIM]<sup>+</sup>[X]<sup>-</sup> bearing anion radii from 0.168 nm to 0.326 nm allowed us to explore the effect of anion type and size on the self-assembly, thermodynamics and ion conduction in the bulk, during flow and following imbibition in AAO nanopores. In the bulk, ILs exhibit weak ordering on different length scales. X-ray diffraction show the usual van der Waals peak of the closest proximity of atoms, contain an intermediate peak due to the anion-cation alteration (charge alteration peak), and an additional peak at longer distances reflecting the weak nanophase separation between the polar and apolar groups. All ILs formed stable glasses on cooling. Most crystallize and melting upon heating. [BMIM]<sup>+</sup>[BF<sub>4</sub>]<sup>-</sup> was an exception and was unable to crystallize. It remained amorphous, independent of the thermal history. Although electrostatic interactions suffice to explain the general dependence of viscosity, conductivity and liquid-to-glass temperature with respect to the anion size, other effects such as charge delocalization play a role as well.

The process of imbibition within nanopores, was governed by an effective viscosity of the order of their viscosity in the bulk. However, following imbibition, their ionic conductivity under confinement was reduced revealing a reduced number of mobile ions. Hydrophobizing the internal AAO surface (silanization) – at least partially – recovered the bulk conductivity. Changes in conductivity on cooling and heating were used as markers of crystallization/melting that allowed to construct the effective phase diagrams of the confined ILs. Employing the depression of the melting temperature for the different pores and the Gibbs-Thomson equation allowed an estimate of the crystal/liquid interfacial energies.

An interesting feature of the phase diagrams was the complete suppression of crystallization of [BMIM]<sup>+</sup>[TFSI]<sup>-</sup> and [BMIM]<sup>+</sup>[PF<sub>6</sub>]<sup>-</sup> within pores with a diameter of 25 nm. This is suggestive of the critical nucleus size needed for crystallization. Since both ILs have favorable ion conductivities and low glass temperatures, confinement proves to be an efficient method to suppress the undesired bulk crystallization during heating. Overall, confinement provides the means to increase conductivity by suppressing crystallization.

### 3.5 References

- (1) Armand, M.; Endres, F.; MacFarlane, D.R.; Ohno, H.; Scrosati, B. Ionic-Liquid Materials for the Electrochemical Challenges of the Future. *Nat. Mater.* **2009**, *8*, 621-629.
- (2) Galiński, M.; Lewandowski, A.; Stepniak, I. Ionic Liquids as Electrolytes. *Electrochim. Acta* **2006**, *51*, 5567-5580.
- (3) Welton, T. Room-Temperature Ionic Liquids. Solvents for Synthesis and Catalysis. *Chem. Rev.* **1999**, *99*, 2071-2083.
- (4) Watanabe, M.; Thomas, M. L.; Zhang, S.; Ueno, K.; Yasuda, T.; Dokko, K. Application of Ionic Liquids to Energy Storage and Conversion Materials and Devices. *Chem. Rev.* **2017**, *117*, 7190-7239.
- (5) Simon, P.; Gogotsi, T. Materials for Electrochemical Capacitors. *Nat. Mater.* **2008**, *7*, 845-854.
- (6) Davenport, M.; Rodriguez, A.; Shea, K. J.; Siwy, Z. S. Squeezing Ionic Liquids through Nanopores. *Nano Lett.* **2009**, *9*, 2125-2128.
- (7) Iacob, C.; Sangoro, J. R.; Papadopoulos, P.; Schubert, T.; Naumov, S.; Valiullin, R.; Karger, J.; Kremer, F. Charge Transport and Diffusion of Ionic Liquids in Nanoporous Silica Membranes. *PCCP* **2010**, *12*, 13798-13803.
- (8) Iacob, C.; Sangoro, J. R.; Kipnusu, W. K.; Valiullin, R.; Kärger, J.; Kremer, F. Enhanced Charge Transport in Nano-Confined Ionic Liquids. *Soft Matter* **2012**, *8*, 289-293.
- (9) Tu, W.; Chat, K.; Szklarz, G.; Laskowski, L.; Grzybowska, K.; Paluch, M.; Richert, R.; Adrjanowicz, K. Dynamics of Pyrrolidinium-Based Ionic Liquids under Confinement. II. The Effects of Pore Size, Inner Surface, and Cationic Alkyl Chain Length. *J. Phys. Chem. C* **2019**, *124*, 5395-5408.
- (10) Sieffert, N.; Wipff, G. Ordering of Imidazolium-Based Ionic Liquids at the  $\alpha$ -Quartz(001) Surface: A Molecular Dynamics Study. *J. Phys. Chem. C* **2008**, *112*, 19590-19603.
- (11) Wang, S.; Li, S.; Cao, Z.; Yan, T. Y. Molecular Dynamic Simulations of Ionic Liquids at Graphite Surface. *J. Phys. Chem. C* **2010**, *114*, 990-995.
- (12) Shi, W.; Sorescu, D. C. Molecular Simulations of CO<sub>2</sub> and H<sub>2</sub> Sorption into Ionic Liquid 1-n-Hexyl-3-methylimidazolium Bis(trifluoromethylsulfonyl)amide ([hmim][Tf<sub>2</sub>N]) Confined in Carbon Nanotubes. *J. Phys. Chem. B* **2010**, *114*, 15029-15041.
- (13) Tu, C.-H.; Steinhart, M.; Butt, H.-J.; Floudas, G. In Situ Monitoring of the Imbibition of Poly(n-butyl methacrylates) in Nanoporous Alumina by Dielectric Spectroscopy. *Macromolecules* **2019**, *52*, 8167-8176.
- (14) Serghei, A.; Chen, D.; Lee, D. H.; Russell, T. P. Segmental Dynamics of Polymers during Capillary Flow into Nanopores. *Soft Matter* **2010**, *6*, 1111-1113.
- (15) Serghei, A.; Lutkenhaus, J. L.; Miranda, D. F.; McEnnis, K.; Kremer, F.; Russell, T. P. Density Fluctuations and Phase Transitions of Ferroelectric Polymer Nanowires. *Small* **2010**, *6*, 1822-1826.
- (16) Tu, C. H.; Zhou, J.; Doi, M.; Butt, H. J.; Floudas, G. Interfacial Interactions During In Situ Polymer Imbibition in Nanopores. *Phys. Rev. Lett.* **2020**, *125*, 127802.
- (17) Tu, C.-H.; Zhou, J.; Butt, H.-J.; Floudas, G. Adsorption Kinetics of cis-1,4-Polyisoprene in Nanopores by In Situ Nanodielectric Spectroscopy. *Macromolecules* **2021**, *54*, 6267-6274.

- (18) Tu, C.-H.; Veith, L.; Butt, H. J.; Floudas, G. Ionic Conductivity of a Solid Polymer Electrolyte Confined in Nanopores. *Macromolecules* **2022**, *55*, 1332-1341.
- (19) Masuda, H.; Fukuda, K. Ordered Metal Nanohole Arrays Made by a Two-Step Replication of Honeycomb Structures of Anodic Alumina. *Science* **1995**, *268*, 1466-1468.
- (20) Masuda, H.; Hasegawa, F.; Ono, S. Self-ordering of Cell Arrangement of Anodic Porous Alumina Formed in Sulfuric Acid Solution. *J. Electrochem. Soc.* **1997**, *144*, L127-L130.
- (21) Masuda, H.; Yada, K.; Osaka, A. Self-ordering of Cell Configuration of Anodic Porous Alumina with Large-Size Pores in Phosphoric Acid Solution. *Jpn. J. Appl. Phys.* **1998**, *37*, L1340- L1342.
- (22) Steinhart, M. Supramolecular Organization of Polymeric Materials in Nanoporous Hard Templates. *Adv. Polym. Sci.* **2008**, *220*, 123-187.
- (23) Wu, S. Interfacial and Surface Tensions of Polymers. *J. Macromol. Sci., Polym. Rev.* **1974**, *10*, 1-73.
- (24) Marmur, A.; Della Volpe, C.; Siboni, S.; Amirfazli, A.; Drelich, J.W. *Contact Angles and Wettability: Towards Common and Accurate Terminology*. In: *Surface Innovations*. Volume 5, Nr. 1, 2017, [ISSN 2050-6252](https://doi.org/10.1680/jsuin.17.00002), S. 3–8, ICE Publishing, London, UK, doi:[10.1680/jsuin.17.00002](https://doi.org/10.1680/jsuin.17.00002).
- (25) Harris, K.R.; Woolf, L.W.; Kanakubo, M. Temperature and Pressure Dependence of the Viscosity of the Ionic Liquid 1-Butyl-3-methylimidazolium Hexafluorophosphate. *J. Chem. Eng. Data* **2005**, *50*, 1777-1782.
- (26) Harris, K.R.; Kanakubo, M.; Woolf, L.W. Temperature and Pressure Dependence of the Viscosity of the Ionic Liquid 1-Butyl-3-methylimidazolium Tetrafluoroborate: Viscosity and Density Relationships in Ionic Liquids. *J. Chem. Eng. Data* **2007**, *52*, 2425-2430.
- (27) Harris, K.R.; Woolf, L.W.; Kanakubo, M. Temperature and Pressure Dependence of the Viscosity of the Ionic Liquids 1-Hexyl-3-methylimidazolium Hexafluorophosphate and 1-Butyl-3-methylimidazolium Bis(trifluoromethylsulfonyl)imide. *J. Chem. Eng. Data* **2007**, *52*, 1080-1085.
- (28) Zhang, S.; Sun, N.; He, X.; Lu, X.; Zhang, X. Physical Properties of Ionic Liquids: Database and Evaluation. *J. Phys. Chem. Ref. Data* **2006**, *35*, 1475-1517.
- (29) Roobottom, H. K.; Jenkins, H. D. B. Thermochemical Radii of Complex Ions. *J. Chem. Educ.* **1999**, *76*, 1570-1573.
- (30) Jenkins, H. D. B.; Thakur, K. P. Reappraisal of Thermochemical Radii for Complex-Ions. *J. Chem. Educ.* **1979**, *56*, 576-577.
- (31) Araque, J. C.; Hettige, J. J.; Margulis, C. J. Modern Room Temperature Ionic Liquids, a Simple Guide to Understanding Their Structure and How It May Relate to Dynamics. *J. Phys. Chem. B* **2015**, *119*, 12727-12740.
- (32) Triolo, A.; Russina, O.; Bleif, H. J.; Di Cola, E. Nanoscale Segregation in Room Temperature Ionic Liquids. *J. Phys. Chem. B* **2007**, *111*, 4641-4644.
- (33) Bradley, A. E.; Hardacre, C.; Holbrey, J. D.; Johnston, S.; McMath, S. E. J.; Nieuwenhuyzen, M. Small-Angle X-ray Scattering Studies of Liquid Crystalline 1-alkyl-3-methylimidazolium Salts. *Chem. Mater.* **2002**, *14*, 629-635.
- (34) Dyre, J. C. The Random Free-Energy Barrier Model for ac Conduction in Disordered Solids. *J. Appl. Phys.* **1988**, *64*, 2456-2468.
- (35) Schroder, T. B.; Dyre, J. C. ac Hopping Conduction at Extreme Disorder Takes Place on the Percolating Cluster. *Phys. Rev. Lett.* **2008**, *101*, 025901.

- (36) Pipertzis, A.; Mühlhngaus, M.; Mezger, M.; Scherf, U.; Floudas, G. Polymerized Ionic Liquids with Polythiophene Backbones: Self-Assembly, Thermal Properties, and Ion Conduction. *Macromolecules* **2018**, *51*, 6440-6450.
- (37) Pipertzis, A.; Papamokos, G.; Mühlhngaus, M.; Mezger, M.; Scherf, U.; Floudas, G. What Determines the Glass Temperature and dc-Conductivity in Imidazolium-Polymerized Ionic Liquids with a Polythiophene Backbone? *Macromolecules* **2020**, *53*, 3535-3550.
- (38) Kanakubo, M.; Harris, K.R.; Tsuchihashi, N.; Ibuki, K.; Ueno, M. Temperature and Pressure Dependence of the Electrical Conductivity of 1-Butyl-3-methylimidazolium Bis(trifluoromethanesulfonyl)amide. *J. Chem. Eng. Data* **2015**, *60*, 1495-1503.
- (39) Stickel, F.; Fischer, E.W.; Richert, R. Dynamics of Glass-forming Liquids I. Temperature Derivative Analysis of Dielectric Relaxation Data. *J. Chem. Phys.* **1995**, *102*, 6251-6257.
- (40) Harris, M.A.; Kinseya, T.; Wagleb, D.V.; Bakerc, G.A.; Sangoro, J. Evidence of a Liquid-Liquid Transition in a Glass-Forming Ionic Liquid. *PNAS* **2021**, *118*, 1-6.
- (41) Wojnarowska, Z.; Cheng, S.; Yao, B.; Swadzba-Kwasny, M.; McLaughlin, S.; McGrogan, A.; Delavoux, Y.; Paluch, M. Pressure-Induced Liquid-Liquid Transition in a Family of Ionic Materials. *Nat Commun.* **2022**, *13*:1342.
- (42) Kirchner, B.; Malberg, F.; Firaha, D.S.; Hollóczki, O. Ion Pairing in Ionic Liquids. *J. Phys.: Condens. Matter* **2015**, *27*, 463002.
- (43) Kashyap, H.K.; Annapureddy, H.V.R.; Raineri, F.O.; Margulis, C.J. How Is Charge Transport Different in Ionic Liquids and Electrolyte Solutions? *J. Phys. Chem. B* **2011**, *115*, 13212-13221.
- (44) Lucas, R. On the Time Law of the Capillary Rise of Liquids. *Colloid Polym. Sci.* **1918**, *23*, 15-22.
- (45) Washburn, E.W. The Dynamics of Capillary Flow. *Phys. Rev.* **1921**, *17*, 273-283.
- (46) Grigoriadis, C.; Duran, H.; Steinhart, M.; Kappl, M.; Butt, H. J.; Floudas, G. Suppression of Phase Transitions in a Confined Rodlike Liquid Crystal. *ACS Nano* **2011**, *5*, 9208-9215.
- (47) Duran, H.; Steinhart, M.; Butt, H. J.; Floudas, G. From Heterogeneous to Homogeneous Nucleation of Isotactic Poly(propylene) Confined to Nanoporous Alumina. *Nano Lett.* **2011**, *11*, 1671-1675.
- (48) Suzuki, Y.; Duran, H.; Steinhart, M.; Butt, H.-J.; Floudas, G. Homogeneous Crystallization and Local Dynamics of Poly(ethylene oxide) (PEO) Confined to Nanoporous Alumina. *Soft Matter* **2013**, *9*, 2621-2628.
- (49) Alcoutlabi, M.; McKenna, G. B. Effects of Confinement on Material Behaviour at the Nanometre Size Scale. *J. Phys.: Condens. Matter.* **2005**, *17*, R461-R524.
- (50) Hamilton, B. D.; Ha, J.-M.; Hillmyer, M. A.; Ward, M. D. Manipulating Crystal Growth and Polymorphism by Confinement in Nanoscale Crystallization Chambers. *Acc. Chem. Res.* **2012**, *45*, 414-423.
- (51) Beiner, M.; Rengarajan, G. T.; Pankaj, S. Enke, D. Steinhart, M. Manipulating the Crystalline State of Pharmaceuticals by Nanoconfinement. *Nano Lett.* **2007**, *7*, 1381-1385.
- (52) Ananiadou, A.; Alagiannis, M.; Steinhart, M.; Skobridis, K.; Floudas, G. Polymorphism of Crystalline Alcohols Under Nanoscale Confinement. *J. Phys. Chem. C* **2022**, *126*, 16409-16420.

### 3.6 Supporting information

#### I. $^1\text{H}$ NMR

To measure the water molar fraction ( $\chi_w$ ) of samples,  $^1\text{H}$  nuclear magnetic resonance ( $^1\text{H}$  NMR) spectra were measured using a Bruker Spectrospin spectrometer (400 MHz) at  $25^\circ\text{C}$ . The samples were transferred to 5 mm NMR tubes equipped with a coaxial capillary containing  $d_6$ -DMSO as internal chemical shift reference. Before testing the ILs, the water molar fraction in DMSO was tested by  $^1\text{H}$  NMR.  $\chi_w$  is 3 % (Figure S1). The water molar fraction ( $\chi_w$ ) in the ILs was obtained as:

$$\chi_w = \frac{(I_{\text{water}} - I_{\text{water}'}) \times Mn_{\text{water}}}{(I_{\text{water}} - I_{\text{water}'} + I_{\text{H}_{6,7}}) \times Mn_{[\text{BMIM}][\text{X}]}}$$

Here,  $I_{\text{water}}$  denotes the integral of the peak of water in  $^1\text{H}$  NMR of ionic liquids,  $I_{\text{water}'}$  is the integral of the peak of water in the  $^1\text{H}$  NMR curve of DMSO.  $I_{\text{H}_{6,7}}$  represents the integral of the peak of  $\text{H}_{6,7}$  of the cation  $^1\text{H}$  NMR spectrum.

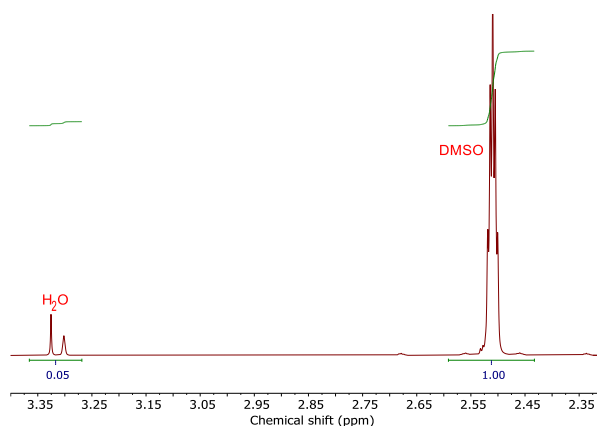


**Figure S1.**  $^1\text{H}$  NMR spectrum of DMSO used for the samples.

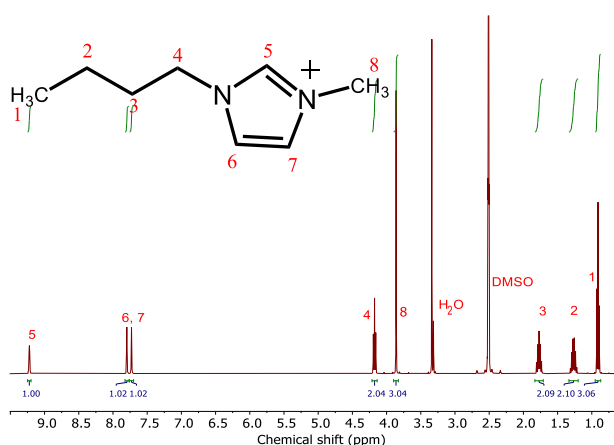


**Figure S2.**  $^1\text{H}$  NMR spectrum of the  $[\text{BMIM}]^+$ . The inserted picture shows the structure of the cation and assignment of protons.

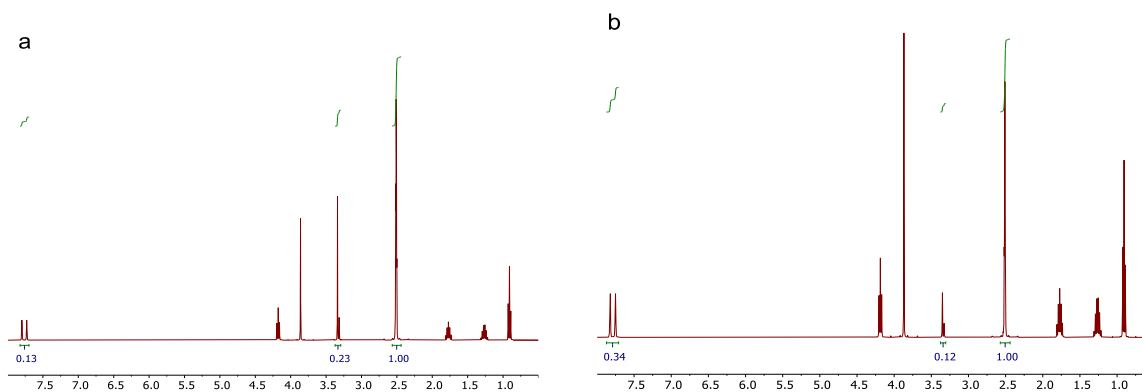


**Figure S3.** <sup>1</sup>H NMR spectrum of [BMIM]<sup>+</sup> in the [BMIM]<sup>+</sup>[Cl]<sup>-</sup> ionic liquid. (a) non-dried,  $\chi_w = 5.98\%$  (b) dried for 12 h,  $\chi_w = 1.76\%$ .

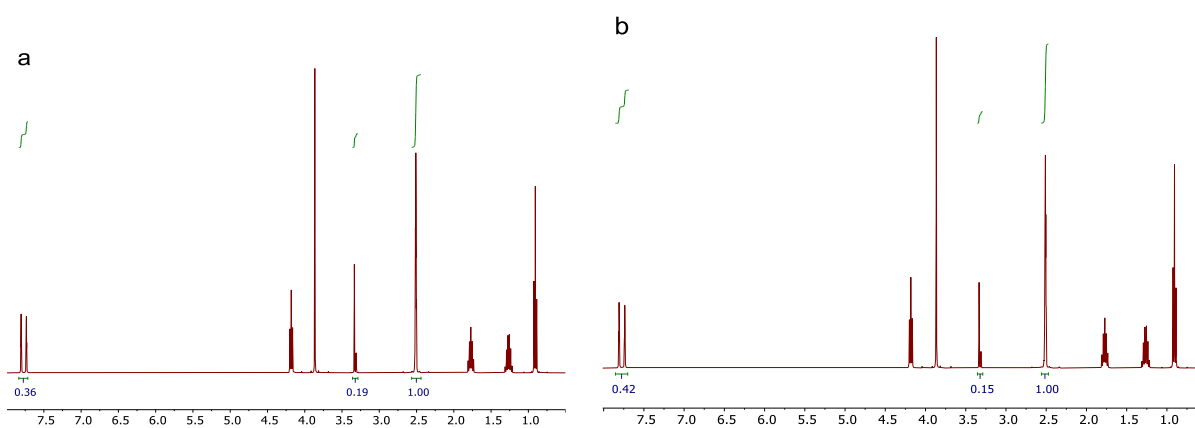


**Figure S4.** <sup>1</sup>H NMR spectrum of [BMIM]<sup>+</sup> cation in the [BMIM]<sup>+</sup>[Br]<sup>-</sup> ionic liquid. (a) non-dried,  $\chi_w = 2.3\%$  (b) dried for 12 h,  $\chi_w = 1.58\%$ .

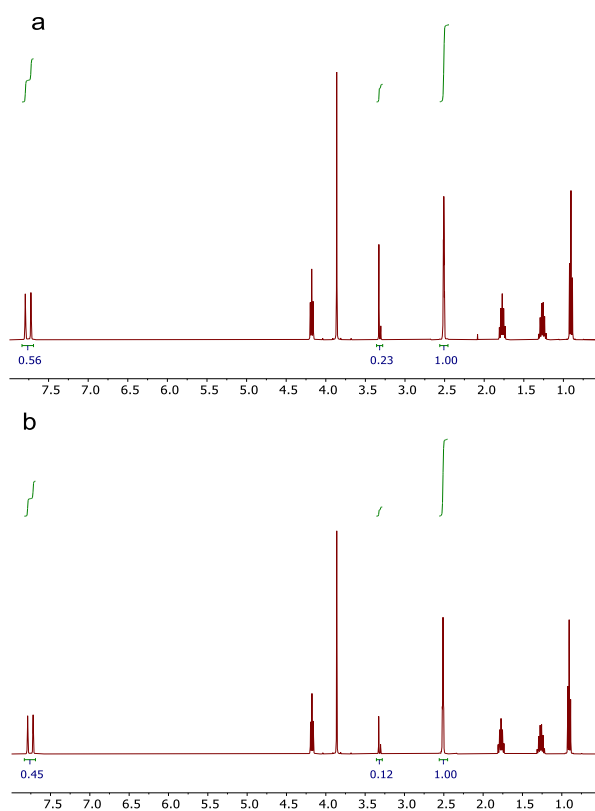


**Figure S5.** <sup>1</sup>H NMR spectrum of [BMIM]<sup>+</sup> in the [BMIM]<sup>+</sup>[I]<sup>-</sup> ionic liquid. (a) non-dried,  $\chi_w = 1.65\%$  (b) dried for 12 h,  $\chi_w = 0.9\%$ .

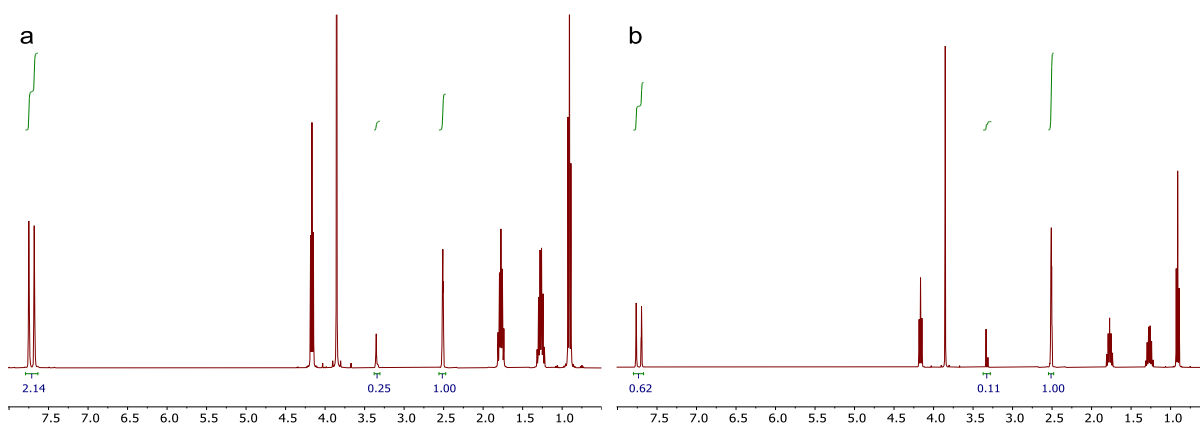


**Figure S6.** <sup>1</sup>H NMR spectrum of [BMIM]<sup>+</sup> in the [BMIM]<sup>+</sup>[BF<sub>4</sub>]<sup>-</sup> ionic liquid. (a) non-dried,  $\chi_w = 0.68\%$  (b) dried for 12 h,  $\chi_w = 0.7\%$ .

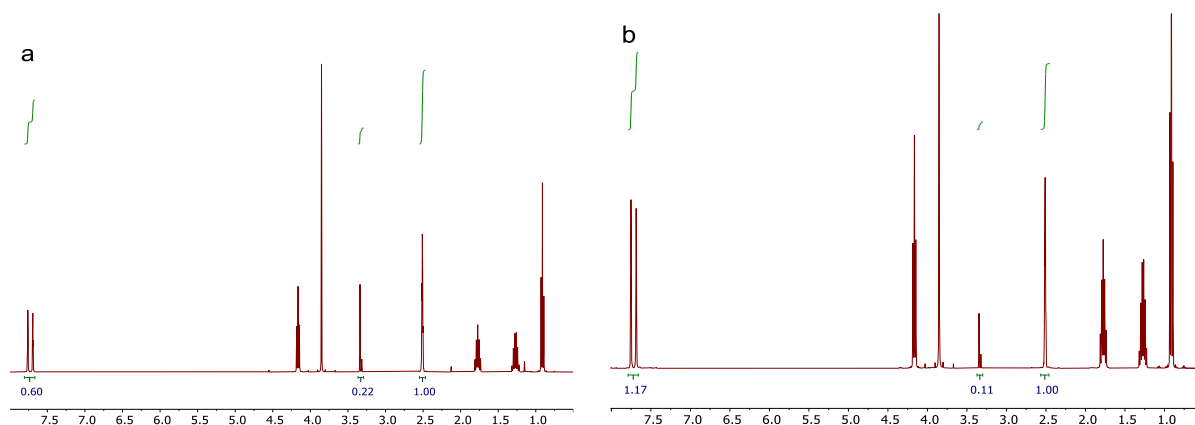


**Figure S7.**  $^1\text{H}$  NMR spectrum of  $[\text{BMIM}]^+$  in the  $[\text{BMIM}]^+[\text{PF}_6]^-$  ionic liquid. (a) non-dried,  $\chi_w = 1.4\%$  (b) dried for 12 h,  $\chi_w = 0.3\%$ .

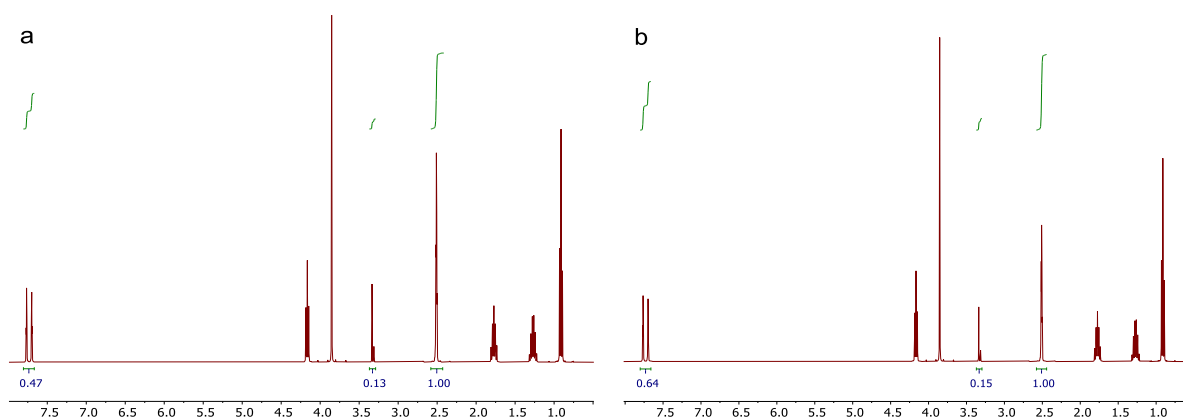


**Figure S8.**  $^1\text{H}$  NMR spectrum of  $[\text{BMIM}]^+$  in the  $[\text{BMIM}]^+[\text{TFSI}]^-$  ionic liquid. DMSO used as the chemical shift reference. (a) non-dried,  $\chi_w = 0.6\%$  (b) dried for 12 h,  $\chi_w = 0.6\%$ .

## II. Thermogravimetric analysis (TGA)

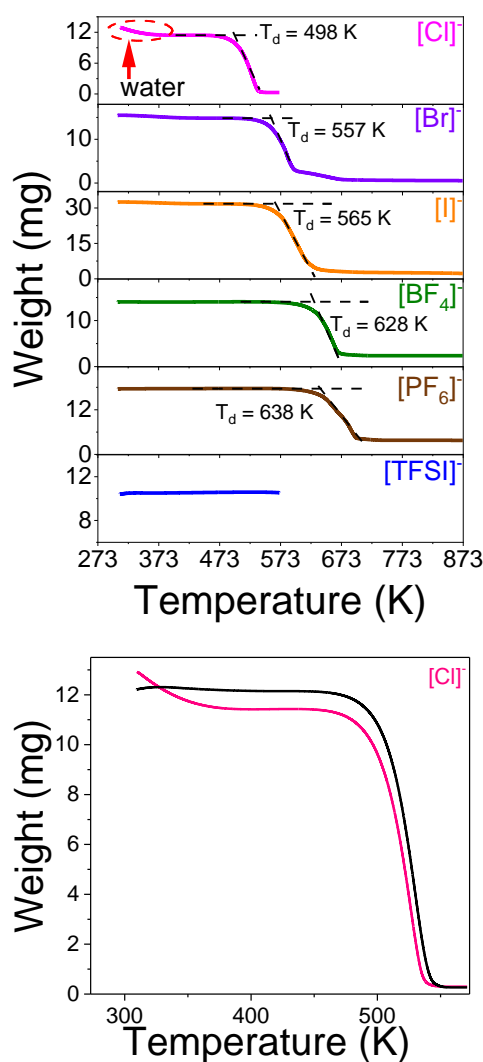


**Figure S9.** (Top) TGA curves for all ILs investigated. Evidently, [Cl]<sup>-</sup>, [Br]<sup>-</sup> and [I]<sup>-</sup> absorb water under normal conditions. Care was taken to remove traces of water for the viscosity and DS measurements. (Bottom) TGA curve of dried (black line) (100 °C, under vacuum for 12 h) and non-dried (pink line) [BMIM][Cl]<sup>-</sup>. The weight of dried sample remains almost the same below 100 °C.

### III. Porosity of AAO templates

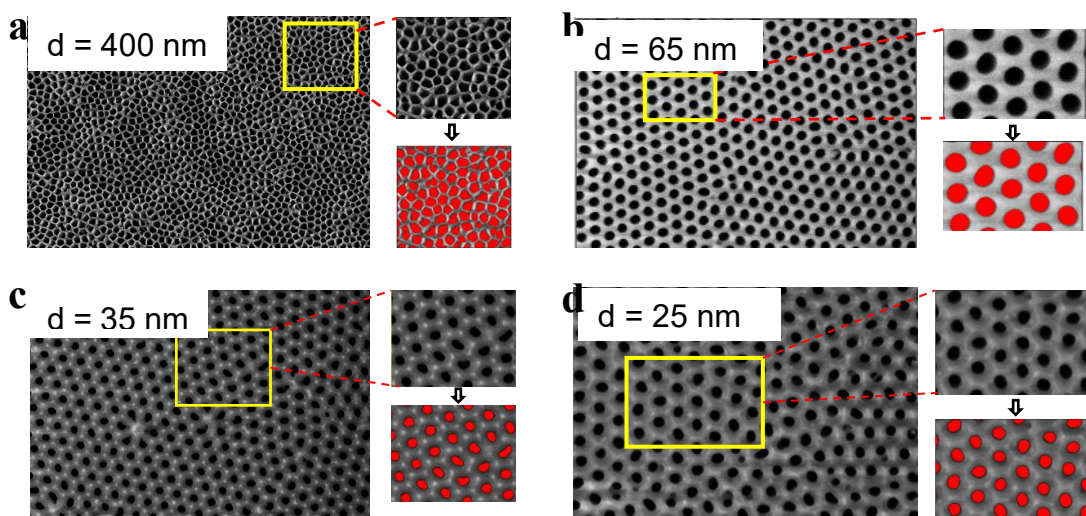


**Figure S10.** Porosity calculation for the indicated AAO templates. Images were digitized with the software *Image J* and the porosity was calculated as  $\varphi = A_{\text{open}}/A_{\text{total}}$ .

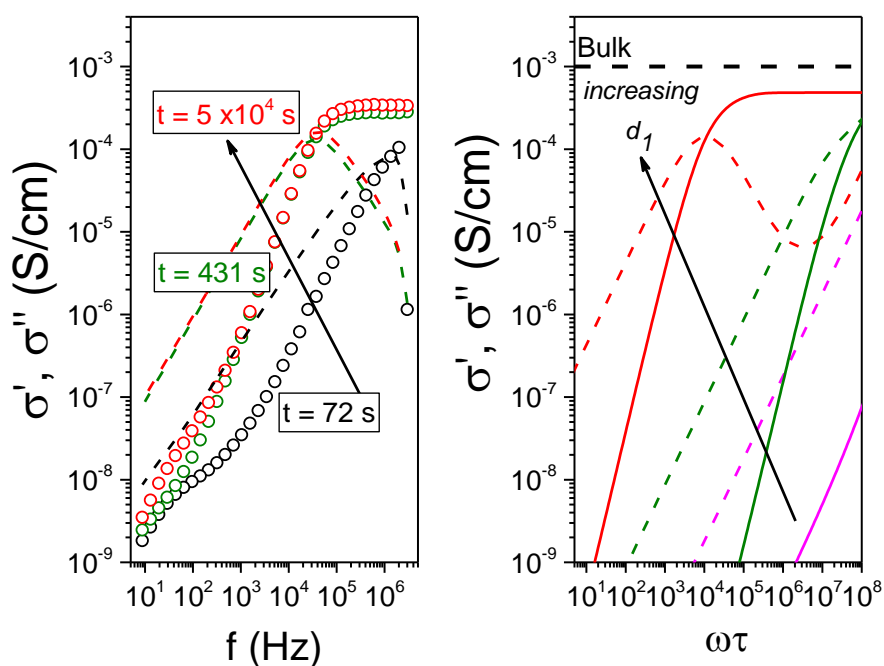


**Figure S11.** (a) Evolution of the real (symbol) and imaginary (dashed lines) parts of the complex conductivity for  $[\text{BMIM}]^+[\text{BF}_4]^-$  within AAO pores with a diameter of 400 nm at 303 K. (b) Simulation of the evolution of the real (solid lines) and imaginary parts (dashed lines) of the complex conductivity corresponding to the process in (a) for different imbibition lengths ( $d_1$ ) via the parallel model. Parameters are as follows:  $\Delta\varepsilon = 20$ ,  $\varepsilon_\infty = 10$ ,  $\sigma_{\text{dc}} = 10^{-3} \text{ S cm}^{-1}$ ,  $\tau = 1 \text{ s}$ ,  $\varphi_{12} (=1 - \varphi_3) = 0.484$ ,  $L = 100 \mu\text{m}$ ,  $\sigma'_3 = \sigma'_{\text{AAO}} = 10^{-10} \text{ S cm}^{-1}$ , and  $\sigma''_3 = \sigma''_{\text{AAO}} = 10^{-8} \text{ S cm}^{-1}$ . Different colors correspond to different imbibition lengths: (magenta)  $d_1 = 30 \mu\text{m}$ , (olive)  $d_1 = 99.5 \mu\text{m}$ , and (red)  $d_1 = 100.0 \mu\text{m}$ .

#### IV. Surface Tension

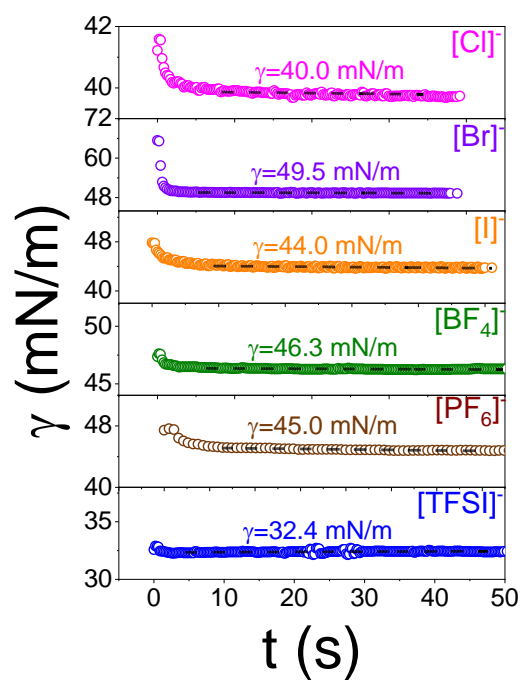


**Figure S12.** Surface tension as a function of time for the different ILs investigated at 303 K.

#### V. Contact Angle

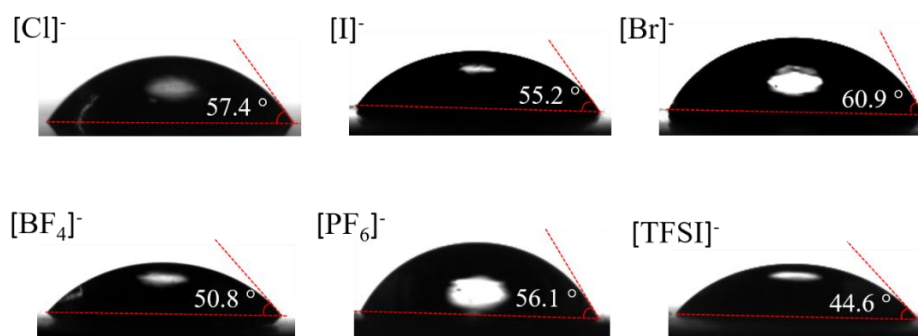


**Figure S13.** Static contact angle for all ILs on an electropolished Al disk coated with a thin oxide layer.

## VI. Differential scanning calorimetry (DSC)

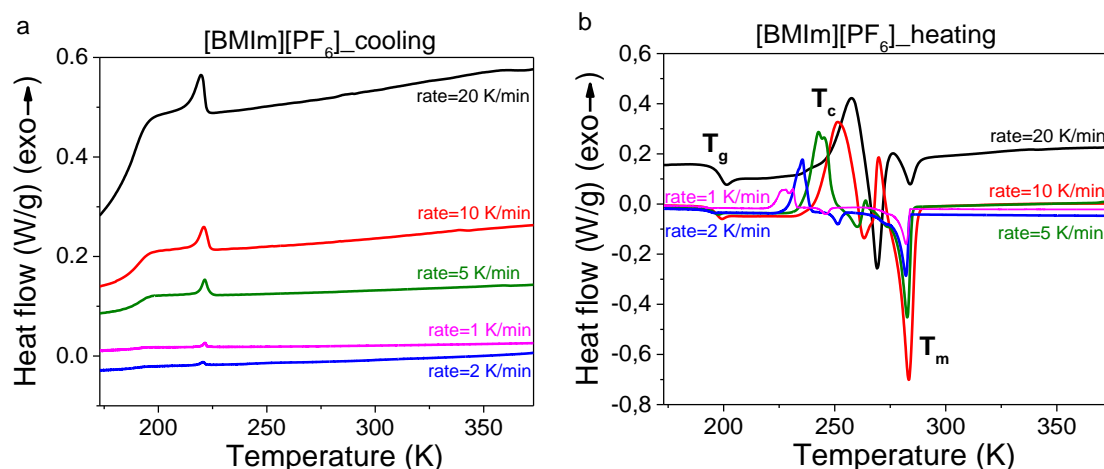


**Figure S14.** DSC traces of [BMIM]+[PF6]<sup>-</sup> at different rates: 1 K·min<sup>-1</sup> (magenta), 2 K·min<sup>-1</sup> (blue), 5 K·min<sup>-1</sup> (olive), 10 K·min<sup>-1</sup> (red), 20 K·min<sup>-1</sup> (black). (a) Traces are obtained from the cooling process. At around 200 K, there is an obvious peak and the position doesn't follow the rate. We believe that this peak is related to the L-L transition, near which the bulk dc-conductivity of the sample also changes (as shown in Figure 3a), but more detailed studies are needed. (b) Traces are obtained from the subsequent heating. [PF6]<sup>-</sup> has a clear crystallization behavior leading to a significant decrease in conductivity.

## VII. Dielectric Spectroscopy (DS)

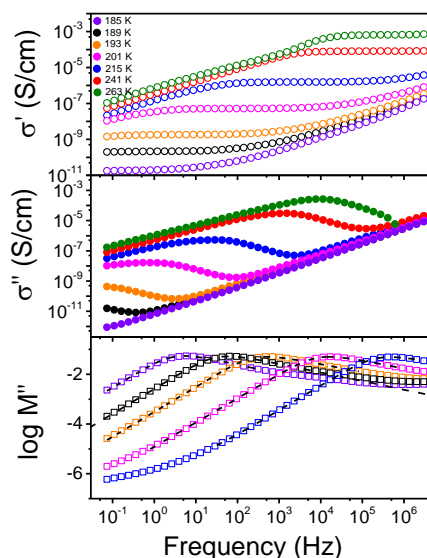


**Figure S15.** Real (top) and imaginary (middle) parts of the ionic conductivity of bulk [BMIM]+[BF4]<sup>-</sup> shown for the indicated temperatures. The modulus representation (bottom) is used to extract the characteristic times of ionic motion (lines represent fits).

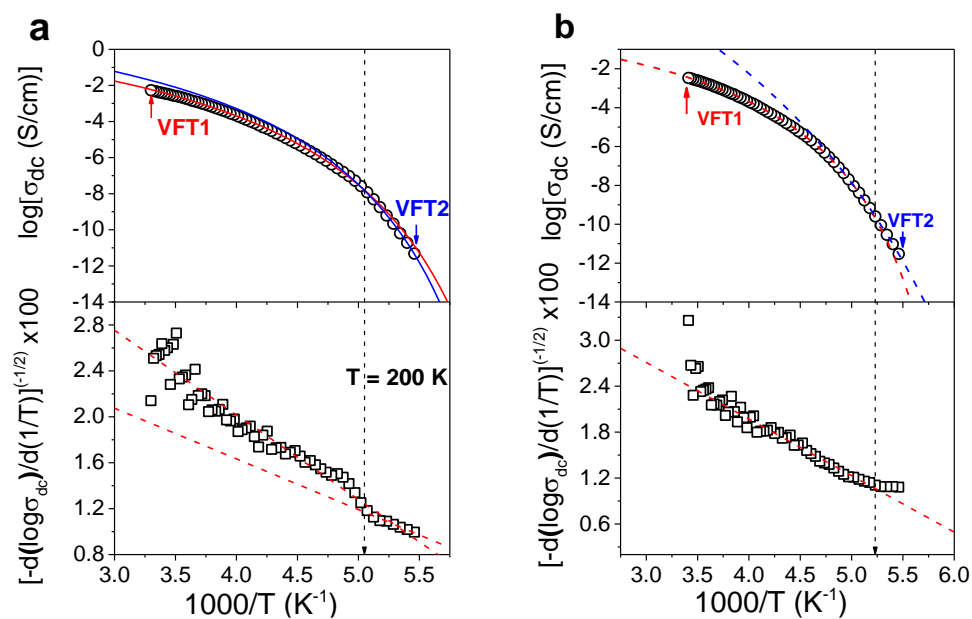


**Figure S16.** Temperature dependence of the conductivity of [BMIM]+[BF<sub>4</sub>]<sup>-</sup> (top) and the first derivative of conductivity with respect to inverse temperature (bottom) upon cooling (a) and subsequent heating (b). The cooling curve can be described by two VFTs indicated by the red and blue lines. On cooling, at  $T \sim 200 \text{ K}$  the change from the high temperature VFT (VFT1) to the low temperature VFT (VFT2) could associate with a liquid-to-liquid transition.

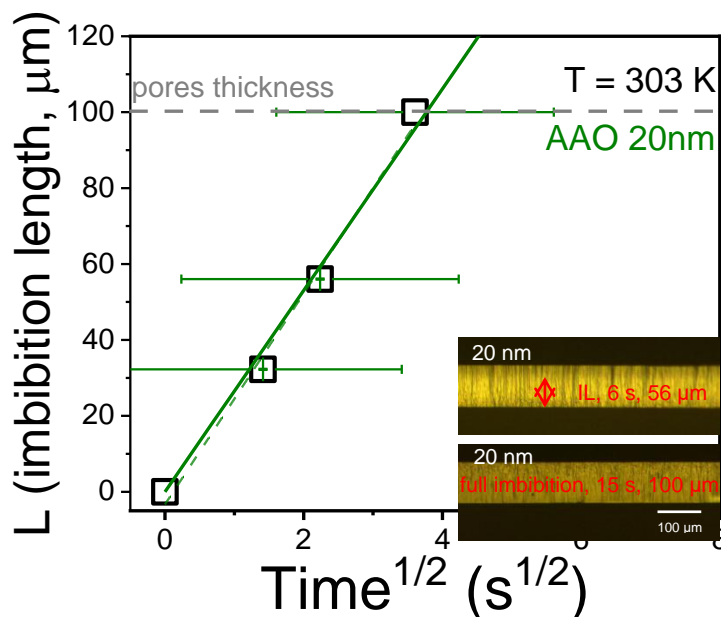


**Figure S17.** Imbibition lengths extracted via reflection optical reflection microscopy at selected times for [BMIM]+[PF<sub>6</sub>]<sup>-</sup> inside AAOs with pore size of  $20 \text{ nm}$  at  $303 \text{ K}$ . The solid line gives the theoretical predictions according to the Lucas-Washburn equation and the bulk viscosity ( $\theta=670$ ,  $\gamma=43.5 \text{ mN/m}$ ,  $\eta=0.170 \text{ Pa}\cdot\text{s}$ ). The inset gives ROM images depicting cross-sections of AAO templates,  $20 \text{ nm}$  in diameter, at different infiltration times. The red arrow gives the imbibition length for the given time.

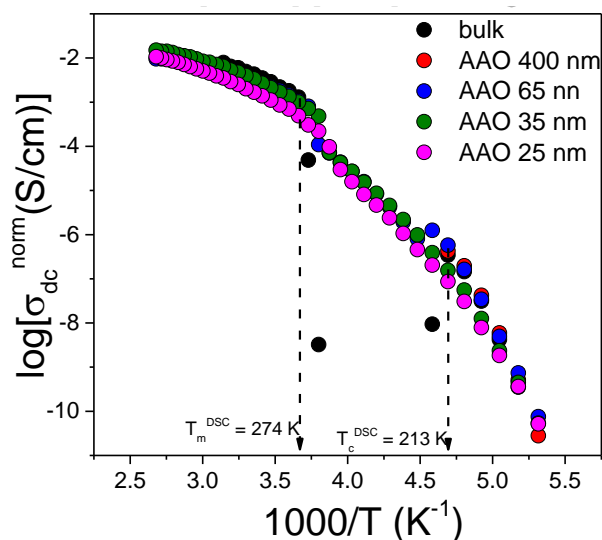


**Figure S18.** Dc-conductivity for [BMIM]+[TFSI]<sup>-</sup> following imbibition in AAO nanopores with different pore diameters plotted as a function of inverse temperature. Measurements were made on heating. Discontinuous changes for the bulk and confined samples indicate cold crystallization (~213 K) and melting (~274 K).

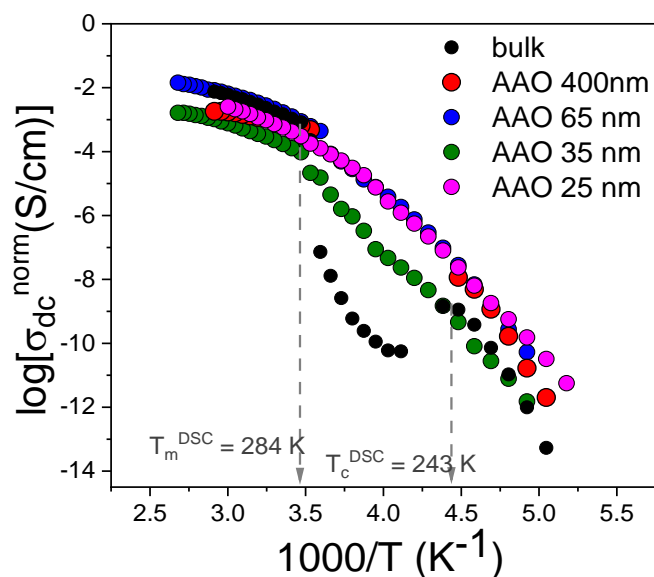


**Figure S19.** Dc-conductivity for [BMIM]+[PF6]<sup>-</sup> following imbibition in AAO nanopores with different pore diameters plotted as a function of inverse temperature. Measurements were made on heating. Discontinuous changes of the conductivity are very evident for the bulk and confined samples indicate cold crystallization (~243 K) and melting (~284 K). Notice the continuous dependence of conductivity for the IL within 25 nm revealing its completely amorphous state.

## VIII. XRD

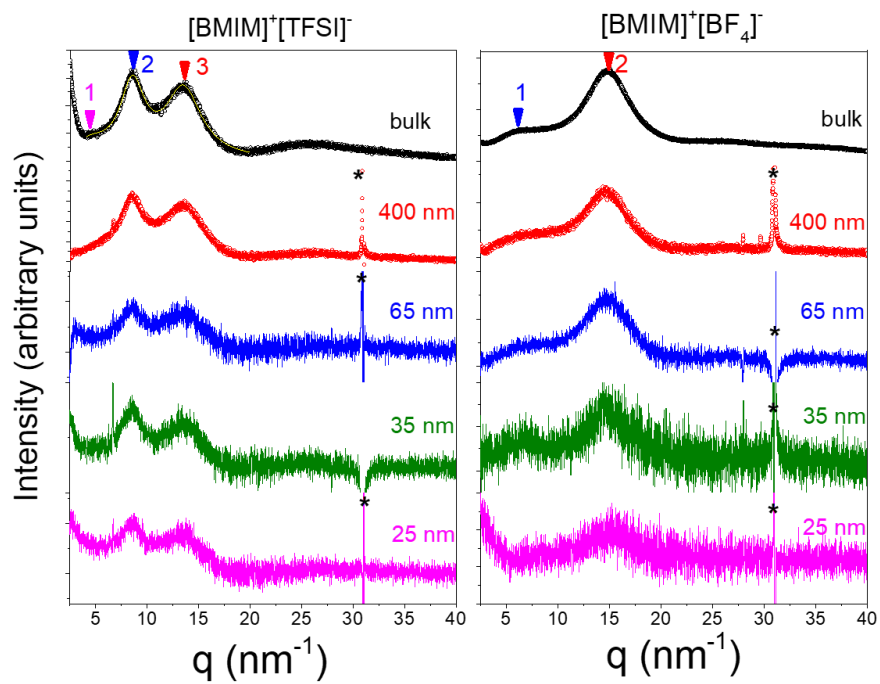


**Figure S20.** XRD curves of [BMIM]<sup>+</sup>[TFSI]<sup>-</sup> and [BMIM]<sup>+</sup>[BF<sub>4</sub>]<sup>-</sup> as a function of pore size. The star indicates a reflection from the AAO template.

**Table S1.** Dc-conductivity values from Fig. 4a (data obtained on cooling)

$\sigma_{dc}$ (S/cm) 1000/T (K <sup>-1</sup> )	[BMIM] <sup>+</sup> [Cl] <sup>-</sup>	[BMIM] <sup>+</sup> [Br] <sup>-</sup>	[BMIM] <sup>+</sup> [I] <sup>-</sup>	[BMIM] <sup>+</sup> [BF <sub>4</sub> ] <sup>-</sup>	[BMIM] <sup>+</sup> [PF <sub>6</sub> ] <sup>-</sup>	[BMIM] <sup>+</sup> [TFSI] <sup>-</sup>
5.46001				2.45×10 <sup>-12</sup>		
5.31491				4.41×10 <sup>-11</sup>		1.25×10 <sup>-11</sup>
5.17732				5.02×10 <sup>-10</sup>		3.10×10 <sup>-10</sup>
5.04668				3.80×10 <sup>-9</sup>		3.77×10 <sup>-9</sup>
4.92247				2.12×10 <sup>-8</sup>	9.28×10 <sup>-13</sup>	2.54×10 <sup>-8</sup>
4.80423				9.67×10 <sup>-8</sup>	9.88×10 <sup>-12</sup>	1.34×10 <sup>-7</sup>
4.69153			1.72×10 <sup>-11</sup>	3.60×10 <sup>-7</sup>	7.70×10 <sup>-11</sup>	5.25×10 <sup>-7</sup>
4.584			1.66×10 <sup>-10</sup>	1.10×10 <sup>-6</sup>	4.06×10 <sup>-10</sup>	1.95×10 <sup>-6</sup>
4.48129			1.17×10 <sup>-9</sup>	3.02×10 <sup>-6</sup>	1.88×10 <sup>-9</sup>	5.68 ×10 <sup>-6</sup>
4.38308	2.61×10 <sup>-10</sup>	7.49×10 <sup>-11</sup>	7.21×10 <sup>-9</sup>	7.16×10 <sup>-6</sup>	1.21×10 <sup>-8</sup>	1.47×10 <sup>-5</sup>
4.28908	2.57×10 <sup>-9</sup>	5.67×10 <sup>-10</sup>	2.99×10 <sup>-8</sup>	1.61×10 <sup>-5</sup>	2.01×10 <sup>-7</sup>	3.02×10 <sup>-5</sup>
4.19903	1.85×10 <sup>-8</sup>	3.25×10 <sup>-9</sup>	1.10×10 <sup>-7</sup>	5.71×10 <sup>-5</sup>	1.66×10 <sup>-6</sup>	6.15×10 <sup>-5</sup>
4.11269	1.09×10 <sup>-7</sup>	1.56×10 <sup>-8</sup>	3.78×10 <sup>-7</sup>	9.98×10 <sup>-5</sup>	7.29×10 <sup>-6</sup>	1.11×10 <sup>-4</sup>
4.02982	5.33×10 <sup>-7</sup>	6.04×10 <sup>-8</sup>	1.00×10 <sup>-6</sup>	1.56×10 <sup>-4</sup>	1.67×10 <sup>-5</sup>	1.91×10 <sup>-4</sup>
3.95023	2.20×10 <sup>-6</sup>	2.08×10 <sup>-7</sup>	2.48×10 <sup>-6</sup>	2.74×10 <sup>-4</sup>	3.16×10 <sup>-5</sup>	3.06×10 <sup>-4</sup>
3.87372	8.10×10 <sup>-6</sup>	6.04×10 <sup>-7</sup>	5.79×10 <sup>-6</sup>	4.11×10 <sup>-4</sup>	5.62×10 <sup>-5</sup>	4.66×10 <sup>-4</sup>
3.80011	2.56×10 <sup>-5</sup>	1.66×10 <sup>-6</sup>	1.18×10 <sup>-5</sup>	5.57×10 <sup>-4</sup>	1.00×10 <sup>-4</sup>	6.65×10 <sup>-4</sup>
3.72926	7.13×10 <sup>-5</sup>	3.86×10 <sup>-6</sup>	2.40×10 <sup>-5</sup>	7.18×10 <sup>-4</sup>	1.66×10 <sup>-4</sup>	9.50×10 <sup>-4</sup>
3.66099	1.83×10 <sup>-4</sup>	8.42×10 <sup>-6</sup>	4.31×10 <sup>-5</sup>	1.01×10 <sup>-3</sup>	2.61×10 <sup>-4</sup>	1.36×10 <sup>-3</sup>
3.59518	4.21×10 <sup>-4</sup>	1.76×10 <sup>-5</sup>	7.25×10 <sup>-5</sup>	1.44×10 <sup>-3</sup>	3.86×10 <sup>-4</sup>	1.72×10 <sup>-3</sup>
3.5317	9.25×10 <sup>-4</sup>	3.26×10 <sup>-5</sup>	1.30×10 <sup>-4</sup>	1.93×10 <sup>-3</sup>	5.65×10 <sup>-4</sup>	2.32×10 <sup>-3</sup>
3.47041	1.82×10 <sup>-3</sup>	6.06×10 <sup>-5</sup>	2.05×10 <sup>-4</sup>	2.44×10 <sup>-3</sup>	7.80×10 <sup>-4</sup>	2.76×10 <sup>-3</sup>
3.41122	3.54×10 <sup>-3</sup>	1.06×10 <sup>-4</sup>	3.04×10 <sup>-4</sup>	2.90×10 <sup>-3</sup>	1.07×10 <sup>-3</sup>	3.50×10 <sup>-3</sup>
3.35402	6.18×10 <sup>-3</sup>	1.66×10 <sup>-4</sup>	4.45×10 <sup>-4</sup>	3.46×10 <sup>-3</sup>	1.47×10 <sup>-3</sup>	4.20×10 <sup>-3</sup>
3.2987	9.54×10 <sup>-3</sup>	2.76×10 <sup>-4</sup>	6.59×10 <sup>-4</sup>		2.03×10 <sup>-3</sup>	5.00×10 <sup>-3</sup>

## Chapter 4. Effects of V-shaped Confinement on the Phase State and Ion Dynamics of Ionic Liquids Containing the 1-Butyl-3-methylimidazolium Cation

This chapter has been published on *Journal of Physical Chemistry. C*.

*Yun Dong, Hans-Jürgen Butt, and George Floudas*

J. Phys. Chem. C 2025, 129, 15, 7530–7540

DOI: 10.1021/acs.jpcc.5c00761

### **Author contributions:**

**Yun Dong:** Dielectric spectroscopy and DSC measurements. AAO template characterization and surface modification. Data analysis and interpretation. Writing of a draft of the manuscript.

**George Floudas:** Design of the research topic. Discussion on the results. Writing the final version based on the original draft.

**Hans-Jürgen Butt:** Acquiring funding for the project. Discussion on the research topic/results. Correction of the manuscript.

## Abstract

Ionic liquids (ILs) with the cation 1-butyl-3-methylimidazolium cation ( $[\text{BMIM}]^+$ ) and three different anions (tetrafluoroborate  $[\text{BF}_4]^-$ , bis(trifluoromethylsulfonyl)imide  $[\text{TFSI}]^-$ , and hexafluorophosphate  $[\text{PF}_6]^-$ ) behave differently under nanometer confinement in comparison to bulk. We utilized a series of V-shaped (V) and cylindrically shaped (C) self-ordered nanoporous aluminum oxide (AAO) templates with a range of pore surfaces, volumes, and surface-to-volume ratios. In the V-shaped (C-shaped) templates pore surface increased by 33 (16)-fold, pore volume by 113 (256) -fold and surface-to-volume ratio by 14 (16) -fold. We show that the shape of nanopores (cylindrical vs V-shaped) affects the ion mobility and the phase state of the confined ILs. Cylindrical confinement in the amorphous  $[\text{BMIM}]^+[\text{BF}_4]^-$ , increased the liquid-to-glass temperature (by  $\sim 5$  K) and decreased the dc-conductivity by  $\sim 2$  orders of magnitude relative to bulk. V-shaped confinement produced smaller effects. Silanization of the internal pore surface restored the bulk behavior revealing the dominant role of electrostatic interactions at the IL/AAO interface. ILs bearing larger anions ( $[\text{BMIM}]^+[\text{TFSI}]^-$  and  $[\text{BMIM}]^+[\text{PF}_6]^-$ ) crystallized both in the bulk and under confinement. The melting temperatures decreased in both V-shaped and cylindrical nanopores according to the Gibbs-Thomson equation. The result suggested a dependence of the solid-liquid interfacial energy on pore geometry.

## 4.1 Introduction

Ionic liquids (ILs) are molten salts at temperatures below 100 °C, formed by a large cation and a charge delocalized anion.<sup>1-5</sup> This combination results in weak electrostatic interactions that give rise to some unique properties and applications. In several applications ILs are confined in porous host matrices. Under these conditions, one needs to consider interactions within the formed interface. This has initiated an effort to explore the effect of confinement and of surfaces/interfaces on the ionic conductivity and phase state of ILs both from experiments<sup>6-15</sup> and simulations.<sup>16-18</sup>

With respect to changes in the ionic conductivity, experimental studies of confined ILs have led to conflicting reports.<sup>6-8</sup> This reflects the different ion-wall interactions and the concomitant effects of density modulation near the surface. Confined 1-hexyl-3-methylimidazolium hexafluorophosphate ([HMIM]<sup>+</sup>[PF<sub>6</sub>]<sup>-</sup>) in oxidized nanoporous silica membranes produced a ten-fold decrease in conductivity.<sup>6</sup> In contrast, an enhancement of charge transport in 1-butyl-3-methylimidazolium tetrafluoroborate ([BMIM]<sup>+</sup>[BF<sub>4</sub>]<sup>-</sup>) inside the same membranes was reported. The temperature dependence of ionic conductivity was shown to change from a Vogel-Fulcher-Tammann (VFT) to Arrhenius-like, resulting to an enhancement of diffusivities by more than two orders of magnitude.<sup>7</sup> In another study,<sup>8</sup> the ionic conductivity in 1-hexyl-1-methylpyrrolidinium bis(trifluoromethylsulfonyl)imide ([C6MPyrr]<sup>+</sup>[TFSI]<sup>-</sup>) infiltrated into self-ordered nanoporous aluminum oxide membranes (abbr. AAO) was also enhanced under confinement.

On the other hand, studies on the phase state of confined ILs are scarce. We have recently reported on the structure, the thermodynamics and the ion dynamics of ILs bearing the same cation, 1-butyl-3-methylimidazolium ([BMIM]<sup>+</sup>) and different anions ([Cl]<sup>-</sup>, [Br]<sup>-</sup>, [I]<sup>-</sup>, [BF<sub>4</sub>]<sup>-</sup>, [PF<sub>6</sub>]<sup>-</sup> and [TFSI]<sup>-</sup>) in the bulk, during flow and under confinement in cylindrically shaped nanopores (AAO) with sizes from 25 nm to 400 nm.<sup>9,10</sup> A feature of the effective phase diagrams (temperature vs.  $1/d$ ,  $d$  is the pore diameter) was the complete suppression of crystallization of [BMIM]<sup>+</sup>[TFSI]<sup>-</sup> and [BMIM]<sup>+</sup>[PF<sub>6</sub>]<sup>-</sup> within pores with a diameter of 25 nm. Confinement proved to be an efficient method to suppress the undesired bulk crystallization during heating. Another study<sup>11</sup> reported the phase behavior and dynamics of two ionic liquids of 1-methyl-3-alkylimidazolium tetrafluoroborate [C<sub>n</sub>MIM]<sup>+</sup>[BF<sub>4</sub>]<sup>-</sup> with  $n$  (10 and 12) being the number of carbon atoms in the alkyl chain, confined within cylindrically shaped AAO templates. The same phases (normal and metastable smectic phases, different crystalline phases and the isotropic phase) were found under confinement within pores of size larger than 20 nm.

For sizes in the range from 10- 20 nm the more organized crystalline and smectic phases were completely suppressed. Moreover, as with the earlier investigation,<sup>9</sup> the transition temperatures were found to decrease linearly with inverse pore diameter following the Gibbs-Thompson equation.

Nanometer confinement not only can alter the ion conductivity and possibly the phase state, but in addition, can result in ion current rectification and selective ion transport.<sup>12-15</sup> When surface charge is coupled to the small size and asymmetric nanopore shapes, new transport phenomena emerge. Two such asymmetric ion transport phenomena in nanofluidic structures are: (a) the rectified ion current, and (b) the net diffusion current. The former originates from a diode-like current-voltage response by switching the voltage bias giving rise to a preferential transport direction. The latter, associates with asymmetric ion diffusion produced by charge selectivity. As an example, ion transport in 1-butyl-3-methylimidazolium methylsulfate ([BMIM]<sup>+</sup>[CH<sub>3</sub>SO<sub>4</sub>]<sup>-</sup>) and in 1-butyl-3-methylimidazolium 2-(2-methoxyethoxy) ethyl sulfate ([BMIM]<sup>+</sup>[C<sub>5</sub>H<sub>11</sub>O<sub>2</sub>SO<sub>4</sub>]<sup>-</sup>), in a single conically shaped nanopore - prepared via track-etching of a polyethylene terephthalate film - was reduced relative to the bulk.<sup>12</sup> Moreover, modulation of the electrostatic interactions by chemically modifying the pore walls resulted in inhomogeneous surface charge patterns giving rise to an ionic diode of the confined IL.<sup>12</sup>

Motivated by these intriguing effects of the asymmetric nanopore shapes we investigate here the effect of conical versus cylindrical confinement in the ionic conductivity and phase state of three model ILs; 1-butyl-3-methylimidazolium tetrafluoroborate [BMIM]<sup>+</sup>[BF<sub>4</sub>]<sup>-</sup>, 1-butyl-3-methylimidazolium bis(trifluoromethylsulfonyl)imide ([BMIM]<sup>+</sup>[TFSI]<sup>-</sup>), and 1-butyl-3-methylimidazolium hexafluorophosphate ([BMIM]<sup>+</sup>[PF<sub>6</sub>]<sup>-</sup>). The different anions provide ILs with distinct phase states: from completely amorphous ([BMIM]<sup>+</sup>[BF<sub>4</sub>]<sup>-</sup>) to crystalline ([BMIM]<sup>+</sup>[TFSI]<sup>-</sup> and [BMIM]<sup>+</sup>[PF<sub>6</sub>]<sup>-</sup>). where the effects of ionic conductivity and phase state, respectively, can be investigated. We found that V-shaped confinement produces smaller changes in the liquid-to-glass temperature,  $T_g$  (e.g. in the amorphous [BMIM]<sup>+</sup>[BF<sub>4</sub>]<sup>-</sup>), and weaker effects in the transition temperatures of crystallizable ILs. Both effects diminish by silanizing the pore surface, suggesting the importance of surface/interface effects. Results are discussed in terms of the charge distribution on the pore surface.

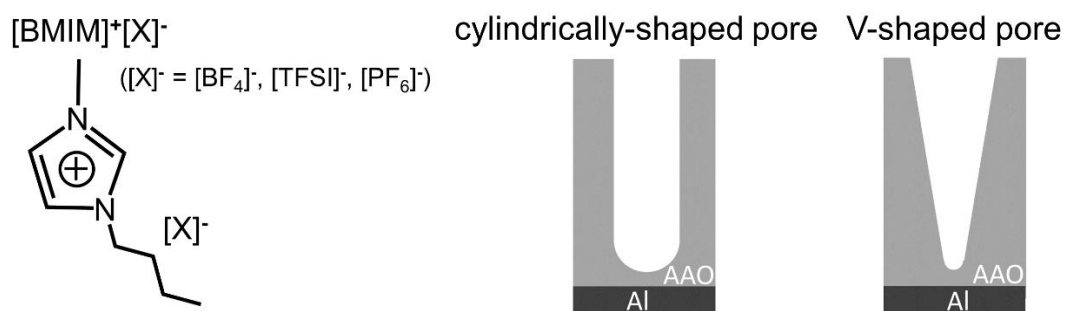
## 4.2 Experimental Section

**Samples.** 1-Butyl-3-methylimidazolium bis(trifluoromethylsulfonyl)imide ([BMIM]<sup>+</sup>[TFSI]<sup>-</sup>, purity  $\geq 98\%$ ), 1-Butyl-3-methylimidazolium tetrafluoroborate ([BMIM]<sup>+</sup>[BF<sub>4</sub>]<sup>-</sup>, purity  $\geq 98\%$ ),

and 1-Butyl-3-methylimidazolium hexafluorophosphate ( $[\text{BMIM}]^+[\text{PF}_6]^-$ , purity  $\geq 98\%$ ) were purchased from Merck and dried in a vacuum oven at 373 K for 24 h before use. The water content was evaluated by  $^1\text{H-NMR}$  measurements in dried samples as reported elsewhere. In addition, the water content was measured by a Karl-Fischer titration method (C20, Mettler Toledo). Following freeze-drying the water content was below 0.06 wt % for  $[\text{BF}_4]^-$ , and below 0.02 wt% for both  $[\text{TFSI}]^-$  and  $[\text{PF}_6]^-$ .<sup>9</sup>

**AAO templates.** We utilized V-shaped (V) and cylindrically shaped (C) self-ordered nanoporous aluminum oxide (AAO) templates, with one open end as shown in **Scheme 1**. V-shaped AAOs were purchased from TopTemplates Technology Ltd. (Shenzhen, China) and had different pore diameters and depths. One set of templates had a top pore diameter of 450 nm and a bottom pore diameter of 100 nm, with varying pore depths of 2.5  $\mu\text{m}$ , 1.5  $\mu\text{m}$ , 0.9  $\mu\text{m}$ , and 0.4  $\mu\text{m}$ , denoted, respectively, as V-450-100-2500, V-450-100-1500, V-450-100-900, and V-450-100-400 (Table 1). Another sample had a top pore diameter of 125 nm, a bottom pore diameter of 40 nm, and a pore depth of 0.25  $\mu\text{m}$  (denoted as V-125-40-250). Cylindrically shaped AAOs (pore diameters of 25, 35, 65, 400 nm; pore depth about 100  $\mu\text{m}$ ) were prepared according to previously reported procedures.<sup>19-22</sup> In both types of templates, the AAO layer was attached to a thick aluminum substrate that served as the bottom electrode in the dielectric measurements. Prior to infiltration, all AAO templates were annealed in a vacuum oven at 423 K for 10-12 h. This procedure removes the majority of OH groups from the AAO surface.<sup>9, 23,</sup>

24



**Scheme 1.** (Left) Schematic of the chemical structure of the ILs. (Right) Schematic of the nanopores in cylindrically (C)- and V-shaped AAOs.

**Table 1.** Parameters of V-shaped and Cylindrically shaped AAO.

Template ID	Top pore diameter (nm)	Bottom pore diameter (nm)	Pore depth ( $\mu\text{m}$ )	Pore surface ( $\times 10^7 \text{ nm}^2$ )	Pore volume ( $\times 10^7 \text{ nm}^3$ )	Surface-to-volume ratio, $S/V$ ( $\text{nm}^{-1}$ )
V-450-100-2500	450	100	2.5	0.233	16.9	0.014
V-450-100-1500	450	100	1.5	0.146	10.1	0.015
V-450-100-900	450	100	0.9	0.0784	6.07	0.016
V-450-100-400	450	100	0.4	0.051	2.70	0.019
V-125-40-250	125	40	0.25	0.0078	0.15	0.052
C-400	400	400	100	12.6	1257	0.010
C-65	65	65	100	2.04	33.2	0.062
C-35	35	35	100	1.10	9.62	0.114
C-25	25	25	100	0.78	4.91	0.159

**Inner pore silanization.** To modify the surface chemistry of V- and cylindrically-shaped AAO templates, hexamethyldisilazane (HMDS) (purity  $\geq 99.0\%$ , purchased from Sigma-Aldrich) was injected into a chamber containing AAOs at 350 K. The templates were completely submerged in HMDS. After 30 min of exposure, the chamber was sealed to maintain pressure and temperature, and the system was kept at 350 K for an additional 3 h to ensure that the reaction was completed. During this process, the hydroxyl (-OH) groups on the template surface were chemically replaced by trimethylsilyl groups. Consequently, this modification rendered the inner surface hydrophobic.

**Infiltration.** Before infiltration, the templates were dried at 423 K under vacuum for 10-12 h to remove possible volatile impurities from the nanopores. Subsequently, the templates were filled with excess IL at ambient temperature by capillary forces. As reported earlier, the IL tested in this study need only a few tens of seconds to completely fill a 100-micrometer-long nanopore.<sup>9, 25-27</sup> The excess IL was removed using soft paper.

**Dielectric spectroscopy (DS).** Isochronal dielectric permittivity measurements of both bulk and confined ILs were made at a frequency of 1 MHz by cooling and subsequent heating. Isothermal measurements of the ionic conductivity as a function of frequency (in the range  $10^{-2}$  to  $10^7$  Hz) were made within the temperature-range from 178 K to 333 K with increment of 5 K. In both cases, a Novocontrol Alpha frequency analyzer, consisting of a broadband dielectric converter and an active sample head was used. For bulk ILs, a Novocontrol cylindrical cell

with electrodes of 10 mm in diameter and sample thickness of 250  $\mu\text{m}$  were used. For the V-shaped and cylindrically shaped AAO templates infiltrated with ILs, a 10 mm electrode was placed on top of the templates, while the Al at the bottom of the templates served as the second electrode. The measured dielectric curves were corrected by modeling the system as two capacitors in parallel, represented by the complex dielectric functions of the IL ( $\epsilon^*_{IL}$ ) and the alumina ( $\epsilon^*_{AAO}$ ).<sup>28,29</sup> The total measured impedance ( $Z^*$ ) is related to the individual impedances through  $1/Z^* = 1/Z^*_{IL} + 1/Z^*_{AAO}$ . In all measurements, the complex dielectric function, denoted as  $\epsilon^* = \epsilon' - i\epsilon''$ , where  $\epsilon'$  and  $\epsilon''$  represent the corresponding real (known as dielectric permittivity) and imaginary (dielectric loss) components. The dc-conductivity was obtained from the complex conductivity function through  $\sigma^* = \sigma' + i\sigma''$ , where  $\sigma'$  and  $\sigma''$  are the real (i.e., the dc-conductivity) and imaginary parts, respectively. The complex conductivity function is related to the complex dielectric function through  $\sigma^* = i\omega\epsilon_0\epsilon^*$ . To extract the dc conductivity, the plateau in the real part  $\sigma'$  was employed.

**X-ray diffraction.** The  $\theta/2\theta$  scans were measured with a Rigaku SmartLab X-ray diffractometer. The X-ray source was a rotating anode (Cu) operating at a voltage of 45 kV and a current of 200 mA. The incident optics employed a monochromator (Ge crystal for the 220 reflection) followed by a parallel slit (incident Soller slit  $2.5^\circ$ ). A diffracted beam monochromator was inserted between the detector slit and the detector to suppress fluorescence radiation and the unwanted  $K_\beta$  radiation. The receiving optics had a parallel slit analyzer (PSA) followed by a receiving Soller slit. The wavelength was 0.154059 nm. A HyPix-3000 2D detector was used (pixel size  $100 \mu\text{m} \times 100 \mu\text{m}$ ; active area  $38.5 \text{ mm} \times 77.5 \text{ mm}$ ). Temperature-dependent measurements of ILs under confinement were performed with the help of a Low-Temperature Chamber (TTK 600, Anton Paar GmbH., Germany) used for sample temperature control between 200 K and 285 K. Initially, the sample was slowly cooled ( $5 \text{ K min}^{-1}$ ) from ambient temperature to 200 K. Scans in the  $2\theta$ -range from  $0$  to  $60^\circ$  in steps of  $0.01^\circ$  were then conducted at selected temperatures (240 K, 255 K, 265 K, and 285 K) during the subsequent heating process. During the XRD measurements the AAO surface was oriented perpendicularly to the plane of the incident and scattered X-ray beams. The measured scattering intensity data were corrected for the background contribution, including scattering from the bare AAO template.

**Scanning Electron Microscopy (SEM).** High-resolution cross-section images of V-shaped AAOs were recorded using a Hitachi 8000 scanning electron microscope. To characterize the pore depth, samples were cut, and the cross-sections were mounted vertically on aluminum

SEM stubs using high-purity carbon tape. Imaging was conducted at a working distance of 4 mm and a voltage of 3 kV (Figure 1). Pore diameters and the corresponding porosities were characterized by SEM and are shown in **Figure S1, Supporting Information**.

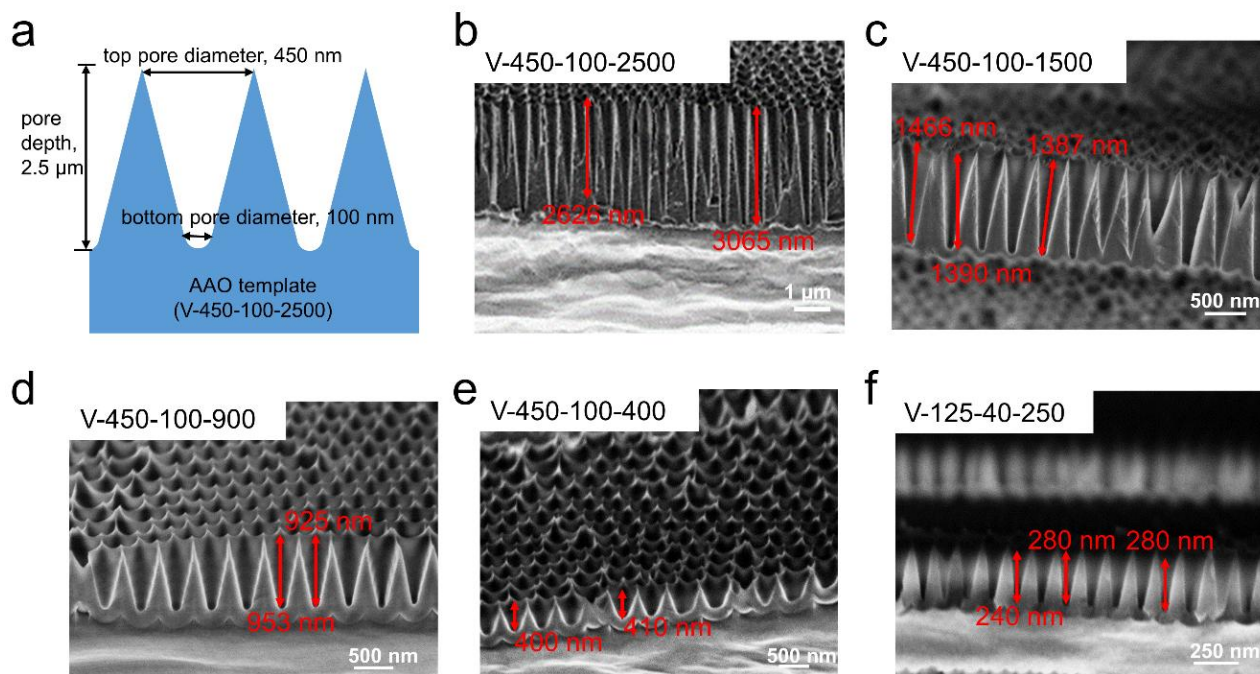


**Figure 1.** (a) Schematic of a V-shaped AAO template and its parameters. (b, c, d, e, f): Cross-sectional SEM micrographs of V-shaped membranes with different pore depths: 2.5  $\mu\text{m}$ , 1.5  $\mu\text{m}$ , 0.9  $\mu\text{m}$ , 0.4  $\mu\text{m}$ , and 0.25  $\mu\text{m}$ , respectively. The red arrow indicates the measured pore depths.

### 4.3 Results and Discussion

First, we investigate the effect of conical versus cylindrical confinement on the ionic conductivity of the amorphous  $[\text{BMIM}]^+[\text{BF}_4]^-$ . We then proceed with the more complex  $[\text{BMIM}]^+[\text{TFSI}]^-$  and  $[\text{BMIM}]^+[\text{PF}_6]^-$ . In contrast to  $[\text{BMIM}]^+[\text{BF}_4]^-$ , they exhibit several first order transitions.

#### a. Effect of pore shape on the freezing behavior of the amorphous $[\text{BMIM}]^+[\text{BF}_4]^-$

The  $[\text{BMIM}]^+[\text{BF}_4]^-$  is completely amorphous as demonstrated by the DSC traces on cooling/heating runs (**Figure S2**). To explore the effects of V-shaped confinement, temperature scans were performed following full imbibition. The temperature dependence of dc-conductivity obtained on cooling, starting from ambient temperature down to the glassy state, as well as the characteristic ion relaxation times extracted from the modulus representation (as

$M^*=1/\varepsilon^*$ ;  $M^*$  is the complex electric modulus) are plotted in Figure 2. In all cases, the  $\sigma_{dc}(T)$  dependence and the characteristic ion relaxation times follow approximately the Vogel-Fulcher-Tammann (VFT) equation written for the conductivity contribution as:

$$\sigma_{dc}(T) = \sigma_0^\ddagger \exp\left(-\frac{B}{T-T_0}\right) \quad (1)$$

Here,  $\sigma_0^\ddagger$  is the dc-conductivity in the limit of very high temperatures,  $B$  is the activation parameter and  $T_0$  is the “ideal” glass temperature. It has been reported earlier that a single VFT function does not suffice to describe adequately the whole  $\sigma(T)$ . Subsequently, a VFT was used from the lowest temperature to a limited high temperature shown with arrows in Figure 2. The thus obtained VFT parameters are summarized in Table 2. We note here that the  $\sigma_{dc}(T)$  results for bulk  $[\text{BMIM}]^+[\text{BF}_4]^-$  are in good agreement with earlier literature values.<sup>8,30</sup> For the confined IL the results reveal a lower dc-conductivity than the bulk for all pore diameters. In this case the electrostatic properties of the native AAO pore walls need to be explored as ions can be immobilized at the pore walls.<sup>9</sup> To prove this possibility, we have first silanized the pores with HMDS and subsequently infiltrated the AAO templates with the IL. The result of this procedure for  $\sigma(T)$  is shown in **Figure S3**. The figure depicts increased conductivity, relative to the untreated pores, approaching the bulk values. The result suggests the immobilization of ions at the untreated pore walls, as the reason for the reduced conductivity.

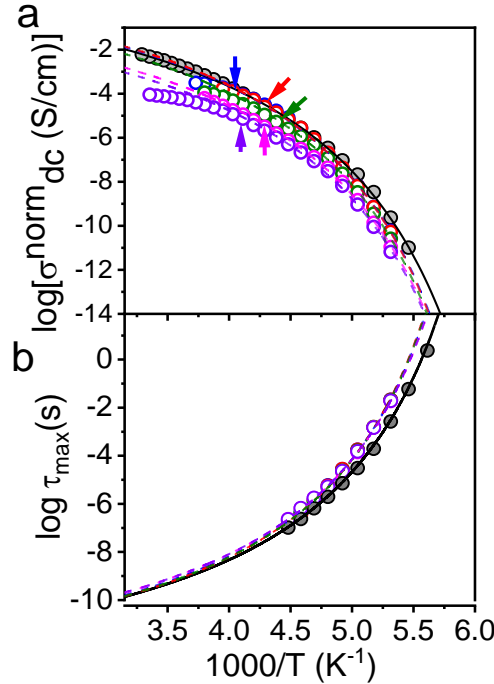


**Figure 2.** (a) Temperature dependence of the dc-conductivity of bulk (gray) and confined  $[\text{BMIM}]^+[\text{BF}_4]^-$  in V-shaped AAO with different pore dimensions following full imbibition: V-

450-100-2500 (red), V-450-100-1500 (blue), V-450-100-900 (olive), V-450-100-400 (magenta), and V-125-40-250 (purple). The dashed line represents VFT fits. Arrows indicate the high temperature limit employed in the VFT fits. (b) Characteristic times of ion relaxation extracted from the maximum of the modulus representation plotted as a function of reciprocal temperature and fitted to the respective VFT equation.

**Table 2.** Parameters of the VFT Equation for [BMIM]<sup>+</sup>[BF<sub>4</sub>]<sup>-</sup> Pertinent to the Temperature Scan Experiments.

Template ID	$-\log_{10}(\tau_0/s)$	$B^\tau$ (K)	$T_0^\tau$ (K)	$\log_{10}[\sigma_0^\tau / (S \cdot cm^{-1})]$	$B^\sigma$ (K)	$T_0^\sigma$ (K)
bulk	12.2	$919 \pm 10$	$147 \pm 1$	0.71	$1080 \pm 18$	$143 \pm 1$
V-450-100-2500	12.2	$919^a$	$150 \pm 1$	0.85	$1080^a$	$145 \pm 1$
V-450-100-1500	12.2	$919^a$	$150 \pm 1$	0.89	$1080^a$	$145 \pm 1$
V-450-100-900	12.2	$919^a$	$150 \pm 1$	0.54	$1080^a$	$145 \pm 1$
V-450-100-400	12.1	$919^a$	$150 \pm 1$	-0.10	$1080^a$	$145 \pm 1$
V-125-40-250	12.1	$919^a$	$150 \pm 1$	-0.32	$1080^a$	$145 \pm 1$

<sup>a</sup>Value held fixed.

To further explore the effect of the pore shape on the ionic conductivity and characteristic relaxation times of [BMIM]<sup>+</sup>[BF<sub>4</sub>]<sup>-</sup> we compare the two quantities within V-shaped and cylindrically shaped AAO in Figure 3. The two types of templates have similar pore volumes – except for C-400 – but very different pore surface and consequently surface to volume ratios ( $S/V$  from  $0.016 \text{ nm}^{-1}$  to  $0.16 \text{ nm}^{-1}$ , within V- and cylindrically-shaped AAO templates, respectively and pore volumes of  $6.07 \times 10^7 \text{ nm}^3$  and  $4.91 \times 10^7 \text{ nm}^3$ ). The dc-conductivity and the characteristic times of ion mobility follow a VFT dependence and the parameters are summarized in Table 3. A lower dc-conductivity is evident within the cylindrically shaped AAO as compared to the V-shaped AAO and to the bulk. We attribute the lower conductivity in C-25 - at least partially - to immobilized ions at the pore surface (e.g. C-25 has ten times the pore surface of V-450-100-900). As we will discuss below with respect to Figure 4, pore surface is not the only parameter affecting the dc-conductivity.

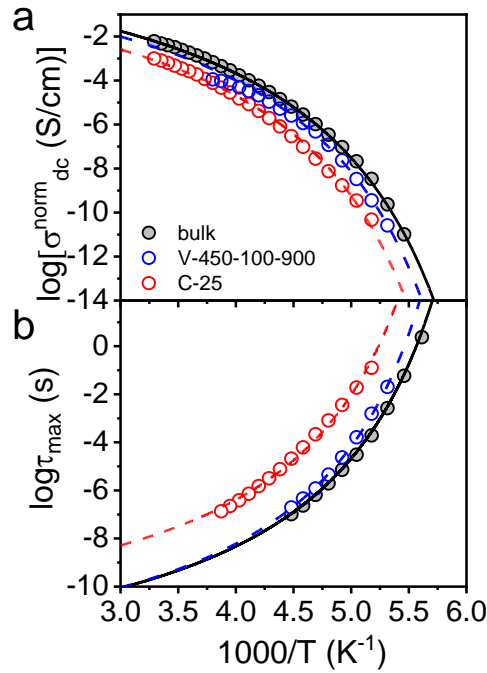


**Figure 3.** (a) Comparison of temperature dependence of dc-conductivity (normalized for the porosity) for bulk (gray) and confined  $[\text{BMIM}]^+[\text{BF}_4]^-$  in V-shaped (blue) and cylindrically shaped AAO (red) following full imbibition. The dashed line represents VFT fits. (b) Characteristic times of ion relaxation extracted from the maximum of the modulus representation plotted as a function of the reciprocal temperature. Lines are fits to the corresponding VFT equation.

**Table 3.** Parameters of the VFT Equation for  $[\text{BMIM}]^+[\text{BF}_4]^-$  under V- and Cylindrically Shaped Templates Pertinent to the Temperature Scan Experiments Following Imbibition.

Template ID	$-\log_{10}(\tau_0/\text{s})$	$B^\tau$ (K)	$T_0^\tau$ (K)	$\log_{10}[\sigma_0^\tau/(\text{S}\cdot\text{cm}^{-1})]$	$B^\sigma$ (K)	$T_0^\sigma$ (K)
bulk	12.2	$919 \pm 10$	$147 \pm 1$	0.71	$1080 \pm 18$	$143 \pm 1$
V-450-100-900	12.2	$919^a$	$150 \pm 1$	0.54	$1080^a$	$145 \pm 1$
C-25	10.5	$919^a$	$153 \pm 1$	0.05	$1080^a$	$149 \pm 1$

<sup>a</sup>Value held fixed.

The glass temperature(s) of  $[\text{BMIM}]^+[\text{BF}_4]^-$  in bulk and V- and cylindrically shaped nanopores were obtained from the dc-conductivity measurements by extrapolating the VFT dependence to a value of  $\sigma_{dc} \sim 10^{-12} \text{ S}\cdot\text{cm}^{-1}$  (Figure 4). Irrespective of nanopore geometry,  $T_g$  is moderately to strongly affected by confinement. In both cases it is higher than in bulk, but the effect is stronger for cylindrical confinement. In the latter,  $T_g$  scales with the pore surface as:  $T_g = (200.0 \pm 0.4) - (1.79 \pm 0.05) \times \log S$ . In V-shaped nanopores it follows:  $T_g = (192 \pm 2) - (1.5 \pm 0.3) \times \log S$ . The scaling with the pore volume is  $T_g = (194.9 \pm 0.2) - (0.89 \pm 0.02) \times \log V$

and  $T_g = (191 \pm 2) - (1.0 \pm 0.3) \times \log V$ , respectively, for cylindrical and V-shaped nanopores. Comparison of the glass temperature as a function of the surface to volume ratio of nanopores gives a parabolic dependence. It suggests the immobilization of ions on the pore surface. To explore this possibility we silanized the pores and the effect on  $T_g$  is shown in Figure 4 with the crossed symbols. In the silanized nanopores  $T_g$  approaches the bulk value, indicating that surface modification reduces the propensity of ions for adsorption. In the smaller pores, the  $T_g$  does not attain the bulk value, likely due to incomplete silanization.

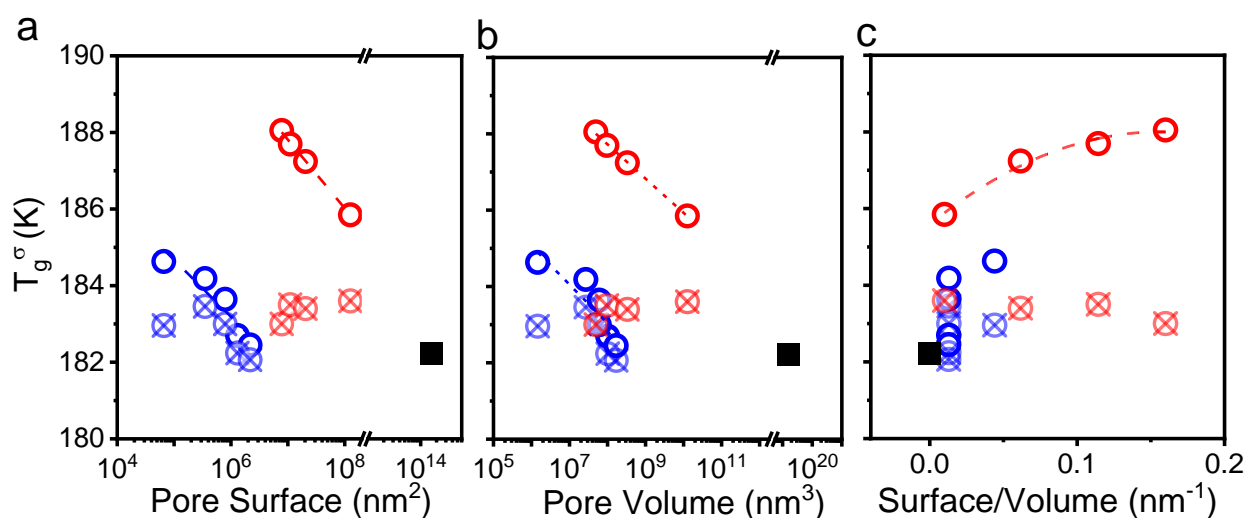


**Figure 4.** Glass temperature ( $T_g$ ) of  $[\text{BMIM}]^+[\text{BF}_4]^-$  in bulk and under V-shaped (in blue) and cylindrical (in red) confinement as a function of pore (a) surface, (b) volume, and (c) surface/volume. The glass temperature is extracted from the  $\sigma_{\text{dc}}(T)$  dependence (by extrapolating the VFT dependence to a value of  $\sigma_{\text{dc}} \sim 10^{-12} \text{ S} \cdot \text{cm}^{-1}$ ). The glass temperatures in the silanized templates are shown with crossed symbols. The  $T_g$  in the bulk IL is shown with a filled square.

In conclusion, confinement of the  $[\text{BMIM}]^+[\text{BF}_4]^-$  in cylindrically shaped nanopores increases the glass temperature and consequently, decreases the dc-conductivity. It suggests the immobilization of ions at the pore surface. Silanization of the internal pore surface partially removes this effect and restores the bulk conductivity. Confinement within V-shaped nanopores produces also an increase in the glass temperature but the effect is small when compared to cylindrical confinement. For the same pore surface or pore volume the increase in  $T_g$  is about 5 K higher for cylindrical nanopores. One possible explanation for the different  $T_g$ -effect is that in cylindrically shaped nanopores, confinement is uniform along the pore length. Contrast this with V-shaped nanopores, where the degree of confinement varies along the pore length. As a result, the distribution of charges on the pore walls is expected to be uniform (not uniform) for cylindrically shaped (V-shaped) nanopores. The uneven distribution of charges at the pore walls

in the V-shaped nanopores could mitigate the Coulomb attractions towards the narrower pore openings and restore – at least partially - the bulk behavior. This requires electrostatic interactions of much longer range than theoretically predicted, e.g. by the Gouy-Chapman theory of the electric double layer. Interestingly, molecular dynamics simulations of the structure of electrical double layer in ILs have shown deviations from the Gouy-Chapman theory.<sup>31,32</sup> They even suggested that the double layer extends over several nm (beyond a single molecular layer).

**b. The effect of V-shaped confinement on [BMIM]<sup>+</sup>[TFSI]<sup>-</sup> and [BMIM]<sup>+</sup>[PF6]<sup>-</sup>**

ILs with larger anions ([TFSI]<sup>-</sup>, [PF6]<sup>-</sup>) exhibit a richer phase behavior. [BMIM]<sup>+</sup>[TFSI]<sup>-</sup> during cooling remains amorphous as with the [BMIM]<sup>+</sup>[BF4]<sup>-</sup>. However, on heating it undergoes cold crystallization ( $T_{cc}$ ) and melting transitions ( $T_m$ ) (**Figure S2**). To construct the effective phase diagram of the two ILs we employ the temperature dependence of dielectric permittivity. The latter is known to be a very sensitive probe of the temperature of phase transformations.<sup>33,34</sup> A comparison of the dielectric permittivity and its derivative with respect to temperature for bulk and confined [BMIM]<sup>+</sup>[TFSI]<sup>-</sup> in V- and cylindrically shaped AAOs is presented in Figure 5. As expected from the DSC study, the dielectric permittivity of the bulk IL on cooling decreases without any discontinuity. On subsequent heating, it first increases up to about 226 K and subsequently decreases to a lower value during the process of cold crystallization. On further heating it increases discontinuously at the melting transition ( $T \sim 267$  K) back to the melt state. We extracted the cold crystallization and melting temperatures from the first derivative of dielectric permittivity with respect to temperature; for the former we employ the temperature where the derivative is zero (blue arrow in Figure 5b), and for the latter the temperature corresponding to the steepest increase of  $\epsilon'$  or the peak in the first derivative (red arrow in Figure 5b). Within V-shaped nanopores, the cold crystallization temperature is strongly affected increasing by  $\sim 14$  K. On the other hand, the melting temperature is solely decreasing on confinement according to the Gibbs-Thomson equation<sup>35,36</sup>:

$$T_m(d) = T_{m,bulk} \left( 1 - \frac{4M\gamma_{sl}}{\Delta_{fus}H \rho_s d} \right) \quad (2)$$

Here,  $T_m(d)$  is melting temperature of the confined IL,  $T_{m,bulk}$  is melting temperature of the bulk IL,  $M$  is the molar mass,  $\gamma_{sl}$  is solid-liquid interfacial energy,  $\Delta_{fus}H$  is the molar enthalpy of fusion,  $\rho_s$  is density of the solid phase, and  $d$  is the pore diameter. The result of the effect of confinement on the transition temperatures along with  $T_g$  derived from the  $\sigma_{dc}(T)$  dependence (**Figure S4**), are plotted as function of the surface-to-volume ratio of nanopores in Figure 6 for

both V-shaped and cylindrically shaped nanopores.

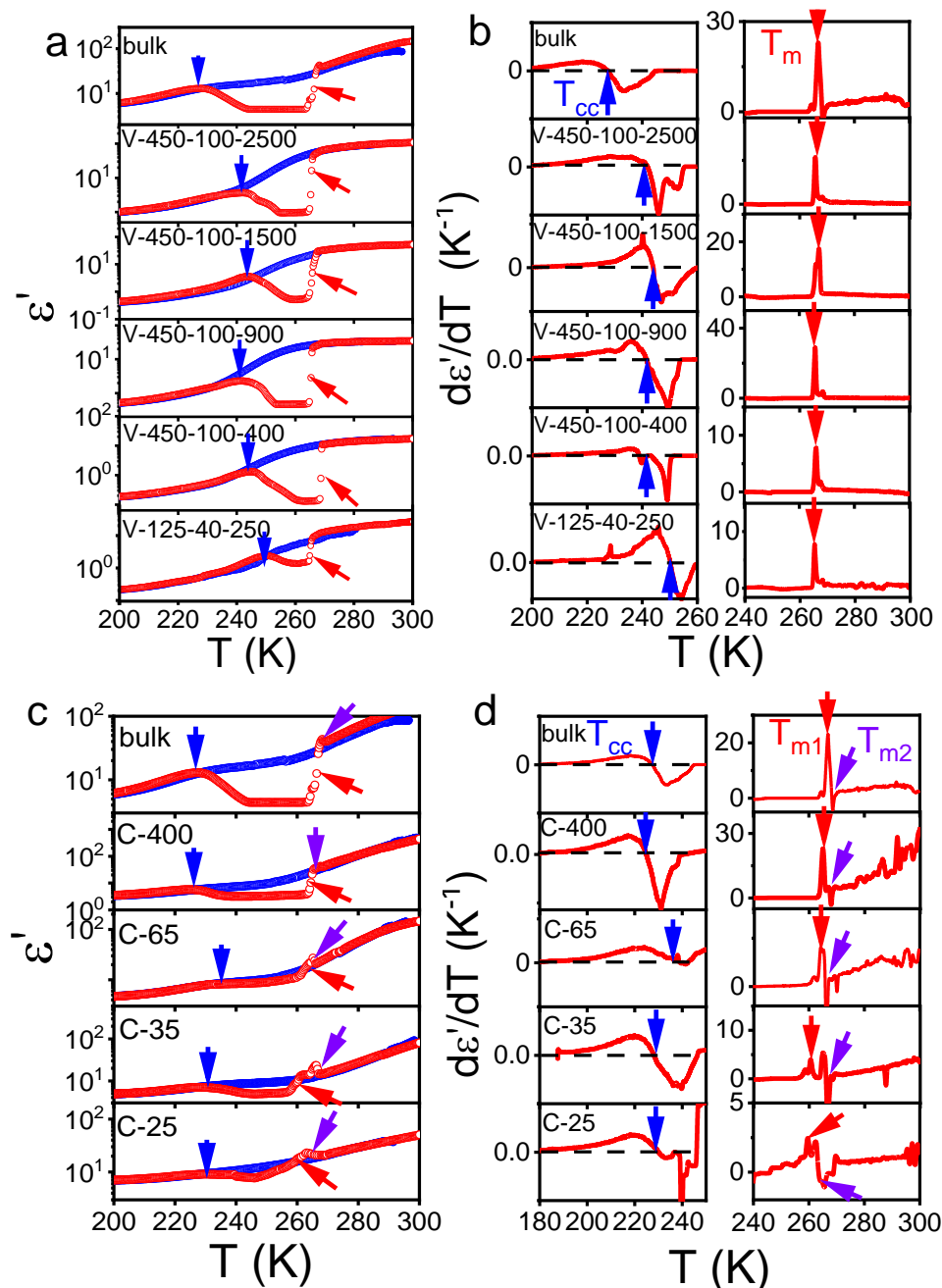


**Figure 5.** Temperature dependence of the dielectric permittivity for bulk [BMIM]<sup>+</sup>[TFSI]<sup>-</sup> and [BMIM]<sup>+</sup>[TFSI]<sup>-</sup> inside AAO with different pore sizes measured at 1 MHz. (a) Dielectric permittivity obtained from V-shaped AAO on cooling (blue) and subsequent heating (red) scans with a rate of 5 K min<sup>-1</sup>. (b) Derivative of dielectric permittivity curves with respect to temperature during heating plotted as a function of temperature. (c) Dielectric permittivity obtained from cylindrical AAO on cooling (blue) and subsequent heating (red) with a rate of 5 K min<sup>-1</sup>. (d) Derivative of dielectric permittivity curves of heating scan in panel c as a function of temperature. Arrows indicate the cold-crystallization temperature (in blue) and melting temperatures (red, violet).

The main effects of the phase behavior is (a) the reduced melting temperatures on confinement, and (b) the temperature range of crystallization ( $\Delta T = T_m(d) - T_{cc}(d)$ ) is reduced substantially under V-confinement indicating suppressed tendency for crystallization and/or slower crystallization kinetics. Indeed, confined  $[\text{BMIM}]^+[\text{TFSI}]^-$  within V-shaped nanopores exhibits a higher  $T_{cc}$  and a lower  $T_m$ . In direct analogy to the Gibbs-Thomson equation, the melting temperature within V-shaped nanopores follows:  $T_m^V = 266.7 \pm 0.4 - (40 \pm 17)S/V$ , whereas within cylindrically-shaped nanopores follows:  $T_m^C = 265.6 \pm 0.5 - (36 \pm 5)S/V$ . The reduced melting temperatures could associate with a reduced solid-liquid interfacial energy.

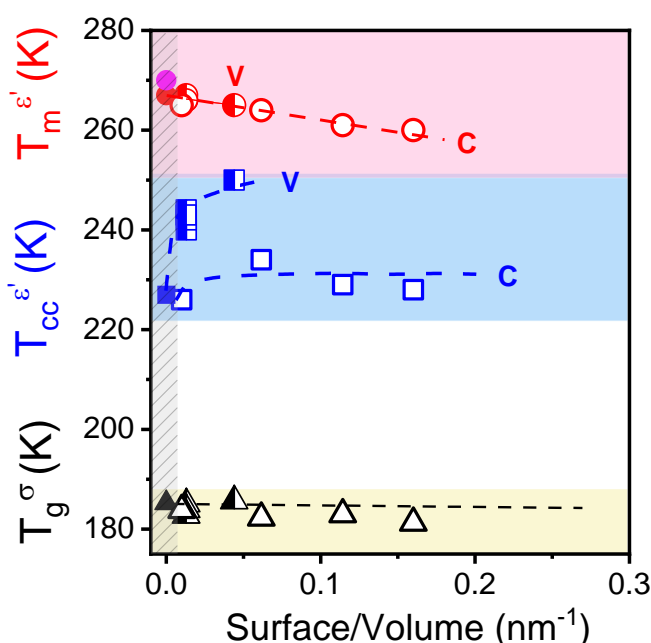


**Figure 6.** Effective phase diagram of  $[\text{BMIM}]^+[\text{TFSI}]^-$  in bulk (solid symbols), V-shaped (half-filled symbols) and cylindrically confined (open symbols) AAO. The  $T_g$  (triangles) was obtained from the  $\sigma_{dc}(T)$  dependence (by extrapolating the VFT dependence to a value of  $\sigma_{dc} \sim 10^{-12} \text{ S}\cdot\text{cm}^{-1}$ ). The cold-crystallization temperature  $T_{cc}$  (squares) and melting temperature  $T_m$  (circles) are obtained from isochronal dielectric spectroscopy measurements at a frequency of 1 MHz and a rate of  $5 \text{ K}\cdot\text{min}^{-1}$ . Dashed lines are to guide the eye. Regions in red, blue and yellow indicate melting, cold crystallization and glass formation, respectively.

Can confinement affect the crystal structure of the ILs? To address this question, we employed XRD. Representative XRD curves for bulk  $[\text{BMIM}]^+[\text{TFSI}]^-$  and  $[\text{BMIM}]^+[\text{TFSI}]^-$  located inside V-shaped AAO (V-450-100-2500) and within cylindrically shaped AAO (C-400) at some selected temperatures following slow cooling (at a rate of  $5 \text{ K}\cdot\text{min}^{-1}$ ) from ambient temperature to the glassy state are depicted in Figure 7. Bulk  $[\text{BMIM}]^+[\text{TFSI}]^-$  demonstrated

an amorphous structure at 278 K, confirmed by the absence of sharp diffraction peaks. In V-shaped AAO (Figure 7a), upon cooling and subsequent heating, cold crystallization was observed at 230 K. It gave rise to the intense diffraction peaks at  $q$  values of  $5.48 \text{ nm}^{-1}$ ,  $11.1 \text{ nm}^{-1}$ ,  $16.6 \text{ nm}^{-1}$  and  $22.0 \text{ nm}^{-1}$ , corresponding to the (100), (110), (200), (300), and (400) reflections from a simple tetragonal unit cell (unit cell parameters of  $a = 1.13 \text{ nm}$ , and  $b = 1.25 \text{ nm}$ ). The structure persists up to the melting at 280 K, indicating stability across the examined temperature range. These observations align with dielectric permittivity data, which showed a single cold crystallization and melting behavior under confinement. The crystal structure of  $[\text{BMIM}]^+[\text{TFSI}]^-$  within the cylindrically shaped AAO (Figure 7c), is the same as within V-shaped nanopores with identical unit cell parameters.

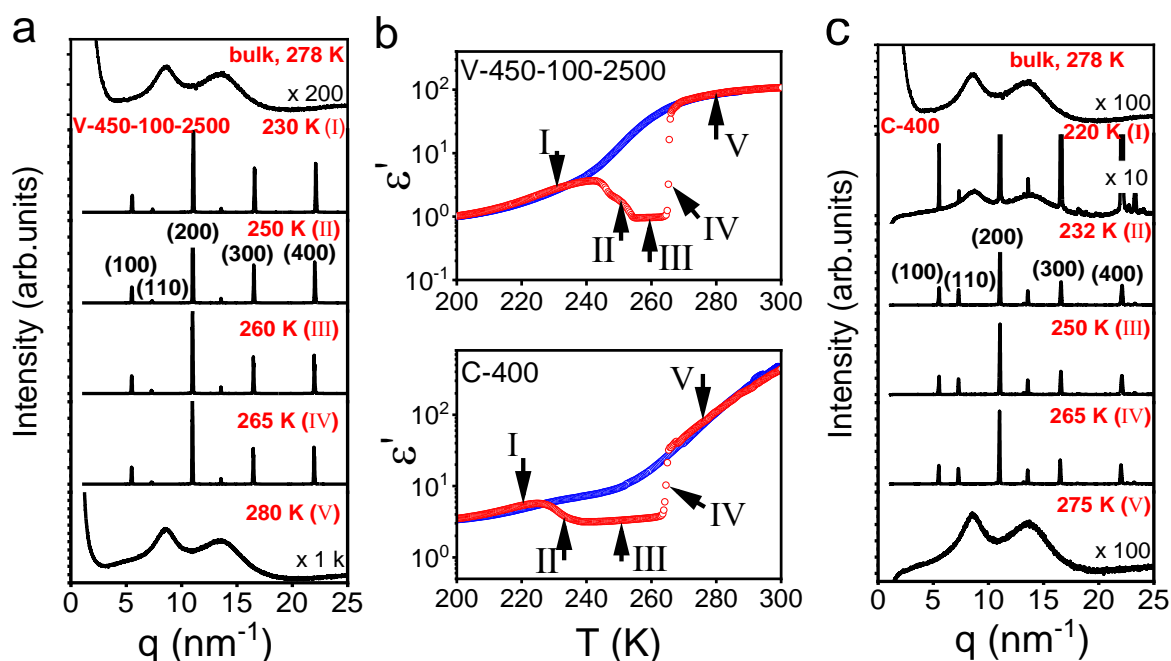


**Figure 7.** Structure analysis of  $[\text{BMIM}]^+[\text{TFSI}]^-$  in bulk and confined within V-shaped (V-450-100-2500), and cylindrically shaped (C-400) AAO nanopores in comparison to (b) dielectric permittivity data obtained under isochronal conditions (1 MHz) on cooling (in blue) and subsequent heating (in red) (rate 5 K/min). (a, c) X-ray scattering curves at various temperatures as a function of the modulus of the scattering vector  $q$ , for  $[\text{BMIM}]^+[\text{TFSI}]^-$  confined in (a) V-shaped, and (c) cylindrically shaped AAO. The dielectric permittivity data were used as a guide in recording the XRD curves at selected temperatures (shown with Latin numbers). Figures are scaled appropriately for visibility (indicated by multipliers).

Overall,  $[\text{BMIM}]^+[\text{TFSI}]^-$  crystallizes in the same structure within cylindrically- and V-shaped nanopores with identical unit cell parameters but the cold crystallization temperatures are affected by the type of confinement. Within V-shaped nanopores  $[\text{BMIM}]^+[\text{TFSI}]^-$  exhibits a higher  $T_{cc}$  and a lower  $T_m$  suggesting a reduced tendency for crystallization and/or slower

crystallization kinetics. Apart from this, the main result of confinement is the reduction in the melting temperature. It suggests a reduced solid-liquid interfacial energy.

The phase behavior of  $[\text{BMIM}]^+[\text{PF}_6]^-$  is even more complex. In the bulk, and in accord with the DSC trace (**Figure S2**), the IL undergoes several transitions on heating: cold crystallization followed by melting, re-crystallization and re-melting. The phase behavior of bulk  $[\text{BMIM}]^+[\text{PF}_6]^-$  and  $[\text{BMIM}]^+[\text{PF}_6]^-$  inside V- and cylindrically shaped AAO was investigated by dielectric permittivity measurements. The thermodynamic transitions are very evident in the dielectric permittivity curves recorded on heating (Figure 8a). For  $[\text{BMIM}]^+[\text{PF}_6]^-$  within V-shaped nanopores the same transitions are evident, however, at somewhat different temperatures. Overall, the re-crystallization and melting process was more evident under V-shaped confinement as compared to the same transitions in cylindrically shaped AAO, especially within the smaller pores where transitions were smeared out (Figure 8c).

The effects of confinement on the transition temperatures of  $[\text{BMIM}]^+[\text{PF}_6]^-$  can be discussed with the help of the phase diagram of Figure 9. The Figure depicts dual crystallization and melting temperatures as a function of the surface to volume ratio of nanopores. All transition temperatures are reduced with increasing confinement (e.g. increasing  $S/V$  ratio).

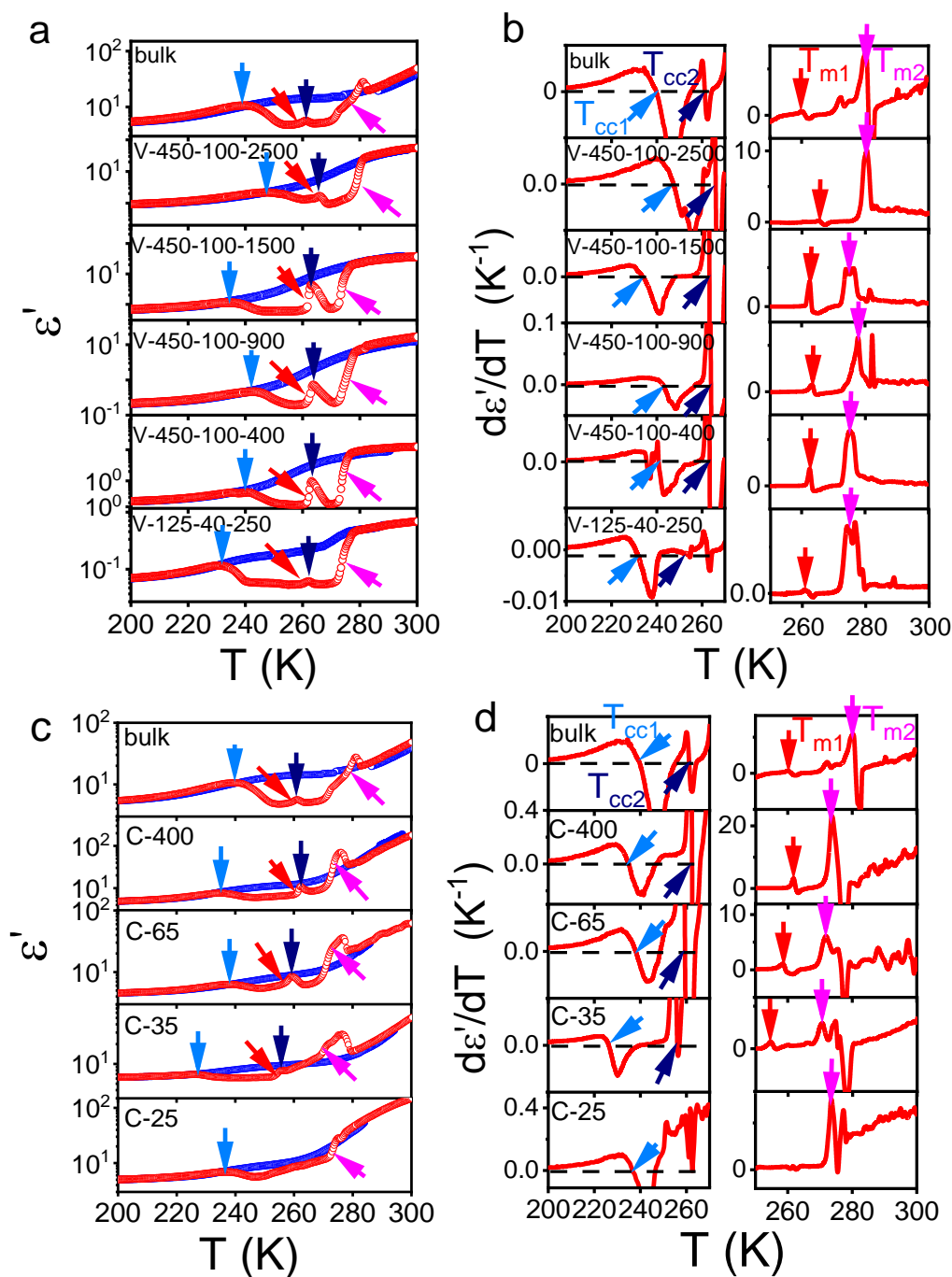


**Figure 8.** Temperature dependence of the dielectric permittivity for bulk [BMIM]<sup>+</sup>[PF<sub>6</sub>]<sup>-</sup> and [BMIM]<sup>+</sup>[PF<sub>6</sub>]<sup>-</sup> inside V- and cylindrically shaped AAO measured at 1 MHz. (a) Dielectric permittivity obtained from V-shaped AAO on cooling (blue) and subsequent heating (red) scans with a rate of 5 K/min. (b) Derivative of dielectric permittivity curves with respect to temperature during heating plotted against temperature. (c) Dielectric permittivity obtained from cylindrically shaped AAO on cooling (blue) and subsequent heating (red) scans with a rate of 5 K/min. (d) Derivative of dielectric permittivity curves with respect to temperature during heating plotted as a function of temperature. Arrows indicate the cold-crystallization temperature  $T_{cc1}$  (navy blue), recrystallization  $T_{cc2}$  (light blue) and melting temperatures  $T_{m1}$  (red),  $T_{m2}$  (magenta).

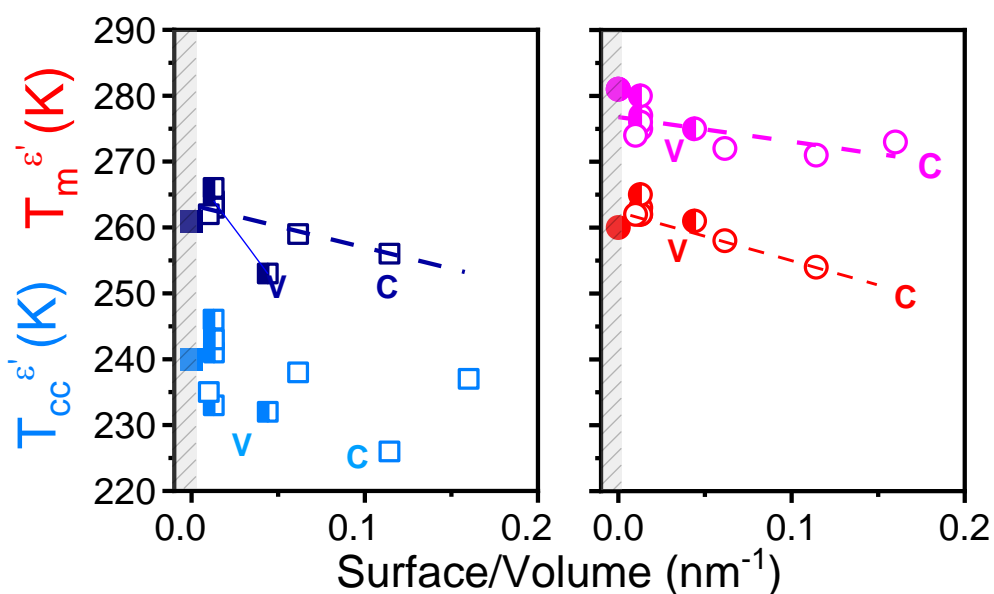


**Figure 9.** Effective phase diagram of  $[\text{BMIM}]^+[\text{PF}_6]^-$  within bulk (solid symbols), V-shaped (half-filled symbols), and cylindrical (open symbols) AAO obtained during the isochronal dielectric measurements at a frequency of 1 MHz and a rate of  $5 \text{ K}\cdot\text{min}^{-1}$ . Navy and blue squares denote temperatures at which cold crystallization and re-crystallization takes place. Red and magenta circles denote two melting processes corresponding to the crystallization and recrystallization processes.

The cold crystallization, melting, and re-crystallization process of  $[\text{BMIM}]^+[\text{PF}_6]^-$  brings forward a question as to whether the crystal structures are equivalent. Figure 10 compiles XRD and isochronal dielectric permittivity measurements of  $[\text{BMIM}]^+[\text{PF}_6]^-$  in V- and cylindrically shaped AAO at different temperatures. The XRD measurements are made at temperatures suggested by the modulations in dielectric permittivity (**Figure 10b**). In V-shaped AAO,  $[\text{BMIM}]^+[\text{PF}_6]^-$  undergoes cold crystallization at 255 K, with several Bragg peaks at  $q$  values of  $4.5 \text{ nm}^{-1}$ ,  $10.5 \text{ nm}^{-1}$ ,  $15.8 \text{ nm}^{-1}$ , and  $20.6 \text{ nm}^{-1}$  that correspond to the (200), (230), (700), and (910) reflections from a simple tetragonal unit cell (parameters  $a = 2.78 \text{ nm}$  and  $b = 1.99 \text{ nm}$ ). At temperatures above 265 K, the diffraction pattern changes and shows Bragg peaks at  $q$  values of  $8.9 \text{ nm}^{-1}$ ,  $10.5 \text{ nm}^{-1}$ ,  $15.0 \text{ nm}^{-1}$ , and  $20.6 \text{ nm}^{-1}$  corresponding to the (120), (200), (300), and (400) reflections again from a simple tetragonal lattice but with reduced unit cell parameters ( $a = 1.20 \text{ nm}$  and  $b = 1.77 \text{ nm}$ ). Hence, the distinct changes in dielectric permittivity correspond to changes from a larger to a smaller simple tetragonal structure.

In cylindrically shaped AAO,  $[\text{BMIM}]^+[\text{PF}_6]^-$  crystallized at 240 K. The structure can be described as a simple tetragonal unit cell with parameters  $a = 2.71 \text{ nm}$  and  $b = 2.08 \text{ nm}$ , *i.e.* as with the V-shaped AAO at 255 K. At temperatures above 265 K there is a structural change to

another simple tetragonal lattice with reduced parameters ( $a = 1.15$  nm and  $b = 1.84$  nm). As a result, the structural changes obtained in cylindrical and V-shaped nanopores are equivalent. They correspond to the collapse of a larger tetragonal cell to a smaller one by increasing temperature. This implies that the critical nucleus size of the two simple tetragonal lattices is smaller than the volumes of nanopores in the V- and C-shaped nanopores. This feature could be definitely addressed by studying even smaller pore volumes that are not accessible to us at the moment.

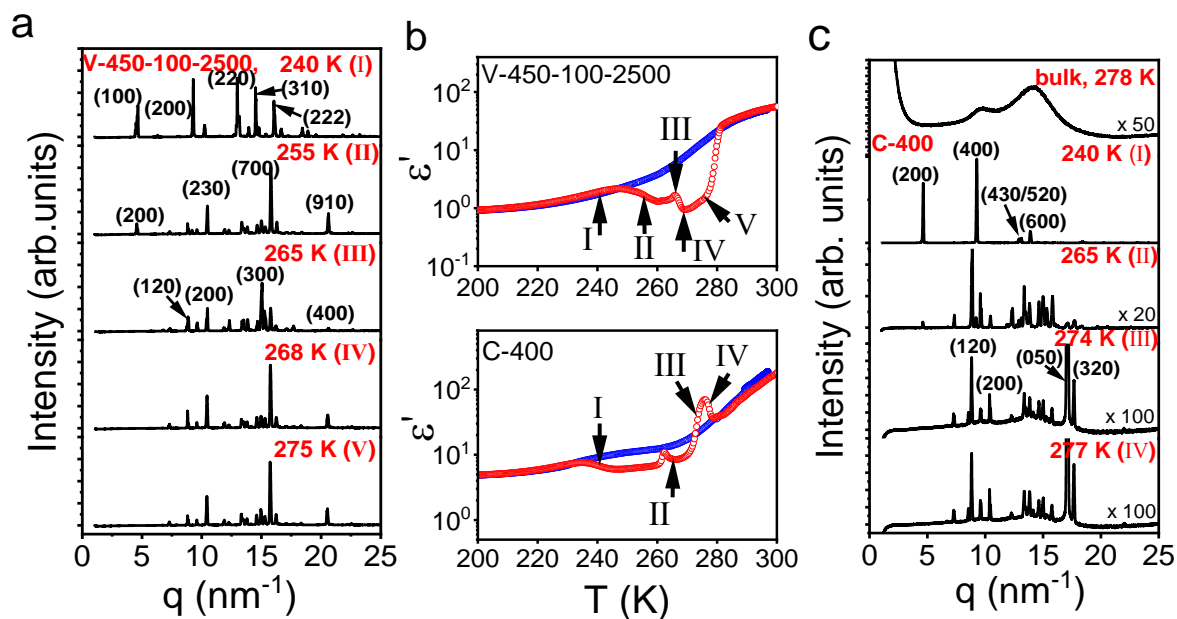


**Figure 10.** XRD curves of  $[\text{BMIM}]^+[\text{PF}_6]^-$  within V- (a) and cylindrically- (c) shaped AAO at different temperatures obtained on heating in comparison to the dielectric permittivity data obtained under isochronal conditions (1 MHz) on cooling (in blue) and subsequent heating (in red) (rate 5 K/min). The main diffraction peaks of confined  $[\text{BMIM}]^+[\text{PF}_6]^-$  are indicated. The dielectric permittivity data are used as a guide in recording the XRD curves at selected temperatures shown by Latin numbers. Curves are scaled appropriately for visibility (indicated by multipliers).

The investigation of the structural changes of  $[\text{BMIM}]^+[\text{PF}_6]^-$  within V- and cylindrically shaped nanopores with smaller pore volumes, e.g. within V-125-40-250 and C-25 AAO, revealed similar changes in the unit cells of the crystallized and re-crystallized IL (**Figure S6**). As with the structurally simpler  $[\text{BMIM}]^+[\text{TFSI}]^-$  case, the main effect of confinement is the reduction in the melting temperature(s) with increasing degree of confinement.

#### 4.4 Conclusion

ILs based on the 1-butyl-3-methylimidazolium cation with three different anions behave differently under nanometer confinement in comparison to the bulk. The shape/geometry of nanopores affects the ion mobility and the phase state of the confined ILs. In the amorphous  $[\text{BMIM}]^+[\text{BF}_4]^-$ , cylindrical confinement increases  $T_g$  (by  $\sim 5\text{K}$ ) and the effect is stronger in the smaller nanopores (e.g. by reducing the pore surface and pore volume). As a result, the dc-conductivity drops by  $\sim 2$  orders of magnitude relative to bulk. V-shaped confinement has similar effects but the decrease in dc-conductivity (and the increase in  $T_g$ ) is much smaller when examined under the same pore surface and volume. Lastly, silanization of the internal pore surface, in both templates, restores the bulk behavior providing further support to interfacial effects. The stronger effects within cylindrically shaped AAO can be explained by a uniform distribution of surface charge. Alternatively, an uneven charge distribution on the V-shaped pore surface can alleviate the Coulomb attractions enhancing the dc-conductivity back to the bulk values. The latter suggests electrostatic interactions extending much beyond a single IL layer.

ILs bearing the same cation but larger anions ( $[\text{BMIM}]^+[\text{TFSI}]^-$  and  $[\text{BMIM}]^+[\text{PF}_6]^-$ ) are structurally more complex. It was shown that V-shaped confinement produces the same structural changes as cylindrical confinement. Namely, changes from a larger to a smaller unit cell were shown in  $[\text{BMIM}]^+[\text{PF}_6]^-$  by increasing temperature. Here we have employed the temperature dependence of dielectric permittivity as a fingerprint of the phase transitions in constructing the effective phase diagrams. Both V-shaped and cylindrical nanopores decreased the transition temperatures according to the Gibbs-Thomson equation. The result suggests a reduced solid-liquid interfacial energy independent of nanopore geometry. These effects need to be investigated in even smaller nanopores and for a series of ILs. Studies in this direction are planned in our lab.

## 4.5 Reference

- (1) Welton, T. Room-Temperature Ionic Liquids. Solvents for Synthesis and Catalysis. *Chem. Rev.* **1999**, *99*, 2071-2083.
- (2) Simon, P.; Gogotsi, T. Materials for Electrochemical Capacitors. *Nat. Mater.* **2008**, *7*, 845-854.
- (3) Armand, M.; Endres, F.; MacFarlane, D.R.; Ohno, H.; Scrosati, B. Ionic-Liquid Materials for the Electrochemical Challenges of the Future. *Nat. Mater.* **2009**, *8*, 621-629.
- (4) Galiński, M.; Lewandowski, A.; Stępnia, I. Ionic Liquids as Electrolytes. *Electrochim. Acta* **2006**, *51*, 5567-5580.
- (5) Watanabe, M.; Thomas, M. L.; Zhang, S.; Ueno, K.; Yasuda, T.; Dokko, K. Application of Ionic Liquids to Energy Storage and Conversion Materials and Devices. *Chem. Rev.* **2017**, *117*, 7190-7239.
- (6) Jacob, C.; Sangoro, J. R.; Papadopoulos, P.; Schubert, T.; Naumov, S.; Valiullin, R.; Karger, J.; Kremer, F. Charge Transport and Diffusion of Ionic Liquids in Nanoporous Silica Membranes. *PCCP* **2010**, *12*, 13798-13803.
- (7) Jacob, C.; Sangoro, J. R.; Kipnusu, W. K.; Valiullin, R.; Kärger, J.; Kremer, F. Enhanced Charge Transport in Nano-Confined Ionic Liquids. *Soft Matter* **2012**, *8*, 289-293.
- (8) Tu, W.; Chat, K.; Szklarz, G.; Laskowski, L.; Grzybowska, K.; Paluch, M.; Richert, R.; Adrjanowicz, K. Dynamics of Pyrrolidinium-Based Ionic Liquids under Confinement. II. The Effects of Pore Size, Inner Surface, and Cationic Alkyl Chain Length. *J. Phys. Chem. C* **2019**, *124*, 5395-5408.
- (9) Dong, Y.; Steinhart, M.; Butt, H.-J.; Floudas, G. Conductivity of Ionic Liquids in the Bulk and During Infiltration in Nanopores. *J. Phys. Chem. B* **2023**, *127*, 6958-6968.
- (10) Dong, Y.; Steinhart, M.; Butt, H.-J.; Floudas, G. Demixing of Polymerized Ionic Liquid/Ionic Liquid Mixtures by Infiltration in Nanopores. *Macromolecules* **2024**, *57*, 5409-5420.
- (11) Nobori, H.; Fujimoto, D.; Yoshioka, J.; Fukao, K.; Konishi, T.; Taguchi, K. Phase Transitions and Dynamics in Ionic Liquid Crystals Confined in Nanopores. *J. Chem. Phys.* **2024**, *160*, 044902.
- (12) Davenport, M.; Rodriguez, A.; Shea, K. J.; Siwy, Z. S. Squeezing Ionic Liquids through Nanopores. *Nano Lett.* **2009**, *9*, 2125-2128.
- (13) Guo, W.; Tian, Y.; Liang, L. Asymmetric Ion Transport through Ion-Channel-Mimetic Solid State Nanopores. *Acc. Chem. Res.* **2013**, *46*, 2834-2846.
- (14) Siwy, Z.S. Ion-Current Rectification in Nanopores and Nanotubes with Broken Symmetry. *Adv. Funct. Mater.* **2006**, *16*, 735-746.
- (15) Li, S.; Zhang, X.; Su, J. Ionic Current Rectification Induced by Charge Polarity in Janus Graphene Channels. *J. Phys. Chem. C* **2023**, *127*, 12276-12286.
- (16) Sieffert, N.; Wipff, G. Ordering of Imidazolium-Based Ionic Liquids at the  $\alpha$ -Quartz(001) Surface: A Molecular Dynamics Study. *J. Phys. Chem. C* **2008**, *112*, 19590-19603.
- (17) Wang, S.; Li, S.; Cao, Z.; Yan, T. Y. Molecular Dynamic Simulations of Ionic Liquids at Graphite Surface. *J. Phys. Chem. C* **2010**, *114*, 990-995.
- (18) Dick, L.; Buchmüller, L.; Kirchner, B. Coordination Behavior of a Confined Ionic Liquid in Carbon Nanotubes from Molecular Dynamics Simulations *J. Phys. Chem. B* **2024**, *28*, 4472-4484.
- (19) Masuda, H.; Fukuda, K. Ordered Metal Nanohole Arrays Made by a Two-Step Replication of Honeycomb Structures of Anodic Alumina. *Science* **1995**, *268*, 1466-1468.
- (20) Masuda, H.; Hasegawa, F.; Ono, S. Self-ordering of Cell Arrangement of Anodic Porous Alumina Formed in Sulfuric Acid Solution. *J. Electrochem. Soc.* **1997**, *144*, L127-L130.

- (21) Masuda, H.; Yada, K.; Osaka, A. Self-ordering of Cell Configuration of Anodic Porous Alumina with Large-Size Pores in Phosphoric Acid Solution. *Jpn. J. Appl. Phys.* **1998**, *37*, L1340- L1342.
- (22) Steinhart, M. Supramolecular Organization of Polymeric Materials in Nanoporous Hard Templates. *Adv. Polym. Sci.* **2008**, *220*, 123-187.
- (23) Slavov, S.V.; Sanger, A.R.; Chuang, K.T. Mechanism of Silation of Alumina with Hexamethyldisilazane. *J. Phys. Chem. B* **1998**, *102*, 5475-5482.
- (24) Tu, W.; Chat, K.; Szklarz, G.; Laskowski, L.; Grzybowska, K.; Paluch, M.; Richert, R.; Adrjanowicz, K. Dynamics of Pyrrolidinium-Based Ionic Liquids under Confinement. II. The Effects of Pore Size, Inner Surface, and Cationic Alkyl Chain Length. *J. Phys. Chem. C* **2020**, *124*, 5395–5408.
- (25) Lucas, R. On the Time Law of the Capillary Rise of Liquids. *Colloid Polym. Sci.* **1918**, *23*, 15–22.
- (26) Washburn, E.W. The Dynamics of Capillary Flow. *Phys. Rev.* **1921**, *17*, 273–283.
- (27) Gorce, J.-B.; Hewitt, I.J.; Vella, D. Capillary Imbibition into Converging Tubes: Beating Washburn’s Law and the Optimal Imbibition of Liquids. *Langmuir* **2016**, *32*, 1560-1567.
- (28) Tu, C. H.; Zhou, J.; Doi, M.; Butt, H. J.; Floudas, G. Interfacial Interactions During In Situ Polymer Imbibition in Nanopores. *Phys. Rev. Lett.* **2020**, *125*, 127802.
- (29) Tu, C.-H.; Zhou, J.; Butt, H.-J.; Floudas, G. Adsorption Kinetics of cis-1,4-Polyisoprene in Nanopores by In Situ Nanodielectric Spectroscopy. *Macromolecules* **2021**, *54*, 6267-6274.
- (30) Kanakubo, M.; Harris, K.R.; Tsuchihashi, N.; Ibuki, K.; Ueno, M. Temperature and Pressure Dependence of the Electrical Conductivity of 1-Butyl-3-methylimidazolium Bis(trifluoromethanesulfonyl) amide. *J. Chem. Eng. Data* **2015**, *60*, 1495-1503.
- (31) Fedorov, M.V.; Konryshev, A.A. Towards Understanding the Structure and Capacitance of Electrical Double Layer in Ionic Liquids. *Electrochim. Acta* **2008**, *53*, 6835-6840.
- (32) Fedorov, M.V.; Konryshev, A.A. Ionic Liquid Near a Charged Wall: Structure and Capacitance of Electrical Double Layer. *J. Phys. Chem. B.* **2008**, *112*, 11868-11872.
- (33) Selevou, A.; Papamokos, G.; Steinhart, M.; Floudas, G., 8OCB and 8CB Liquid Crystals Confined in Nanoporous Alumina: Effect of Confinement on the Structure and Dynamics. *J. Phys. Chem. B* **2017**, *121*, 7382-7394.
- (34) Grigoriadis, C.; Duran, H.; Steinhart, M.; Kappl, M.; Butt, H.-J.; Floudas, G., Suppression of Phase Transitions in a Confined Rodlike Liquid Crystal. *ACS Nano* **2011**, *5*, 9208-9215.
- (35) Alcoutlabi, M.; McKenna, G. B. Effects of Confinement on Material Behaviour at the Nanometre Size Scale. *J. Phys.: Condens. Matter.* **2005**, *17*, R461-R524.
- (36) Hamilto, Hamilton, B. D.; Ha, J.-M.; Hillmyer, M. A.; Ward, M. D. Manipulating Crystal Growth and Polymorphism by Confinement in Nanoscale Crystallization Chambers. *Acc. Chem. Res.* **2012**, *45*, 414–423.

## 4.6 Supporting information

### 1. SEM characterization

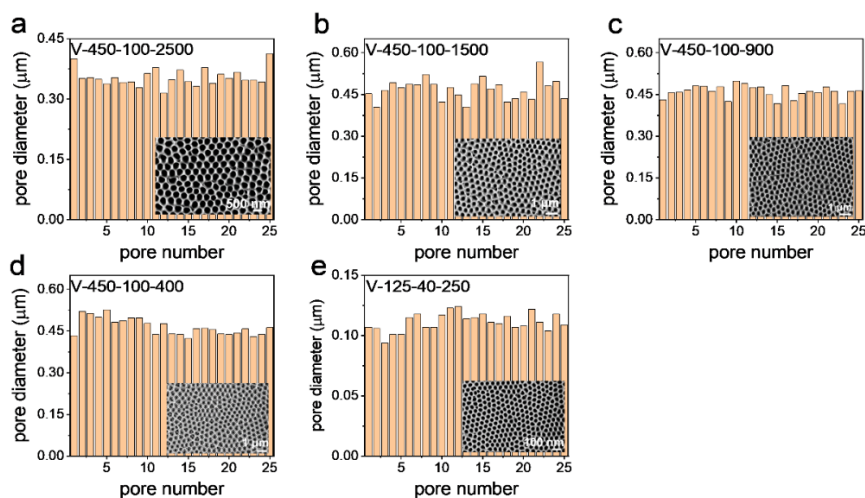


**Figure S1.** Characterization of top pore diameter of V-shaped AAO templates with different pore depths: (a) V-450-100-2500, (b) V-450-100-1500, (c) V-450-100-900, (d) V-450-100-400, and (e) V-125-40-250, respectively. The insert images represent SEM photos of the corresponding top pores. Pore porosity was calculated through the equation:  $\varphi = \frac{V_{pore,all}}{V_{area}} = \frac{n \left( \frac{\pi}{3} (R^2 + rR + r^2) h \right)}{Sh}$ , where  $r$  is the bottom pore diameter,  $R$  is the top pore diameter,  $h$  is the pore depth,  $n$  is the number of pores in selected area, and  $S$  represents the area.

### 2. Differential Scanning Calorimetry (DSC)

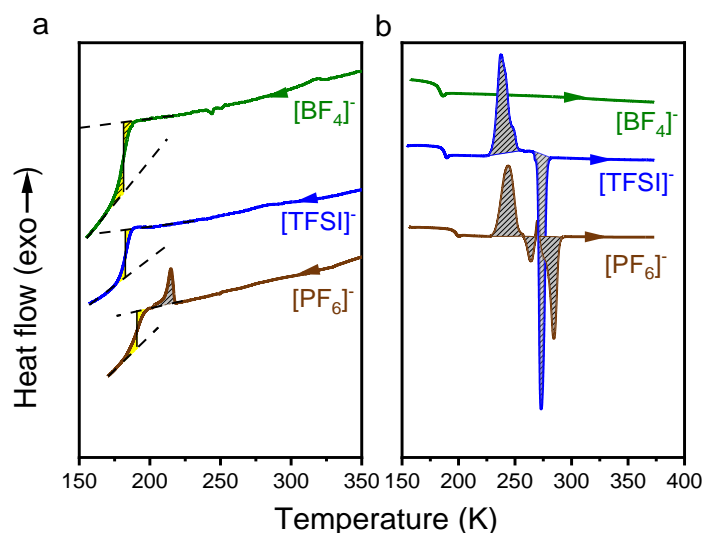


**Figure S2.** DSC traces of [BMIM]<sup>+</sup>[BF<sub>4</sub>]<sup>-</sup> (olive), [BMIM]<sup>+</sup>[TFSI]<sup>-</sup> (blue), [BMIM]<sup>+</sup>[PF<sub>6</sub>]<sup>-</sup> (brown). Traces are obtained on cooling (a) and subsequent heating (b) runs with a rate of 10 K·min<sup>-1</sup>.

## 3. Dc-Conductivity

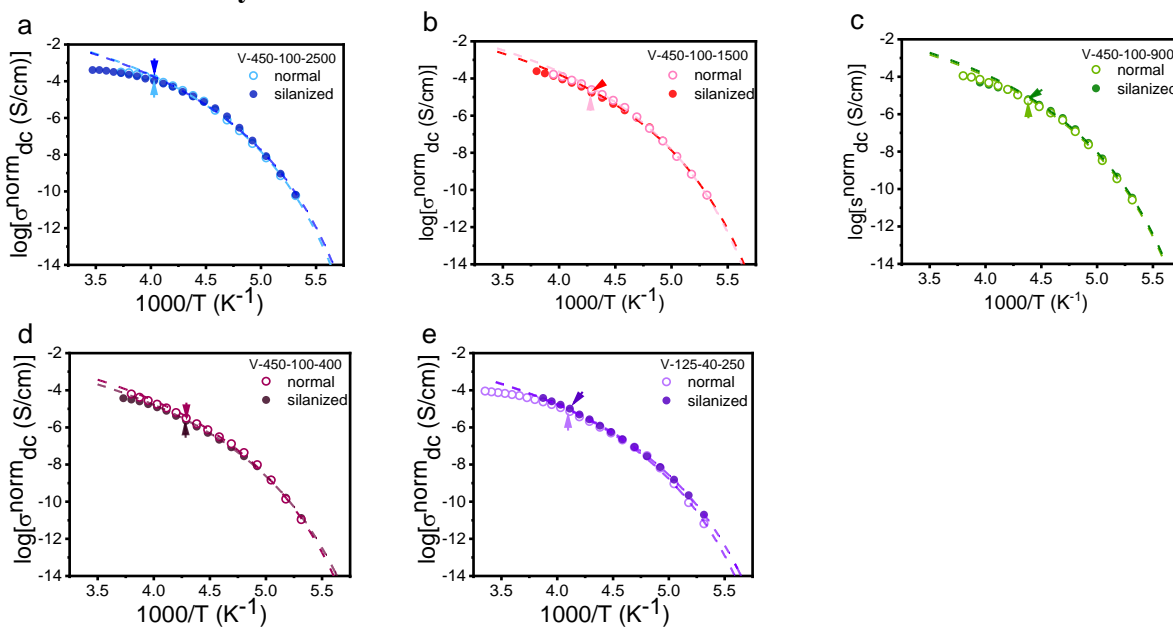


**Figure S3.** Temperature dependence of the dc-conductivity for  $[\text{BMIM}]^+[\text{BF}_4]^-$  in native and silanized V-shaped AAOs. Arrows indicate the limiting temperature from the high temperature side used in the VFT fits.

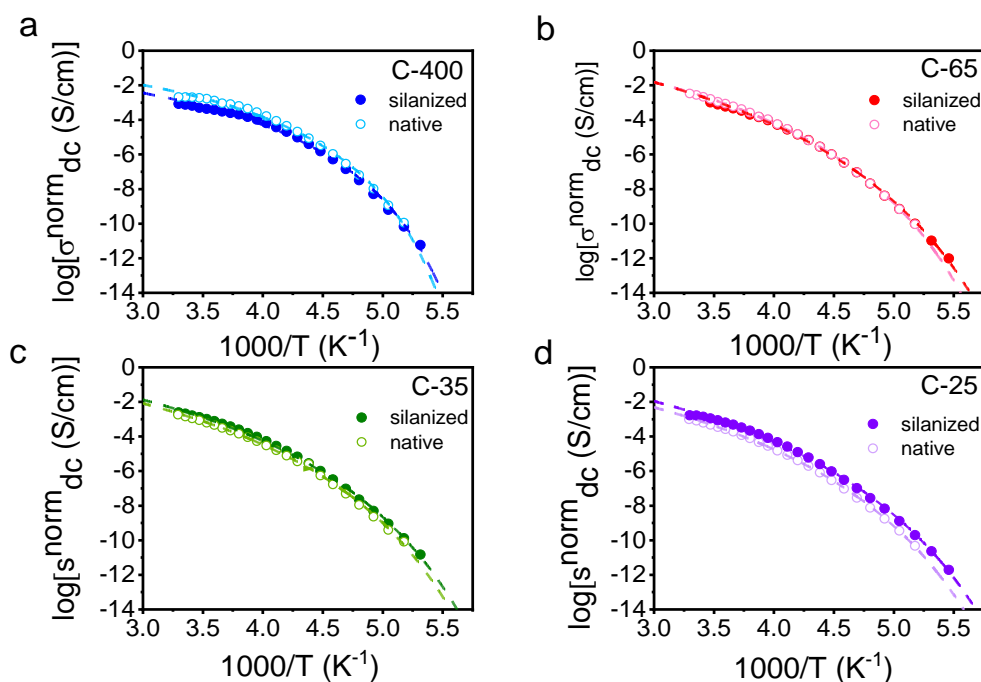


**Figure S4.** Temperature dependence of the dc-conductivity for  $[\text{BMIM}]^+[\text{BF}_4]^-$  in native and silanized cylindrically shaped AAOs. Dashed lines represent VFT fits.

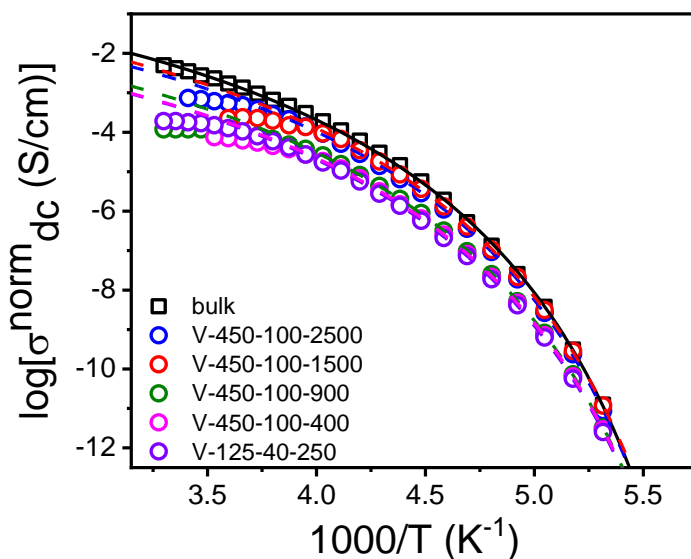


**Figure S5.** Dc-conductivity for  $[\text{BMIM}]^+[\text{TFSI}]^-$  following imbibition in V-shaped AAO nanopores with different pore volumes plotted as a function of inverse temperature. Measurements were made on cooling. Dashed lines represent VFT fits.

#### 4. XRD of $[\text{BMIM}]^+[\text{PF}_6]^-$ in smaller nanopores.

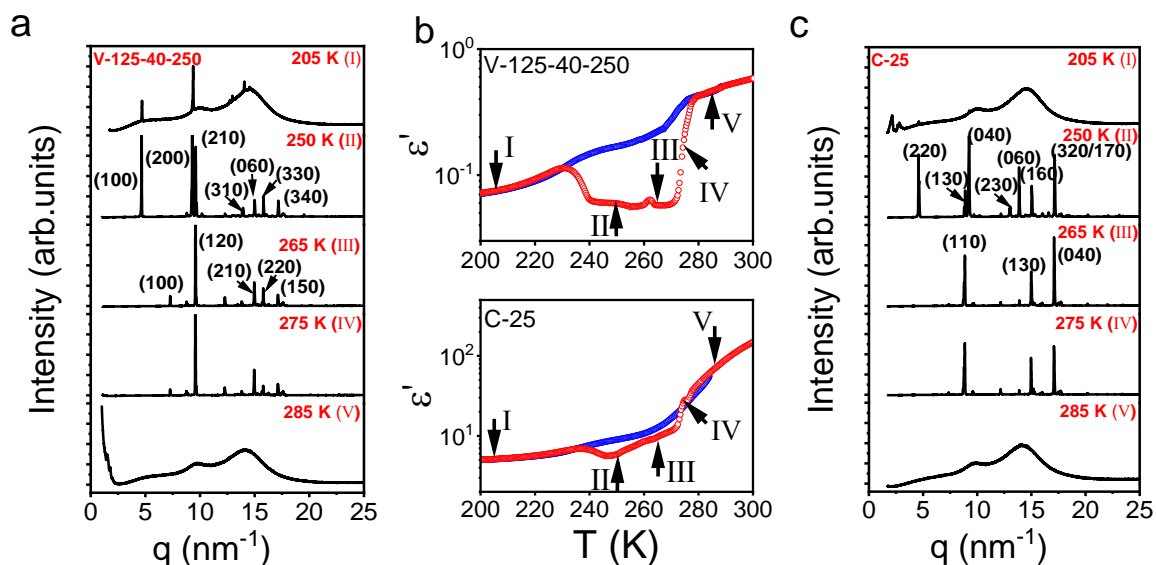


**Figure S6.** Structure analysis of  $[\text{BMIM}]^+[\text{PF}_6]^-$  in bulk and confined within V-shaped (V-125-40-250) and cylindrically shaped (C-25) AAO nanopores in comparison to (b) dielectric permittivity data obtained under isochronal conditions (1 MHz). (a, c) X-ray scattering curves at various temperatures, showing the crystalline peaks as a function of the modulus of the scattering vector  $q$  for  $[\text{BMIM}]^+[\text{PF}_6]^-$  confined in V-shaped (a) and cylindrical (c) AAO. The XRD curves at each temperature illustrate the phase evolution from the amorphous state (I), to the different crystalline phases (II, III, IV) to the melt (V).

## Chapter 5. Tethered Cation Size Affects the Imbibition of Polymerized Ionic Liquids and the Ionic Conductivity in Nanopores

This chapter has been published as a research paper in *Macromolecules*.

*Yun Dong, Hongkun He, Kriti Kapil, Martin Steinhart, Krzysztof Matyjaszewski, Hans-Jürgen Butt, and George Floudas*

*Macromolecules* 2025, 58, 7534-7543.

DOI: 10.1021/acs.macromol.5c01449

### **Author contributions:**

**Yun Dong:** Dielectric spectroscopy and DSC measurements. AAO template characterization and surface modification. Synthesis of ionic liquid [VBBI]<sup>+</sup>[TFSI]<sup>-</sup>. Data analysis and interpretation. Writing of the original draft of the manuscript.

**Hongkun He:** Synthesis and characterization of the poly[VBBI]<sup>+</sup>[TFSI]<sup>-</sup> sample.

**Kriti Kapil:** Characterization of the poly[VBBI]<sup>+</sup>[TFSI]<sup>-</sup> sample.

**Krzysztof Matyjaszewski:** Discussion on the research topic/results. Correction of the manuscript.

**George Floudas:** Design of the research topic. Discussion on the results. Writing the final version based on the original draft.

**Hans-Jürgen Butt:** Acquiring funding for the project. Discussion on the research topic/results. Correction of the manuscript.

**Martin Steinhart:** AAO template fabrication.

## Abstract

There is a growing interest in new polymerized ionic liquids (PILs) with enhanced ion transport properties especially at low temperatures, in the vicinity of the liquid-to-glass temperature,  $T_g$ . We employed two structurally similar ionic liquids (ILs), namely, 1-butyl-3-methylimidazolium bis(trifluoromethylsulfonyl)imide ([BMIM]<sup>+</sup>[TFSI]<sup>-</sup>) and 1-(4-vinylbenzyl)-3-butylimidazolium bis(trifluoromethane)sulfonimide ([VBBI]<sup>+</sup>[TFSI]<sup>-</sup>) and synthesized the corresponding PILs, poly[BVIM]<sup>+</sup>[TFSI]<sup>-</sup> and poly[VBBI]<sup>+</sup>[TFSI]<sup>-</sup>. The main difference was the positioning of the cation – and hence the cation/anion coordination – with respect to the backbone. This small structural variation had implications in anion transport in the bulk. Ion coordination in proximity to the backbone restricted backbone mobility, increased  $T_g$  and reduced ionic conductivity. A strategy towards increasing ion conductivity at lower temperatures was by nanometer confinement. As a confining medium we employed self-ordered anodic aluminum oxide (AAO) nanopore templates and investigated the kinetics of imbibition and the ion dynamics following imbibition by *ex situ* polarizing optical microscopy and by *in situ* nanodielectric spectroscopy. These methods provided access to the effective viscosity and to the ionic conductivity of a PIL during and following imbibition in nanopores. PILs penetrated nanopores with a lower speed than expected from their bulk viscosity. At lower temperatures, in the vicinity of  $T_g$ , confinement effects took over and decoupled the ion dynamics from the arrested backbone dynamics. Under these conditions, the temperature dependence of ion conductivity deviated from the Vogel-Fulcher-Tammann law and followed an Arrhenius temperature dependence with an activation energy that was reduced from 142 kJ/mol in the bulk to ~ 108 kJ/mol under confinement. The results offer new insights into how molecular structure and confinement affect ion transport in PILs.

## 5.1 Introduction

Polymerized ionic liquids (PILs) are a unique class of materials composed of polymer backbones bearing covalently attached ionic groups.<sup>1,2</sup> Unlike conventional ionic liquids (ILs), i.e., low-molecular-weight salts composed solely of mobile ions, PILs incorporate at least one ionic species – typically the cation – into the polymeric chain, while the counterion remains mobile.<sup>3,4</sup> This hybrid architecture combines the desirable physicochemical features of ILs (e.g. high ionic conductivity,<sup>5,6</sup> tunability, and thermal stability<sup>7</sup>) with the mechanical robustness and processability of polymers.<sup>8</sup> The cationic components in PILs are often based on imidazolium, pyridinium, ammonium, or phosphonium structures, while the anions include bis(trifluoromethylsulfonyl)imide ([TFSI]<sup>-</sup>), tetrafluoroborate ([BF<sub>4</sub>]<sup>-</sup>), or hexafluorophosphate ([PF<sub>6</sub>]<sup>-</sup>).<sup>9-11</sup> The chemical diversity of these ions allows for fine-tuning of the properties to meet specific requirements in a range of electrochemical and soft material applications. These include solid-state electrolytes for lithium-ion batteries and supercapacitors, ion-conducting membranes for fuel cells and electro dialysis, actuators, sensors, and stimuli-responsive materials.<sup>12-17</sup> Their high ionic content, combined with low volatility, non-flammability and thermal stability, makes them particularly attractive for replacing liquid electrolytes in next-generation energy storage and conversion technologies.

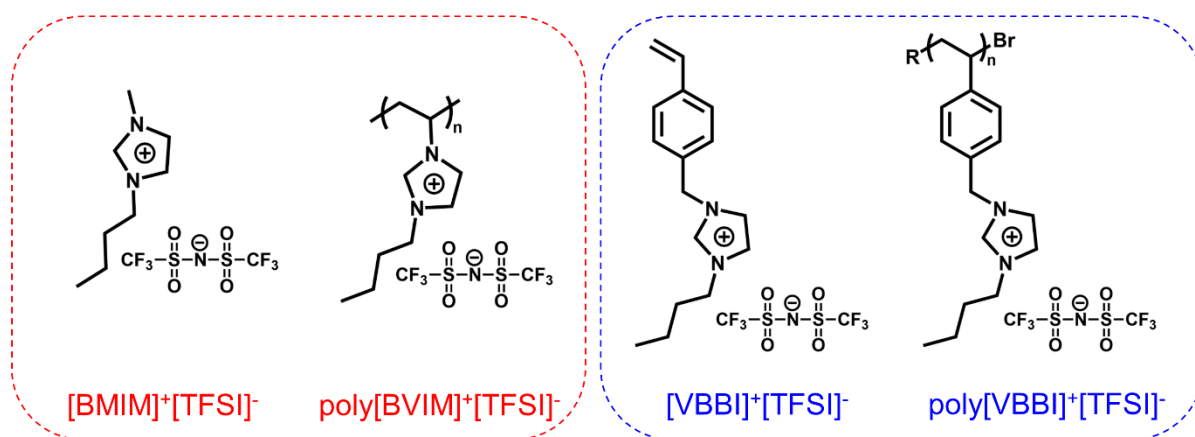
In recent years there has been a growing interest in employing PILs within nanostructured environments, such as nanoporous materials, in an effort to modulate or even to enhance their ionic transport properties. Under confinement, the ion dynamics can be altered because of spatial constraints and surface interactions leading to adsorption.<sup>18-21</sup> In the first study<sup>18</sup> of the archetypal polymer electrolyte poly(ethylene oxide)/LiTFSI during imbibition in nanopores by *in situ* nanodielectric spectroscopy, it was shown that ion conductivity is controlled by PEO adsorption at the pore walls. The molar mass dependence of the characteristic adsorption times ( $\tau_{\text{ads}} \sim N^2$ ,  $N$  is the degree of polymerization) was in agreement with the scaling theory proposed by de Gennes. In another study of PIL/IL mixtures, it was shown that *in situ* conductivity measurements during imbibition in nanopores can be used to separate the mixture to its individual components.<sup>19</sup> However, despite the growing body of research on ILs and PILs<sup>22-27</sup>, relatively little is known about how subtle molecular modifications, such as side-group variations in PILs, influence their behavior in bulk and under confinement. Especially, the effect of polymer adsorption and the concomitant immobilization of the cation on the pore walls on the (anion) mobility needs to be investigated. Molecular architecture/topology as well as confinement effects can influence cation-anion association, which is expected to affect ion conductivity.

In this work, we focus on how the cation molecular structure affects ion transport in ILs and the corresponding PILs in the bulk and under nanometer confinement. For this purpose, two structurally similar ILs were synthesized: one bearing a simple imidazolium ring (1-butyl-3-methylimidazolium, [BMIM]<sup>+</sup>), the other featuring a phenyl-substituted imidazolium (1-(4-vinylbenzyl)-3-butylimidazolium, [VBBI]<sup>+</sup>), while keeping the same anion, bis(trifluoromethylsulfonyl)imide [TFSI]<sup>-</sup>. Next, the respective polymers were synthesized comprising: poly[BVIM]<sup>+</sup>[TFSI]<sup>-</sup> and poly[VBBI]<sup>+</sup>[TFSI]<sup>-</sup>. The results show that the more compact cation structure in the former allows for anion/cation association more closely to the polymer backbone, effectively restricting backbone mobility. The expectation is that this feature will reduce ion conductivity. Building on this molecular-level understanding of ion transport, we focus particularly on the role of cation structure in modulating ion dynamics during and following flow of PILs in nanopores. For this purpose, we employ self-ordered anodic aluminum oxide (AAO) nanopores, and a combination of dielectric spectroscopy, thermodynamic and viscosity measurements, to probe how confinement, polymer-AAO interactions, and ion-polymer interactions collectively influence ion conductivity and ion relaxation. Of particular interest is the possibility to decouple the ion motion from the polymer segmental dynamics, known as ion-polymer decoupling.<sup>28-31</sup> According to the latter, ion motion can decouple from the polymer backbone dynamics and persist even below the liquid-to-glass temperature ( $T_g$ ). We investigate how this decoupling is impacted by cation structure in the bulk and under spatial confinement. With respect to the latter, we show that confinement enhances ion decoupling below  $T_g$ . The activation energy for ion diffusion reduces from 142 kJ/mol in the bulk to 108 kJ/mol under confinement. The results offer new insights into how molecular structure (cation size in particular) and confinement effects affect ion transport in PILs.

## 5.2 Experimental section

**Materials.** 1-Butyl-3-methylimidazolium bis(trifluoromethylsulfonyl)imide ([BMIM]<sup>+</sup>[TFSI]<sup>-</sup>, purity  $\geq$  98%), 1-butyl-3-vinylimidazolium bromide ([BVIM]<sup>+</sup>[Br]<sup>-</sup>, purity  $\geq$  98%), 4-Vinylbenzyl chloride (purity  $\geq$  90%), 1-butylimidazole (purity  $\geq$  98%), Lithium bis(trifluoromethanesulfonyl)imide (LiTFSI, purity  $\geq$  98%), Acetonitrile (purity  $\geq$  99.8%), Dichloromethane (DMF, extra dry  $\geq$  99.9%), Silver nitrate solution (AgNO<sub>3</sub>), 2,2'-azobisisobutyronitrile (AIBN, purity  $\geq$  98%), Ultra-15 Centrifugal Filter Unit (10 kDa MWCO), Tetrahydrofuran (THF, purity  $\geq$  98%), Anhydrous MgSO<sub>4</sub> and Ethanol were

purchased from Merck and used without further purification. Deionized water was purified using a Millipore Milli-Q Synergy with a resistivity approximately  $18 \text{ M}\Omega \cdot \text{cm}^{-1}$ . The water content of ILs was measured by a Karl-Fischer titration method (C20, Mettler Toledo). Following freeze-drying the water content was below 0.02 wt%. The chemical structures of the ILs and PILs used in this study are presented in **Scheme 1**.



**Scheme 1.** Chemical structures of ILs, [BMIM]<sup>+</sup>[TFSI]<sup>-</sup>, [VBBI]<sup>+</sup>[TFSI]<sup>-</sup>, and of the corresponding PILs, poly[BVIM]<sup>+</sup>[TFSI]<sup>-</sup>, poly[VBBI]<sup>+</sup>[TFSI]<sup>-</sup>.

**Synthesis of [VBBI]<sup>+</sup>[TFSI]<sup>-</sup>.** The preparation of IL, [VBBI]<sup>+</sup>[TFSI]<sup>-</sup>, was conducted according to an established procedure.<sup>32</sup> 4-vinylbenzyl chloride (40.0 g, 0.26 mol) was mixed with 1-butylimidazole (32.5 g, 0.26 mol) in acetonitrile (100 mL), and the reaction mixture was stirred at 45 °C for 24 h. The resulting product, 1-(4-vinylbenzyl)-3-butylimidazolium chloride (VBIC), was precipitated, washed thoroughly with excess diethyl ether, and dried under vacuum at room temperature to yield a viscous liquid. Subsequently, VBIC (27.0 g, 96.1 mmol) was dissolved in deionized water (200 mL), and LiTFSI (30.4 g, 105.8 mmol) was added. An oily liquid immediately formed at the bottom of the reaction flask. The mixture was stirred at room temperature for 24 h, after which the oil was extracted with ethyl acetate (200 mL) and washed with deionized water ( $3 \times 50 \text{ mL}$ ). The organic phase was dried over anhydrous  $\text{MgSO}_4$ , filtered, and concentrated by rotary evaporation. Residual solvent was removed under vacuum, yielding a highly viscous liquid identified as 1-(4-vinylbenzyl)-3-butylimidazolium bis(trifluoromethane)sulfonimide ([VBBI]<sup>+</sup>[TFSI]<sup>-</sup>). The corresponding PIL, poly[VBBI]<sup>+</sup>[TFSI]<sup>-</sup>, was synthesized using atom transfer radical polymerization (ATRP).<sup>33-37</sup> ATRP is a controlled/living radical polymerization and is used to prepare polymers with high uniformity and well-defined architecture.

**Synthesis of Poly[BVIM]<sup>+</sup>[TFSI]<sup>-</sup>.** The synthesis of poly[BVIM]<sup>+</sup>[TFSI]<sup>-</sup> was made following a previously reported procedure.<sup>38,39</sup> Briefly, [BVIM]<sup>+</sup>[Br]<sup>-</sup> (9 g, 38.9 mmol) and AIBN (6.5 mg, 0.396 mmol) were dissolved in 18 mL of DMF. The solution was purged with argon for 1 h to remove dissolved oxygen. The reaction mixture was then stirred at 348 K under an argon atmosphere for 24 h. Following the reaction, DMF was removed via rotary evaporation, yielding a viscous oil. This crude product was dissolved in 20 ml of deionized water and dialyzed against water using a cellulose tube with 10 kDa MWCO for two days, with the dialysate being replaced twice to ensure effective removal of low-molecular-weight impurities. To facilitate anion exchange, the dialyzed solution was divided into three equal portions. Each portion was treated with an aqueous solution of LiTFSI (approximately 1.5-fold molar excess) and stirred for 5 days. The resulting polymer was isolated by filtration, thoroughly washed with deionized water until no bromide could be detected in the washing water (confirmed by the absence of AgBr precipitation upon the addition of AgNO<sub>3</sub> solution). Finally, the obtained poly[BVIM]<sup>+</sup>[TFSI]<sup>-</sup> (4.48 g,  $M_n = 85$  kDa) was dried under vacuum at 313 K to remove residual solvent. Gel permeation chromatography (GPC) was used to determine the molecular weights of obtained PILs (**Figure S1**). The molecular characteristics of poly[BVIM]<sup>+</sup>[TFSI]<sup>-</sup> and poly[VBBI]<sup>+</sup>[TFSI]<sup>-</sup> are given in **Table 1**.

**Table 1.** Molecular Characteristics of PILs (Number- and Weight-Averaged Molar Mass, Degree of Polymerization and Dispersity) Used in the Present Investigation.

	$M_n$ (kg·mol <sup>-1</sup> )	$M_w$ (kg·mol <sup>-1</sup> )	DP	$\bar{D}$
poly[BVIM] <sup>+</sup> [TFSI] <sup>-</sup>	85	255	525	3.02
poly[VBBI] <sup>+</sup> [TFSI] <sup>-</sup>	180	246	477	1.36

**AAO templates.** Self-ordered nanopores aluminium oxide (AAO) templates with specified pore diameters of 25, 35, 65, and 400 nm, and a uniform pore depth of approximately 100  $\mu$ m, were fabricated following established literature protocols.<sup>40-43</sup> The AAO layers were supported on 900  $\mu$ m thick aluminium substrates. Prior to the infiltration process, all AAO templates were annealed in a vacuum oven at 433 K for 12 hours. This annealing step eliminates a substantial portion of hydroxyl (-OH) groups from the surface of the AAO. The templates have been characterized by different methods including SEM, FIB, AFM<sup>44</sup> and laser interferometry.<sup>45</sup> The optical experiments have shown that AAO nanopores are characterized by a slight conicity. A model provided an improved description of nanoscale fluid dynamics and allowed geometric characterization of the nanoporous membranes by their imbibition kinetics.<sup>45</sup>

**Differential Scanning Calorimetry (DSC).** The thermal behaviour of ILs and their corresponding PILs was investigated using differential scanning calorimetry (DSC) during cooling and subsequent heating cycles at a rate of  $10 \text{ K} \cdot \text{min}^{-1}$ . Measurements were performed with a Mettler Toledo DSC-822 calorimeter, using an empty aluminium pan as a reference. Samples were accurately weighed with a Mettler Toledo AX205 balance, and approximately 10 mg of each sample was sealed in 100  $\mu\text{L}$  aluminium pans. To eliminate prior thermal history, samples were heated to 373 K under a nitrogen atmosphere before further analysis. Each thermal cycle was repeated twice to ensure reproducibility.

**Dielectric spectroscopy (DS).** The dielectric properties of bulk and confined ILs, PILs were performed by usual dielectric spectroscopy and *in situ* nanodielectric spectroscopy (*nDS*). In both cases, a Novocontrol Alpha frequency analyzer was used, which consists of a broadband dielectric converter and an active sample head. For bulk samples, a dielectric cell with two electrodes (20 mm diameter) and a 250  $\mu\text{m}$  Teflon spacer to ensure constant thickness was used. The frequency range employed spanned from  $10^{-2}$  to  $10^7$  Hz. For the investigation of the effect of nanoconfinement, a 35 nm thick gold layer (9 mm diameter) was deposited onto the AAO template to serve as the top electrode, while the aluminium substrate of the AAO acted as the bottom electrode. Deposition of a gold layer was carried out via sputtering under vacuum conditions (better than  $2 \times 10^{-5}$  Pa) using a Bal-tec MED 020 system with a current density of 35 mA. The samples were then placed on top of the AAO template, and imbibition kinetics were investigated using *nDS*. In this case, a narrower frequency range (1 -  $10^6$  Hz) was employed for faster data acquisition. Impedance measurements were conducted to obtain the complex conductivity function, denoted as  $\sigma^* = \sigma' + i\sigma''$ , where  $\sigma'$  and  $\sigma''$  are the real (*i.e.*, the dc-conductivity) and imaginary parts, respectively. The plateau observed in the real part  $\sigma'$  was used to extract the dc-conductivity. *nDS* can be used to monitor the increase in imbibition length during pore filling by tracking the rise in dc-conductivity with imbibition time. Briefly, a simple Debye model for the frequency-dependent complex conductivity ( $\sigma^*(\omega)$ ) can be employed as:

$$\sigma^*(\omega) = \sigma'(\omega) + i\sigma''(\omega) = i\omega\varepsilon_0\varepsilon^*(\omega),^{46,47}$$

$$\sigma'(\omega) = \omega\varepsilon_0\varepsilon''(\omega) = \sigma_{dc} + \frac{\omega^2\tau\varepsilon_0\Delta\varepsilon}{1+(\omega\tau_D)^2} \quad (1)$$

$$\sigma''(\omega) = \omega\varepsilon_0\varepsilon'(\omega) = \omega\varepsilon_0 \left( \varepsilon_\infty + \frac{\Delta\varepsilon}{1+(\omega\tau_D)^2} \right) \quad (2)$$

Here,  $\Delta\varepsilon$  is the dielectric strength,  $\tau_D$  is the characteristic relaxation time,  $\sigma_{dc}$  is the dc-conductivity, and  $\varepsilon_\infty$  is the dielectric permittivity in the limit of very high frequencies. A parallel model can describe the total equivalent capacitance, comprising the capacitance of the sample

( $C_1$ ) and air ( $C_2$ ) connected in series, whereas the combined sample/air capacitance ( $C_{12}$ ) connects in parallel with the AAO ( $C_3$ ). As a result,

$$\frac{1}{C_{12}} = \frac{1}{C_1} + \frac{1}{C_2}, \text{ and } C_{123} = C_{12} + C_3 \quad (3)$$

Using the above equations, the definition  $\sigma_{123}^* = i\omega\varepsilon_0\varepsilon^*$ , and the porosity  $\varphi_{12}$  results to:

$$\sigma_{123}^* = \sigma' + i\sigma'' = \left\{ \left[ \frac{Ld_1\sigma_1'(\omega\varepsilon_0)^2}{(d_2\sigma_1')^2 + (d_1\omega\varepsilon_0 + d_2\sigma_1')^2} \right] \varphi_{12} + \sigma_3' \varphi_3 \right\} + i \left\{ \left[ \frac{L[d_2[(\sigma_1')^2 + (\sigma_1'')^2]\omega\varepsilon_0 + \sigma_1''(\omega\varepsilon_0)^2 d_1]}{(d_2\sigma_1')^2 + (d_1\omega\varepsilon_0 + d_2\sigma_1'')^2} \right] \varphi_{12} + \sigma_3'' \varphi_3 \right\} \quad (4)$$

Where  $\varphi_3 (=1 - \varphi_{12})$  is the AAO content. As have been reported previously,<sup>48</sup> equation (4) predicts a conductivity plateau (e.g. the dc-conductivity), only when the pores are fully infiltrated.

**X-ray diffraction.** X-ray diffraction measurements were performed using a Rigaku SmartLab X-ray diffractometer. The X-ray source was a rotating Cu anode, operating at 45 kV and 200 mA. The incident optics included a Ge crystal monochromator (220 reflection) followed by a parallel slit (incident Soller slit 2.5°). A diffracted beam monochromator was inserted between the detector slit and the detector to minimize fluorescence and  $K_\beta$  radiation. The receiving optics consisted of a parallel slit analyzer (PSA) followed by a receiving Soller slit. The X-ray wavelength was 0.154059 nm. Data were collected using a HyPix-3000 2D detector (pixel size: 100  $\mu\text{m} \times 100 \mu\text{m}$ ; active area: 38.5 mm  $\times$  77.5 mm). The scans were conducted in the  $2\Theta$  range from 0° to 60° with a step size of 0.01° at 358 K.

**Reflection Optical Microscopy.** The imbibition length measurements were made by employing *ex situ* reflection optical microscopy (ROM) (Zeiss AxioTech vario) at 358 K (infiltration temperature). The PIL, poly[VBBI]<sup>+</sup>[TFSI]<sup>-</sup>, was infiltrated into nanopores by capillary force. At predefined time intervals, the AAO templates were immersed into liquid nitrogen to prevent further infiltration. The imbibition length, representing the distance the PIL penetrated under capillary pressure, was determined from cross-sectional images captured by ROM.

**Contact Angle.** The apparent advancing contact angle of poly[VBBI]<sup>+</sup>[TFSI]<sup>-</sup> was measured by placing nearly spherical polymer particles (~1 mm in diameter) onto an electropolished Al substrate. To form the spherical particle, around 1 mg of sample was placed on a superamphiphobic surface, heated to 393 K, and maintained under vacuum for 24 h to allow surface tension to shape the polymer into spheres. The polymer spheres were then slowly cooled and transferred onto the electropolished Al disk, which was coated with a thin native oxide layer to simulate the AAO surface. The contact angle was measured using a commercial goniometer (OCA35, DataPhysics) with IDS uEye software, at 358 K which corresponds to the infiltration

temperature.

**Surface Tension.** The Wilhelmy plate method was employed to measure the surface tension of poly[VBBI]<sup>+</sup>[TFSI]<sup>-</sup>. A platinum-iridium rod with a diameter of 1.2 mm was vertically immersed into the heated PIL (at 358 K). The downward force ( $F$ ) exerted by the surface tension was measured using a tension meter (DCAT 11BC, DataPhysics) after allowing the system to equilibrate for approximately 2000 s. The surface tension ( $\gamma$ ) was then calculated from  $F = l\gamma$ , where  $l$  is the circumference of the rod.

**Rheology.** The zero-shear viscosity was investigated using a shear rheometer (ARES) equipped with an environmental test chamber. Measurements were conducted as a function of temperature. Samples were placed on the lower plate of an 8 mm diameter parallel plate geometry, with the upper plate brought into contact and the sample thickness adjusted. The storage ( $G'$ ) and loss ( $G''$ ) shear moduli were monitored as a function of frequency,  $\omega$ , in the range  $10^{-1} < \omega < 10^2 \text{ rad}\cdot\text{s}^{-1}$ , within the linear viscoelastic regime. The complex viscosity ( $\eta^*$ ) was calculated using  $\eta^* = G''/\omega - iG'/\omega$ . Master curves were made by use of the time-temperature superposition principle ( $tT_s$ ). The latter allows the frequency  $\omega$  dependence of the complex modulus  $G^*$  at any temperature  $T$  to be determined from a master curve at a reference temperature. At each temperature  $T$ , a single frequency-scale shift factor ( $a_T$ ) enables the superposition of all viscoelastic data at temperature  $T$  onto the data at the reference temperature,  $T_{ref}$ , as  $G^*(\omega; T) = G^*(a_T\omega; T_{ref})$ . Master-curves used to extract the zero-shear viscosity,  $\eta_0$ , are presented in **Figures S2**.

### 5.3 Results and discussion

#### A. Bulk properties

The thermodynamic properties of two ILs sharing the same anion, [TFSI]<sup>-</sup>, and of the corresponding PILs are strongly influenced by cation molecular structure and size. Figure 1 presents the DSC traces, highlighting these differences. The cooling traces (rate of 10 K·min<sup>-1</sup>) reveal a step-like decrease of heat flow at the glass temperature ( $T_g$ ), representing the transformation from the liquid to the glass. All samples were found to be fully amorphous, with the exception of [BMIM]<sup>+</sup>[TFSI]<sup>-</sup> that exhibited cold-crystallization and melting during heating. Among the ILs, [VBBI]<sup>+</sup>[TFSI]<sup>-</sup> exhibits a higher  $T_g$  compared to [BMIM]<sup>+</sup>[TFSI]<sup>-</sup>. It can be attributed to the reduced mobility introduced by the extra phenyl group within [VBBI]<sup>+</sup>. However, in the PILs, it is the poly[BVIM]<sup>+</sup>[TFSI]<sup>-</sup> that exhibits the higher  $T_g$ . The proximity of the

imidazolium cation to the main chain in poly[BVIM]<sup>+</sup>[TFSI]<sup>-</sup> restricts the backbone mobility and gives rise to a higher  $T_g$  as compared to poly[VBBI]<sup>+</sup>[TFSI]<sup>-</sup>.

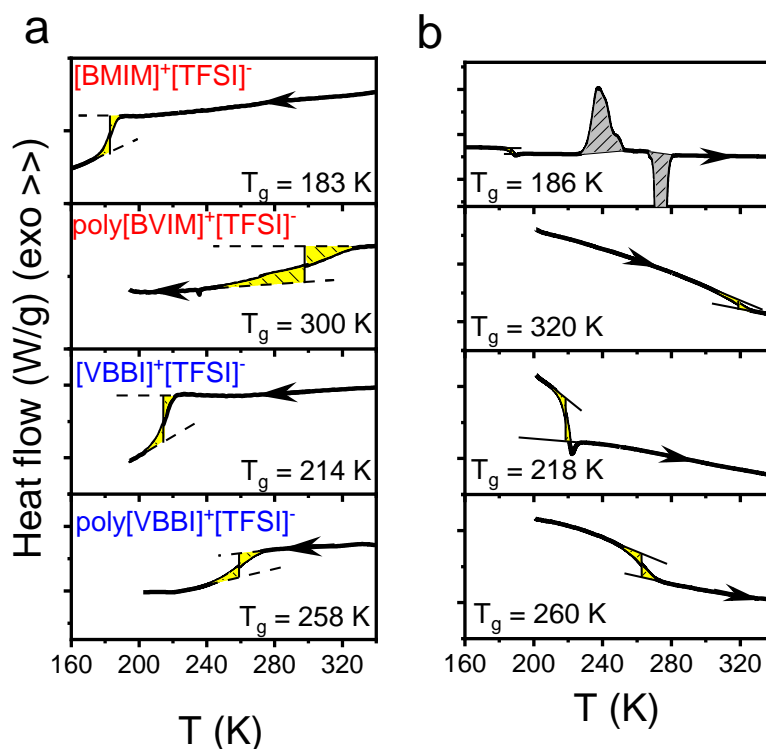


**Figure 1.** DSC traces of ILs, [BMIM]<sup>+</sup>[TFSI]<sup>-</sup>, [VBBI]<sup>+</sup>[TFSI]<sup>-</sup>, and the corresponding PILs, poly[BVIM]<sup>+</sup>[TFSI]<sup>-</sup> and poly[VBBI]<sup>+</sup>[TFSI]<sup>-</sup> in the bulk. Traces are shown during cooling (a) and subsequent heating (b) runs with a rate of 10 K·min<sup>-1</sup>.

ILs (and PILs) have a higher level of organization as compared to normal liquids.<sup>19,48</sup> Information about their local packing can be obtained through X-ray diffraction. The diffraction patterns of the ILs and their corresponding PILs are shown in Figure 2a. In the ILs, arrows 1, 2, and 3 correspond to the smectic layering of polar-apolar groups, the charge alternation peak, and the van der Waals peak of nearest neighbors, respectively. For PILs, similar correlation distances are observed (denoted as I, II, and III), but with a significant difference: Peak I, representing backbone-to-backbone correlations, becomes the dominant feature, especially for poly[BVIM]<sup>+</sup>[TFSI]<sup>-</sup>, revealing improved smectic layering.

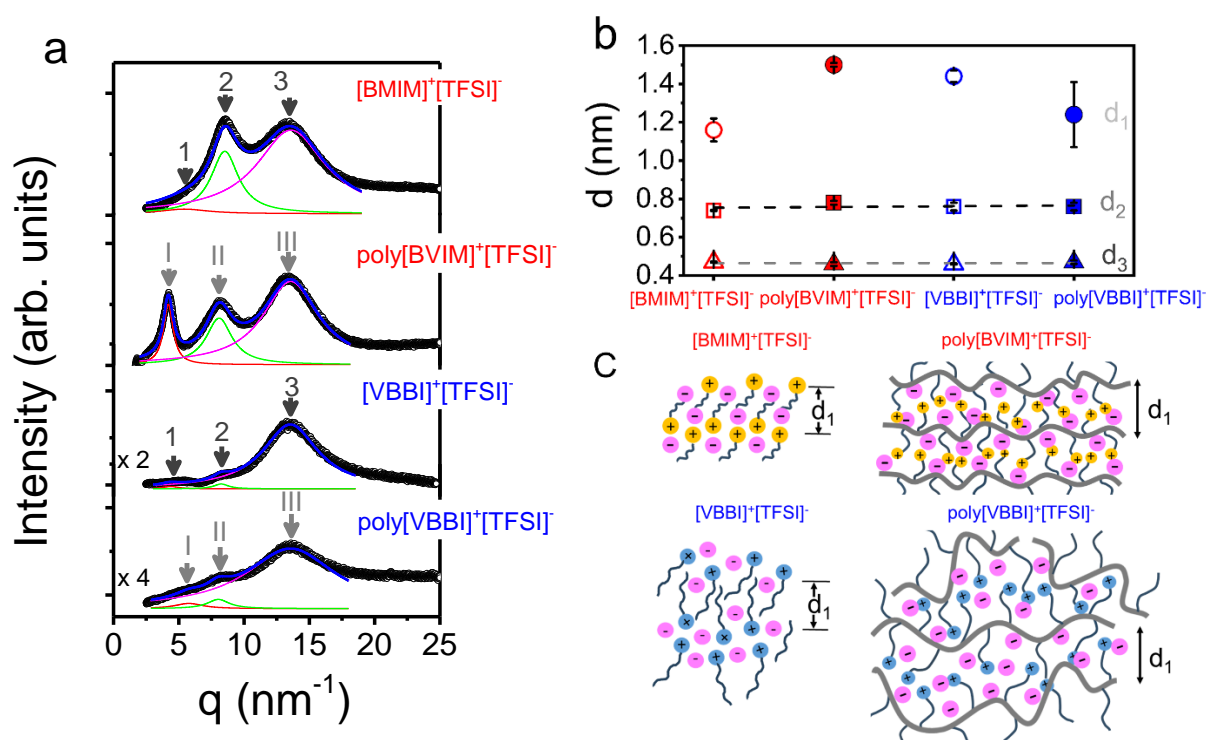


**Figure 2.** (a) XRD curves of the ILs and corresponding PILs at 358 K. For the ILs, arrows 1, 2, 3 indicate, respectively, the smectic layering of polar-apolar groups, the charge alteration peak, and the van der Waals peak of nearest neighbours. For the PILs, arrows I, II, III indicate, respectively, the distance between backbones, the anion-anion correlation distance, and the van der Waals contacts of atoms. Red, green and magenta lines are the respective component contributions to the scattering curve (blue). (b) Characteristic spacings (obtained as  $d=2\pi/q$ ) giving the period of smectic layering ( $d_1$ ), the charge alteration distances ( $d_2$ ) and the nearest approach of atoms ( $d_3$ ). The brown and grey dashed lines are linear fits to  $d_2$ ,  $d_3$ . (c) Schematic representation of the correlation distances in the ILs and the corresponding PILs. The schematic depicts ordered backbones in the case of poly[BVIM]<sup>+</sup>[TFSI]<sup>-</sup>, and relatively disordered domains in poly[VBBI]<sup>+</sup>[TFSI]<sup>-</sup>.

Compared to [BMIM]<sup>+</sup>[TFSI]<sup>-</sup> and poly[BVIM]<sup>+</sup>[TFSI]<sup>-</sup>, correlations in [VBBI]<sup>+</sup>[TFSI]<sup>-</sup> and poly[VBBI]<sup>+</sup>[TFSI]<sup>-</sup>, appear weaker, suggesting a more disordered packing (Figure 2c). In poly[VBBI]<sup>+</sup>[TFSI]<sup>-</sup>, the bulky phenyl-imidazole side group increases the rigidity of polymer backbone, resulting in an appreciable amount of packing frustration that disrupts the formation of a layered structure. In contrast, poly[BVIM]<sup>+</sup>[TFSI]<sup>-</sup> has a more compact structure with a smaller imidazolium-based side group, allowing for denser packing. This facilitates the formation of a more ordered layered domains. The variation in local packing can influence the anion transport. The impact on ionic mobility is reflected in the measured dc-conductivities for both IL and PILS pairs, as presented in Figure 3.

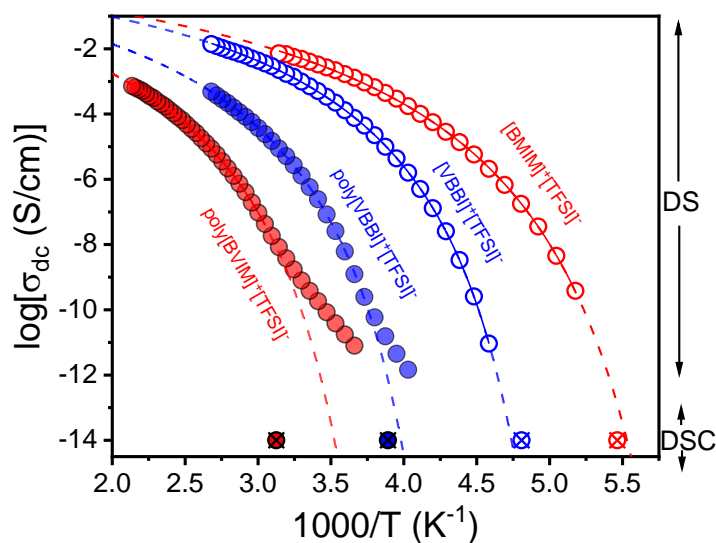


**Figure 3.** Temperature dependence of dc-conductivity for the ILs, shown with open circles, and corresponding PILs shown as spheres obtained on cooling; [BMIM]<sup>+</sup>[TFSI]<sup>-</sup> (open red circles), [VBBI]<sup>+</sup>[TFSI]<sup>-</sup> (open blue circles), poly[BVIM]<sup>+</sup>[TFSI]<sup>-</sup> (solid red circles), poly[VBBI]<sup>+</sup>[TFSI]<sup>-</sup> (solid blue circles). The solid/dashed lines are the results of fits to the Vogel-Fulcher-Tammann (VFT) equation. The crossed symbols represent the  $T_g$  obtained from DSC with a rate of 10 K·min<sup>-1</sup>.

The dc-conductivities and their dependence on temperature,  $\sigma'_{dc}(T)$ , shown in Figure 3. The values were obtained on cooling from the plateau at intermediate frequencies (Figure S3). In general,  $\sigma'_{dc}(T)$ , follows the Vogel-Fulcher-Tammann (VFT) equation written for the conductivity contribution as:

$$\sigma_{dc}(T) = \sigma_0 \exp\left(-\frac{B}{T-T_0}\right) \quad (5)$$

Here,  $\sigma_0$  is the dc-conductivity in the limit of very high temperatures,  $B$  is the activation parameter, and  $T_0$  is the “ideal” glass temperature (the parameters are summarized in **Table 1**, below). The glass temperatures of the ILs as obtained by DS are in good agreement with the DSC results. For poly[BVIM]<sup>+</sup>[TFSI]<sup>-</sup> and to a lesser degree for poly[VBBI]<sup>+</sup>[TFSI]<sup>-</sup>, the  $\sigma_{dc}(T)$  dependence follows the VFT dependence down to a temperature where a weaker (Arrhenius-like) dependence is obtained as:

$$\sigma_{dc}(T) = \sigma'_0 \exp\left(-\frac{E}{RT}\right) \quad (6)$$

Here  $E$  is the activation energy and  $R$  is the gas constant. At this temperature, ion dynamics decouple from the slower backbone dynamics as the system goes out of equilibrium. This temperature nicely corresponds to the DSC  $T_g$ .

**Figure 3** includes the estimated conductivity value at  $T_g$  as obtained from the Nernst-Einstein equation:

$$\sigma_{dc} = \frac{ne^2 \left(\frac{d_2}{2}\right)^2}{k_B T 6\tau} \quad (7)$$

Here,  $e$  is the elementary charge,  $n = \frac{\rho N_A}{M}$  ( $\rho = 1.44 \text{ g}\cdot\text{cm}^{-3}$  applicable to  $[\text{BMIM}]^+[\text{TFSI}]^-$ ) is the mass density,  $M = M_w^{\text{cation}} + M_w^{\text{anion}}$  is the molar mass of the cation and/or the backbone repeat unit and of the anion,  $d_2/2$  is the distance between two adjacent ions of opposite charge extracted from **Figure 2**,  $\tau$  is the characteristic structural relaxation time at  $T_g$  ( $\tau \sim 100 \text{ s}$ ; the typical relaxation time associated with the dynamics at the liquid-to-glass temperature) and  $k_B$  is the Boltzmann constant. Using  $d_2/2 \sim 0.38 \text{ nm}$  in Eq. 7 results to  $\sigma_{dc} \sim 10^{-14} \text{ S}\cdot\text{cm}^{-1}$ . The obtained conductivity values were used to determine the DS glass temperature (**Table 2**). Due to the small size and low viscosity, ILs inherently exhibit higher dc conductivity as compared to their PILs counterparts. Conversely, within the PILs, poly $[\text{VBBI}]^+[\text{TFSI}]^-$  demonstrates higher conductivity. This enhancement can be attributed to the electrostatic interactions between the  $[\text{TFSI}]^-$  anion and the phenyl-substituted imidazolium cation, taking place away from the backbone, that maintains significant mobility. In addition, the loose packing structure in poly $[\text{VBBI}]^+[\text{TFSI}]^-$  prevent the formation of tightly bound ion clusters thus promoting segmental mobility. In contrast, in poly $[\text{BVIM}]^+[\text{TFSI}]^-$ , electrostatic interactions between the cation and anion occur in close proximity to the polymer backbone thus restricting backbone dynamics and limiting ion mobility. In support of this notion, the zero-shear viscosity of poly $[\text{VBBI}]^+[\text{TFSI}]^-$  and poly $[\text{BVIM}]^+[\text{TFSI}]^-$  was examined and plotted in **Figure S4** as a function of the  $T_g$ -scaled temperature. Across the entire temperature range, poly $[\text{VBBI}]^+[\text{TFSI}]^-$  exhibits consistently lower zero-shear viscosity than poly $[\text{BVIM}]^+[\text{TFSI}]^-$ . These findings align with DSC results, as both conductivity and thermal behaviour reflect the influence of the cation structure on ion dynamics. Similar effects could be observed in imidazolium based PILs of the type  $\text{P}[\text{ECnVim}]^+[\text{PF}_6]^-$ .<sup>49</sup> There, increasing the size of the alkyl chain spacer  $n$  - therefore placing the ion association away from the backbone - resulted to an increased conductivity.

In conclusion, DS measurements of ion transport in the bulk ILs and PILs revealed that ion-conductivity in the latter is influenced by the cation size and in particular by the proximity of the cation to the backbone. In addition, anion dynamics were decoupled from the slower backbone on approaching  $T_g$  from higher temperatures and the decoupling was stronger for the backbone with the higher  $T_g$ . In a second part we investigate the effects of confinement.

**Table 2.** Parameters of the VFT Equation for the Conductivity (data obtained on Cooling).

	$\sigma_0/$ ( $S \cdot cm^{-1}$ )	$B$ (K)	$T_0$ (K)	$T_g^{DS}$ (K) (at $\sigma = 10^{-14} S/cm$ )	$T_g^{DSC}$ (K) <sup>a</sup>
[BMIM] <sup>+</sup> [TFSI] <sup>-</sup>	1.6	860 ± 10	155 ± 1	181 ± 1	183 ± 2
[VBBI] <sup>+</sup> [TFSI] <sup>-</sup>	1.5	880 ± 5	185 ± 1	210 ± 1	208 ± 2
poly[BMIM] <sup>+</sup> [TFSI] <sup>-</sup>	0.52	1505 ± 25	235 ± 1	284 ± 1	320 ± 2
poly[VBBI] <sup>+</sup> [TFSI] <sup>-</sup>	0.72	1150 ± 15	215 ± 1	252 ± 1	257 ± 2

<sup>a</sup> $T_g$  obtained from DSC is also shown for comparison.

### B. Confinement and flow effects on ion transport

There exists a growing interest on the way ionic systems penetrate nanopores. ILs of [BMIM]<sup>+</sup>[Cl]<sup>-</sup> were shown to penetrate AAO nanopores with their bulk viscosity.<sup>48</sup> In bulk PIL the high zero-shear viscosity precluded any investigation of the imbibition kinetics. Instead, mixtures of PILs with their corresponding ILs had a lower zero-shear viscosity that allowed an investigation of the imbibition kinetics within AAO nanopores.<sup>19</sup> It was shown that capillary action separates the IL from the PIL and effectively enriches the pores with the low viscosity component (IL).<sup>19</sup> Herein, we carefully select the molar masses and monitor the imbibition kinetics of the two PILs by *ex situ* reflection optical microscopy (ROM), and by *in situ* nano-dielectric microscopy (*nDS*). Figure 4a,c, gives the results of the imbibition length of poly[VBBI]<sup>+</sup>[TFSI]<sup>-</sup> and poly[BVIM]<sup>+</sup>[TFSI]<sup>-</sup> within AAO cross-sections by ROM obtained for different time intervals. The imbibition length for the two PILs is plotted as a function of the square root of time in Figure 4b under conditions  $\Delta T = T_{imbibition} - T_g = 100$  K.

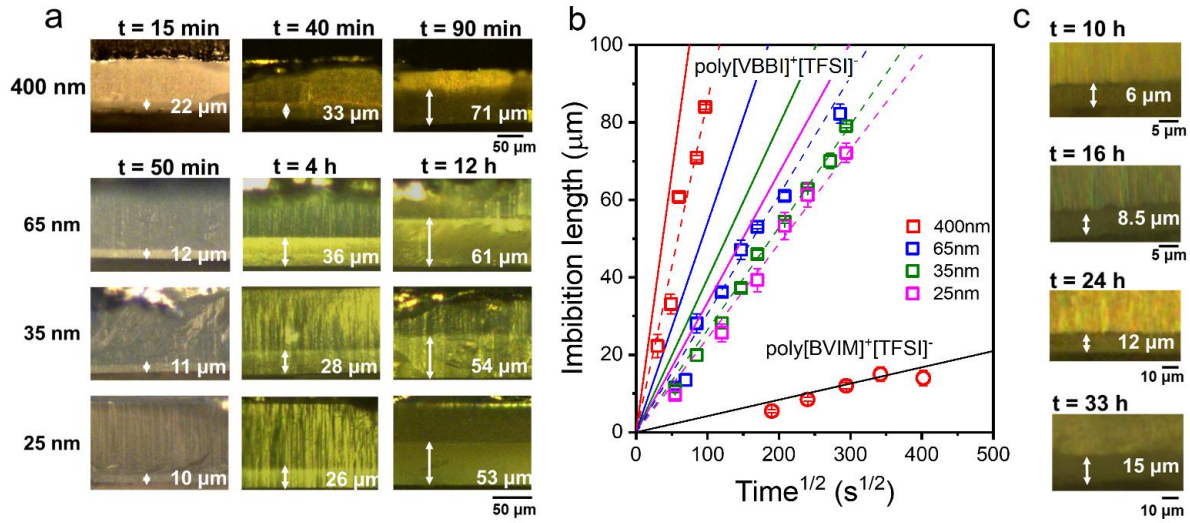


**Figure 4.** Optical images of the imbibition of (a) poly[VBBI]<sup>+</sup>[TFSI]<sup>-</sup> in AAO templates with different pore sizes measured at 358 K and (c) poly[BVIM]<sup>+</sup>[TFSI]<sup>-</sup> in AAO templates with a diameter of 400 nm at 400 K. At the corresponding imbibition temperature, the temperature difference from the respective  $T_g$  is constant (i.e.,  $\Delta T = T_{\text{imbibition}} - T_g = 100$  K for both PILs). The white double-headed arrows indicate the imbibition length at the specified time interval. (b) Imbibition lengths for poly[VBBI]<sup>+</sup>[TFSI]<sup>-</sup> and poly[BVIM]<sup>+</sup>[TFSI]<sup>-</sup> measured at 358 K and 400 K, respectively, by *ex situ* ROM within AAOs with different pore sizes: 400 nm (red), 65 nm (blue), 35 nm (olive), and 25 nm (magenta). Solid lines are theoretical predictions based on the Lucas-Washburn equation (LWE) with parameters:  $\eta_0$  (bulk, poly[VBBI]<sup>+</sup>[TFSI]<sup>-</sup>) =  $10^3$  Pa·s,  $\eta_0$  (bulk, poly[BVIM]<sup>+</sup>[TFSI]<sup>-</sup>) =  $7 \times 10^5$  Pa·s,  $\gamma_L = 27.4$  mN/m, and  $\cos \theta = 0.5$ . Dashed lines represent the result of a linear fit to the data.

According to the Lucas-Washburn equation,<sup>50,51</sup> the imbibition length,  $L$ , follows:  $L = \left(\frac{\gamma R \cos \theta}{2\eta}\right)^{1/2} \sqrt{t}$ , where  $\gamma$  is the surface tension,  $\theta$  is the contact angle,  $\eta$  is the zero-shear viscosity, and  $R$  is the pore radius. The LWE was derived for Newtonian liquids. Figure 4a, c present ROM images with values of imbibition lengths obtained across several nanopores. Averaged  $L$  values are plotted in Figure 4b. These data together with the LWE can be used to extract an effective viscosity applicable to the PIL during flow in nanopores. For poly[VBBI]<sup>+</sup>[TFSI]<sup>-</sup>, in all pore diameters investigated, the extracted effective viscosity (using  $\cos \theta = 0.5$  and  $\gamma_L = 27.4$  mN/m) is higher than in bulk (bulk  $\eta_0 = 10^3$  Pa·s). The effective viscosities were determined as  $1.9 \times 10^3$ ,  $2.4 \times 10^3$ ,  $1.7 \times 10^3$  and  $1.5 \times 10^3$  Pa·s within pores of 400, 65, 35, and 25 nm, respectively. This deviation from bulk behaviour is expected to influence the dc-conductivity values. For poly[BVIM]<sup>+</sup>[TFSI]<sup>-</sup>, the imbibition length within 400 nm nanopores increases again with the square root of time, but imbibition is significantly slower compared to poly[VBBI]<sup>+</sup>[TFSI]<sup>-</sup>. This suggests a higher effective viscosity ( $\eta = 1.1 \times 10^6$  Pa·s) for poly[BVIM]<sup>+</sup>[TFSI]<sup>-</sup> that hinder

infiltration despite the same  $\Delta T_g$ . The result is consistent with a higher zero-shear viscosity in the bulk (**Figure S4**).

We compare the imbibition kinetics in the two PILs by following the increase in conductivity at a selected frequency using *in situ* nDS. The comparison is made under the same temperature difference ( $\Delta T$ ) from the respective  $T_g$  in Figure 5. Poly[VBBI]<sup>+</sup>[TFSI]<sup>-</sup> demonstrates faster imbibition kinetics. Despite the identical  $\Delta T_g$ , poly[BVIM]<sup>+</sup>[TFSI]<sup>-</sup> penetrate slower into the same nanopores. This is described by a higher effective viscosity for poly[BVIM]<sup>+</sup>[TFSI]<sup>-</sup> at the imbibition temperature. Indeed, the  $T_g$ -scaled zero-shear viscosity (**Figure S4**) shows 2 orders of magnitude higher zero-shear viscosity in poly[BVIM]<sup>+</sup>[TFSI]<sup>-</sup> as compared to poly[VBBI]<sup>+</sup>[TFSI]<sup>-</sup> at the imbibition temperature.

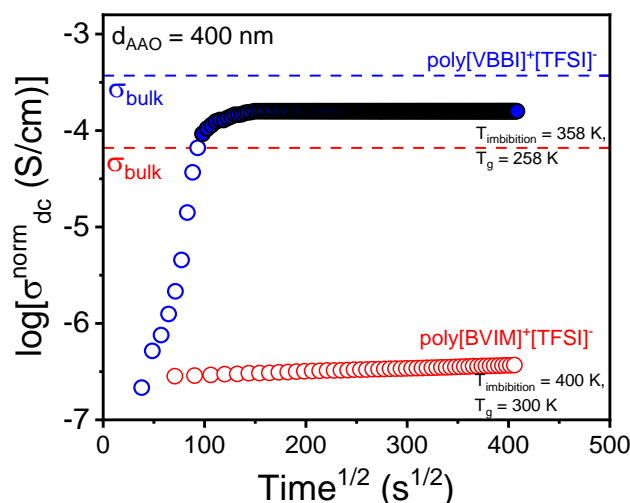


**Figure 5.** Comparison of the evolution in ionic conductivity from *in situ* nDS for poly[VBBI]<sup>+</sup>[TFSI]<sup>-</sup> (blue) and poly[BVIM]<sup>+</sup>[TFSI]<sup>-</sup> (red) within AAO with a pore size of 400 nm at different temperatures corresponding to the same temperature difference from the respective  $T_g$  ( $\Delta T = T_{\text{imbibition}} - T_g = 100$  K). The dashed lines respect the dc-conductivity of PILs in bulk.

Because of the extremely slow imbibition kinetics in poly[BVIM]<sup>+</sup>[TFSI]<sup>-</sup>, we explored the pore-size dependence of the conductivity evolution in poly[VBBI]<sup>+</sup>[TFSI]<sup>-</sup>. The results at the imbibition temperature of 358 K are shown in Figure 6. In 400 nm pores, there is a fast initial increase of ionic conductivity followed by a constant value (e.g. dc-conductivity) at later times (Figure 6a). The open symbols in Figure 5 and Figure 6b denote an initial rise of conductivity in the absence of a conductivity plateau, e.g., the values do not correspond to the dc-conductivity, but to the ac-conductivity (at a frequency of  $10^5$  Hz). It is only at later times that the plateau is developed (Figure 6a). The timescale for the development of the conductivity plateau nicely corresponds with the complete filling of nanopores as suggested by ROM (Figure 4). We note

that for all investigated pore sizes, the dc-conductivity following the full imbibition remains consistently lower than the bulk value. Based on our previous studies,<sup>18,19</sup> this reduction can be attributed to polymer-pore wall interactions, which induced polymer adsorption and restricted the mobility of polymer segments. The adsorbed polymer chains inevitably immobilize some counterions at the pore walls. Since the latter are unable to diffuse, they do not participate in charge transport, leading to a reduced overall conductivity compared to the bulk.

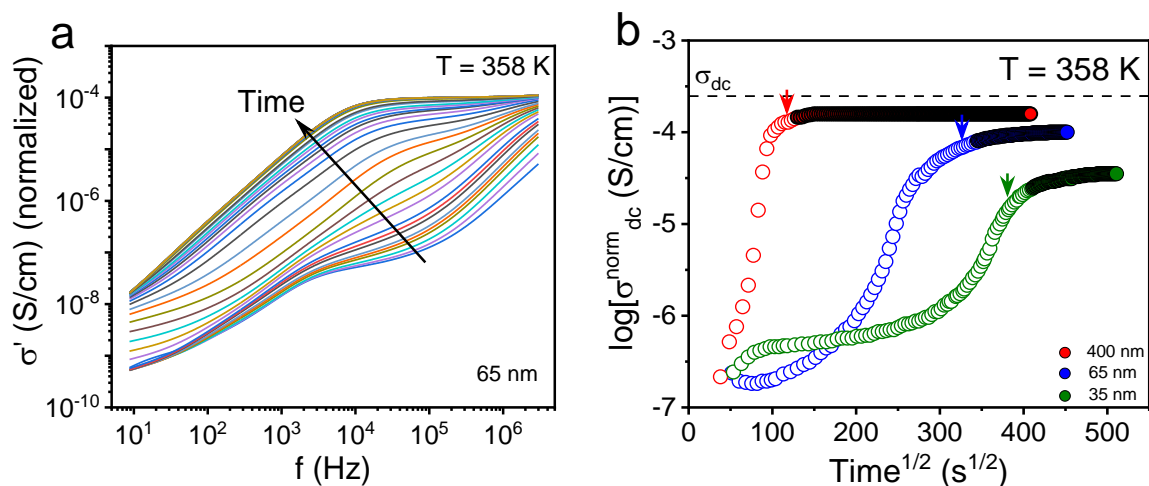


**Figure 6.** (a) Evolution of the real part of the normalized conductivity (for the porosity) of poly[VBBI]<sup>+</sup>[TFSI]<sup>-</sup> within AAO template with a diameter of 65 nm at 358 K. (b) Evolution of dc-conductivity during the imbibition of poly[VBBI]<sup>+</sup>[TFSI]<sup>-</sup> within AAO templates with varying pore sizes at 358 K. The conductivity values are corrected for porosity. The dashed line indicates the dc-conductivity for the bulk PIL at the same temperature. Open circles provide the (ac) conductivity of the poly[VBBI]<sup>+</sup>[TFSI]<sup>-</sup> during flow within AAO, while filled circles provide the respective dc-conductivities. Arrows indicate the time of full imbibition of the PIL, as determined from ex situ ROM experiments (**Figure 4**).

To explore confinement effects on the ion dynamics we performed temperature scans of the dc-conductivity starting from the imbibition temperature by cooling down to the glassy state. The dc-conductivity values can be discussed with the help of Figure 7. In addition, the figure includes the zero-shear viscosity in the bulk. In the same figure we plot the characteristic ion relaxation times as extracted from the modulus representation as  $M^* = 1/\varepsilon^*$  (**Figure S3**). At high temperatures, the dc-conductivity and the characteristic times of ion relaxation follows a VFT dependence, with the corresponding VFT parameters listed in **Table 3**. As we discussed earlier with respect to Figure 3, the  $\sigma_{dc}(T)$  dependence for poly[VBBI]<sup>+</sup>[TFSI]<sup>-</sup> follows the VFT dependence down to a temperature where ion dynamics decouple from the backbone as the system goes out of equilibrium. As shown in Figure 7, the decoupling depends on pore diameter. At higher temperatures, the dc-conductivity is lower than the bulk because of adsorption during

imbibition that drives some ions at the pore walls. At lower temperatures, confinement results in a stronger decoupling from the backbone dynamics according to eq. 6. From an apparent activation energy ( $E$ ) of  $142 \pm 6$  kJ/mol in the bulk, to  $109 \pm 4$  kJ/mol and to  $108 \pm 4$  kJ/mol in nanopores with diameters of 400 nm and 35 nm, respectively. Spatial constraints alter local cation – anion correlations and modify the distribution of accessible pathways for ion transport.

The activation energy in the bulk is in proximity to the predictions of a recent model discussing the dependence of the activation energy of ion diffusion on ion size.<sup>30</sup> The activation energy for the ion diffusion shows a non-monotonous dependence on the mobile ion size, indicating competition between Coulombic and elastic forces. It was suggested that the former dominates the mobility of small ions, while the latter controls mobility of large ions (e.g., TFSI). The term due to elastic forces has its origin on the shoving model of the glass "transition".<sup>52</sup> The model considers the motion of a structural unit in a frozen environment and suggests that the activation energy for molecular motion is controlled by thermal fluctuations creating an increase in local volume that is comparable to the volume of the moving ion. The reduced activation energy under confinement could suggest additional packing effects in the contribution of the elastic forces.

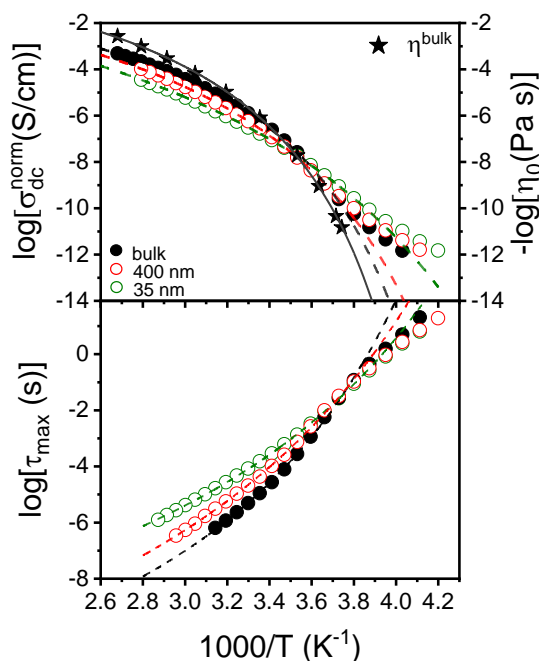


**Figure 7.** (Top) Temperature dependence of the dc-conductivity (left) and the zero-shear viscosity (right) for bulk poly[VBBI]<sup>+</sup>[TFSI]<sup>-</sup> (filled spheres) and confined poly[VBBI]<sup>+</sup>[TFSI]<sup>-</sup> in AAO nanopores with diameters 400 nm (red circles) and 35 nm (green symbols) following the imbibition experiments (shown in Figure 6b). (Bottom) Corresponding ion relaxation times extracted from the modulus representation plotted as a function of inverse temperature. In both cases the dashed lines represent VFT fits.

**Table 3.** Parameters of the VFT Equation for the poly[VBBI]<sup>+</sup>[TFSI]<sup>-</sup> pertinent to the Temperature Scan Experiments Following Imbibition

Pore diameter, $d$ (nm)	$-\log_{10}(\tau_0/s)$	$B^r$ (K)	$T_0^r$ (K)	$\log_{10}[\sigma_0/(S \cdot cm^{-1})]$	$B^\sigma$ (K)	$T_0^\sigma$ (K)
bulk	$11 \pm 0.1$	$1230 \pm 30$	$215 \pm 2$	$-0.14 \pm 0.1$	$1150 \pm 15$	$215 \pm 1$
400	$12 \pm 0.3$	$1970 \pm 150$	$190 \pm 5$	$0.19 \pm 0.1$	$1500 \pm 30$	$202 \pm 1$
35	$12 \pm 0.2$	$2650 \pm 130$	$150 \pm 4$	$0.44 \pm 0.1$	$2060 \pm 50$	$170 \pm 2$
				$-\log_{10}[\eta_0/(Pa \cdot s)]$	$A$ (K)	$T_0$ (K)
bulk				$0.9 \pm 0.1$	$1235 \pm 40$	$220 \pm 1$

Overall PILs, contrary to ILs, penetrate AAO nanopores with a higher effective viscosity than the bulk (by approximately a factor of 2). Following imbibition, the conductivity data show the manifestation of adsorption and confinement effects. At higher temperatures, PILs exhibit reduced ionic conductivity as compared to bulk. Polymer adsorption controls ionic mobility in this limit. By decreasing temperature towards the bulk  $T_g$ , anion motion decouples from the sluggish backbone dynamics and restores part of the ionic conductivity. Overall, confinement can be employed as a tool of decoupling anion dynamics from the backbone.

## 5.4 Conclusion

Precise synthesis of ILs and of the corresponding PILs bearing identical anions but different cation sizes provided the means of testing the effects of ion association on ion mobility in the bulk and under nanometer confinement.

In the bulk PILs, ion conductivity was influenced by cation size, and in particular, by the distance of the cation from the backbone. Placing the cation near the backbone resulted to ion association that effectively rigidified the chain. This had an effect on the glass temperature (increasing) and on the ion conductivity (decreasing). In PILs there was a decoupling of ion motion from the backbone dynamics by decreasing temperature near  $T_g$ ; the higher the  $T_g$  of the PIL the stronger the decoupling. The temperature dependence of ion conductivity deviated from the Vogel-Fulcher-Tammann law and followed an Arrhenius temperature dependence with an activation energy of 142 kJ/mol in the case of poly[BVIM]<sup>+</sup>[TFSI]<sup>-</sup>.

When the same PILs were located within nanopores, the ionic mobility was influenced by two effects: *adsorption* and *confinement*. PILs penetrated nanopores with higher effective viscosity than in bulk, reflecting adsorption effects. The latter effects dominated ion mobility at  $T \gg T_g$  and gave rise to reduced conductivity. As temperature was lowered near  $T_g$ ,

confinement enhanced the decoupling of ion motion from the polymer backbone by reducing the activation energy in the smaller pores. Under these conditions, the temperature dependence of ion conductivity followed an Arrhenius temperature dependence with an activation energy that was reduced to  $\sim 108$  kJ/mol under confinement. It suggested that confinement provides the means of increasing conductivity at temperatures in the vicinity of  $T_g$  where, intrinsically, ion mobility is reduced.

The results offer some new insights into how molecular structure and confinement affect ion transport in PILs. Placing the cation away from the polymer backbone and further confining the PIL with nanopores can increase the ionic conductivity at lower temperatures, and this, despite adsorption effects that act at higher temperatures but in an opposite direction.

## 5.5 References

- (1) Li, Q.; Yan, F.; Texter, J. Polymerized and Colloidal Ionic Liquids – Syntheses and Applications. *Chem. Rev.* **2024**, *24*, 3813-3931.
- (2) Mecerreyes, D. Polymeric Ionic Liquids: Broadening the Properties and Applications of Polyelectrolytes. *Progress in Polymer Science* **2011**, *36*, 1629–1648.
- (3) Marcilla, R.; Blazquez, J. A.; Rodriguez, J.; Pomposo, J. A.; Mecerreyes, D. Tuning the Solubility of Polymerized Ionic Liquids by Simple Anion-Exchange Reactions. *J Polym Sci Part A Polym Chem*, **2004**, *42*, 208-212.
- (4) Armand, M. Polymers with Ionic Conductivity. *Adv. Mater.*, **1990**, *2*, 278–286.
- (5) Galiński, M.; Lewandowski, A.; Stepniak, I. Ionic Liquids as Electrolytes. *Electrochim. Acta* **2006**, *51*, 5567-5580.
- (6) Watanabe, M.; Thomas, M. L.; Zhang, S.; Ueno, K.; Yasuda, T.; Dokko, K. Application of Ionic Liquids to Energy Storage and Conversion Materials and Devices. *Chem. Rev.* **2017**, *117*, 7190-7239.
- (7) Simon, P.; Gogotsi, T. Materials for Electrochemical Capacitors. *Nat. Mater.* **2008**, *7*, 845-854.
- (8) Green, M.D.; Salas-de la Cruz, D.; Ye, Y.; Layman, J.M.; Elabd, Y.A.; Winey, K.I.; Long, T.E. Alkyl-Substituted N-Vinylimidazolium Polymerized Ionic Liquids: Thermal Properties and Ionic Conductivities. *Macromol. Chem. Phys.* **2011**, *212*, 2522-2528.
- (9) Ito, K.; Nishina, N.; Ohno, H. Enhanced Ion Conduction in Imidazoliumtype Molten Salts. *Electrochim Acta*, **2000**, *45*, 1295–1298.
- (10) Marcilla, R.; Blazquez, J. A.; Fernandez, R.; Grande, H.; Pomposo, J. A.; Mecerreyes, D. Synthesis of Novel Polycations Using the Chemistry of Ionic Liquids. *Macromol Chem Phys*, **2005**, *206*, 299–304.
- (11) Li, M.; Yang, L.; Fang, S.; Dong, S. Novel Polymeric Ionic Liquid Membranes as Solid Polymer Electrolytes with High Ionic Conductivity at Moderate Temperature. *J Membr Sci*, **2011**, *366*, 245–250.
- (12) Pont, A. L.; Marcilla, R.; Meatza, I.; Grande, H.; Mecerreyes, D. Pyrrolidinium-Based Polymeric Ionic Liquids as Mechanically and Electrochemically Stable Polymer Electrolytes. *J Power Sources* **2009**, *188*, 558–563.
- (13) Lee, M.; Choi, U. H.; Colby, R.; Gibson, H. R. Ion Conduction in Imidazolium Acrylate Ionic Liquids and Their Polymers. *Chem Mater*, **2010**, *22*, 814–822.
- (14) Appetecchi, G. B.; Kim, G. T.; Montanina, M.; Carewska, M.; Marcilla, R.; Mecerreyes, D.; DeMeatza, I. Ternary Polymer Electrolytes Containing Pyrrolidinium-Based Polymeric Ionic Liquids for Lithium Batteries. *J Power Sources*, **2010**, *195*, 3668–3675.
- (15) Marcilla, R.; Mecerreyes, D.; Winroth, G.; Brovelli, S.; Rodriguez, M.; Cacialli, F. Light Emitting Electrochemical Cells Using Polymeric Ionic Liquid/Polyfluorene Blends as Luminescent Material. *Appl Phys Lett*, **2010**, *96*, 1–3.
- (16) Yu, B.; Zho, F.; Wang, C.; Liu, W. A Novel Gel Polymer Electrolyte Based on Poly Ionic Liquid 1-Ethyl 3-(2-Methacryloxyloxy Ethyl) Imidazolium Iodide. *Eur Polym J*, **2007**, *43*, 2699.
- (17) Matsumi, N. K.; Miyake, S. M.; and Ohno, H. Polymerized Ionic Liquids via Hydroboration Polymerization as Single Ion Conductive Polymer Electrolytes. *Macromolecules*, **2006**, *39*, 6924–6927.
- (18) Tu, C.-H.; Veith, L.; Butt, H. J.; Floudas, G. Ionic Conductivity of a Solid Polymer Electrolyte Confined in Nanopores. *Macromolecules* **2022**, *55*, 1332-1341.
- (19) Dong, Y.; Steinhart, M.; Butt, H. J.; Floudas, G. Demixing of Polymerized Ionic Liquid/Ionic Liquid Mixtures by Infiltration in Nanopores. *Macromolecules*, **2024**, *57*, 5409–5420

- (20) Nishimura, N.; Ohno, H. 15th Anniversary of Polymerized Ionic Liquids, *Polymer* **2014**, *55*, 3289–3297.
- (21) Kinsey, T.; Glynn, K.; Cosby, T.; Jacob, C.; Sangoro, J. Ion Dynamics of Monomeric Ionic Liquids Polymerized In Situ within Silica Nanopores. *ACS Appl. Mater. Interfaces* **2020**, *12*, 44325–44334.
- (22) Choi, U. H.; Mittal, A.; Price, T. L.; Lee, M.; Gibson, H. W.; Runt, J.; Colby, R. H. Molecular Volume Effects on the Dynamics of Polymerized Ionic Liquids and their Monomers. *Electrochim. Acta* **2015**, *175*, 55–61.
- (23) Bocharova, V.; Wojnarowska, Z.; Cao, P.-F.; Fu, Y.; Kumar, R.; Li, B.; Novikov, V. N.; Zhao, S.; Kisliuk, A.; Saito, T.; Mays, J. W.; Sumpter, B. G.; Sokolov, A. P. Influence of Chain Rigidity and Dielectric Constant on the Glass Transition Temperature in Polymerized Ionic Liquids. *J. Phys. Chem. B* **2017**, *121*, 11511–11519.
- (24) Choi, U. H.; Ye, Y.; Salas de la Cruz, D.; Liu, W.; Winey, K. I.; Elabd, Y. A.; Runt, J.; Colby, R. H. Dielectric and Viscoelastic Responses of Imidazolium-Based Ionomers with Different Counterions and Side Chain Lengths. *Macromolecules* **2014**, *47*, 777–790.
- (25) Mogurampelly, S.; Keith, J. R.; Ganesan, V. Mechanism Underlying Ion Transport in Polymerized Ionic Liquids. *J. Am. Chem. Soc.* **2017**, *139*, 9511–9514.
- (26) Zhang, Z.; Nasrabudi, A.T.; Aryal, D.; Ganesan, V. Mechanisms of Ion Transport in Lithium Salt-Doped Polymeric Ionic Liquid Electrolytes, *Macromolecules* **2020**, *53*, 6995–7008.
- (27) Pipertzis, A.; Papamokos, G.; Mühlinghaus, M.; Mezger, M.; Scherf, U.; Floudas, G. What Determines the Glass Temperature and dc-Conductivity in Imidazolium-Polymerized Ionic Liquids with a Polythiophene Backbone? *Macromolecules* **2020**, *53*, 3535–3550.
- (28) Wang, Y.; Agapov, A.L.; Fan, F.; Hong, K.; Yu, X.; Mays, J.; Sokolov, A.P. Decoupling of Ionic Transport from Segmental Relaxation in Polymer Electrolytes. *Phys. Rev. Lett.* **2012**, *108*, 088303.
- (29) Sangoro, J. R.; Jacob, C.; Agapov, A. L.; Wang, Y.; Berdzinski, S.; Rexhausen, H.; Strehmel, V.; Friedrich, C.; Sokolov, A. P.; Kremer, F. Decoupling of Ionic Conductivity from Structural Dynamics in Polymerized Ionic Liquids. *Soft Matter* **2014**, *10*, 3536–3540.
- (30) Stacy, E.W.; Gainaru, K.P.; Gobet, M.; Wojnarowska, Z.; Bocharova, V.; Greenbaum, S.G.; Sokolov, A.P. Fundamental Limitations of Ionic Conductivity in Polymerized Ionic Liquids. *Macromolecules* **2018**, *51*, 8637–8645.
- (31) Kuray, P.; Noda, T.; Matsumoto, A.; Jacob, C.; Hickner, M.A.; Runt, J. Ion Transport in Pendant and Backbone Polymerized Ionic Liquids. *Macromolecules* **2019**, *52*, 6438–6448.
- (32) He, H.; Luebke, D.; Nulwala, H.; Matyjaszewski, K. Synthesis of Poly(ionic liquid)s by Atom Transfer Radical Polymerization with ppm of Cu Catalyst. *Macromolecules* **2014**, *47*, 6601–6609.
- (33) He, H.; Zhong, M.; Adzima, B.; Luebke, D.; Nulwala, H.; Matyjaszewski, K. A Simple and Universal Gel Permeation Chromatography Technique for Precise Molecular Weight Characterization of Well-Defined Poly(ionic liquid)s. *J. Am. Chem. Soc.* **2013**, *135*, 4227–4230.
- (34) Harrison, S.; Whitfield, R.; Anastasaki, A.; Matyjaszewski, K., Atom Transfer Radical Polymerization, *Nature Reviews Methods Primers* **2025**, *5*, 2.
- (35) Matyjaszewski, K., Current Status and Outlook for ATRP, *Eur. Polym. J.* **2024**, *211*, 113001.

- (36) Lorandi, F.; Fantin, M.; Matyjaszewski, K., Atom Transfer Radical Polymerization: A Mechanistic Perspective, *J. Am. Chem. Soc.* **2022**, *144*, 15413-15430.
- (37) Matyjaszewski, K., Advanced Materials by Atom Transfer Radical Polymerization, *Adv. Mater.* **2018**, *30*, 1706441.
- (38) Xiao, W. C.; Yang, Q.; Zhu, S. L. Comparing Ion Transport in Ionic Liquids and Polymerized Ionic Liquids. *Sci. Rep.*, **2020**, *10*, 7825.
- (39) He, F.; Wang, B.; Zhao J.; Yin, J. B. Influence of Tethered Ions on Electric Polarization and Electrorheological Property of Polymerized Ionic Liquids. *Molecules* **2020**, *25*, 2896.
- (40) Masuda, H.; Fukuda, K. Ordered Metal Nanohole Arrays Made by a Two-Step Replication of Honeycomb Structures of Anodic Alumina. *Science* **1995**, *268*, 1466–1468.
- (41) Masuda, H.; Hasegawa, F.; Ono, S. Self-ordering of Cell Arrangement of Anodic Porous Alumina Formed in Sulfuric Acid Solution. *J. Electrochem. Soc.* **1997**, *144*, L127–L130.
- (42) Masuda, H.; Yada, K.; Osaka, A. Self-ordering of Cell Configuration of Anodic Porous Alumina with Large-Size Pores in Phosphoric Acid Solution. *Jpn. J. Appl. Phys.* **1998**, *37*, L1340–L1342.
- (43) Steinhart, M. Supramolecular Organization of Polymeric Materials in Nanoporous Hard Templates. *Adv. Polym. Sci.* **2008**, *220*, 123–187.
- (44) Suzuki, Y.; Steinhart, M.; Kappl, M.; Butt, H.-J.; Floudas, G. Effects of Polydispersity, Additives, Impurities and Surfaces on the Crystallization of Poly(ethylene oxide)(PEO) Confined to Nanoporous Alumina. *Polymer* **2016**, *99*, 273- 280.
- (45) Cench, L.G.; Huber, P.; Kappl, M.; Floudas, G.; Steinhart, M.; Berli, C.L.A.; Urteaga, R. Nondestructive High-Throughput Screening of Nanopore Geometry in Porous Membranes by Imbibition. *Appl. Phys. Lett.* 2019, *115*, 113701.
- (46) Kremer, A. Schönhal, in *Broadband Dielectric Spectroscopy*, Springer, Berlin, (2002).
- (47) Floudas, G.; Paluch, M.; Grzybowski, A.; Ngai, K.L. in *Molecular Dynamics of Glass-Forming Systems. Effects of Pressure*, Springer (2011).
- (48) Dong, Y.; Steinhart, M.; Butt, H.-J.; Floudas, G. Conductivity of Ionic Liquids in the Bulk and During Infiltration in Nanopores. *J. Phys. Chem. B* **2023**, *127*, 6958–6968.
- (49) He, F.; Xue, B.; Zhao, X.; Yin, J. Electrorheological Effect and Dielectric Properties of Poly(ionic liquid) microspheres with different length of alkyl chain spacer between ion pair and backbone. *Polymer* **2023**, *268*, 125714.
- (50) Lucas, R. On the Time Law of the Capillary Rise of Liquids. *Colloid Polym. Sci.* **1918**, *23*, 15–22.
- (51) Washburn, E.W. The Dynamics of Capillary Flow. *Phys. Rev.* **1921**, *17*, 273–283.
- (52) Dyre, J. C. Colloquium: The glass transition and elastic models of glass-forming liquids. *Rev. Mod. Phys.* **2006**, *78*, 953–972.

## 5.6 Supporting information

**Gel permeation chromatography (GPC).** The molecular weight of poly[VBBI]<sup>+</sup>[TFSI]<sup>-</sup> was measured using a series of PILs containing [TFSI]<sup>-</sup> anions synthesized by reversible addition-fragmentation chain-transfer (RAFT) polymerization from 4-vinylbenzyl chloride (denote as poly[VBBI]<sup>+</sup>[TFSI]<sup>-</sup><sub>RAFT</sub>) as the standards.<sup>1,2</sup> To prepare a solution of polymer for GPC measurement, *ca.* 2 mg of poly[VBBI]<sup>+</sup>[TFSI]<sup>-</sup> was dissolved in 1 mL THF containing 10 mM LiTFSI and 10 mM 1-butylimidazole, and the solution was filtered through 0.2 μm polytetrafluoroethylene (PTFE) membrane filter before injecting into GPC columns. For poly[BVIM]<sup>+</sup>[TFSI]<sup>-</sup>, the linear PS standards was used for the calibration of the GPC measurement. The eluent was also THF solution containing 10 mM LiTFSI and 10 mM 1-butylimidazole.

### FIGURES

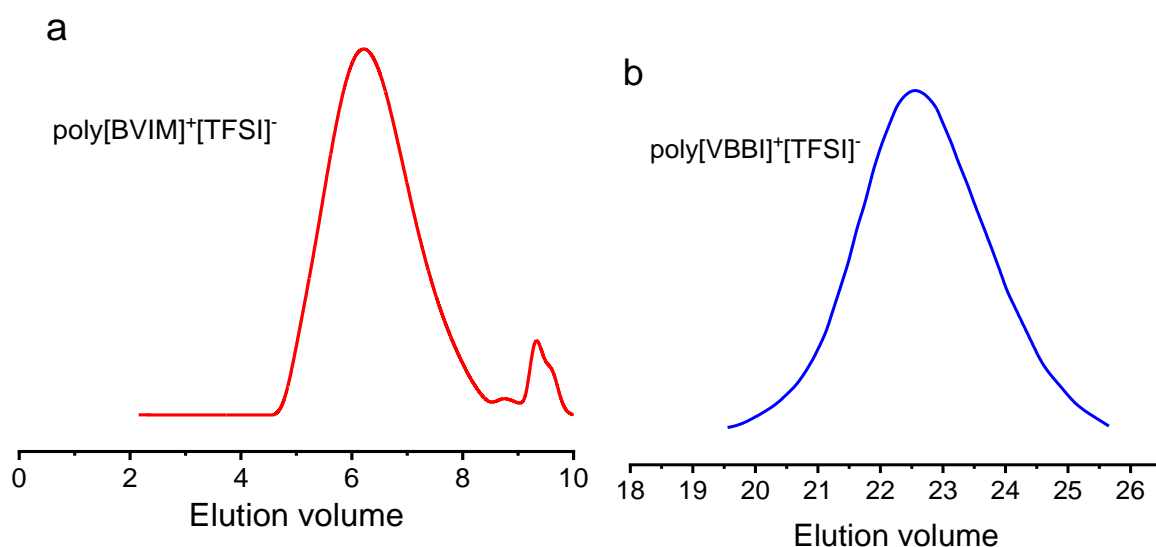


**Figure S1.** GPC curves of poly[BVIM]<sup>+</sup>[TFSI]<sup>-</sup> (a)<sup>3</sup> and poly[VBBI]<sup>+</sup>[TFSI]<sup>-</sup> (b)<sup>1</sup>.

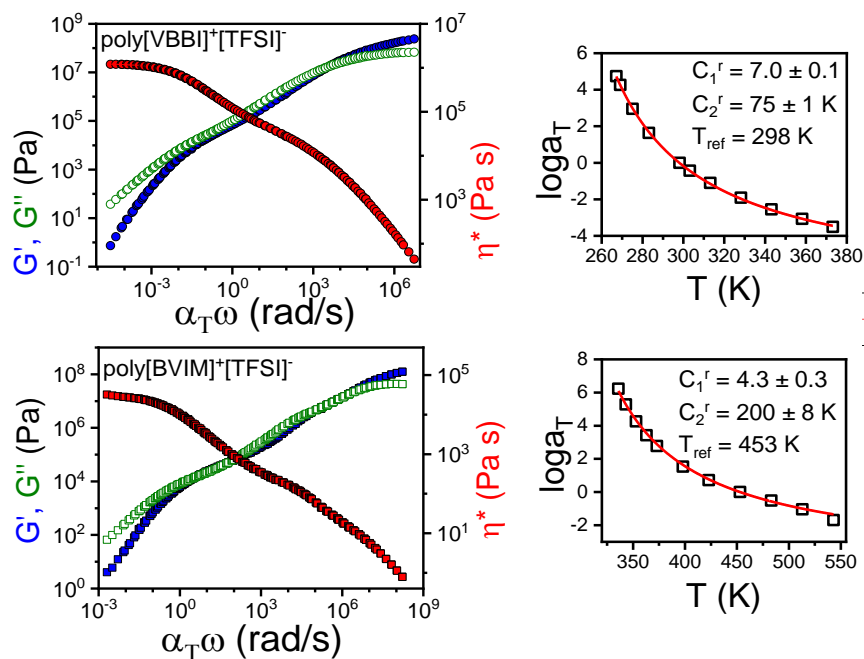


**Figure S2.** Master curves for the storage (blue), the loss (green) modulus and shear viscosities (red) of poly[VBBI]<sup>+</sup>[TFSI]<sup>-</sup> and poly[BVIM]<sup>+</sup>[TFSI]<sup>-</sup>. Inset plots indicate the shaft factors at the corresponding reference temperature.

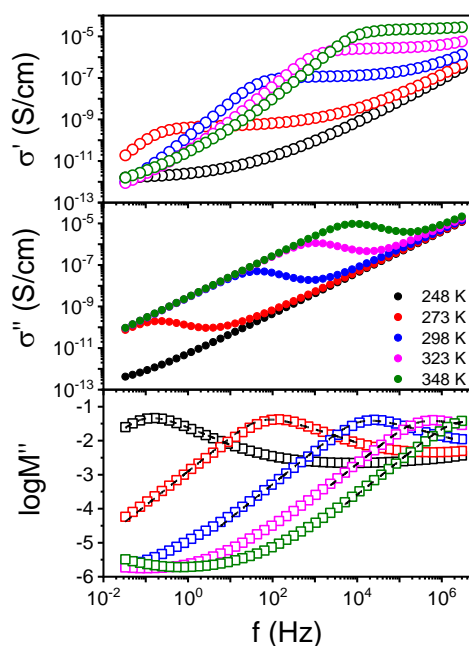


**Figure S3.** Real (top) and imaginary (middle) parts of the ionic conductivity of poly[VBBI]<sup>+</sup>[TFSI]<sup>-</sup> in AAO templates with a diameter of 400 nm shown for the indicated temperatures. The modulus representation (bottom) is used to extract the characteristic relaxation times of ionic motion (dashed lines indicate representative fits).

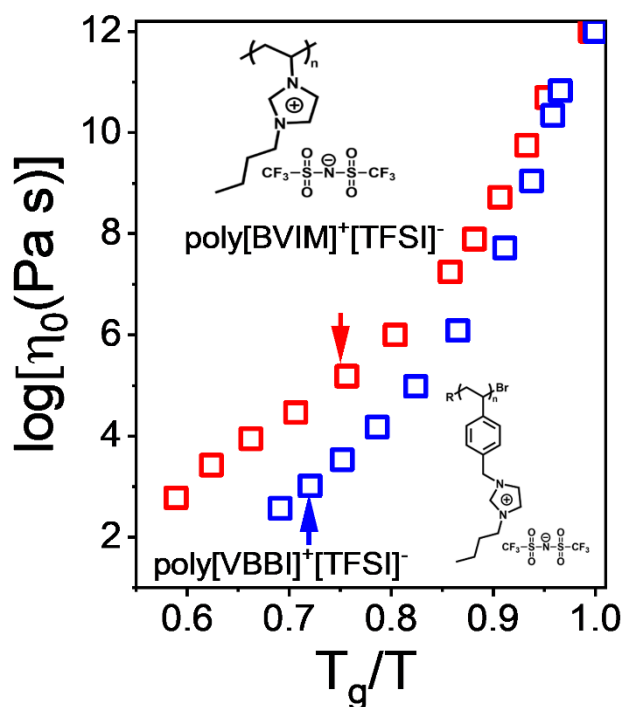


**Figure S4.** Temperature dependence of the  $T_g$ -scaled zero-shear viscosity ( $\eta_0$ ) of poly[BVIM]<sup>+</sup>[TFSI]<sup>-</sup> (red) and poly[VBBI]<sup>+</sup>[TFSI]<sup>-</sup> (blue). Arrows indicate the imbibition temperatures (400 K and 358 K, respectively).

#### REFERENCE

- [1] He, H.; Luebke, D.; Nulwala, H.; Matyjaszewski, K. *Macromolecules* **2014**, *47*, 6601–6609.
- [2] He, H.; Zhong, M.; Adzima, B.; Luebke, D.; Nulwala, H.; Matyjaszewski, K. *J. Am. Chem. Soc.* **2013**, *135*, 4227–4230.
- [3] Dong, Y.; Steinhart, M.; Butt, H. J.; Floudas, G. Demixing of Polymerized Ionic Liquid/Ionic Liquid Mixtures by Infiltration in Nanopores. *Macromolecules*, 2024, *57*, 5409–5420.

## Chapter 6. Demixing of Polymerized Ionic Liquid/Ionic Liquid Mixtures by Infiltration in Nanopores

This chapter has been published as a research paper in *Macromolecules*.

*Yun Dong, Martin Steinhart, Hans-Jürgen Butt, and George Floudas,*

*Macromolecules* 2024, 57, 5409–5420

DOI: 10.1021/acs.macromol.4c00391

### **Author contributions:**

**Yun Dong:** Dielectric spectroscopy and DSC measurements. AAO template characterization and surface modification. Data analysis and interpretation. Writing of the original draft of the manuscript.

**George Floudas:** Design of the research topic. Discussion on the results. Writing the final version based on the original draft.

**Hans-Jürgen Butt:** Acquiring funding for the project. Discussion on the research topic/results. Correction of the manuscript.

**Martin Steinhart:** AAO template fabrication.

## Abstract

Ion transport through membrane nanopores is pertinent to several applications including water desalination and energy harvesting. We synthesized a series of polymerized ionic liquids (PILs) based on the 1-butyl-3-vinylimidazolium cation ([BVIM]<sup>+</sup> with three different anions ([X]<sup>-</sup>: [TFSI]<sup>-</sup>, [BF<sub>4</sub>]<sup>-</sup>, [PF<sub>6</sub>]<sup>-</sup>). We explored how mixtures of the PIL with the corresponding IL (poly[BVIM]<sup>+</sup>[X]<sup>-</sup>/[BMIM]<sup>+</sup>[X]<sup>-</sup>) penetrate nanopores. For this purpose we employ ex situ reflection optical microscopy of the evolution of the imbibition length and in situ conductivity measurements by nanodielectric spectroscopy. The latter provides details of ion motion during and following imbibition. In the bulk, symmetric poly[BVIM]<sup>+</sup>[X]<sup>-</sup>/[BMIM]<sup>+</sup>[X]<sup>-</sup> mixtures are locally heterogeneous composed of nearly pure IL domains and mixed PIL/IL domains. When the mixture is placed on top self-ordered nanoporous aluminum oxide templates (AAO) the ionic liquid is dragged by capillary action into the pores. During imbibition the two components partially demix. At the end of the filling process the pores contain an excess of the IL and a minority of PIL chains. Subsequently we explored the effect of polymer adsorption and surface functionality on the kinetics of ion transport. The results suggest the possibility to separate a mixture of ionic compounds (IL and PIL in this case) by the difference in the imbibition kinetics of its constituent components. Applications of AAOs as separation membranes for ionic systems are discussed.

## 6.1. Introduction

Nature employs ions and liquids at small scales in a very efficient way. As an example, mammalian cells employ ionic pumps to set the membrane potential to a specified value.<sup>1</sup> Skeletal muscles are composed of long cylindrical multifunctional cells. Within the cells,  $\text{Ca}^{2+}$  control muscle contraction and relaxation through interactions with motor proteins (e.g. tropomyosin). Ion transport through membrane nanopores is also pertinent to water desalination and energy harvesting. In this area the transport of ions is related to salinity difference between sea water and river water (known as blue or osmotic energy). Current methodologies to extract and convert osmotic energy involve salinity gradients and partially permeable membranes with nanosize pores.<sup>2</sup> Apart from several applications there is a fundamental interest in understanding ion transport in channels. As an example, we refer to recent studies suggesting the breakdown of electroneutrality in highly confined dielectric materials.<sup>3</sup> The transport of ions in the presence of polymer chains is another important area. Here, understanding the way that ions that are coupled to macromolecules penetrate narrow pores is of particular importance with relevance to biology and materials science (sequencing DNA and inkjet printing).<sup>4</sup>

In the present work we investigate how polymerized ionic liquids (PILs) penetrate nanopores. The work builds on two earlier studies on ion transport in nanopores. One on the evolution of ionic conductivity of a solid polymer electrolyte (SPE) confined in nanopores<sup>5</sup> and another on the ion mobility of ionic liquids in the same nanopores.<sup>6</sup> The respective studies highlighted the role of polymer adsorption and of ion-wall interactions in dictating the ionic conductivity. PILs combine the unique properties of ILs, e.g., solvent-free single-ion conduction, with the improved mechanical properties and processability of polymers.<sup>7,8</sup> These features made PILs suitable candidates as materials for energy storage, energy conversion and for electromechanical devices. With respect to ion conduction, there is consensus that reducing the glass temperature,  $T_g$ , is a key feature to enhance ionic conductivity. Recent studies explored the dependence of  $T_g$  in PILs on several factors including chain topology, chain rigidity, dielectric permittivity, morphology and the volume of a structural unit  $V_m$  ( $V_m$  is the combined volume of the repeat unit with the mobile ion).<sup>9-14</sup> Another study<sup>11</sup> suggested that ion transport is controlled by a competition between Coulombic and elastic forces with the former (Coulombic) dominating for the smaller ions and the latter (elastic) by the larger ions. To explain the slower charge diffusion from the ion diffusion in PILs they suggested a backflow mechanism, whereby concerted ion rearrangements could provide ion diffusion with minimal

or no charge diffusion. Atomistic molecular dynamics simulations were also employed to identify the mechanisms underlying ion motion in PILs,<sup>15,16</sup> and more recently, in PIL/IL mixtures.<sup>17</sup> By considering a system where the cation was polymerized, they have shown that anions are coordinated to four cations from two adjacent polymer chains. Subsequent ion transport took place via anion hopping along the polymer backbone by a mechanism involving the formation and breaking of ion-associations.

A more recent study<sup>14</sup> employed a PIL composed from a polythiophene backbone and several differently substituted imidazolium salts with four different n-alkyl side chain lengths (with  $n = 4 - 10$ ) and for several anions. They addressed the role of morphology, polymer architecture, anion size, charge delocalization and complexation energy between unlike ions. Ion conductivity was strongly influenced by the size of the anion. From the various length scales involved, ion conductivity was found to couple to a local length scale associated with the charge alteration (accessible in X-rays). The conclusion was that ion conduction is facilitated by local anion jumps with a length scale on the order of the charge alteration distance. A simple “stick and jump” model was proposed by some of us to account for the increased backbone mobility (reduced  $T_g$ ) and the concomitant enhanced ion conductivity for anions with intermediate size.<sup>14</sup> Among the different anions, [TFSI]<sup>-</sup> with its comparably large size and broad charge delocalization was only weakly coordinated with the cation. This best facilitated anion motion within the “ion paths” of the hexagonally packed cylinders (hpc) and smectic morphologies.

The aim of this work is to identify the principles underlying ion transport in PIL/IL mixtures within nanochannels, and possibly, to suggest new processes with efficient ion transport. For this purpose, we synthesized a series of PILs based on 1-butyl-3-vinylimidazolium cation ([BVIM]<sup>+</sup>) with three different anions ([X]<sup>-</sup>: [TFSI]<sup>-</sup>, [BF4]<sup>-</sup>, [PF6]<sup>-</sup>). Then we explored the way that mixtures of the PIL with the corresponding IL (based on the 1-butyl-3-methylimidazolium cation [BMIM]<sup>+</sup>, i.e. mixtures of poly[BVIM]<sup>+</sup>[X]<sup>-</sup>/[BMIM]<sup>+</sup>[X]<sup>-</sup>) penetrate nanopores. Specifically, we investigate: (i) the kinetics of imbibition, for the first time, using the newly established method of in situ nano-dielectric spectroscopy,<sup>18-23,5,6</sup> capable of measuring the ion dynamics during flow in nanopores, and (ii) the ion dynamics under confinement. We aim to address the following open questions: How do PIL/IL mixtures penetrate nanopores? What is the effective viscosity and dc-conductivity? Can we decouple ion-conductivity from viscosity? Can we enhance ion conduction by confinement, or does it decrease? Can we separate the constituent components by the difference in imbibition

kinetics? How does polymer adsorption influence the conductivity? What is the effect of pore surface functionality? Addressing these issues requires different but complementary techniques. We applied dielectric spectroscopy for the bulk liquids as well as in situ measurements by nanodielectric spectroscopy (nDS), differential scanning calorimetry (DSC), ex situ reflection optical microscopy, several surface characterization techniques including SEM, contact angle, surface tension, as well as structural characterization by X-rays. As for the confining systems, we employ model self-ordered nanoporous aluminum oxide (AAO) templates with controlled pore diameters and a constant pore depth.

The results show that PIL/IL mixtures in their bulk state are locally heterogeneous composed of IL and PIL/IL domains. This heterogeneity is enhanced by imbibition in nanopores. The components of a symmetric PIL/IL mixture placed on top a nanopore membrane penetrate the pores with different speeds, with the IL component penetrating faster. This gives rise to the separation of the components in a PIL/IL mixture. Possible applications suggest the use of nanoporous templates as nanofluidic devices, and in particular, as separation membranes for mixed ionic systems. In addition, we explored the effects of surface functionalization and confinement on ion dynamics.

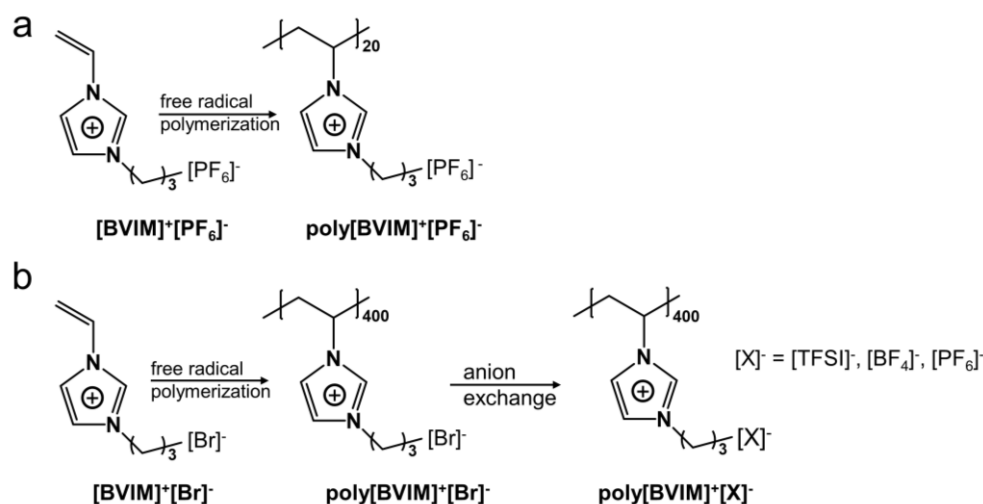
## 6.2. Experimental

**Materials.** 1-butyl-3-vinylimidazolium hexafluorophosphate ( $[\text{BVIM}]^+[\text{PF}_6]^-$ ,  $\geq 98\%$ ), 1-butyl-3-vinylimidazolium bromide ( $[\text{BVIM}]^+[\text{Br}]^-$ ,  $\geq 98\%$ ), Lithium bis(trifluoromethanesulfonyl)imide ( $\text{LiTFSI}$ ,  $\geq 98\%$ ), Sodium tetrafluoroborate ( $\text{NaBF}_4$ ,  $\geq 97\%$ ), Dichloromethane ( $\text{DMF}$ , extra dry  $\geq 99.9\%$ ), Potassium hexafluorophosphate ( $\text{KPF}_6$ , extra pure  $\geq 99\%$ ), Silver nitrate solution ( $\text{AgNO}_3$ ), 2,2'-azobisisobutyronitrile ( $\text{AIBN}$ ,  $\geq 98\%$ ), Ultra-15 Centrifugal Filter Unit (10 kDa MWCO), Tetrahydrofuran ( $\text{THF}$ ,  $\geq 98\%$ ) and Ethanol were purchased from Merck and used without further purification. Deionized water was purified using a Millipore Milli-Q Synergy with a resistivity approximately  $18 \text{ M}\Omega \cdot \text{cm}^{-1}$ .

**Synthesis of poly $[\text{BVIM}]^+[\text{PF}_6]^-$ .** For the synthesis of the PILs we have followed known literature procedures.<sup>24,25</sup> Briefly, in a dry 100 mL round-bottom flask, we prepare a mixture of  $[\text{BVIM}]^+[\text{PF}_6]^-$  (5 g, 16.9 mmol) and AIBN (55 mg, 0.34 mmol). Anhydrous DMF (10 mL) was then added to the flask. The obtained mixture was degassed via freeze-vacuum-thaw cycles for three times and flushed with argon. The reaction was initiated by heating the system to 343 K and maintained at this temperature for 22 h. After completion of the reaction, the system was allowed to cool to room temperature and the mixture was stirred in the atmosphere for 30 min.

The solution was then precipitated into deionized water, and the resulting precipitate was filtered. The precipitate was re-dissolved with THF and re-precipitated with ethanol for three times in order to remove unreacted monomers and oligomers. The obtained polymerized ionic liquid (4.2 g,  $M_n = 6$  kDa;  $M_w = 8$  kDa) was dried at 313 K under high vacuum to completely remove any residual solvent before use.

**Synthesis of PILs with different anions.** [BVIM]<sup>+</sup>[Br]<sup>-</sup> (9 g, 38.9 mmol) and AIBN (6.5 mg, 0.396 mmol) were dissolved in 18 mL of DMF. In order to remove oxygen, argon was bubbled through the solution over a period of 1 h. After stirring the reaction mixture at 348 K for 24 h under argon atmosphere, DMF was removed by rotary evaporation. The remaining viscous oil was dissolved in 20 ml of deionized water and dialyzed against water using a cellulose tube with 10 kDa MWCO for two days. Throughout this period, the dialysate was exchanged twice to ensure optimal removal of low molecular weight impurities. To facilitate anion exchange, the resulting solution was divided into three equal parts. Each part was treated with a solution of the appropriate salt (LiTFSI, KPF<sub>6</sub>, NaBF<sub>4</sub>) in 10 ml of water in approximately 1.5-fold excess and stirred for 5 days. The precipitated polymer was then collected by filtration, washed with an abundant amount of water until no bromide could be detected in the washing water, verified by the absence of precipitation upon introduction of AgNO<sub>3</sub> solution. The obtained PILs, poly[BVIM]<sup>+</sup>[TFSI]<sup>-</sup> (4.48 g,  $M_n = 85$  kDa) poly[BVIM]<sup>+</sup>[PF<sub>6</sub>]<sup>-</sup> (3.31 g,  $M_n = 85$  kDa), poly[BVIM]<sup>+</sup>[BF<sub>4</sub>]<sup>-</sup> (3.23 g,  $M_n = 85$  kDa) were dried at 313 K under vacuum to completely remove residual solvent (since PILs with different anions, [TFSI]<sup>-</sup>, [BF<sub>4</sub>]<sup>-</sup>, [PF<sub>6</sub>]<sup>-</sup>, are insoluble in the eluting solvent, the molecular weight of poly[BVIM]<sup>+</sup>[Br]<sup>-</sup> is employed to indicate all three PILs). We further assumed that the counterion conversion reaction did not affect the average molecular weight of the obtained PILs. The purity of the poly[BVIM]<sup>+</sup>[X]<sup>-</sup> was confirmed with elemental analysis (**Supporting Information**). Scheme 1 provides the synthesis of the poly[BVIM]<sup>+</sup>[PF<sub>6</sub>]<sup>-</sup> with the lower molar mass and the synthesis of the poly[BVIM]<sup>+</sup>[X]<sup>-</sup> with [X]<sup>-</sup>: [TFSI]<sup>-</sup>, [BF<sub>4</sub>]<sup>-</sup> and [PF<sub>6</sub>]<sup>-</sup>. Gel permeation chromatography (GPC) was used to determine the molecular weights of obtained PILs. The weight-average molecular weight ( $M_w$ ) and dispersity ( $\mathcal{D}$ ) of PILs were determined at 298 K using an Agilent Technologies 1260 Infinity II RI detector on one Novema Max Lin M (PSS) 300 × 8 mm column. 0.1 mol NaCl and 0.1 % trifluoroacetyl chloride (TFAc) in water was chosen as the eluting solvent at a flow rate of 1.0 mL/min and the calibration was carried out using poly(2-vinylpyridine).



**Scheme 1.** Synthesis of (a) poly[BVIM]<sup>+</sup>[PF<sub>6</sub>]<sup>-</sup> with  $M_n = 6$  kDa and (b) poly[BVIM]<sup>+</sup>[X]<sup>-</sup> with [X]<sup>-</sup>: [TFSI]<sup>-</sup>, [BF<sub>4</sub>]<sup>-</sup> and [PF<sub>6</sub>]<sup>-</sup> with  $M_n = 85$  kDa by free radical polymerization.

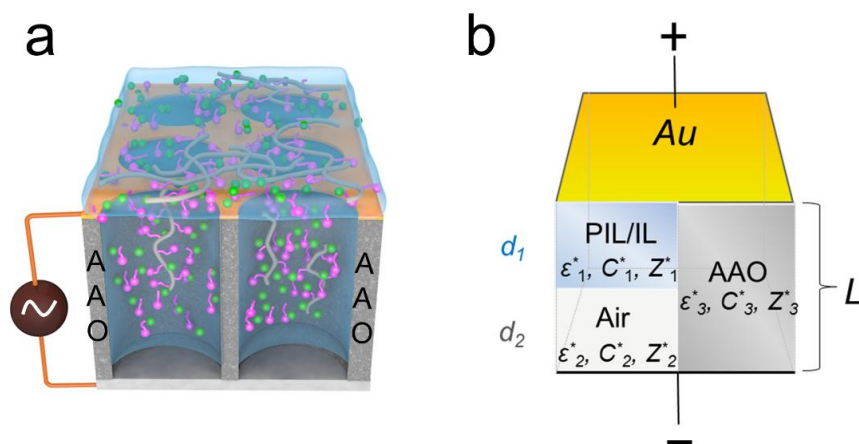
**PIL/IL mixture preparation.** Polymerized ionic liquids and ionic liquids bearing the same anion and the [BMIM]<sup>+</sup> cation (e.g. poly[BVIM]<sup>+</sup>[PF<sub>6</sub>]<sup>-</sup>/[BMIM]<sup>+</sup>[PF<sub>6</sub>]<sup>-</sup>; poly[BVIM]<sup>+</sup>[TFSI]<sup>-</sup>/[BMIM]<sup>+</sup>[TFSI]<sup>-</sup>; poly[BVIM]<sup>+</sup>[BF<sub>4</sub>]<sup>-</sup>/[BMIM]<sup>+</sup>[BF<sub>4</sub>]<sup>-</sup>) were dissolved in THF (~30 mL) in a 1:1 weight ratio. After sufficient dissolution, THF was removed by rotary evaporation. The mixtures were dried at 373 K under vacuum to completely remove residual solvent and water before use. We mention here that poly[BVIM]<sup>+</sup>[BF<sub>4</sub>]<sup>-</sup> alone does not dissolve in THF. However, as reported earlier<sup>26</sup> and confirmed by us, the mixture poly[BVIM]<sup>+</sup>[BF<sub>4</sub>]<sup>-</sup>/[BVIM]<sup>+</sup>[BF<sub>4</sub>]<sup>-</sup> was soluble in THF.

**AAO templates.** The preparation of self-ordered nanoporous aluminum oxide (AAO) templates with specified pore diameter (25, 35, 65, 400 nm) and a constant pore depth of approximately 100 μm, following literature procedures.<sup>27-30</sup> The AAO layers were attached to 900 μm thick aluminium substrates that functioned as the bottom electrode. Before the infiltration process, all AAO templates underwent an annealing step in a vacuum oven at a temperature ( $T$ ) of 150 °C for 10-12 hours. This annealing step eliminates a substantial portion of hydroxyl (-OH) groups from the surface of the AAO.

**Inner pore silanization.** For the inner surface modification, hexamethyldisilazane (HMDS) (purity ≥ 99.0%, purchased from Sigma-Aldrich) was injected into the chamber containing the AAOs at 350 K and the AAOs were completely submerged. After 30 min, the chamber was evacuated for 3 h at 350 K. By treating the original membranes (e.g. before annealing) with HMDS, -OH groups were replaced with trimethylsilyl groups turning the inner surface to hydrophobic.

**Differential Scanning Calorimetry (DSC).** The thermal behavior of the mixtures were studied by differential scanning calorimetry on cooling and subsequent heating at a rate of 10, 20  $\text{K}\cdot\text{min}^{-1}$  with a Mettler Toledo (DSC-822) calorimeter. DSC traces were acquired using an empty pan as reference. Samples were weighed using a Mettler Toledo AX205 balance. Approximately 20 mg of sample was sealed in aluminum pans (100  $\mu\text{L}$ ). All samples were heated to 453 K under a nitrogen atmosphere to remove any thermal history. The same cycle was repeated twice. Some DSC traces of the PIL, the IL and the respective PIL/IL mixtures are provided in **Figure S1, Supporting Information**.

**Dielectric spectroscopy (DS).** The dynamics of bulk and confined PIL, IL and the PIL/IL mixtures were performed by dielectric spectroscopy and *in situ* nanodielectric spectroscopy (*nDS*) with a Novocontrol Alpha frequency analyzer. It consists of a broadband dielectric converter and an active sample head. For bulk samples, the dielectric cell had two electrodes, with a diameter of 20 mm and a 500  $\mu\text{m}$  Teflon spacer to maintain a constant thickness. A broad frequency range was employed from  $10^{-2}$  to  $10^7$  Hz. For the investigation of the effect of nanoconfinement, a gold layer with a diameter of 9 mm and thickness of 35 nm was deposited onto the AAO template, serving as the top electrode. The aluminum substrate of the AAO templates functioned as the bottom electrode. The deposition of the gold layer was performed through a sputtering process under vacuum conditions (vacuum better than  $2 \times 10^{-5}$  Pa) using a Bal-tec MED 020 with a current density of 40 mA. The samples were subsequently placed on top the AAO template, and the investigation of imbibition kinetics was conducted by *nDS* (Scheme 2). In this case a narrower frequency range (1 -  $10^6$  Hz) was employed for a faster acquisition.



**Scheme 2.** (a) Schematic of the nanodielectric spectroscopy set-up used for the separation of PIL/IL mixtures; the cation is indicated by magenta, the anion by the green color. (b) Equivalent capacitor circuit.

Impedance measurements were conducted to obtain the complex conductivity function, denoted as  $\sigma^* = \sigma' + i\sigma''$ , where  $\sigma'$  and  $\sigma''$  are the real (*i.e.*, the dc-conductivity) and imaginary parts, respectively. The plateau observed in the real part  $\sigma'$  was used to extract the dc-conductivity. The study demonstrated the applicability of *n*DS in monitoring the increase in imbibition length during pore filling. This was achieved by tracking the rise in conductivity during flow within the AAO templates. Briefly, a simple Debye model for the frequency-dependent complex conductivity ( $\sigma^*(\omega)$ ) can be expressed as:  $\sigma^*(\omega) = \sigma'(\omega) + i\sigma''(\omega) = i\omega\varepsilon_0\varepsilon^*(\omega)$ ,

$$\sigma'(\omega) = \omega\varepsilon_0\varepsilon''(\omega) = \sigma_{dc} + \frac{\omega^2\tau\varepsilon_0\Delta\varepsilon}{1+(\omega\tau_D)^2} \quad (1)$$

$$\sigma''(\omega) = \omega\varepsilon_0\varepsilon'(\omega) = \omega\varepsilon_0\left(\varepsilon_\infty + \frac{\Delta\varepsilon}{1+(\omega\tau_D)^2}\right) \quad (2)$$

Here,  $\Delta\varepsilon$  is the dielectric strength,  $\tau_D$  is the characteristic relaxation time,  $\sigma_{dc}$  is the sample dc-conductivity, and  $\varepsilon_\infty$  is the dielectric permittivity in the limit of very high frequencies. A parallel model can describe the total equivalent capacitance, comprising the capacitance of the sample ( $C_1$ ) and air ( $C_2$ ) connected in series, whereas the combined sample/air capacitance ( $C_{12}$ ) connects in parallel with the AAO ( $C_3$ ). Therefore,

$$\frac{1}{C_{12}} = \frac{1}{C_1} + \frac{1}{C_2}, \text{ and } C_{123} = C_{12} + C_3 \quad (3)$$

Using the above equations, the definition  $\sigma_{123}^* = i\omega\varepsilon_0\varepsilon^*$ , and the porosity  $\varphi_{12}$  results to:

$$\sigma_{123}^* = \sigma' + i\sigma'' = \left\{ \left[ \frac{Ld_1\sigma_1'(\omega\varepsilon_0)^2}{(d_2\sigma_1')^2 + (d_1\omega\varepsilon_0 + d_2\sigma_1'')^2} \right] \varphi_{12} + \sigma_3'\varphi_3 \right\} + i \left\{ \left[ \frac{L[d_2(\sigma_1')^2 + (\sigma_1'')^2]\omega\varepsilon_0 + \sigma_1''(\omega\varepsilon_0)^2d_1}{(d_2\sigma_1')^2 + (d_1\omega\varepsilon_0 + d_2\sigma_1'')^2} \right] \varphi_{12} + \sigma_3''\varphi_3 \right\} \quad (4)$$

Where  $\varphi_3 (=1 - \varphi_{12})$  is the AAO content. By employing typical values for the real and imaginary parts of the AAO conductivity, as well as typical values for the bulk sample, the equation can be analysed to demonstrate that a conductivity plateau (dc-conductivity) arises only when the pores are fully infiltrated by the sample (**Figure S2, Supporting Information**).

**X-ray diffraction.** The  $\Theta/2\Theta$  scans were taken with a Rigaku SmartLab X-ray diffractometer. The X-ray source was a rotating anode (Cu) operating at a voltage of 45 kV and a current of 200 mA. The incident optics employed a monochromator (Ge crystal for the 220 reflection) followed by a parallel slit (incident Soller slit 2.5<sup>0</sup>). A diffracted beam monochromator was inserted between the detector slit and the detector to suppress fluorescence radiation and the unwanted  $K_\beta$  radiation. The receiving optics had a parallel slit analyzer (PSA) followed by a receiving Soller slit. The wavelength was 0.154059 nm. A HyPix-3000 2D detector was used

(pixel size  $100\ \mu\text{m} \times 100\ \mu\text{m}$ ; active area  $38.5\ \text{mm} \times 77.5\ \text{mm}$ ). Scans in the  $2\Theta$ -range from  $0$  to  $60^\circ$  in steps of  $0.01^\circ$  were made at ambient temperature.

**Reflection Optical Microscopy.** The imbibition length measurements were made by employing *ex situ* reflection optical microscopy (ROM) (Zeiss Axiotech vario). The PIL/IL mixture was infiltrated into nanopores by capillary force. After defined time intervals the AAO templates were immersed into liquid nitrogen to prevent further infiltration. The distance penetrated by the mixture under capillary pressure (*i.e.*, the imbibition length) was determined from cross sections by ROM.

**Surface Tension.** The Wilhelmy plate method was employed to measure the surface tension of all mixtures. A platinum-iridium rod with a diameter of  $1.2\ \text{mm}$  was vertically placed into the heated PIL/IL mixture (at the imbibition temperature). The liquid had a contact angle of around  $0^\circ$  on the platinum-iridium rod surface. The surface tension exerted a downward force ( $F$ ), which was measured with a tension meter (DCAT 11BC, DataPhysics) after letting the system equilibrate for about  $2000\ \text{s}$ . The surface tension ( $\gamma$ ) was then calculated from  $F = l\gamma$ , where  $l$  is the circumference of the rod. Exemplary surface tension measurements for some PIL/IL mixtures are depicted in **Figure S3, Supporting Information**.

**Contact Angle.** The apparent advancing contact angle of the PIL/IL mixtures was measured by placing nearly spherical polymer particles of  $\sim 1\ \text{mm}$  diameter onto an electropolished Al substrate. To form spherical particles, around  $1\ \text{mg}$  of sample was placed on a superamphiphobic surface. The sample was heated and kept at  $393\ \text{K}$  for  $24\ \text{h}$  under vacuum to form a spherical shape caused by the surface tension of the polymer. Subsequently, the polymer sphere was slowly cooled and transferred onto the electropolished Al disk coated by a thin native oxide layer. The latter comprises a flat model surface that mimics the AAO surface. The contact angle was measured with a commercial goniometer (OCA35, DataPhysics) using the software IDS uEye. Samples were kept at a temperature which corresponds to the infiltration temperature ( $318\ \text{K}$  for  $[\text{TFSI}]^-$  (85 k),  $368\ \text{K}$  for  $[\text{BF}_4]^-$  (85 k),  $393\ \text{K}$  for  $[\text{PF}_6]^-$  (85 k),  $333\ \text{K}$  for  $[\text{PF}_6]^-$  (6 k)) for  $2\ \text{h}$ . **Figure S4, Supporting Information** provides images of contact angles for PIL/IL mixtures with different anions. The results are summarized in **Table 1**. **Figure S5**, provides the contact angle of the PIL/IL  $[\text{PF}_6]^-$  mixture with molar mass of  $85\ \text{kg}\cdot\text{mol}^{-1}$  as a function of temperature.

**Table 1.** Surface Tension and Contact Angles for the Mixtures.

Mixture	$T$ (K)	Surface Tension (mN/m)	Advancing Contact Angle ( $^{\circ}$ )
poly[BVIM] <sup>+</sup> [TFSI] <sup>-</sup> /[BMIM] <sup>+</sup> [TFSI] <sup>-</sup> (85k)	318	24.6	40
poly[BVIM] <sup>+</sup> [BF <sub>4</sub> ] <sup>-</sup> /[BMIM] <sup>+</sup> [BF <sub>4</sub> ] <sup>-</sup> (85k)	368	19.0	43
poly[BVIM] <sup>+</sup> [PF <sub>6</sub> ] <sup>-</sup> /[BMIM] <sup>+</sup> [PF <sub>6</sub> ] <sup>-</sup> (85 k)	393	21.1*	53
poly[BVIM] <sup>+</sup> [PF <sub>6</sub> ] <sup>-</sup> /[BMIM] <sup>+</sup> [PF <sub>6</sub> ] <sup>-</sup> (6k)	333	13.5	55

\*: measured at 368 K

**Rheology.** The zero shear viscosities and shift factors were investigated using a shear rheometer (ARES). Measurements were performed with an environmental test chamber as a function of temperature. Samples were prepared on the lower plate of the 8 mm diameter parallel plate geometry. The upper plate was brought into contact, and the sample thickness was adjusted. The storage ( $G'$ ) and loss ( $G''$ ) shear moduli were monitored as a function of frequency,  $\omega$ , for frequencies in the range  $10^{-1} < \omega < 10^2$  rad·s<sup>-1</sup>. All measurements refer to the linear viscoelastic range. Subsequently, the complex viscosity ( $\eta^*$ ) follows as  $\eta^* = G''/\omega - iG'/\omega$ . Master curves were made by use of the time–temperature superposition principle ( $tT_s$ ). The latter allows the frequency  $\omega$  dependence of the complex modulus  $G^*$  at any temperature  $T$  to be determined from a master curve at a reference temperature. At each temperature  $T$ , a single frequency-scale shift factor allows superposition of  $a_T$  allow superposition of all viscoelastic data at temperature  $T$  with the data at the reference temperature,  $T_{ref}$ , as  $G^*(\omega; T) = G^*(a_T\omega; T_{ref})$ . Master-curves for all systems investigated are shown in **Figures S6-S9, Supporting Information**.

### 6.3. Results and discussion

#### Bulk behavior

DSC was employed to follow the phase state of the bulk ILs ([BMIM]<sup>+</sup>[X]<sup>-</sup>), the bulk PILs (poly([BVIM]<sup>+</sup>[X]<sup>-</sup>)) and their mixtures PIL/IL. Corresponding DSC traces are shown in **Figure S1, Supporting Information**, where each mixture was examined with respect to the pure components and in Figure 1 below. The pure ILs crystallize on heating ([BF<sub>4</sub>]<sup>-</sup> is an exception), but the mixtures remain amorphous (**Figure S1**). In addition, the PIL/IL mixture bearing the larger anion (the [TFSI]<sup>-</sup>) exhibits a dual glass temperature; one at 202 K and another at 243

K, suggesting some local segregation of the IL and the PIL. Notably, the lower glass temperature is shifted to low temperatures as compared to the smaller anions.

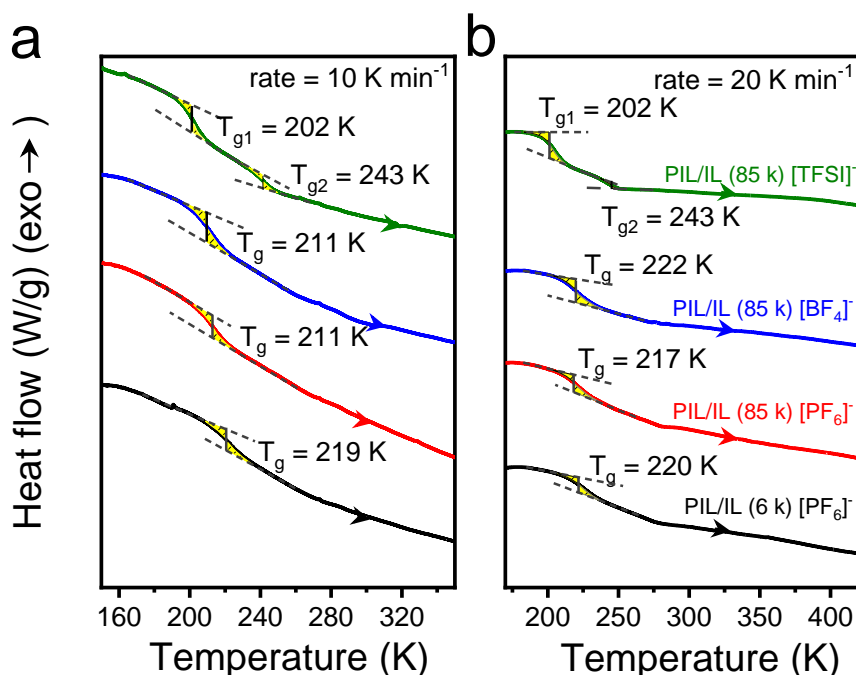


**Figure 1.** DSC heating traces of imidazolium-based PIL mixtures (PIL/IL) with different anions: [TFSI]<sup>−</sup> (green), [BF<sub>4</sub>]<sup>−</sup> (blue), [PF<sub>6</sub>]<sup>−</sup> (red), [PF<sub>6</sub>]<sup>−</sup> with a lower  $M_n$  (black). Traces are obtained from the subsequent heating run with a rate of (a) 10 K·min<sup>−1</sup> and (b) 20 K·min<sup>−1</sup>.

The measured dc-conductivities for the ILs ([BMIM]<sup>+</sup>[X]<sup>−</sup>), the PILs (poly([BVIM]<sup>+</sup>[X]<sup>−</sup>)) and their mixtures PIL/IL are compared in Figure 2. The  $\sigma'_{dc}(T)$  dependencies obtained on cooling follow the Vogel-Fulcher-Tammann (VFT) equation written for the conductivity contribution as:

$$\sigma_{dc}(T) = \sigma_0 \exp\left(-\frac{B}{T-T_0}\right) \quad (5)$$

Here,  $\sigma_0$  is the dc-conductivity in the limit of very high temperatures,  $B$  is the activation parameter and  $T_0$  is the “ideal” glass temperature (the parameters are summarized in **Table 2**, below). The glass temperatures obtained from DSC and DS are in good agreement. Both values, however, are lower than in ref[10], presumably because of the lower molar mass of the tested PILs.

**Table 2.** Parameters of the VFT Equation for the Conductivity Obtained on Cooling.

	$\sigma_0$ ( $\text{S}\cdot\text{cm}^{-1}$ )	$B$ (K)	$T_0$ (K)	$T_g^{DS}$ (K) (at $\sigma = 10^{-14}$ $\text{S}/\text{cm}$ )	$T_{g1}^{DSC}$ (K) <sup>a</sup>	$T_{g2}^{DSC}$ (K) <sup>a</sup>
IL [TFSI] <sup>-</sup>	1.6	880 ± 11	154 ± 1	181 ± 1	183 ± 2	--
IL [PF <sub>6</sub> ] <sup>-</sup>	10.0	1055 ± 60	163 ± 3	195 ± 1	191 ± 2	--
IL [BF <sub>4</sub> ] <sup>-</sup>	5.4	915 ± 18	153 ± 1	177 ± 1	181 ± 2	--
PIL/IL [TFSI] <sup>-</sup>	2.0	1160 ± 20	160 ± 1	194 ± 20	202 ± 2	243 ± 2
PIL/IL [PF <sub>6</sub> ] <sup>-</sup>	3.5	1900 ± 44	154 ± 2	210 ± 20	217 ± 2	--
PIL/IL [BF <sub>4</sub> ] <sup>-</sup>	7.0	1200 ± 23	142 ± 1	203 ± 20	222 ± 2	--

<sup>a</sup>  $T_g$  obtained from DSc is also shown for comparison.

Figure 2 includes the estimated conductivity value at  $T_g$  as obtained from the Nernst-Einstein equation:

$$\sigma_{dc} = \frac{ne^2 \left(\frac{d_2}{2}\right)^2}{k_B T \ 6\tau} \quad (6)$$

Here,  $e$  is the elementary charge,  $n = \frac{\rho N_A}{M}$ , is the number density,  $\rho$  is the mass density applicable to [BMIM]<sup>+</sup>[X]<sup>-</sup> (we have used <sup>31,32</sup> 1.44, 1.38, and 1.20  $\text{g}\cdot\text{cm}^3$ , respectively, for [BMIM]<sup>+</sup>[TFSI]<sup>-</sup>, [BMIM]<sup>+</sup>[PF<sub>6</sub>]<sup>-</sup>, and [BMIM]<sup>+</sup>[BF<sub>4</sub>]<sup>-</sup>),  $M = M_w^{cation} + M_w^{anion}$  is the molar mass of the cation and/or the backbone repeat unit and of the anion (428, 293 and 234  $\text{g}\cdot\text{mol}^{-1}$ , respectively, for [BMIM]<sup>+</sup>[TFSI]<sup>-</sup>, [BMIM]<sup>+</sup>[PF<sub>6</sub>]<sup>-</sup>, and [BMIM]<sup>+</sup>[BF<sub>4</sub>]<sup>-</sup>),  $d_2/2$  is the distance between two adjacent ions of opposite charge extracted from Figure 5 (below),  $\tau$  is the characteristic structural relaxation time at  $T_g$  and  $k_B$  is the Boltzmann constant. Using  $d_2/2 \sim 0.34$  nm applicable to PIL/IL [BF<sub>4</sub>]<sup>-</sup> ( $d_2/2$  is 0.38 nm for PIL/IL [TFSI]<sup>-</sup> and 0.33 nm for [PF<sub>6</sub>]<sup>-</sup>) and  $\tau = 10^2$  s in Eq. 6 results to  $\sigma_{dc} \sim 5 \times 10^{-14}$   $\text{S}\cdot\text{cm}^{-1}$ . This value of the conductivity is used in extracting the DS glass temperature (Table 2). Because the pure ILs crystallize on cooling (with the exception of [BF<sub>4</sub>]<sup>-</sup>), the VFT lines refer to data in the quenched amorphous state. Evidently, the dc-conductivities of the PIL/IL mixtures are biased towards the pure IL conductivities, suggesting ion transport within domains enriched by ILs.

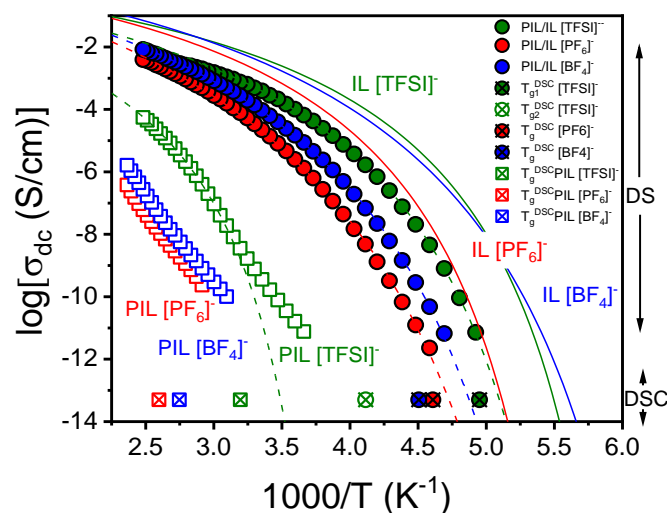


**Figure 2.** Temperature dependence of dc-conductivity for the pure ILs ( $[\text{BMIM}]^+[\text{X}]^-$ ) shown with solid lines, the pure PILs (poly( $[\text{BVM}]^+[\text{X}]^-$ ) all with  $M_n=85 \text{ kg}\cdot\text{mol}^{-1}$ ), shown with open symbols, and their mixtures PIL/IL shown with the filled symbols;  $[\text{TFSI}]^-$  (green),  $[\text{BF}_4]^-$  (blue), and  $[\text{PF}_6]^-$  (red). The solid and dashed lines for the ILs and the mixtures, respectively, are the results of fits to the Vogel-Fulcher-Tammann (VFT) equation. The crossed symbols represent the  $T_g$  obtained from DSC with a rate of  $20 \text{ K}\cdot\text{min}^{-1}$ . Notice the two DSC  $T_g$ 's for the mixture bearing the  $[\text{TFSI}]^-$ ; one (the filled symbol) is in proximity with the  $T_g$  obtained from the  $\sigma(T)$  dependence in the same mixture, whereas the second (the open symbol) is in proximity with the  $T_g$  of the pure PIL (green open squares).

More informative is a comparison of the ionic conductivities with the zero shear viscosities measured for the same mixtures. The comparison is shown in Figure 3 for the mixtures with the  $M_n=85 \text{ kg}\cdot\text{mol}^{-1}$ . The data violate the proportionality  $\sigma_{\text{dc}}\sim\eta^{-1}$ ; the zero-shear viscosity in the mixtures has a steeper temperature dependence as compared to the dc-conductivity and attains a value of  $10^{-14} \text{ Pa}\cdot\text{s}$  at a higher temperature (e.g. higher  $T_g$ ). This suggests that the zero-shear viscosity in the PIL/IL mixtures is dominated by the PIL whereas the dc-conductivity by the ILs.

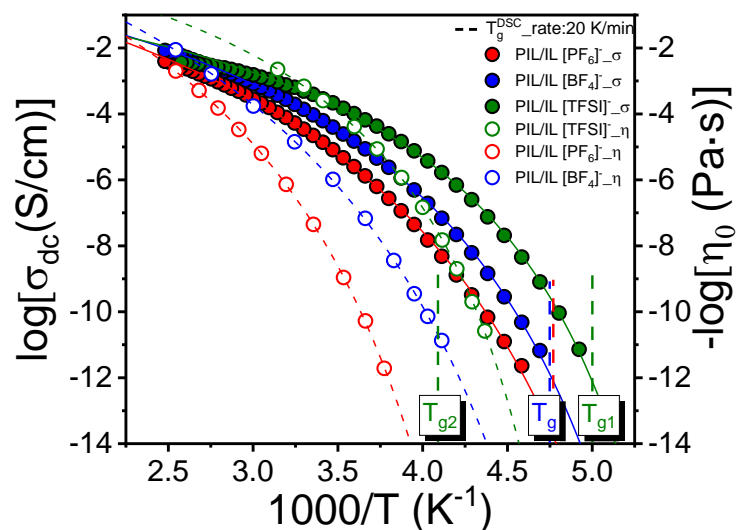


**Figure 3.** Temperature dependence of dc-conductivity (filled symbols) and zero-shear viscosity (open symbols) for PIL/IL mixtures ( $M_n=85 \text{ kg}\cdot\text{mol}^{-1}$ ), bearing different anions, (red)  $[\text{PF}_6]^-$ , (blue)  $[\text{BF}_4]^-$ , (green)  $[\text{TFSI}]^-$ . The dashed lines are the results of Vogel-Fulcher-Tammann (VFT) fit. The vertical dashed lines represent the  $T_g$  obtained from DSC (rate of  $20 \text{ K}\cdot\text{min}^{-1}$ ).

The results on the glass temperature(s) obtained from DSC, rheology and dc-conductivity can be compared for the PIL/IL mixtures with  $M_n=85 \text{ kg}\cdot\text{mol}^{-1}$  in relation to the pure ILs and the PILs with the help of Figure 4. Independent of the anion, the  $T_g$  from the dc-conductivity is in excellent agreement with the (low) DSC  $T_g$ . On the other hand, the  $T_g$  obtained from rheology is always higher and in proximity to the second (high)  $T_g$  found in  $[\text{TFSI}]^-$ . The combined results suggest the local segregation in nearly pure IL domains and mixed PIL/IL domains.

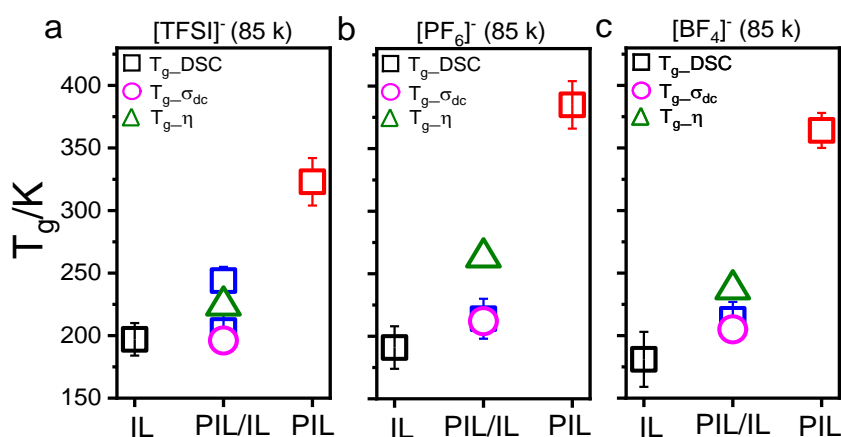


**Figure 4.** Glass temperature ( $T_g$ ) for the PIL/IL mixtures with  $M_n=85 \text{ kg}\cdot\text{mol}^{-1}$  for the different anions: (a)  $[\text{TFSI}]^-$ , (b)  $[\text{PF}_6]^-$ , and (c)  $[\text{BF}_4]^-$ . The squares, circles, and triangles represent the  $T_g$  obtained from DSC (rate of  $20 \text{ K}\cdot\text{min}^{-1}$ ), the dc-conductivity through the Nernst-Einstein equation, and the zero-shear viscosity, respectively.

Pertinent information on the local packing can be obtained through X-ray diffraction. ILs are structurally heterogeneous and usually exhibit three peaks.<sup>33-35,6</sup> At longer range there exists nanophase separation between polar and apolar groups giving rise to a smectic-like layering. At shorter distances, the nearest proximity of atoms gives rise to the van der Waals peak (typical correlation distances of  $\sim 0.4 - 0.5$  nm). At intermediate distances, the scattering from the different form factors of the cation and the anions give rise to the charge alteration peak. The diffraction patterns of the ILs, the PILs and their mixture are shown Figure 5. Arrows 1, 2 and 3 for the ILs indicate, respectively, the smectic layering of polar-apolar groups, the charge alteration peak, and the van der Waals peak of nearest neighbors. In an earlier investigation for the structurally similar ILs 1-butyl-3-methylimidazolium ( $[\text{BMIM}]^+$ ) with six different anions ( $[\text{Cl}]^-$ ,  $[\text{Br}]^-$ ,  $[\text{I}]^-$ ,  $[\text{BF}_4]^-$ ,  $[\text{PF}_6]^-$  and  $[\text{TFSI}]^-$ ) (with radii from 0.168 nm to 0.326 nm), the period of smectic layering ( $d_1$ ) corresponded to the summation of radii of the cation and the anion.<sup>6</sup> On the other hand, the charge alteration distance was given by the summation of radii of the imidazolium ring and the anion ( $0.41+R^-$  in nm). In the PILs similar correlation distances are evident (indicated as I, II, and III), with one main difference. Peak I, giving the backbone-to-backbone correlations is now the dominant feature. With a backbone-to-backbone correlation distance of  $\sim 1.54$  nm for the PIL with  $[\text{TFSI}]^-$ , being similar to the correlation distance of the smectic layering of polar-apolar groups in the pure IL, it suggests the inter-digitation of the side groups in the PIL. In the case of the PIL/IL mixtures, the first peak - despite being weaker and broader - exhibits longer backbone-to-backbone correlations (from 1.54 nm in the PIL to 1.89 nm in the PIL/IL mixture). The XRD results, revealed increased correlation distances in the PIL/IL mixtures with respect to bulk PIL, due to the incorporation of some IL in the PIL domains. In addition, the position of the charge-alteration peak is largely unaffected in the mixtures (from 0.78 nm in the IL to 0.76 nm in the PIL/IL mixture) suggesting some local segregation of the IL domains. We note, however, that peak II, due to the charge alteration, appears in all mixtures except for the PIL/IL  $[\text{PF}_6]^-$  with the higher molar mass. Since the peak is evident in the XRD pattern of the PIL/IL  $[\text{PF}_6]^-$  with the lower molar mass we hypothesize that is present also in the higher molar mass sample but is only broader.

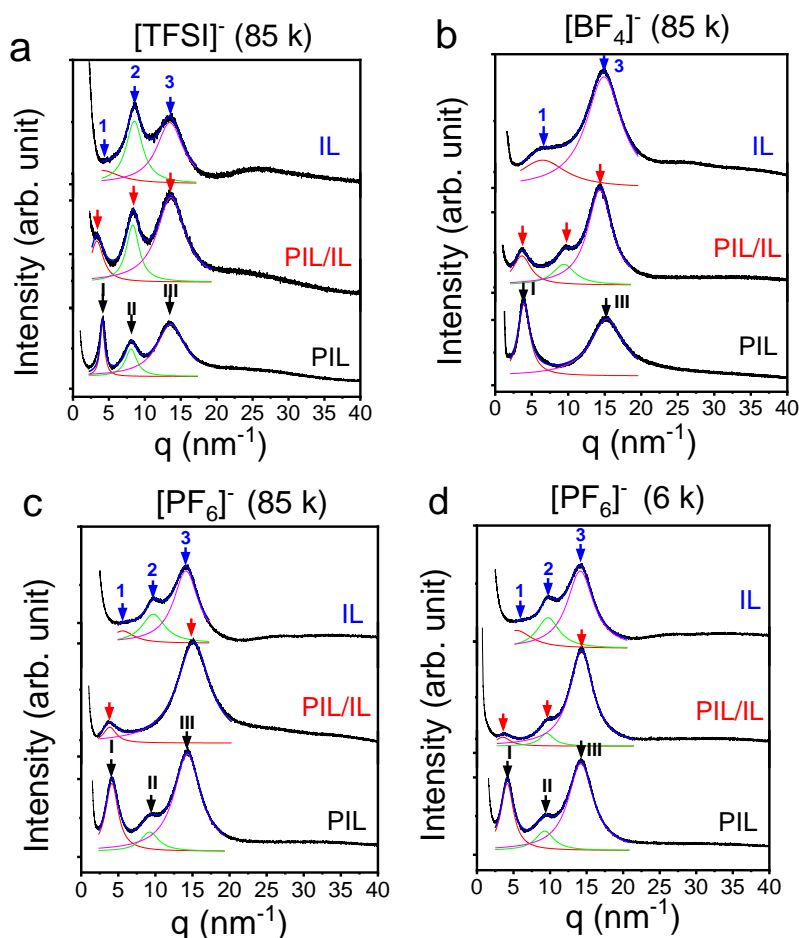


**Figure 5.** XRD curves of ILs, PILs and PIL/IL mixtures with the different anions, [TFSI]<sup>-</sup>, [BF<sub>4</sub>]<sup>-</sup>, [PF<sub>6</sub>]<sup>-</sup>, the latter for two different molar masses ( $M_n$  of 85 kg·mol<sup>-1</sup> and 6 kg·mol<sup>-1</sup>) at ambient temperature. Arrows 1, 2, 3 for the ILs indicate respectively, the smectic layering of polar-apolar groups, the charge alteration peak, and the van der Waals peak of nearest neighbors. Arrows I, II, III for the PILs indicate, respectively, the distance between backbones, the anion-anion correlation distance, and the van der Waals contacts of atoms. Red, green and magenta lines are the respective component contributions to the scattering curve (blue).

The experimental results can be compared with the simulations<sup>17</sup> of PIL/IL mixtures of poly[BVIM]<sup>+</sup>[PF<sub>6</sub>]<sup>-</sup>/[BMIM]<sup>+</sup>[PF<sub>6</sub>]<sup>-</sup>. Their study have shown that anions are coordinated to four cations from two adjacent polymer chains. Ion transport took place via anion hopping along the polymer backbone by a mechanism involving the formation and breaking of ion-associations. Snapshots of the mixtures provide some evidence of segregation in agreement with the present investigation.<sup>17</sup> A decoupling of the ion mobilities from  $T_g$  was found, although a single  $T_g$  was discussed. In addition, a stronger coordination of [PF<sub>6</sub>]<sup>-</sup> with the poly[BVIM]<sup>+</sup> segments relative to the [BMIM]<sup>+</sup> cations is not in line with the experimental findings.

## Imbibition in nanopores

The imbibition of the PIL/IL mixture in AAO does not follow the bulk viscosity. As an example, the imbibition length of the PIL/IL [TFSI]<sup>-</sup> with a molar mass of 85 kg·mol<sup>-1</sup> measured by ex situ reflection optical microscopy in AAO cross-sections is plotted as a function of the square root of time in Figure 6. According to the Lucas-Washburn equation<sup>36,37</sup> applicable to Newtonian liquids, the imbibition length increases according to:  $L = \left(\frac{\gamma R \cos\theta}{2\eta}\right)^{1/2} \sqrt{t}$ , where  $\gamma$  is the surface tension,  $\theta$  is the contact angle,  $\eta$  is the zero-shear viscosity, and  $R$  is the pore radius. The imbibition length was typically measured over several nanopores and the average value is shown in the figure (depth analysis is shown in **Figure S10, Supporting Information**). As shown in Figure 6, the latter follow the  $t^{1/2}$  dependence; a typical dependence for a process that is fast at the beginning and slower at the end. For all pore diameters investigated, the extracted effective viscosity (using  $\cos\theta = 0.77$  and  $\gamma_L = 24.6$  mN/m applicable to PIL/IL [TFSI]<sup>-</sup> at 318 K) is lower than in bulk (bulk  $\eta_0 = 445$  Pa·s). The ratio  $\eta_{\text{eff}}/\eta_0$ , decreases with pore diameter from 0.33 in 400 nm pores, to 0.21 in 65 nm pores, to 0.02 and 0.014 in 35 and 25 nm pores. This reveals that the pores are infiltrated by an excess of the IL and only by a small fraction of the PIL, e.g. away from bulk composition. Employing a linear mixing law for the zero-shear viscosities and the respective values for the IL ( $\eta_0=0.03$  Pa·s) and the PIL ( $\eta_0=2.6\times 10^{13}$  Pa·s) (shown in **Figure S6, Supporting Information**) at the imbibition temperature ( $T=318$  K) results to nearly 99% of IL in the nanopores. We will return to this point with respect to Figure 8 below.

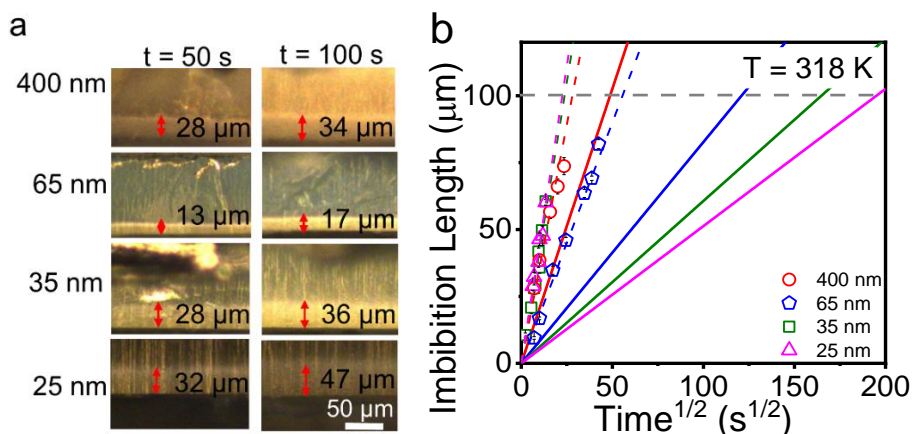


**Figure 6.** (a) Optical images of the imbibition length of PIL/IL [TFSI]<sup>-</sup> with a molar mass of  $85 \text{ kg}\cdot\text{mol}^{-1}$  in AAO templates with different pore sizes measured at the same time intervals. The red double-headed arrows indicate the imbibition length. The bar indicates  $50 \mu\text{m}$ . (b) Imbibition lengths for PIL/IL [TFSI]<sup>-</sup> measured at 318 K *ex situ* by reflection optical microscopy at selected times within AAOs with different pore sizes: 400 nm (red), 65 nm (blue), 35 nm (olive), 25 nm (magenta). The solid lines are the theoretical predictions of the Lucas-Washburn equation (LWE) with parameters:  $\eta_0(\text{bulk}) = 445 \text{ Pa}\cdot\text{s}$ ,  $\gamma_L = 24.6 \text{ mN/m}$  and  $\cos \theta = 0.77$ . The dashed lines represent the result of a linear fit to the actual data.

We investigated the imbibition kinetics *in situ* by *nDS* by continuous monitoring the conductivity under isothermal conditions. First conductivity increases. This reflects the filling process of nanopores (**Figure S2**). It is only after the full imbibition (e.g. zero air in nanopores) that the plateau corresponding to the dc-conductivity develops. In Figure 7a we plot the evolution of conductivity during imbibition of the PIL/IL [TFSI]<sup>-</sup> mixture at 318 K in AAO templates with different pore sizes. In 400 nm pores, the conductivity exhibits a constant value following the complete filling of pores. In the smaller pores, the dc-conductivity has a non-monotonic behaviour, following the initial increase to complete filling (indicated by the open symbols in Fig. 9a) it shows a plateau at intermediate times that is followed by a decrease at longer time. The value of dc-conductivity at the plateau exceeds the conductivity of the bulk PIL/IL mixture at the same temperature (shown in Fig. 7 by the dashed line) revealing the enrichment of nanopores by the IL. Results presented in Figures 6 & 7 suggest the separation of a PIL/IL mixture into its constituent components by the kinetics of imbibition in nanopores. The plateau at short times reflects the adsorption of the IL, as reported earlier in the same AAOs.<sup>6</sup> The decrease of dc-conductivity at longer times originates from the adsorption of the minority component (PIL). This is also reminiscent to the polymer adsorption by solid polymer electrolytes in the same nanopores.<sup>5</sup> As the PIL chains are adsorbed at the AAO pore walls, they inevitably transport some ions that are immobilised at the walls. As these ions do not

diffuse they do not contribute to the ion-conduction mechanism. Depending on the fraction of immobilized ions, the ionic conductivity can decrease below the bulk value.

The experimental observations can be interpreted in the following way (Figure 7b). The schematic depicts the filling process at two time intervals. At short times ( $t \sim t_0$ ), the pores are penetrated by a PIL/IL mixture enriched by the IL. At longer times ( $t \sim t_1$ ), a fraction of the minority component (PIL) is adsorbed at the pore walls, further decreasing the number of mobile ions. Similar results were obtained for the PIL/IL  $[\text{PF}_6]^-$  (shown in **Figures S11** and **Figure S12, Supporting Information**). The characteristic time scale of the adsorption process,  $\tau_{\text{ads}}$ , can be extracted from an exponential fit as:  $\sigma_{\text{dc}}(t) = (\sigma_{\text{dc}})_{\text{max}} \exp(-t/\tau_{\text{ads}})$  shown in Figure 7a inset. We note here that the reduction in dc-conductivity is small as compared to the SPE case in the same nanopores.<sup>5</sup> This is due to the small fraction of PIL in the infiltrated pores.

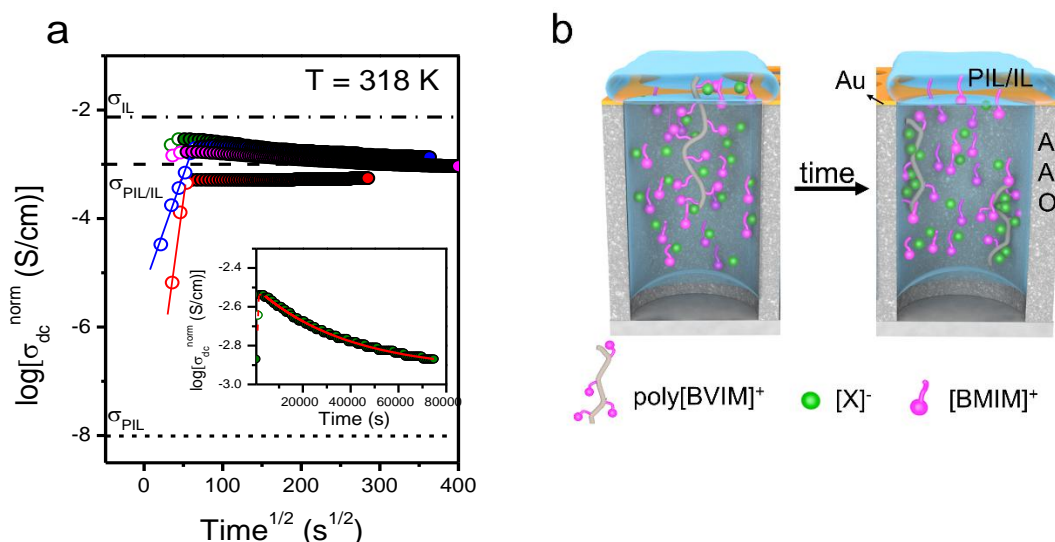


**Figure 7.** (a) Ionic conductivity from *in situ* nDS for the PIL/IL  $[\text{TFSI}]^-$  with a  $M_n$  of  $85 \text{ kg} \cdot \text{mol}^{-1}$  during and after flow in AAO nanopores with different pore sizes: 400 nm (red), 65 nm (blue), 35 nm (olive), 25 nm (magenta) plotted as a function of the square root of time at 318 K. The open circles represent the (ac) conductivity of the PIL/IL  $[\text{TFSI}]^-$  during flow within AAO. Filled symbols provide the respective dc-conductivities. All conductivity values are corrected for the porosity. The dash-dotted, short dashed, and dashed lines provides with the respective dc-conductivity values of the pure IL, the pure PIL and their mixture at the imbibition temperature. In the inset the evolution of conductivity within 35 nm pores is shown together with an exponential fit at the longer times. (b) Schematic of the imbibition process of PIL/IL  $[\text{TFSI}]^-$  (i) during ( $t \sim t_0$ ) and (ii) after flow ( $t \sim t_1$ ) in AAO nanopores.

The extracted time scale ( $\tau_{\text{ads}} \sim 10^4 \text{ s}$ ) is much slower than any molecular time scale, as anticipated from earlier study in a solid polymer electrolyte.<sup>5</sup> In comparison, the time scale of the polymer terminal relaxation (obtained from linear fits at the terminal relaxation with slopes 1 and 2 for the loss and storage moduli, respectively), and of the local dynamics associated

with  $T_g$  (obtained from the crossing of the storage and loss modulus at the liquid-to-glass regions), are at 3 s and  $2 \times 10^{-6}$  s, respectively, at the imbibition temperature ( $T=318$  K).

The enrichment of nanopores by the IL can be verified by extracting the material using an organic solvent and testing for its conductivity. For this test we employed PIL/IL [TFSI]<sup>-</sup> following the imbibition in AAO nanopores with diameter of 65 nm. After removing the top layer, THF was used for extracting the material from the nanopores. Following slow solvent removal, the ionic conductivity was measured using the normal procedure for bulk samples. The result is shown in Figure 8 in comparison to the conductivities of the bulk PIL, the neat IL and their symmetric blend PIL/IL. Evidently, the measured ionic conductivity from the material extracted from the nanopores is biased towards the neat IL in agreement with the notion that the IL enriches the nanopores.

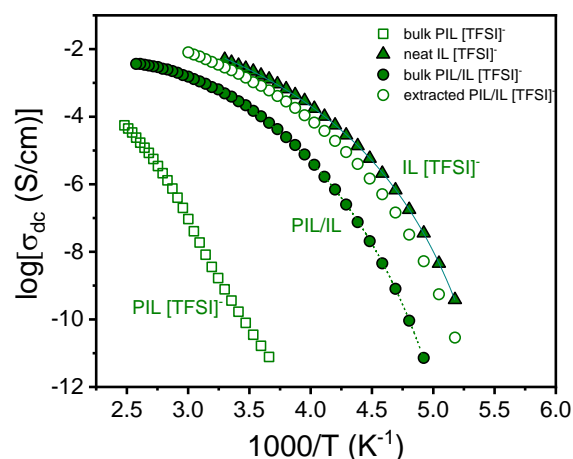


**Figure 8.** Ionic conductivity of the material extracted from AAO nanopores of 65 nm in diameter following the *in situ* nDS (open circles). The conductivity data are compared with the neat IL (filled triangles), the bulk PIL (open squares) and the bulk PIL/IL blend (spheres).

To test the effect of surfaces on adsorption and ion transport, we have silanized the pores by HMDS. The result on the evolution of dc-conductivity is shown in Figure 9 for the imbibition kinetics of the PIL/IL [TFSI]<sup>-</sup> mixture within AAO nanopores 35 nm in diameter at 318 K. The measured dc-conductivity exhibits a moderate decrease, in contrast to the stronger decrease observed in native pores. AAO silanization passivates the surface and decreases the propensity for adsorption and charge accumulation.

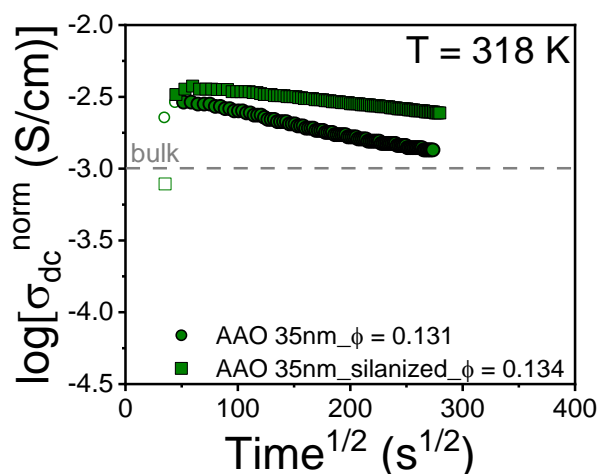


**Figure 9.** Evolution of the ionic conductivity during the *in situ* nDS of the PIL/IL [TFSI]<sup>-</sup> with a  $M_n$  of 85 kg·mol<sup>-1</sup> inside native (solid circle) and silanized (solid square) AAO nanopores with a pore diameter of 35 nm at 318 K. The conductivity values are corrected for the porosity. The dashed line indicates the dc-conductivity of the bulk PIL/IL [TFSI]<sup>-</sup> at the same temperature.

To further explore any effects of confinement following imbibition, temperature scans were performed immediately after imbibition (Figure 7). The temperature dependence of dc-conductivity obtained on cooling, starting from the imbibition temperature down to the glassy state, is shown in Figure 10 for different pore diameters. The figure includes the characteristic ion mobility times as extracted from the modulus representation as  $M^*=1/\varepsilon^*$  (**Figure S13, Supporting Information**). As expected, the dc-conductivity and the characteristic time of ion mobility follows a VFT dependence. The parameters were, however, different than in bulk. Under confinement and at lower temperatures, the ion conductivity is decoupled from the bulk values and extrapolates to a lower “freezing” temperature. Hence, the different VFT dependences extrapolate to a lower glass temperature, that further depends on the degree of confinement. The VFT parameters are included in **Table 3**. This is inline with the majority fraction of the IL in the nanopores.

**Table 3.** Parameters of the VFT Equation for the PIL/IL [TFSI]- pertinent to the Temperature Scan Experiments Following Imbibition

Pore diameter, $d$ (nm)	$-\log_{10}(\tau_0/s)$	$B^r$ (K)	$T_0^r$ (K)	$\log_{10}[\sigma_0/(S \cdot cm^1)]$	$B^\sigma$ (K)	$T_0^\sigma$ (K)
bulk	$11 \pm 0.6$	$980 \pm 140$	$165 \pm 4$	$0.18 \pm 0.1$	$1150 \pm 20$	$160 \pm 1$
400	$12 \pm 0.2$	$1680 \pm 70$	$130 \pm 2$	$0.65 \pm 0.1$	$1610 \pm 40$	$135 \pm 1$
65	$11 \pm 0.1$	$1470 \pm 40$	$132 \pm 1$	$0.55 \pm 0.1$	$1460 \pm 25$	$130 \pm 1$
35	$10 \pm 0.1$	$1200 \pm 30$	$133 \pm 1$	$0.65 \pm 0.1$	$1425 \pm 30$	$130 \pm 1$
25	$11 \pm 0.2$	$1410 \pm 65$	$130 \pm 2$	$0.41 \pm 0.1$	$1530 \pm 30$	$125 \pm 1$

To further explore any connection to non-equilibrium dynamics, established recently for confined polymers within nanopores,<sup>38,39</sup> we have followed the ion conductivity on heating back to the imbibition temperature. Identical  $\sigma(T)$  dependencies were found possibly suggesting equilibrium values.

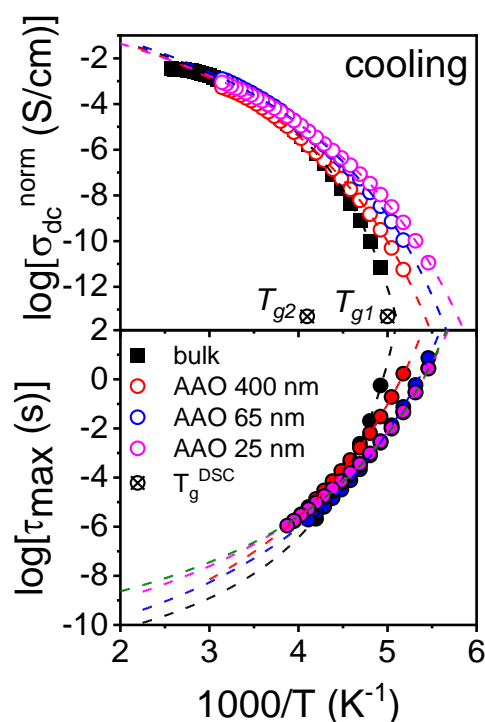


**Figure 10.** (Top) Temperature dependence of the dc-conductivity for bulk and confined PIL/IL [TFSI] following the imbibition experiments obtained on cooling. The dashed lines represent VFT fits. (Bottom) Characteristic ion relaxation times, extracted from the maximum of the modulus representation, as a function of reciprocal temperature.

The reduction in the glass temperature with confinement is further documented by the DSC traces obtained from the same samples that were employed for the imbibition kinetics (Figure 7) and the subsequent temperature scans (Figure 10). The DSC traces of the confined PIL/IL mixture shown in Figure 11a, display dual  $T_g$ 's that are further shifted to lower temperatures on confinement. Evidently, the lower  $T_g$  under confinement approaches the value of the bulk IL  $T_g$  ( $T_g \sim 183$  K) revealing the enrichment of pores by the mobile IL during and following imbibition (the latter during polymer adsorption). Furthermore, silanization only partially alleviates this effect (Figure 11b).

The results have shown the application of porous membranes for the separation of PIL/IL mixtures into its constituents. Within nanopores, the capillary force is strong and drives the lower viscosity compound (IL) to penetrate first. This is reminiscent to the component separation of blends composed of lower and higher molar mass polymers<sup>21</sup> as well as the separation of blends of different polymer topologies<sup>22,23</sup> (e.g. topology sorting in linear/star polymer blends). Further studies will explore the limitations in the relative viscosity of the components required for the separation process.

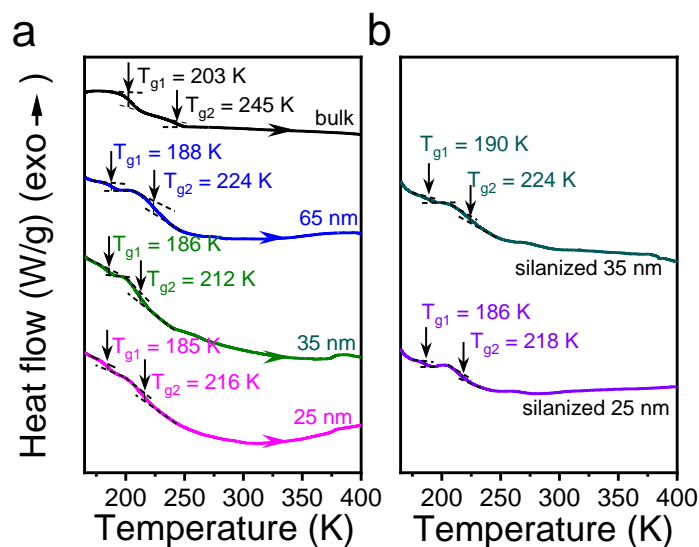


**Figure 11.** (a) Thermal properties under confinement: DSC heating traces of PIL/IL [TFSI]<sup>-</sup> with a molar mass of 85 kg·mol<sup>-1</sup> in the bulk (black line) and under confinement within AAO nanopores with diameters: 65 nm (blue), 35 nm (olive), and 25 nm (magenta). (b) Effect of surface treatment: DSC heating traces of PIL/IL [TFSI]<sup>-</sup> confined within silanized AAOs, with diameters of 35 nm (orange), and 25 nm (purple) recorded with a rate of 20 K·min<sup>-1</sup>.

#### 6.4. Conclusion

Ionic liquids have been explored in several applications including separation for extraction, as stationary phases in chromatography, and in membranes for the selective transport of organic compounds. In all cases, ionic interactions play the dominant role. This study explored another aspect of separation, namely, the possibility to separate PIL/IL mixtures by imbibition in nanopores.

In the bulk, thermal, viscosity, and conductivity measurements in symmetric PIL/IL mixtures revealed that they are locally heterogeneous. The viscosity in the PIL/IL mixtures has a VFT dependence that is biased towards the bulk PIL. In contrast, the dc-conductivity closely resembles that of pure IL. When the same symmetric mixtures are brought into contact with nanoporous membranes the capillary force enhances the heterogeneity and triggers demixing in macroscopic length scales. By a combination of *ex situ* polarized optical microscopy measurements of the evolution of the imbibition length, and *in situ* dc-conductivity measurements, the latter by nanodielectric spectroscopy, it was shown that the IL penetrates first the nanopores followed by a minority of the PIL. At later times, part of the minority PIL is adsorbed at the pore walls, producing a further reduction in dc-conductivity. Temperature dependent conductivity measurements following the imbibition process further demonstrate the enrichment of pores by the IL. The results demonstrate, for the first time, the separation of a mixture of ionic compounds composed from an IL and a PIL by the different imbibition speeds in nanopores. In addition, polymer adsorption and surface functionality play significant role in the ion dynamics. Overall, nanoporous templates can be viewed as model systems for the separation and adsorption of ionic systems.

## 6.5 References

- (1) Berchtold, M.W.; Brinkmeier, H.; Müntemer, M. Calcium Ion in Skeletal Muscle: Its Crucial Role for Muscle Function, Plasticity, and Disease. *Physiological Reviews* **2000**, *80*, 1215–1265.
- (2) Su, Y.-S.; Hsu, S.-C.; Peng, P.-H.; Yang, J.-Y., Gao, M.; Yeh, L.-H. Unraveling the Anomalous Channel-Length-Dependent Blue Energy Conversion Using Engineered Alumina Nanochannels. *Nano Energy* **2021**, *84*, 105930.
- (3) de Souza, J.P.; Levy, A.; Bazant, M.Z. Electroneutrality Breakdown in Nanopore Arrays. *Phys. Rev. E* **2021**, *104*, 044803.
- (4) Aksimentiev, A.; Heng, J. B.; Timp, G.; Schulten, K. Microscopic Kinetics of DNA Translocation through Synthetic Nanopores. *Biophys. J.* **2004**, *87*, 2086-2097.
- (5) Tu, C.-H.; Veith, L.; Butt, H.-J.; Floudas, G. Ionic Conductivity of a Solid Polymer Electrolyte Confined in Nanopores. *Macromolecules* **2022**, *55*, 1332–1341.
- (6) Dong, Y.; Steinhart, M.; Butt, H.-J.; Floudas, G. Conductivity of Ionic Liquids in the Bulk and During Infiltration in Nanopores. *J. Phys. Chem. B* **2023**, *127*, 6958–6968.
- (7) Nishimura, N.; Ohno, H. 15th Anniversary of Polymerized Ionic Liquids, *Polymer* **2014**, *55*, 3289–3297.
- (8) Yuan, J.; Antonietti, M. Poly(ionic liquid)s: Polymers Expanding Classical Property Profiles. *Polymer* **2011**, *52*, 1469-1482.
- (9) Green, M.D.; Salas-de la Cruz, D.; Ye, Y.; Layman, J.M.; Elabd, Y.A.; Winey, K.I.; Long, T.E. Alkyl-Substituted N-Vinylimidazolium Polymerized Ionic Liquids: Thermal Properties and Ionic Conductivities. *Macromol. Chem. Phys.* **2011**, *212*, 2522-2528.
- (10) Nakamura, K.; Fukao, K.; Inoue, T. Dielectric Relaxation and Viscoelastic Behavior of Polymerized Ionic Liquids with Various Counteranions. *Macromolecules* **2012**, *45*, 3850-3858.
- (11) Bocharova, V.; Sokolov, A.P. Perspectives for Polymer Electrolytes: A View from Fundamentals of Ionic Conductivity. *Macromolecules* **2020**, *53*, 4141–4157.
- (12) Sangoro, J. R.; Iacob, C.; Agapov, A. L.; Wang, Y.; Berdzinski, S.; Rexhausen, H.; Strehmel, V.; Friedrich, C.; Sokolov, A. P.; Kremer, F. Decoupling of Ionic Conductivity from Structural Dynamics in Polymerized Ionic Liquids. *Soft Matter* **2014**, *10*, 3536–3540.
- (13) Choi, U. H.; Ye, Y.; Salas de la Cruz, D.; Liu, W.; Winey, K. I.; Elabd, Y. A.; Runt, J.; Colby, R. H. Dielectric and Viscoelastic Responses of Imidazolium-Based Ionomers with Different Counterions and Side Chain Lengths. *Macromolecules* **2014**, *47*, 777–790.
- (14) Pipertzis, A.; Papamokos, G.; Mühlinghaus, M.; Mezger, M.; Scherf, U.; Floudas, G. What Determines the Glass Temperature and dc-Conductivity in Imidazolium-Polymerized Ionic Liquids with a Polythiophene Backbone? *Macromolecules* **2020**, *53*, 3535–3550.
- (15) Mogurampelly, S.; Keith, J. R.; Ganesan, V. Mechanism Underlying Ion Transport in Polymerized Ionic Liquids. *J. Am. Chem. Soc.* **2017**, *139*, 9511–9514.

- (16) Zhang, Z.; Nasrabudi, A.T.; Aryal, D.; Ganesan, V. Mechanisms of Ion Transport in Lithium Salt-Doped Polymeric Ionic Liquid Electrolytes. *Macromolecules* **2020**, *53*, 6995–7008.
- (17) Mogurampelly, S.; Ganesan, V. Ion Transport in Polymerized Ionic Liquid–Ionic Liquid Blends. *Macromolecules* **2018**, *51*, 9471–94.
- (18) Serghei, A.; Chen, D.; Lee, D. H.; Russell, T. P. Segmental Dynamics of Polymers During Capillary Flow into Nanopores. *Soft Matter* **2010**, *6*, 1111–1113.
- (19) Tu, C.-H.; Steinhart, M.; Butt, H.-J.; Floudas, G. In Situ Monitoring of the Imbibition of Poly(n-butyl methacrylates) in Nanoporous Alumina by Dielectric Spectroscopy. *Macromolecules* **2019**, *52*, 8167–8176.
- (20) Tu, C.-H.; Zhou, J.; Doi, M.; Butt, H.-J.; Floudas, G. Interfacial Interactions During In Situ Polymer Imbibition in Nanopores. *Phys. Rev. Lett.* **2020**, *125*, 127802.
- (21) Tu, C.-H.; Zhou, J.; Butt, H.-J.; Floudas, G. Adsorption Kinetics of cis-1,4-Polyisoprene in Nanopores by In Situ Nanodielectric Spectroscopy. *Macromolecules* **2021**, *54*, 6267–6274.
- (22) Kardasis, P.; Sakellariou, G.; Floudas, G. Ultraslow Adsorption of Star cis-1,4-Polyisoprenes by In Situ Imbibition in Nanopores. *Macromolecules*, **2024**, *57*, 481–489.
- (23) Kardasis, P.; Tzourtzouklis, I.; Nega, A.D.; Sakellariou, G.; Steinhart, M.; Floudas, G. Topology Sorting: Separating Linear/Star Polymer Blend Components by Imbibition in Nanopores. *J. Chem. Phys.* **2024**, *160*, 044912.
- (24) Xiao, W. C.; Yang, Q.; Zhu, S. L. Comparing Ion Transport in Ionic Liquids and Polymerized Ionic Liquids. *Sci. Rep.*, **2020**, *10*, 7825.
- (25) He, F.; Wang, B.; Zhao J.; Yin, J. B. Influence of Tethered Ions on Electric Polarization and Electrorheological Property of Polymerized Ionic Liquids. *Molecules* **2020**, *25*, 2896.
- (26) Marcilla, R.; Blazquez, J.A.; Rodriguez, J.; Pomposo, J.A.; Mecerreyes, D. Tuning the Solubility of Polymerized Ionic Liquids by Simple Anion-Exchange Reaction. *J. Polym. Sci. Part A: Polym. Chem.* **2004**, *42*, 208-212.
- (27) Dullius, J. E. L.; Suarez, P. A. Z.; Einloft, S.; de Souza, R. F.; Dupont, J.; Fischer, J.; De Cian, A. Selective Catalytic Hydrodimerization of 1,3-Butadiene by Palladium Compounds Dissolved in Ionic Liquids. *Organometallics* **1998**, *17*, 815–819.
- (28) Han, D.; Row, K. H. Recent Applications of Ionic Liquids in Separation Technology. *Molecules* **2010**, *15*, 2405-2426.
- (29) Araque, J. C.; Hettige, J. J.; Margulis, C. J. Modern Room Temperature Ionic Liquids, a Simple Guide to Understanding Their Structure and How It May Relate to Dynamics. *J. Phys. Chem. B* **2015**, *119*, 12727–12740.
- (30) Triolo, A.; Russina, O.; Bleif, H. J.; Di Cola, E. Nanoscale Segregation in Room Temperature Ionic Liquids. *J. Phys. Chem. B* **2007**, *111*, 4641–4644.
- (31) Bradley, A. E.; Hardacre, C.; Holbrey, J. D.; Johnston, S.; McMath, S. E. J.; Nieuwenhuyzen, M. Small-Angle X-ray Scattering Studies of Liquid Crystalline 1-alkyl-3-methylimidazolium Salts. *Chem. Mater.* **2002**, *14*, 629–635.

- (32) Lucas, R. On the Time Law of the Capillary Rise of Liquids. *Colloid Polym. Sci.* **1918**, 23, 15–22.
- (33) Washburn, E.W. The Dynamics of Capillary Flow. *Phys. Rev.* **1921**, 17, 273–283.
- (34) Adrjanowicz, K.; Paluch, M., Discharge of the Nanopore Confinement Effect on the Glass Transition Dynamics via Viscous Flow. *Phys. Rev. Lett.* **2019**, 122, 176101.
- (35) Kardasis, P.; Sakellariou, G.; Steinhart, M.; Floudas, G. Nonequilibrium Effects of Polymer Dynamics under Nanometer Confinement: Effects of Architecture and Molar Mass. *J. Phys. Chem. B* **2022**, 126, 5570–5581.

## 6.6 Supporting information

## DSC traces

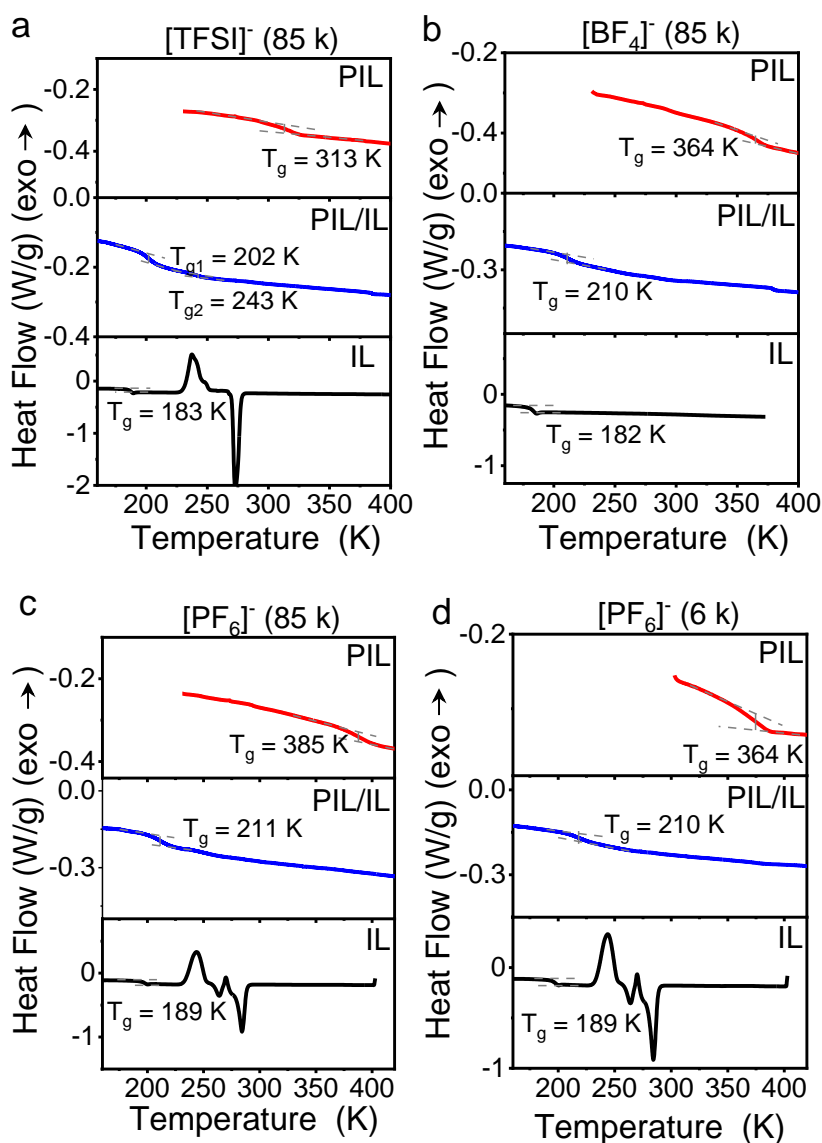


**Figure S1.** DSC heating traces of PIL, IL and PIL/IL mixtures with different anions, (a) [TFSI]<sup>-</sup>, (b) [BF<sub>4</sub>]<sup>-</sup>, (c) [PF<sub>6</sub>]<sup>-</sup> and (d) [PF<sub>6</sub>]<sup>-</sup> with a low  $M_n$  (6 kg·mol<sup>-1</sup>) at a rate of 10 K·min<sup>-1</sup>.

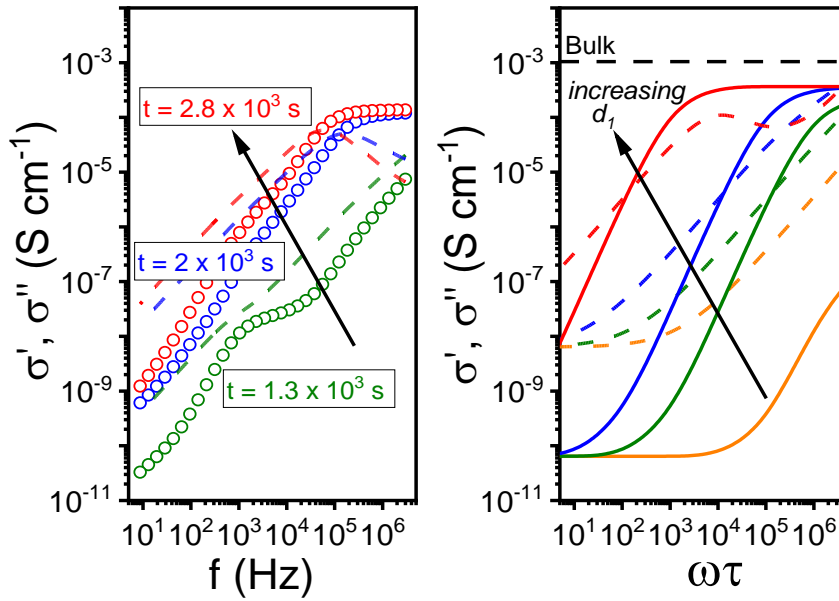
## Chemistry-Elemental Analysis

The elemental analysis of carbon (C), hydrogen (H), and nitrogen (N) were conducted using a Vario EL cube elemental analyzer (ELEMENTAR, Vario EL CUBE, Germany). Found (%): C, 43.66; H, 6.61; N, 10.97; calcd for C<sub>9</sub>H<sub>15</sub>N<sub>2</sub>B<sub>1</sub>F<sub>4</sub> (%): C, 45.41; H, 6.35; N, 11.77 for poly[BVIM][BF<sub>4</sub>]. Found (%): C, 36.07; H, 6.67; N, 8.97; calcd for C<sub>9</sub>H<sub>15</sub>N<sub>2</sub>P<sub>1</sub>F<sub>6</sub> (%): C, 36.50; H, 5.11; N, 9.46 for poly[BVIM][PF<sub>6</sub>]. Found (%): C, 30.77; H, 5.65; N, 8.76; calcd for

C<sub>11</sub>H<sub>15</sub>N<sub>3</sub>O<sub>4</sub>S<sub>2</sub>F<sub>6</sub> (%): C, 30.63; H, 3.51; N, 9.74 for poly[BVIM][TFSI]. It indicates that the samples contain a small number of impurities.

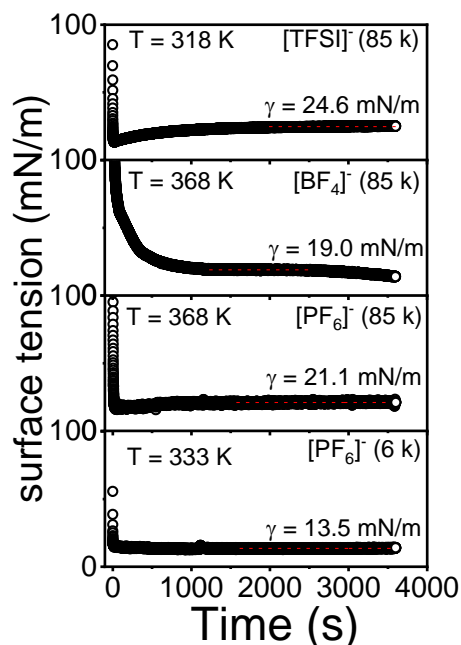
### Dielectric Spectroscopy

Dielectric spectroscopy and in situ nanodielectric spectroscopy (*n*DS) were employed to follow the dynamics of bulk and confined PIL, IL and the PIL/IL mixtures. In all cases, a Novocontrol Alpha frequency analyzer, consisting of a broadband dielectric converter and an active sample head was used. For bulk samples, the ILs, PILs and mixtures were embedded between two stainless steel electrodes with a diameter of 20 mm accompanied by a 50  $\mu$ m Teflon spacer to maintain a constant thickness (the capacitor geometry was subsequently corrected for the Teflon spacer). A broad frequency range from 10<sup>-2</sup> to 10<sup>7</sup> Hz was employed for the bulk DS measurements. From the measured impedance,  $Z^*(\omega)$ , the dielectric and conductivity functions are calculated, respectively, as  $\epsilon^*(\omega)=1/(i\omega Z^*(\omega)C_0)$  and  $\sigma^*(\omega)=d/Z^*(\omega)A$ , where  $C_0$  is the vacuum capacitance, and  $d, A$  the sample thickness and electrode area, respectively. For a typical capacitance of  $\sim 100$  pF, and within the frequency range 0.1 to 10<sup>6</sup> Hz, the absolute accuracy of the loss factor is  $\tan\delta \sim 3 \times 10^{-5}$ . The complex conductivity function,  $\sigma^* = \sigma' + i\sigma''$ , where  $\sigma'$  and  $\sigma''$  are the real (*i.e.*, the dc-conductivity) and imaginary parts, respectively, was obtained from the impedance measurements. The plateau in the real part  $\sigma'$  was used to extract the dc-conductivity. We have recently shown that *n*DS can be employed to follow the increase in the imbibition length of a substance by monitoring the increase of conductivity during and after flow in AAO. For the investigation of the effect of nanoconfinement, a gold layer with a diameter of 9 mm and thickness of 35 nm was deposited onto the AAO template, serving as the top electrode. The aluminum substrate of the AAO templates functioned as the bottom electrode. The deposition of the gold layer was performed through a sputtering process under vacuum conditions (vacuum better than  $2 \times 10^{-5}$  Pa) using a Bal-tec MED 020 with a current density of 40 mA. The samples were subsequently placed on top the AAO template, and the investigation of imbibition kinetics was conducted by *n*DS (Scheme 2). In this case a narrower frequency range (1 - 10<sup>6</sup> Hz) was employed for a faster acquisition.

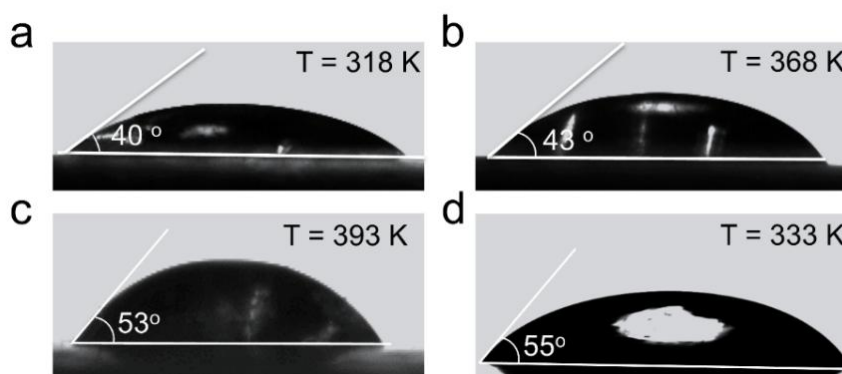


**Figure S2.** (a) Evolution of the real (symbol) and imaginary (dashed lines) parts of the complex conductivity for PIL/IL [TFSI]<sup>-</sup> within AAO pores with a diameter of 400 nm at 318 K. (b) Simulation of the evolution of the real (solid lines) and imaginary parts (dashed lines) of the complex conductivity corresponding to the process in (a) for different imbibition lengths ( $d_1$ ) via the parallel model. Parameters are as follows:  $\Delta\varepsilon = 20$ ,  $\varepsilon_\infty = 28$ ,  $\sigma_{dc} = 10^{-3} \text{ S cm}^{-1}$ ,  $\tau = 1 \text{ s}$ ,  $\varphi_{12} (=1 - \varphi_3) = 0.358$ ,  $L = 100 \mu\text{m}$ ,  $\sigma'_3 = \sigma'_{AAO} = 10^{-10} \text{ S cm}^{-1}$ , and  $\sigma''_3 = \sigma''_{AAO} = 10^{-8} \text{ S cm}^{-1}$ . Different colors correspond to different imbibition lengths: (orange)  $d_1 = 30 \mu\text{m}$ , (olive)  $d_1 = 99 \mu\text{m}$ , (blue)  $d_1 = 99.9 \mu\text{m}$  and (red)  $d_1 = 99.999 \mu\text{m}$ .

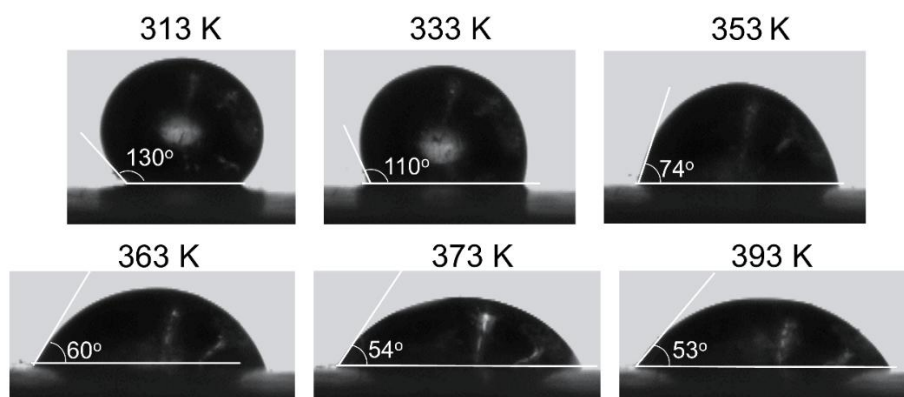
## Surface Tension and Contact Angle



**Figure S3.** Surface tension of the PIL/IL mixture bearing different anions and polymer molar mass:  $[\text{TFSI}]^-$  ( $85 \text{ kg}\cdot\text{mol}^{-1}$ ),  $[\text{BF}_4]^-$  ( $85 \text{ kg}\cdot\text{mol}^{-1}$ ),  $[\text{PF}_6]^-$  ( $85 \text{ kg}\cdot\text{mol}^{-1}$ ), and  $[\text{PF}_6]^-$  ( $6 \text{ kg}\cdot\text{mol}^{-1}$ ) measured at the corresponding imbibition temperature, 318 K, 368 K, 368 K (due to the limitation of instrument,  $[\text{PF}_6]^-$  ( $85 \text{ kg}\cdot\text{mol}^{-1}$ ) was measured at 368 K, instead of the infiltration temperature, 393 K), 333 K, respectively.

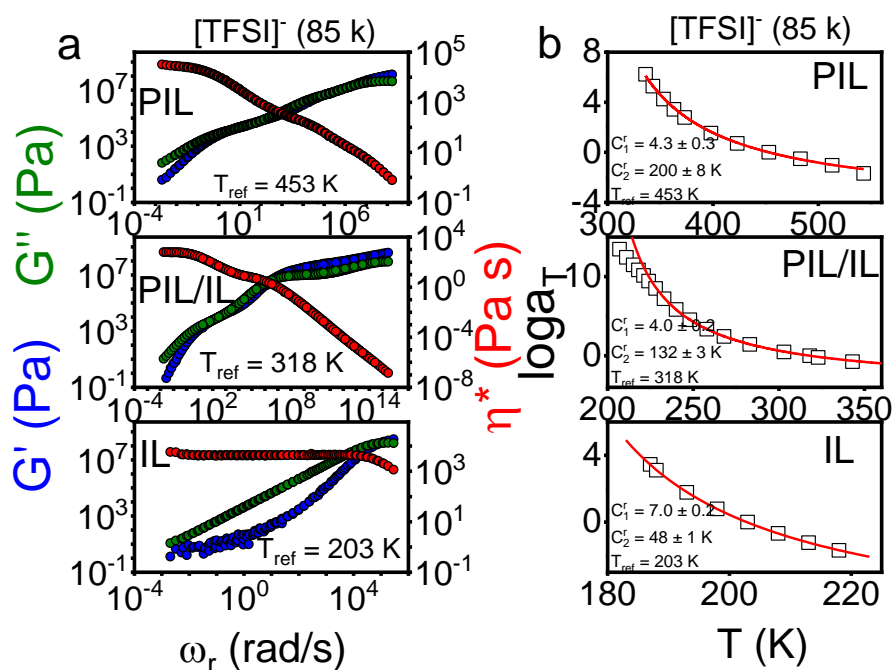


**Figure S4.** Contact angles of the PIL/IL mixture with different anions and polymer molar mass: (a)  $[\text{TFSI}]^-$  with a  $M_n$  of  $85 \text{ kg}\cdot\text{mol}^{-1}$ , (b)  $[\text{BF}_4]^-$  with a  $M_n$  of  $85 \text{ kg}\cdot\text{mol}^{-1}$ , (c)  $[\text{PF}_6]^-$  with a  $M_n$  of  $85 \text{ kg}\cdot\text{mol}^{-1}$ , (d)  $[\text{PF}_6]^-$  with a  $M_n$  of  $6 \text{ kg}\cdot\text{mol}^{-1}$ , at the corresponding infiltration temperature, 318 K, 368 K, 393 K, 333 K, respectively.

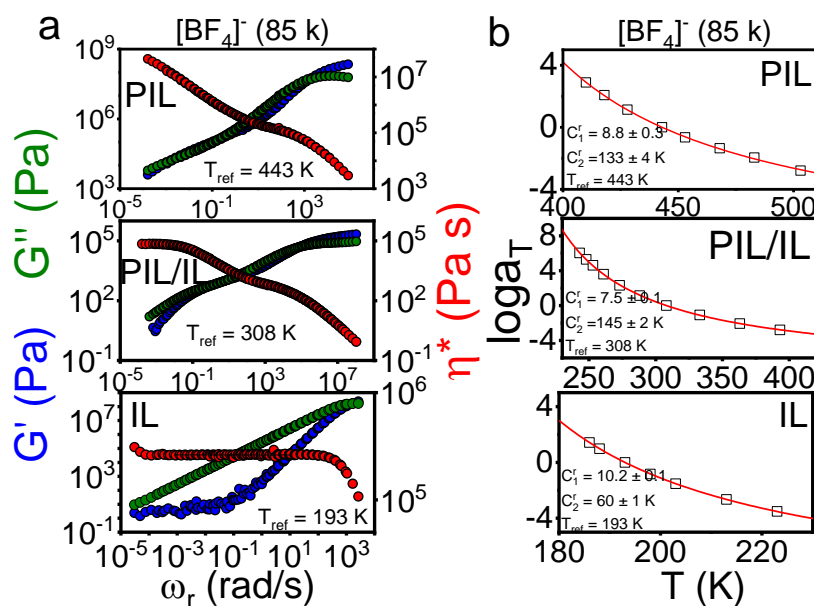


**Figure S5.** Contact angle of PIL/IL  $[\text{PF}_6]^-$  with a  $M_n$  of  $85 \text{ kg}\cdot\text{mol}^{-1}$  at different temperature.

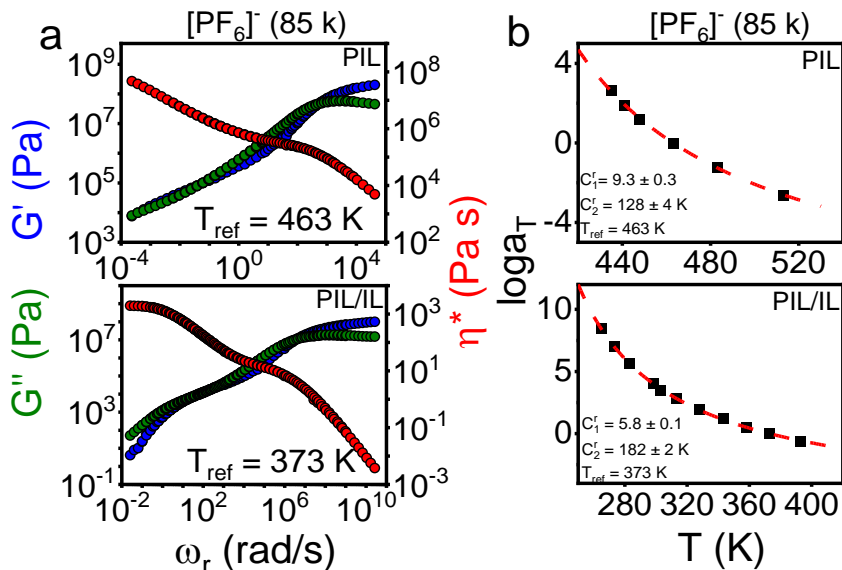
### Rheology



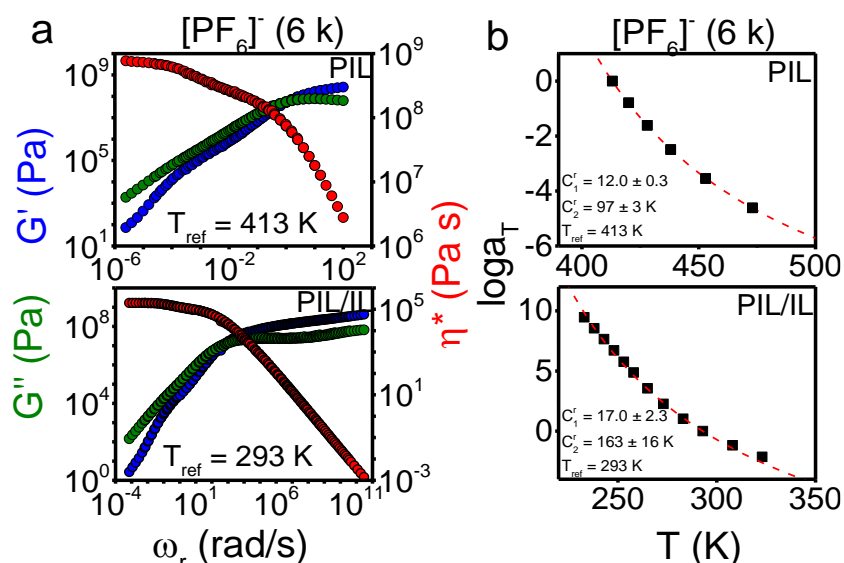
**Figure S6.** (a) Master curves for the storage (blue), the loss (green) modulus and shear viscosities (red) of PIL, IL and PIL/IL mixture with a fixed anion  $[\text{TFSI}]^-$ . (b) Shift factors of PIL, IL and PIL/IL mixture at the corresponding reference temperature. Dashed lines represent fits to the WLF equation. The WLF parameters are given in the inset.



**Figure S7.** (a) Master curves for the storage (blue), the loss (green) modulus and shear viscosities (red) of PIL/IL mixture and IL with a fixed anion [BF<sub>4</sub>]<sup>-</sup>. (b) Shift factors of PIL/IL mixture and IL at the corresponding reference temperature. Dashed lines represent fits to the WLF equation. The WLF parameters are given in the inset.

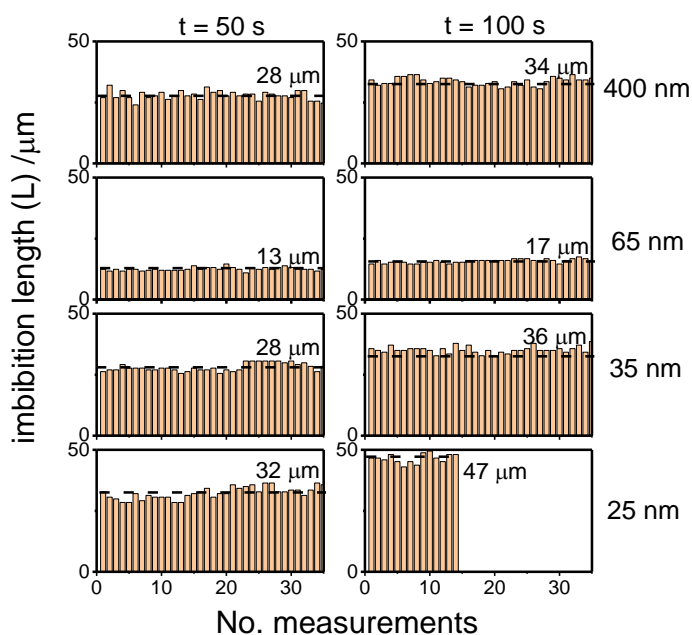


**Figure S8.** (a) Master curves for the storage (blue), the loss (green) modulus and shear viscosities (red) of PIL and PIL/IL mixture with a fixed anion [PF<sub>6</sub>]<sup>-</sup>. (b) Shift factors of PIL and PIL/IL mixture at the corresponding reference temperature. Dashed lines represent fits to the WLF equation. The WLF parameters are given in the inset.

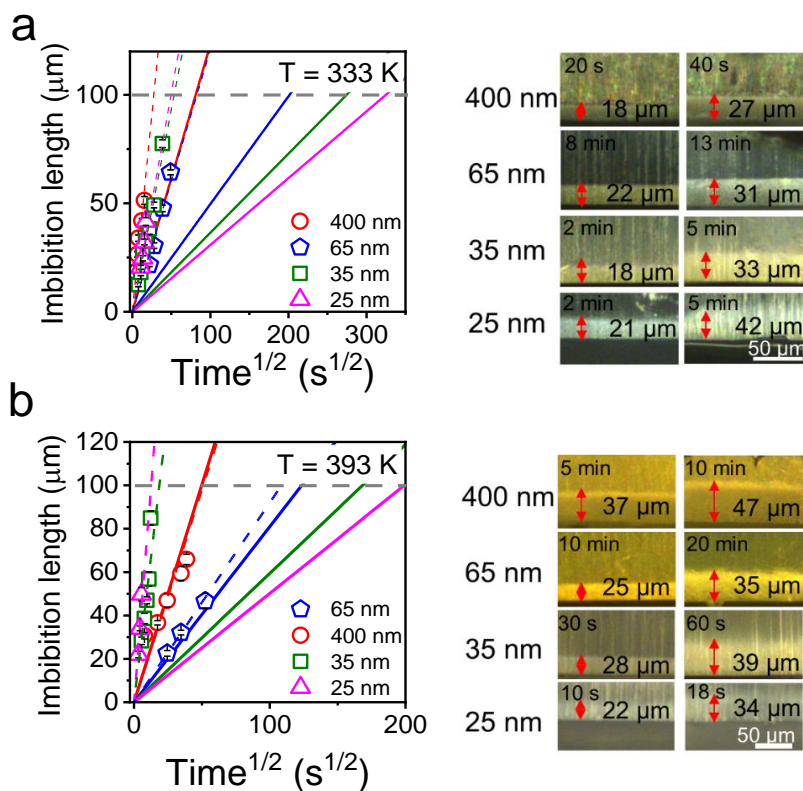


**Figure S9.** (a) Master curves for the storage (blue), the loss (green) modulus and shear viscosities (red) of PIL and PIL/IL mixture with a fixed anion  $[\text{PF}_6]^-$ , and a low  $M_n$ ,  $6 \text{ kg}\cdot\text{mol}^{-1}$ . (b) Shift factors of PIL and PIL/IL mixture at the corresponding reference temperature. Dashed lines represent fits to the WLF equation. The WLF parameters are given in the inset.

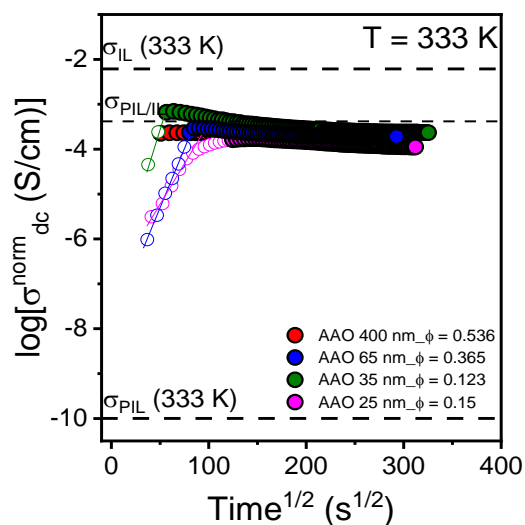
### Lucas-Washburn Equation



**Figure S10.** Imbibition length statistical analysis referring to the data shown in Figure 6a for the mixture PIL/IL  $[\text{TFSI}]^-$  and measured over several nanopores. The average of the measured values was employed in Figure 6b.



**Figure S11.** (a) Imbibition lengths and optical images for PIL/IL  $[\text{PF}_6]^-$  with a  $M_n$  of  $6 \text{ kg}\cdot\text{mol}^{-1}$  measured *ex situ* by reflection optical microscopy at selected times within AAO templates of different pore sizes at 333 K: 400 nm (red), 65 nm (blue), 35 nm (olive), 25 nm (magenta). The solid lines are the theoretical predictions of the Lucas-Washburn equation (LWE) with parameters:  $\eta_0(\text{bulk}) = 500 \text{ Pa}\cdot\text{s}$ ,  $\gamma_L = 24.6 \text{ mN m}^{-1}$  and  $\cos \theta = 0.82$ . The dashed lines represent the result of a linear fit. (b) Imbibition lengths and optical images for PIL/IL  $[\text{PF}_6]^-$  with a  $M_n$  of  $85 \text{ kg}\cdot\text{mol}^{-1}$  measured *ex situ* by reflection optical microscopy at selected times within AAO templates of different pore sizes at 393 K.

In situ DS of PIL/IL [PF<sub>6</sub>]<sup>-</sup>

**Figure S12.** Ionic conductivity from *in situ* nDS for PIL/IL [PF<sub>6</sub>]<sup>-</sup> with a  $M_n$  of 6 kg·mol<sup>-1</sup> inside AAO nanopores with different pore sizes at 333 K: 400 nm (red), 65 nm (blue), 35 nm (olive), 25 nm (magenta) plotted as a function of the square root of time. The open circles represent the conductivity of PIL/IL [PF<sub>6</sub>]<sup>-</sup> during flow within AAOs. The conductivity values were corrected for porosity.

## Ion relaxation times (DS)

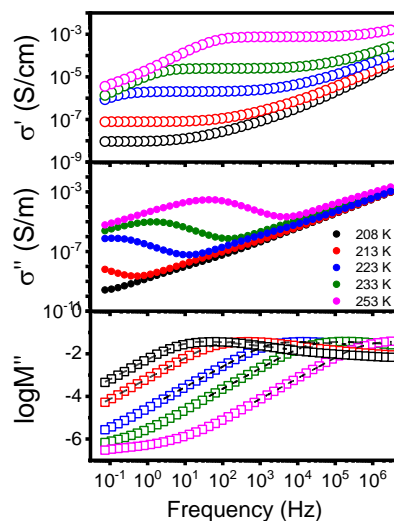


**Figure S13.** Real (top) and imaginary (middle) parts of the ionic conductivity of PIL/IL [TFSI]<sup>-</sup> in the bulk shown for the indicated temperatures. The modulus representation (bottom) is used to extract the characteristic relaxation times of ionic motion (dashed lines indicate representative fits) using the H-N function. The decrease in  $\sigma'(f)$  at low frequencies signifies the process of electrode polarization.

# Chapter 7. Fiber Formation of Semi-crystalline Polymers within Nanopores: The Role of Chain Entanglement and Infiltration Depth

## 7.1. Introduction

Understanding polymer behavior under nanoscale confinement is critical for applications ranging from nanofluidics to controlled release systems.<sup>1-5</sup> When polymers infiltrate nanopores, their molecular characteristics—particularly crystallinity<sup>6,7</sup>, molecular weight<sup>8</sup>, and entanglement<sup>9</sup>—play essential roles in dictating their morphology and structural evolution. One fascinating manifestation of this interplay is the spontaneous formation of nanofibers, which has been observed here under specific confinement and infiltration conditions. However, the mechanisms behind such fiber formation remain elusive.

We have employed SEM and explored fiber formation in a range of polymers with different degree of crystallinity and molar mass—specifically PEO, poly( $\epsilon$ -caprolactone) (PCL), poly(ethyl methacrylate) (PEMA), and poly(methyl methacrylate) (PMMA)—all infiltrated within V-shaped and cylindrical nanopores. We explored the conditions (amorphous vs semi-crystalline polymers, entangled vs unentangled, cylindrical vs V-shaped confinement, full vs partial imbibition) that resulted in stable fiber formation.

## 7.2. Experimental

**Materials.** Amorphous and semi-crystalline homopolymers were employed in the present study (**Table 1**). Polycaprolactone (PCL), poly(methyl methacrylate) (PMMA) and poly(ethyl methacrylate) (PEMA) were purchased from Polymer Source and used without further purification. The PEO samples with different molecular weights (PEO 1M, PEO 2k) were synthesized by Dr. Wagner and Mr. Thiel (MPI-P).<sup>10,11</sup>

**Table 1.** Summary of polymers and their characteristics used in this study.

Sample	$M_w$ (kg·mol <sup>-1</sup> )	$\bar{D}$	$M_e$ (kg·mol <sup>-1</sup> )	$T_m$ /K	$T_g$ /K
PEO 1M	100k	1.15	1.7	343	
PEO 2k	2	1.01	1.7	326	
PCL	7.7	1.81	1.8	348	
PEMA	7		--	--	343
PMMA	25	1.28	--	--	375

**Scanning Electron Microscopy (SEM).** High-resolution surface and cross-section images of AAOs were recorded using a Hitachi 8000 scanning electron microscope. To characterize the fiber formation, samples were cut, and the cross-sections were mounted vertically on aluminum SEM stubs using high-purity carbon tape. Imaging was conducted at a working distance of 4 mm. To assess the influence of accelerating voltage on fiber morphology, images were captured under varying conditions: 0.7 kV (30 mA), 1.5 kV (30 mA), 2.0 kV (10 mA), and 3.0 kV (10 mA).

**AAO templates.** We utilized V-shaped (V) and cylindrically-shaped (C) self-ordered nanoporous aluminum oxide (AAO) templates with only one open end. V-shaped AAOs were purchased from TopTemplates Technology Ltd. (Shenzhen, China). They featured a top pore diameter of 450 nm and a bottom pore diameter of 100 nm, with a pore depth of 2.5  $\mu\text{m}$ . Cylindrically-shaped AAOs (the pore diameter of 400 nm; pore depth about 100  $\mu\text{m}$ ) were prepared according to previously reported procedures.<sup>12-15</sup>

**Infiltration.** Polymer films were placed onto the surface of V- and C-AAO templates and allowed to infiltrate into the nanopores via capillary force. Each sample was held at a specific infiltration temperature—chosen to be above the melting point (for semicrystalline polymers) or glass temperature (for amorphous polymers)—for designated time intervals to achieve either partial or complete infiltration. Following infiltration, the samples were immediately quenched to room temperature to arrest further motion or crystallization.

### 7.3. Results and discussion

**A. PEO.** AAO templates were infiltrated with high molar mass PEO 1M at 358 K. The infiltration process was controlled based on Lucas-Washburn equation (LWE)  $L = \sqrt{\frac{\gamma R \cos \theta}{2\eta}} \sqrt{t}$ , where  $\gamma$  is the surface tension ( $= 28$  mN/m at 358 K),  $\eta$  is zero-shear viscosity in bulk ( $= 2.6 \times 10^6$  Pa s),  $\theta$  is the contact angle ( $= 48^\circ$ ), to achieve either partial or complete filling of the nanopores (**Figure 2**).

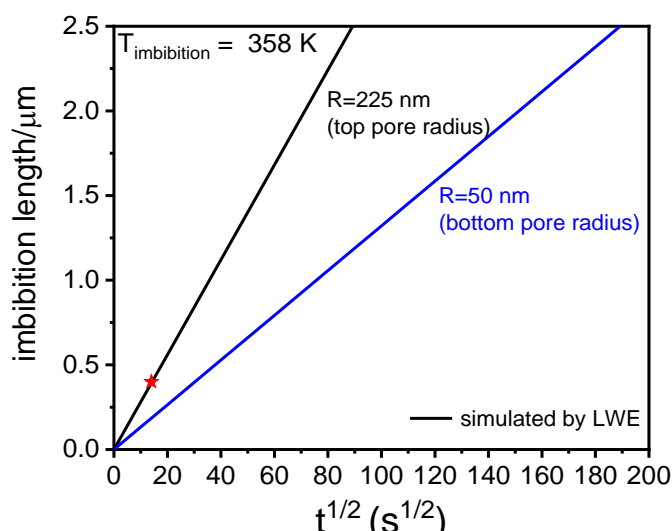


**Figure 1.** Imbibition lengths as a function of inverse of time. Solid lines represent imbibition lengths calculated from the LWE. Star point represents the measured imbibition length of PEO 1M for an imbibition time of 6 min.

**Figure 2a** presents SEM images of V-shaped AAO templates partially and fully infiltrated with PEO 1M. When the pores are only partially infiltrated (imbibition time,  $t \sim 6$  min), long and well-aligned polymer fibers are observed. These fibers elongate over time, and in some cases, they can eventually merge or break due to stretching. In contrast, complete infiltration (duration  $\gg 12$  h) suppressed fiber formation, producing a continuous amorphous film. Similar trends were observed in cylindrical nanopores (**Figure 2b**), although the resulting fibers were shorter and more disordered.

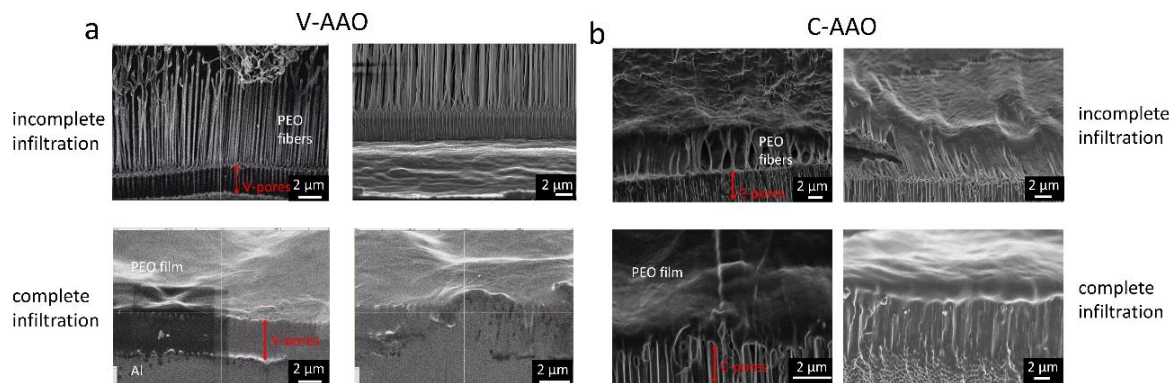


**Figure 2.** SEM images of PEO 1M infiltration into AAO templates under different conditions. (a) V-shaped AAO (V-AAO) and (b) cylindrical AAO (C-AAO) nanopores. Top panels show partially infiltrated samples where aligned PEO fibers are extracted from the nanopores. Bottom panels show completely infiltrated samples where no fibers are observed with an amorphous PEO film across the pore openings.

To better understand the mechanism of fiber formation, the evolution of PEO 1M fibers was quantitatively analysed over the course of time. **Figure 3a** depicts measurements of selected fibers with respect to the fiber length ( $L$ ) and width ( $W$ ). Evidently, fiber length increases whereas the width decreases, revealing elongation and thinning. In **Figure 3b**, the initial fiber volumes are already close to the theoretical infiltration volume ( $V_{theo} = 0.056 \mu\text{m}^3$ ) derived from the Lucas-Washburn equation ( $t = 196 \text{ s}$ ,  $L = 0.4 \mu\text{m}$ ). Furthermore, **Figure 3c** compares the evolution of fiber length for different applied voltages. A significant increase in fiber length is observed at higher voltages. Given the close match between measured fiber volume and the estimated polymer volume within the partially infiltrated nanopores, we propose that the fibers are formed by extracting material from the pore interior – a “digging” mechanism driven by the applied SEM voltage.

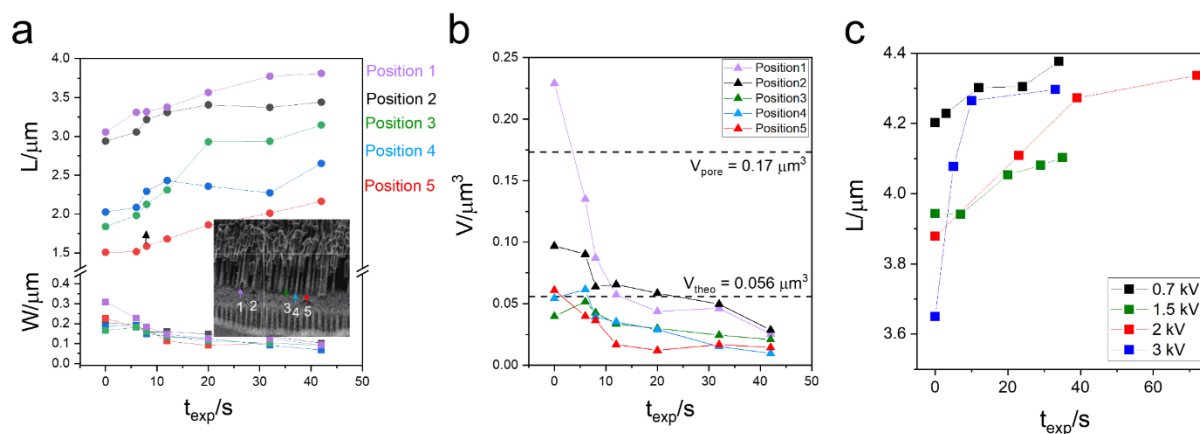


**Figure 3.** Evolution of PEO 1M fiber morphology and volume following partial infiltration into V-shaped AAO templates in SEM (Voltage is set to 3 kV). (a) Fiber length ( $L$ , circles) and width ( $W$ , squares) as a function of exposure time ( $t_{\text{exp}}$ ) at five lateral positions across the AAO membrane (positions indicated in the SEM inset). (b) Calculated evolution of fiber volume ( $V$ ) compared with the theoretical infiltrated volume ( $V_{\text{theo}} = 0.056 \mu\text{m}^3$ , dashed line) and total pore volume ( $V_{\text{pore}} = 0.17 \mu\text{m}^3$ , dashed line). (c) Fiber length as a function of exposure time at different voltages in SEM.

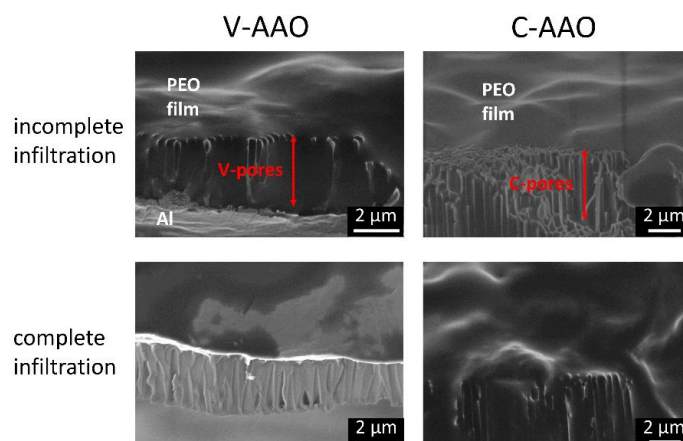


**Figure 4.** SEM images of low molar mass PEO (PEO 2k) partially or completely infiltrated into AAO templates. Images show cross-sectional views of (left) V-AAO and (right) C-AAO under two infiltration conditions: top row—partial infiltration; bottom row—complete infiltration. In all cases, PEO 2k remains as bulk-like without showing any fiber formation.

To further examine the influence of molecular weight and chain entanglement, we investigate the behavior of low molar mass PEO (PEO 2k). Its molar mass is below the entanglement molar mass. As shown in **Figure 4**, in both V-shaped and cylindrical nanopores, PEO 2k does not form fibers regardless of the infiltration length (partial infiltration,  $t = 2$  s, vs. complete infiltration,  $t = 12$  h). Instead, it remains in a continuous bulk-like film. These results

emphasize that chain entanglements, in addition to crystallinity, is a prerequisite for fiber formation. It suggests the role of entanglements to support fiber elongation.

**B. PCL.** Next, we explore the possibility of fiber formation in PCL, a semi-crystalline polymer with a molar mass  $M_w = 7.7 \text{ kg mol}^{-1}$ , above its entanglement ( $M_e = 1.8 \text{ kg mol}^{-1}$ ). The infiltration temperature was 403 K, much higher than the glass temperature (at this temperature,  $\eta = 3 \times 10^4 \text{ Pa s}$ ,  $\gamma = 8.8 \text{ mN/m}$ ,  $\theta = 55^\circ$ ). As shown in **Figure 5**, PCL fibers are formed under partial infiltration ( $t = 50 \text{ s}$ ) in both V-shaped and cylindrical nanopores. However, these fibers are generally disordered and short, even in the V-shaped nanopores whereas PEO 1M formed more ordered structures. Under complete infiltration conditions ( $t = 12 \text{ h}$ ), PCL did not form distinct fibers. In V-shaped nanopores, it showed some tendency toward fiber-like structures, but they remained embedded in a bulk-like morphology. These observations suggest that while PCL is entangled and semi-crystalline, its lower molar mass restricts the homogeneous fiber formation.

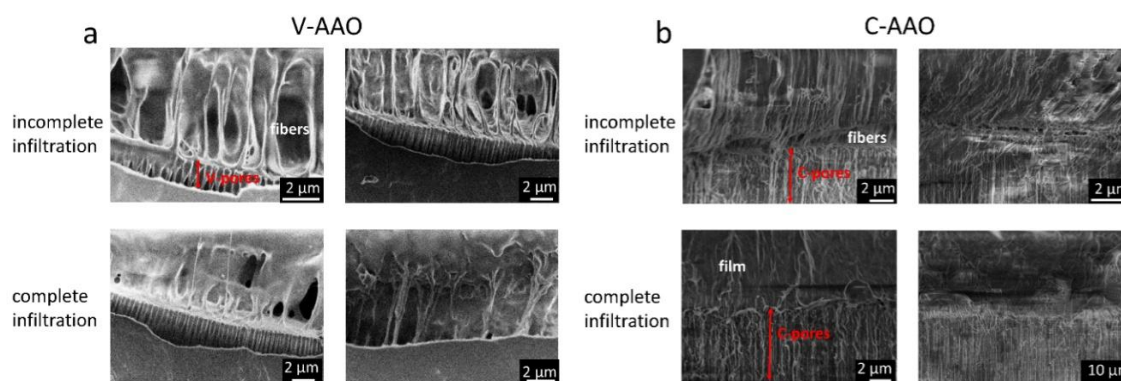


**Figure 5.** SEM images of PCL infiltrated into AAO templates with varying pore geometries and infiltration depths. (a) V-AAO and (b) C-AAO. Top panels: under incomplete infiltration, short and disordered PCL fibers are observed within both V-AAO and C-AAO, indicating limited fiber growth. Bottom panels: under complete infiltration, distinct fibers are not formed; instead, PCL adopts a bulk-like or film morphology, particularly evident in V-AAO.

**C. PEMA & PMMA.** Lastly, we investigated the infiltration behavior of two amorphous polymers, PEMA ( $M_w = 7 \text{ kg mol}^{-1}$ ) and PMMA ( $M_w = 25 \text{ kg mol}^{-1}$ ). For PEMA, infiltration was carried out at 403 K. Based on the Lucas-Washburn equation (where  $\eta = 0.14 \text{ MPa s}$ ,  $\gamma = 28.2 \text{ mN/m}$ ,  $\theta = 35^\circ$ ), imbibition times of 5 minutes and 12 hours were used for partial and complete infiltration, respectively. As shown in **Figure 6a**, PEMA maintains a continuous, non-fibrous morphology regardless of infiltration depth or pore geometry. This result aligns with expectations, confirming that the absence of crystallinity inhibits the development of structured, aligned fibers in AAO templates. Similarly, PMMA did not form fibers under any infiltration

conditions. As shown in **Figure 6b**, PMMA maintains a homogeneous, continuous film across both V-shaped and cylindrical nanopores, regardless of partial or complete imbibition. These observations suggest the key role of crystallinity and molar mass in enabling nanofiber formation. Evidently, long chains that can tie several crystallites are necessary to support the elongation of polymer fibers in half-infiltrated pores.

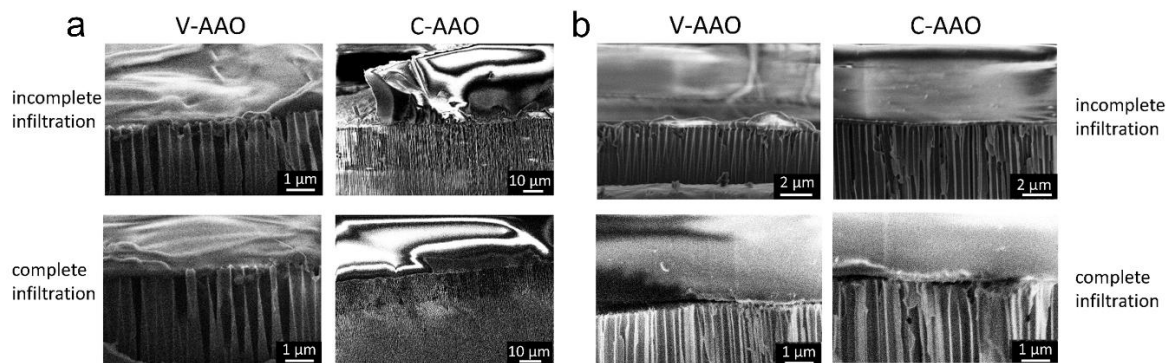


**Figure 6.** SEM images of amorphous polymers PEMA (a) and PMMA (b) infiltrated into AAO templates. In each case, V-AAO and C-AAO are shown under both incomplete (top rows) and complete (bottom rows) infiltration conditions. Both polymers exhibit continuous, film-like morphologies across all conditions, with no evidence of fiber formation.

#### 7.4. Conclusion

This study reported – for the first time- the formation of nanofibers in AAO templates from polymers with varying degree of crystallinity and molar mass. Our results demonstrate that fiber formation within confined nanopores occurs only when two key conditions are met: (i) the polymer is semi-crystalline, and (ii) its molar mass must exceed the entanglement molar mass. For PEO 1M, aligned fibers formed under partial infiltration in both V-shaped and cylindrical nanopores. Complete infiltration suppressed this behavior, leading to amorphous films instead. PEO 2k did not form fibers under any condition, highlighting the essential role of chain entanglement. PCL (semi-crystalline and with  $M > M_e$ ) formed only short and disordered fibers, likely due to the lower molar mass as compared to PEO. Amorphous polymers such as PEMA and PMMA did not form fibers, regardless of the molar mass, the infiltration depth or template geometry.

We proposed a mechanism in which fibers are pulled out of the nanopores by the applied voltage in SEM—a "digging" process that relies on partial infiltration. In order for the fibers to remain intact the polymer needs to have high molar mass (above  $M_e$ ) and to be semi-crystalline. Both result to high moduli that stabilize the fibers. We argue that long polymer chains that can tie several crystalline domains are required for fiber formation. While this

model offers a consistent explanation for the observed behavior, it remains a working hypothesis that requires further experimental validation.

## 7.5 References

- (1) Krutyeva M, Wischniewski A, Monkenbusch M, *et al.* Effect of Nanoconfinement on Polymer Dynamics: Surface Layers and Interphases. *Physical Review Letters*, **2013**, *110*, 108303.
- (2) Duan X, Chen H L, Guo C. Polymeric Nanofibers for Drug Delivery Applications: A Recent Review. *J Mater Sci Mater Med*, **2022**, *33*, 78.
- (3) Roth C B. Polymers under Nanoconfinement: Where Are We Now in Understanding Local Property Changes?. *Chem. Soc. Rev*, **2021**, *50*, 8050-8066.
- (4) Yang J, Chen Y, Yang Z, *et al.* Unveiling the Nanoconfinement Effect on Crystallization of Semicrystalline Polymers Using Coarse-Grained Molecular Dynamics Simulations. *Polymers*, **2024**, *16*, 1155.
- (5) Bocquet L, Charlaix E. Nanofluidics, from bulk to interfaces. *Chem. Soc. Rev.* **2010**, *39*, 1073-1095.
- (6) Yao Y, Alexandris S, Henrich F, *et al.* Complex Dynamics of Capillary Imbibition of Poly(Ethylene Oxide) Melts in Nanoporous Alumina. *Journal of Chemical Physics*, **2017**, *146*, 203320.
- (7) Schlegel I, Muñoz-Espí R, Renz P, *et al.* Crystallinity Tunes Permeability of Polymer Nanocapsules. *Macromolecules*, **2017**, *50*, 4725-4732.
- (8) Tu C-H, Steinhart M, Butt H-J, *et al.* In Situ Monitoring of the Imbibition of Poly(N-Butyl Methacrylates) in Nanoporous Alumina by Dielectric Spectroscopy. *Macromolecules*, **2019**, *52*, 8167-8176.
- (9) Yao Y, Butt H-J, Zhou J, *et al.* Capillary Imbibition of Polymer Mixtures in Nanopores. *Macromolecules*, **2018**, *51*, 3059-3065.
- (10) Yao, Y.; Alexandris, S.; Henrich, F.; Auernhammer, G.; Steinhart, M.; Butt, H. J.; Floudas, G. Complex dynamics of capillary imbibition of poly(ethylene oxide) melts in nanoporous alumina. *J Chem Phys* **2017**, *146*, 203320.
- (11) Tu, C. H.; Veith, L.; Butt, H. J.; Floudas, G. Ionic Conductivity of a Solid Polymer Electrolyte Confined in Nanopores. *Macromolecules* **2022**, *55*, 1332-1341.
- (12) Masuda, H.; Fukuda, K. Ordered Metal Nanohole Arrays Made by a Two-Step Replication of Honeycomb Structures of Anodic Alumina. *Science* **1995**, *268*, 1466–1468.
- (13) Masuda, H.; Hasegawa, F.; Ono, S. Self-ordering of Cell Arrangement of Anodic Porous Alumina Formed in Sulfuric Acid Solution. *J. Electrochem. Soc.* **1997**, *144*, L127–L130.
- (14) Masuda, H.; Yada, K.; Osaka, A. Self-ordering of Cell Configuration of Anodic Porous Alumina with Large-Size Pores in Phosphoric Acid Solution. *Jpn. J. Appl. Phys.* **1998**, *37*, L1340–L1342.
- (15) Steinhart, M. Supramolecular Organization of Polymeric Materials in Nanoporous Hard Templates. *Adv. Polym. Sci.* **2008**, *220*, 123–187.

## Conclusion

Ionic systems, including ILs and PILs, are central to a wide range of electrochemical applications including batteries, supercapacitors, fuel cells, and ion-conducting membranes. Their unique transport, thermal, and structural properties make them promising candidates for next-generation energy storage technologies. To optimize device performance, porous electrode materials are often employed, making it essential to understand how spatial confinement affects ion transport. Nanoscale environments can lead to significant deviations in transport behavior compared to the bulk. Yet, the mechanisms underlying these changes remain poorly understood. In particular, how pore geometry, surface interactions, and molecular structure influence ion mobility at the nanometer scale is a fundamental question with scientific and technological relevance.

This thesis addresses this gap by investigating ion transport in confined ionic systems using *in situ* nanodielectric spectroscopy. A diverse range of ionic systems (ILs, PILs, and their mixtures) were studied under various confinement geometries, enabling a broad exploration of ion dynamics at the nanoscale.

For ILs, the study revealed that while bulk conductivity is governed primarily by ion size and Coulomb interactions, nanoscale confinement introduces surface adsorption effects that drastically reduce the number of mobile ions, thereby suppressing conductivity. In addition, in some crystallizable ILs, confinement also inhibits crystallization, highlighting the importance of the critical nucleus size. In such cases confinement provides the means towards increasing conductivity by suppressing crystallization. Among pore geometries, V-shaped nanopores consistently provide higher ionic conductivity than cylindrical ones, despite both being lower than bulk values. This difference is attributed to variations in surface charge distribution: uniform in cylindrical pores and more uneven in V-shaped geometries. However, both geometries induce similar structural changes in ILs. Future studies will extend these investigations to smaller pore diameters and a broader range of ILs.

In PIL systems, where only a single ion is mobile, the interplay between polymer architecture and ion dynamics was explored. Ion conductivity and glass “transition” behavior in bulk are closely linked to the structural features of the tethered cation. Cations positioned near the polymer backbone tend to associate strongly with counterions, stiffening the chain, increasing the glass temperature, and decreasing conductivity. In contrast, cations with more

flexible linkers exhibit enhanced mobility and reduced glass temperatures. Under confinement, a pronounced *decoupling* between ion motion and polymer segmental dynamics was observed, especially near the glass temperature. This decoupling becomes more significant in smaller pores, where confinement reduces the activation energy required for ion transport. These results indicate that spatial confinement can serve as a means of enhancing conductivity at low temperatures by mechanically softening the local environment around mobile ions.

Finally, the behavior of IL/PIL mixtures was investigated. In the bulk, thermal, viscosity, and conductivity measurements in symmetric IL/PIL mixtures revealed that they are locally *heterogeneous*. When the same symmetric mixtures are brought into contact with nanoporous membranes the capillary force enhances the heterogeneity and triggers *demixing* in macroscopic length scales. By a combination of *ex situ* polarized optical microscopy measurements of the evolution of the imbibition length, and *in situ* dc-conductivity measurements, the latter by nanodielectric spectroscopy, it was shown that the IL penetrates first the nanopores followed by a minority of the PIL. At later times, part of the minority PIL is adsorbed at the pore walls, producing a further reduction in dc-conductivity. Temperature dependent conductivity measurements following the imbibition process further demonstrate the enrichment of pores by the IL. The results demonstrate, for the first time, the separation of a mixture of ionic compounds composed from an IL and a PIL by the different imbibition speeds in nanopores.

These findings not only elucidate the fundamental role of nanoscale confinement in modifying transport and structural behavior, but also point toward new strategies for controlling material properties through confinement engineering. While the current study focused on static, well-defined geometries, future work should explore more complex pore architectures, chemically active surfaces, and dynamically tunable confining membranes. Additionally, coupling nanodielectric spectroscopy with molecular simulations could provide deeper mechanistic insights.

## Acknowledgements

Finally, I have come to this section of my thesis, which also marks the end of my student journey. The path of pursuing a Ph.D. has been filled with both challenges and surprises. Research is often a process of “rise and fall... and fall again”, frequently placing me in a state of self-doubt. Yet it is precisely through these ups and downs that I have grown stronger and more resilient.

First and foremost, I would like to express my deepest gratitude to my two supervisors, Prof. Dr. Hans-Jürgen Butt and Prof. Dr. George Floudas, for giving me the opportunity to pursue my doctoral studies at the Max Planck Institute for Polymer Research (MPIP), an institution with a truly international academic environment. I sincerely thank Prof. Dr. Hans-Jürgen Butt, a highly professional and kind-hearted scientist, for his unwavering support and guidance throughout my research. His constant support and positivity have been instrumental in boosting my confidence. I consider myself extremely fortunate to have been a part of AK Butt group!

I am especially indebted to Prof. Dr. George Floudas, my direct supervisor. It has been a privilege to be mentored by someone with such outstanding accomplishments in his field. In every discussion, he could always pinpoint the core issues in my work and provide clear and constructive advice. Prof. Dr. George Floudas is a scientist who approaches research with great seriousness and rigor, and he holds his students to equally high standards. Although I once struggled to meet these expectations, I now look back and feel deeply grateful for his demanding yet supportive guidance. It has helped me grow rapidly, and more importantly, instilled in me a strong work ethic and discipline that I will carry with me both in research and in life.

I would also like to thank all the members in MPIP. Everyone has been incredibly friendly and helpful, always ready to support me whether in academic work or daily life. Special thanks to Mr. Gunnar Glaßer for his SEM guidance (and his wonderful sense of humor); Mr. Andreas Hanewald for the rheological measurements; Mr. Andreas Best for sharing his knowledge of optics. I am also grateful to Prof. Dr. Martin Steinhart (University of Osnabrück) for provided

the AAO templates. Many thanks to the colleagues in the Greek research group. You are truly lovely people, and I cherish the beautiful memories we made together at the BDS conferences.

My heartfelt thanks go to Dr. Chien-Hua Tu. From picking me up at the airport, to guiding me in the lab and doing experiments together, and even after he left the institute, he has always patiently answered my questions and generously shared his expertise in dielectric spectroscopy. He was like a personal mentor in the early stages of my Ph.D., and his support made a huge difference. I also want to thank Dr. Yazhi Liu. When I first arrived in Germany and felt lost and overwhelmed, she was the first person to warmly reach out, invite me to group activities, and help me integrate into a new environment. Love and miss you!

I am also grateful to all the wonderful friends I met in the AK Butt group: Dr. Yaolei Xiang, Franjo Weber, Liying Shen, Jiaqi Xing, Xiaotang Shi, Dr. Jianwei Zhang, Zhongyuan Ni, Lin Jian, Xicheng Bao, Minqi Zou, Hexuan Mao. Though we will part ways, the joyful moments we shared will always remain with me.

Last but certainly not least, I would like to thank my parents and my younger brother. Thank you for your unconditional support and trust in every decision I have made. Your love is my eternal source of strength.

My deepest gratitude in the end goes to the younger version of myself, who, with fearless determination, came alone to a foreign land and began this extraordinary journey.

Grateful for every encounter! Looking forward to what comes next 😊

Yun Dong  
Mainz  
August 2025

# Curriculum Vitae

## Yun Dong

14<sup>th</sup>, February, 1996

Max-Planck-Institute for Polymer Research

Tel: +49-1748627661

Email: [dongy@mpip-mainz.mpg.de](mailto:dongy@mpip-mainz.mpg.de)

Address: Room 0.203, Ackermannweg 10, 55128 Mainz, Germany

## EDUCATION

---

**Ph. D.** Max-Planck-Institute for Polymer Research **Mainz, Germany**  
Materials Science Sept. 2021 - present

- Supervisor: Prof. Dr. Hans-Jürgen Butt & Prof. Dr. George Floudas

**M. S.** Tianjin University **Tianjin, China**  
Materials Science and Engineering Sept. 2018 – June. 2021

- Supervisor: Prof. Dr. Dong-po Song

**B. Sc.** Qingdao University of Science and Technology **Shandong, China**  
Polymer Science and Engineering Sept. 2014 – June. 2018

- Thesis title: Effect of Different Bonding Systems on The Interfacial Adhesion of EPDM/Polyester Cord

## RESEARCH EXPERIENCE

---

Max-Planck-Institute for Polymer Research, *PhD researcher*

Lab of Prof. Dr. Hans-Jürgen Butt and Prof. Dr. George Floudas Sept. 2021 – present

**Project 1:** Developed in situ nanodielectric techniques to study ionic liquid behavior inside cylindrical nanopores

- Techniques: Broadband Dielectric Spectroscopy (BDS), SEM, Rheology, DSC, Anodic Aluminum Oxide (AAO) nanopores, Chemical Etching, Metal Sputtering, Static- and Dynamic Contact Angle

**Project 2:** Investigated ion transport in polymerized ionic liquids under confinement

- Techniques: In-situ Nanodielectric Spectroscopy (self-developed setup, novel characterization method), Polymerized Ionic Liquid Synthesis

**Project 3:** Studied cooperative motion between ions and polymer chains (ionic liquids/polymerized ionic liquids mixture) during nanopore infiltration

- Techniques: Membranes Modification, Surface Tension Measurements

**Project 4:** Analyzed effects of nanopore shape on structure and dynamics of ion systems

- Techniques: V-shaped Nanopores, AFM

## Tianjin University

Lab of Prof. Dr. Dong-po Song Sept. 2018 – June. 2021

**Project 1:** Design and fabricate tunable photonic microspheres with elastic properties via self-assembly of bottlebrush block copolymers

- Techniques: Bottlebrush Block Copolymer Polymerization (ATRP, ROMP), Self-Assembly in 3D Confinement, Micro-Spectroscopy, Photo-cross-linking, Micro Compression Test

**Project 2:** Explored the effect of confinement on morphology and optical properties of photonic microspheres

- Techniques: Microfluidic Emulsification, In situ Observation of Droplet Evaporation, TEM

## PUBLICATIONS

---

1. **Dong, Y.**; Matyjaszewski, K.; Steinhart, M.; Butt, H.-J.; Floudas, G. “Effect of imidazolium-based cations with different structure on ion dynamics under confinement” *Macromolecules*, **2025**, 58, 7534-7543.
2. **Dong, Y.**; Steinhart, M.; Butt, H.-J.; Floudas, G. “Effects of V-shaped Confinement on the Phase State and Ion Dynamics of Ionic Liquids Containing the 1-Butyl-3-methylimidazolium Cation” *J. Phys. Chem. C* **2025**, 129, 7530-7540.
3. **Dong, Y.**; Steinhart, M.; Butt, H.-J.; Floudas, G. “Demixing of Polymerized Ionic Liquid/Ionic Liquid Mixtures by Infiltration in Nanopores” *Macromolecules* **2024**, 57, 11, 5409-5420.
4. **Dong, Y.**; Steinhart, M.; Butt, H.-J.; Floudas, G. “Conductivity of Ionic Liquids In the Bulk and during Infiltration in Nanopores” *J. Phys. Chem. B* **2023**, 127, 31, 6958–6968.
5. **Dong, Y.**; Ma, Z.; Song, D.-P.; Ma, G.-Q.; Li, Y.-S. “Rapid Responsive Mechanochromic Photonic Pigments with Alternating Glassy-Rubbery Concentric Lamellar Nanostructures” *ACS Nano* **2021**, 15, 5, 8770–8779.
6. Kardasis, P.; Tzourtzouklis, I.; **Dong, Y.**; Meier-Merziger, M.; Butt, H.-J.; Frey, H.; Floudas, G. “Imbibition and Adsorption of a Bottlebrush Polymer in Nanopores” *Macromolecules* **2025** (10.1021/acs.macromol.4c02952)
7. Leibauer, B.; Pop-Georgievski, O.; Sosa, M. D.; **Dong, Y.**; Tremel, W.; Butt, H.-J.; Steffen, W. “How Surface and Substrate Chemistry Affect Slide Electrification” *J. Am. Chem. Soc.* **2024**, 146, 14, 10073–10083.
8. Darvish, F.; Shumaly, S.; Li, X.; **Dong, Y.**; Diaz, D.; Khani, M.; Vollmer, D.; Butt, H.-J. “Control of spontaneous charging of sliding water drops by plasma-surface treatment” *Sci Rep* **2024**, 14, 10640.
9. Li, Y.-L.; Chen, X.; Geng, H.; **Dong, Y.**; Wang, B.; Ma, Z.; Pan, L.; Ma, G.-Q.; Song, D.-P.; Li, Y.-S. “Oxidation Control of Bottlebrush Molecular Conformation for Producing Libraries of Photonic Structures” *Angew. Chem. Int. Ed.* **2021**, 60, 3647 – 3653.

## PRESENTATIONS in CONFERENCES

---

- ◆ Sept. 2024 Demixing of Polymerized ionic liquid/ionic liquid Mixtures by Infiltration in Nanopores  
*12<sup>th</sup> Conference on Broadband Dielectric Spectroscopy and its applications*  
Lisbon, Portugal (**Best Poster Award**)
- ◆ Sept. 2023 Ion Mobility of a Polymerized Ionic Liquid under Confinement  
*Ostwald Colloquium: Interface-Mediated Process in Soft Matter*,  
Darmstadt, Germany (**Poster Presentation**)
- ◆ Sept. 2022 Conductivity of Ionic Liquids During and After Infiltration in Nanopores  
*11<sup>th</sup> Conference on Broadband Dielectric Spectroscopy and its applications*,  
Donostia-San Sebastian, Spain (**Poster Presentation**)

## SKILLS & TECHNIQUES

---

- ◆ Polymer and Block Copolymer Synthesis (ATRP, RAFT, ROMP)
- ◆ Nanoporous Membrane Fabrication and Surface Modification
- ◆ In-situ Broadband Dielectric Spectroscopy (custom setup)
- ◆ Characterization Tools: SEM, Rheometer, XRD, TEM, Confocal Microscope, Microspectroscopy